Galactic Centers near and far

Sub-millimeter Observations of three Seyfert galaxies and the Galactic Center

INAUGURAL-DISSERTATION

zur
Erlangung des Doktorgrades
der Mathematisch-Naturwissenschaftlichen Fakultät
der Universität zu Köln

vorgelegt von

Lydia Moser
aus Köln

Köln 2017

Berichterstatter:	Prof. Dr. Andreas Eckart
	Prof. Dr. Anton Zensus

Tag der mündlichen Prüfung:	3. Juni 2016

Abstract

The evolution of galaxies in terms of mass accretion and matter transport is still an open topic in research. My thesis consists of two parts that are bridged by a common theme: the properties of the interstellar medium interstellar matter (ISM) and star formation in centers of galaxies, studied in the (sub-)mm wavelength regime.

The first part of my thesis deals with the results from Submillimeter Array (SMA) observations of molecular gas (low CO transitions) at sub-kpc (~3″) resolution of three Seyfert 1 galaxies from the 'low-luminosity quasi stellar object (LLQSO) sample', which covers a redshift range of z ~ 0.01 - 0.06. The goal of the LLQSO sample is investigate the signs of internal or external triggers enhanced activity (i.e., star formation and accretion onto the supermassive black hole (SMBH)) in the centers of galaxies and their frequency with respect to the nuclear activity.

Two sources, HE 0433-1028 and HE 1108-2813, were observed in ^{12}CO(2–1) and ^{13}CO(2–1) and the third, HE 1029-1831, in ^{12}CO(3–2) and HCO^{+}(4–3) line emission. Intriguingly, in all three galaxies the molecular gas accumulates at the center within a radius < 2 kpc and the gas kinematics indicate the presence of a decoupled central unresolved component. The R_{21} =^{12}CO/^{13}CO(2–1) line luminosity ratios obtained for HE 0433-1028 and HE 1108-2813 are significantly enhanced with $R_{21} \gtrsim 20$ in the central region, indicating them to be warm and/or turbulent. Strikingly, also the ^{12}CO(3–2)/(1–0) line luminosity ratio in HE 1029-1831 suggests a higher excitation phase with $r_{31} \sim 1$, apart from the cold or diffuse gas phase implied by $r_{21} \sim 0.5$ for all three of them. From this, together with the Luminous Infrared Galaxy (LIRG) typical infrared luminosities of $L_{\rm IR} \geq 10^{11} L_{\odot}$, I conclude that the emission in the centers of these Seyferts is strongly affected by diffuse gas due to violent star formation. Indeed, the centers of these galaxies seem to contain a circumnuclear starburst with minimum molecular gas mass and starformation rate (SFR) surface densities around Σ_{mol} = 70 - 540 $M_{\odot}$ pc^{-2} and $\Sigma_{\rm SFR}$ = 1.3 - 3.8 $M_{\odot}$ kpc^{-2}yr^{-1}. Therefore, the galaxies' ISM state is likely to be better described by a mass conversion factor typical for Ultraluminous Infrared Galaxies (ULIRGs), as suggested by the dynamical and dust masses. My work on these data shows how much information on the state of the molecular gas can already be obtained from these medium spatial resolutions, i.e. on 0.5 - 1 kpc-scales.

The second part covers interferometric continuum and line emission data from the Atacama Large Millimeter/submillimeter Array (ALMA) of the inner 4 parsec (approximately 100″) surrounding the SMBH, Sagittarius A* (Sgr A*), at the Galactic Center (GC).

It is a region of extreme conditions not only in terms of intense IR to UV radiation from the nuclear stellar/star cluster (NSC) and X-ray emission from a population of stellar remnants and Sgr A*, but especilly in terms of turbulence and shocks due to stellar winds and tidal shear. Furthermore, it comprises several overlapping molecular and ionized structures that can be studied in term of feeding inflow and star formation potential. Its proximity makes the GC a unique laboratory for our understanding of galactic nuclei and galaxy evolution on the smallest accessible scales.

I present serendipitous detections of line emission towards Sgr A* and its environment with ALMA in band 3, 6, and 7. This up to now highest resolution ($<0.75''$) view of the GC in the sub-millimeter (sub-mm) domain shows molecular gas at projected distances $\lesssim 1''$ from the SMBH. Among the highlights are: the very first 340 GHz map of the minispiral, the very first and highly resolved detection of sub-mm molecular emission in the immediate vicinity of the SMBH, and the highly resolved structures of circumnuclear disk (CND) features, especially of a region comprising a methanol class I maser closest to the SMBH.

The emission in H39α and of the 100 GHz continuum imply a uniform electron temperature around $T_e \sim 6000$ K for the minispiral. Sgr A* has a spectral index ($S \propto \nu^{\alpha}$) of $\alpha \sim 0.5$ at 100 - 250 GHz and $\alpha \sim 0.0$ at 230 - 340 GHz. The spectral indices of the luminous objects in the inner minispiral tend to -0.1 indication Bremsstrahlung emission, while the minispiral exterior shows the growing importance of the dust component with increasing frequency.

The clumpy molecular gas distribution is represented best by the CS emission. Further species detected are $H^{13}CO^+$, HC_3N, SiO, SO, C_2H, CH_3OH, ^{13}CS and N_2H^+. Most of the emission can be found at positive velocities and in a region limited by the sources IRS 3 and 7, and the minispiral Bar and Northern Arm. For some few regions in the field, the molecular emission appears at velocities of up to 200 km s^{-1}. Probably, this central association (CA) of clouds is an infalling group of clouds composed of denser cloud cores and diffuse gas. I calculated three times higher CS/X (X: any other observed molecule) ratios for the CA than for the CND which hints at a combination of higher excitation - by a temperature gradient and/or IR-pumping - and abundance enhancement due to UV- and/or X-ray emission. Assuming the NSC as the cause, CA must be closer to the center than the CND is to the center.

Within the CND itself, I discerned two interesting regions: One region emits in lines of all molecular species and higher energy levels observed in this and earlier studies. Furthermore, it harbours a methanol class I maser. The other region shows line ratios similar to the CA. Beyond the CND, I discover that the largest accumulations of traditionally quiescent gas tracer N_2H^+ match the largest infared (IR) dark clouds in the field. The previously detected methanol class I masers in these infrared dark clouds (IRDCs) coincide with the methanol emission observed by ALMA. I conclude, that all of these special regions should be investigated in more detail in the context of hot/cold core and extreme photon dominated region (PDR)/X-ray dominated region (XDR) chemistry and consequent star formation in the GC. My work on these ALMA Cycle 0 data give a prospect on the many riddles to solve - and to discover - thanks to the superb resolution of the current ALMA facility.

Zusammenfassung

Die Evolution von Galaxien, in Form von Massenakkretion und dem Transport von Materie, ist weiterhin Gegenstand aktueller Forschung. Diese Thematik bildet auch den Rahmen, in den sich meine Dissertation einordnet. Sie besteht aus zwei Teilen, die durch eine gemeinsame Fragestellung im Zusammenhang stehen: Den Eigenschaften des interstellaren Mediums und der Sternentstehung in Galaxien, gestützt auf Untersuchungen im (sub-)mm Wellenlängenbereich.

Im ersten Teil meiner Dissertation präsentiere ich die Ergebnisse aus interferometrischen Beobachtungen von molekularem Gas (basierend auf niedrigen CO Übergängen) mit sub-kpc ($\sim 3''$) Auflösung in drei Seyfert 1 Galaxien mit dem Submillimeter Array. Diese Galaxien sind Teil des 'low luminosity quasi stellar object (LLQSO) sample', einer Auswahl an LLQSOs mit einer Rotverschiebung im Bereich von z ~ 0.01 - 0.06 mit dem Ziel, Anzeichen interner und externer Auslöser für erhöhte Aktivität, d.h. Sternentstehung und Akkretion auf das zentrale, supermassive schwarze Loch (SMBH), in Galaxienkernen zu untersuchen. Zwei der Quellen, HE 0433-1028 und HE 1108-2813, wurden in ^{12}CO(2–1) und ^{13}CO(2–1) und die dritte, HE 1029-1831, in ^{12}CO(3–2) und HCO^{+}(4–3) Linienemission beobachtet. Bemerkenswerterweise sammelt sich in allen drei Galaxien das molekulare Gas innerhalb eines Radius von 2 kpc um die Galaxienkerne an, und die Gas-Kinematik zeigt Hinweise dafür, dass sich eine entkoppelte, rÃ¤umlich unaufgelöste Komponente im Zentrum gebildet hat. Die R_{21} =^{12}CO/^{13}CO(2–1) Linienleuchtkraftverhältnisse für HE 0433-1028 und HE 1108-2813 sind signifikant erhöht mit $R_{21} \gtrsim 20$ im Zentrum, was auf warmes und/oder turbulente Gas hinweist. Selbst das ^{12}CO(3–2)/(1–0) Linien Leuchtkraftverhältnis für HE 1029-1831 weist auf eine höher angeregte Gasphase hin mit $r_{31} \sim 1$, abgesehen von der kalten oder diffusen Gasphase, die von $r_{21} \sim 0.5$ für alle drei Objekte angedeutet wird. Zusammen mit den für LIRG typischen Infrarotleuchtkräften von $L_{\rm IR} \geq 10^{11} L_\odot$ komme ich zu dem Schluss, dass die Emission in den Zentren dieser Seyfert Galaxien wegen heftiger Sternentstehung stark von dem diffusen Gas beeinflusst wird. Tatsächlich beherbergen die Zentren dieser Galaxien einen zirkumnuklearen Starburst, mit einer unteren Grenze für die molekularer Gasmassen- und Sternentstehungsratenoberflächendichten um Σ_{mol} = 70 - 540 $M_\odot$ pc^{-2} and $\Sigma_{\rm SFR}$ = 1.3 - 3.8 $M_\odot$ kpc^{-2}yr^{-1}. Daher wird das interstellare Medium hier höchstwahrscheinlich besser von einem für ULIRGs typischen Massenkonversionsfaktor beschrieben, wie es auch von den dynamischen Massen und den Gasmassen suggeriert wird. Die Ergebnisse meiner Arbeit zeigen deutlich, wie viele Erkenntnisse über den Zustand des molekularen Gases schon bei

solch moderater räumlichen Auflösung erzielt werden können.

Im zweiten Teil behandele ich interferometrische Daten zu Kontinuum- und Linienemission mit Atacama Large Millimeter/submillimeter Array (ALMA) von den inneren 4 parsec (ca. 100″) des Galaktischen Zentrums (GC), die das SMBH Sgr A* umgeben. Diese Region ist von extremen Bedingungen geprägt, nicht nur in Form von intensiver IR und UV Strahlung des nuklearen Sternenhaufens, sondern insbesondere auch auf Grund von Turbulenzen und Schocks, die durch stellare Winde und Gezeitenkräfte verursacht werden. Darüber hinaus beherbergt diese Region auch mehrere überlappende molekulare und ionisierte Strukturen, die auf Zufluss von Materie und Sternentstehung untersucht werden können. Seine Nähe macht das Galaktische Zentrum zu einem einzigartigen Labor für die Untersuchung von Galaxienkernen und Galaxienevolution auf kleinsten Skalen.

Ich präsentiere zufällige Detektionen von Linienemission in einem projezierten Abstand von >1″ zu Sgr A* in den ALMA Bändern 3, 6 und 7 mit einer für das GC bisher höchsten Auflösung (<0.75″) im sub-Millimeter Wellenlängenbereich. Herausragende Ergebnisse sind unter anderem: Die erste 340 GHz Karte der Minispirale, die erste (und hoch aufgelöste) Detektion von molekularer sub-mm Linienemission in der direkten Umgebung des SMBH und hoch aufgelöste Strukturen der zirkumnuklearen Scheibe CND, insbesondere in einer Region mit dem dem GC nächstgelegenen Methanol Klasse I Maser. Basierend auf der 100 GHz Kontinuum- und H39α Emission erhalte ich eine Elektronentemperatur von ca. $T_e \sim 6000$ K für die Minispirale. Der Spektralindex ($S \propto \nu^{\alpha}$) von Sgr A* ist ~ 0.5 bei 100 - 250 GHz und ~ 0.0 bei 230 - 340 GHz. Die hellen Quellen im Zentrum zeigen Bremsstrahlung ($\alpha \sim -0.1$), während Staubemission im Äußeren der Minispirale auftritt ($\alpha > 0$). Insgesamt finde ich die Moleküle CS, $H^{13}CO^+$, HC_3N, SiO, SO, C_2H, CH_3OH, ^{13}CS und N_2H^+. Der Großteil der klumpig verteilten Emissions weist positive Geschwindigkeiten auf und liegt in einer Region zwischen dem nördlichen Arm der Minispirale, dem Balken sowie den Quellen IRS 3 und 7. Die Erklärung könnte eine einfallende Wolke sein, die aus dichteren, in diffusem Gas eingebetteten Klumpen besteht. Die zentrale Ansammlung (CA) von Wolken zeigt dreimal höhere CS/X (X: beliebiges anderes beobachtetes Molekül) Linienleuchtkraftverhältnisse an als die CND, was auf eine Kombination aus höherer Anregung (Temperaturgradient oder IR-Pumpen) und eine erhöhte Häufigkeit von CS auf Grund von UV- und/oder Röntgenstrahlung hinweist. Daher schließe ich, dass sich die CA näher am Zentrum befindet als die CND. Zwei Regionen in der CND zeigen sich besonders auffällig. Die eine zeigt Emission in allen Molekülarten, auch in höheren Energieniveaus, sowie einen Methanol Klasse I Maser. Die andere zeigt ähnliche Linienverhältnisse wie die der CA. Außerhalb der CND finde ich Emission des ruhigen Gas-Tracer N_2H^+ im Gebiet der größten IR-dunklen Wolken in der Region. Mehanol Emission wird in und um die Methanol Klasse I Maser der selben Region detektiert. Ich halte diese speziellen Regionen besonders interessant für weitere Studien im Kontext der Astrochemie in heißen/kalten Kernen und extremen PDR/XDR, und der Sternentstehung im GC. Meine Arbeit an den ALMA Cycle 0 Daten gibt hier einen eindrucksvollen Ausblick auf viele Rätsel, die es noch, dank der hervorragenden Auflösung der neuen ALMA Beobachtungseinrichtung, zu lösen - und zu entdecken - gilt.

Contents

Chapter 1

Introduction

Where do we come from? Where do we go to?

These fundamental questions are not restricted to the human life time, but can be extended up to the life of galaxies, the Universe, and maybe beyond. My thesis can, as for the most of us astronomers, only give an infinitesimal contribution to the answer to the puzzle of the evolution of galaxies.

Hierarchical ("bottom-up") structure formation, as predicted by the Λ Cold Dark Matter (ΛCDM) cosmology, is the currently best model to describe the growth of galaxies: As the young universe cooled due to expansion, quantum-fluctuations in the Cold Dark Matter (CDM) could grow to larger and larger overdensities (halos) and began to condense slowly towards the honeycomb-like large-scale structure ("cosmic web"), as we see the distribution of galaxies and galaxy clusters today, while the baryonic matter was still coupled to the photons. Once the universe had cooled down towards the recombination of electrons and protons ($z \sim 1000$), the baryonic matter followed the potential wells created by the CDM halos to form the protogalaxies and within them the first stellar clusters. By further accretion of baryonic and non-baryonic matter or even collisions between each other, these protogalaxies developed a central black hole (BH), globular clusters and halo stars, while they evolved into stellar bulges, and eventually into galaxies. It might be indeed this coevolutional scenario of galaxies' stellar bulges and their SMBH (e.g. Hopkins *et al.* 2008) that manifests itself in the observed strong correlations between the mass of a SMBH and the host galaxy properties, like the bulge mass, bulge luminosity, or central stellar velocity dispersion (Gebhardt *et al.* 2000; Merritt and Ferrarese 2001; Tremaine *et al.* 2002; Ferrarese and Ford 2005,$M_{\rm BH}$–σ).

While the bottom-up model gives us the framework for galaxy evolution, i.e. larger structures form by the merging of smaller structures, the details on the SMBH and spheroid growth

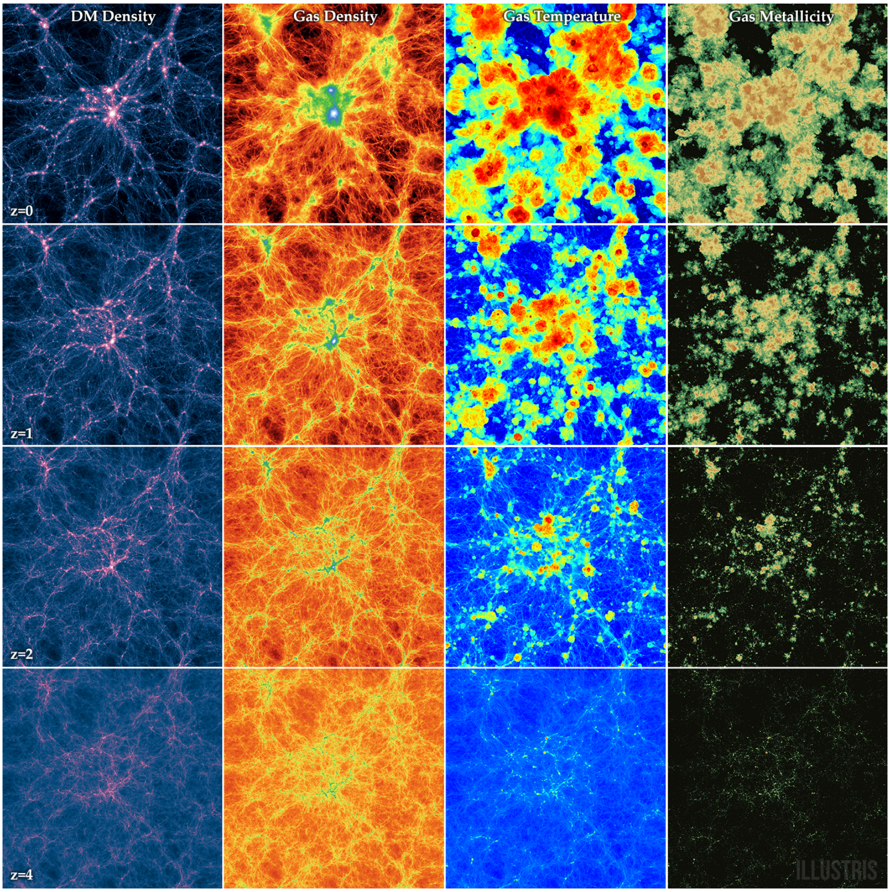

Figure 1.1: *Evolution of (from left to right) dark matter density, gas density, gas temperature, and gas metallicity with redshift z=4 to z=0 (bottom to top). Credit to "Illustris Collaboration" / "Illustris Simulation" (http://www.illustris-project.org/media/).*

are not fully understood. While galaxy interactions up to mergers are an obvious and efficient tool to remove angular momentum from the gas so that it can fall towards the potential well, the centers of galaxies can accrete gas even without such violent encounters via secular evolution. In this way, specific transient hydrodynamic density patterns, e.g. bars or spiral arms, appear to be able to transport the angular momentum of the gas within a galactic disk to its outer regions. The efficiency, size scales, and the frequency of these internal triggers over a galaxy's lifetime as well as the correlation of the different secular feeding mechanism with the galaxy's properties, redshift, and the SMBH's accretion activity level are far from being understood. The picture on the feeding in general gets even more complicated due to a likely feedback from the infall induced star formation and accretion onto the SMBH in the form of radiation and outflows/jets.

Therefore, to gain insight into the processes for matter transport in galaxies over time, statistically robust multi-wavelength and diagnostic line emission studies at all redshifts are necessary. A high angular resolution (pc to kpc scales) is crucial to assess the distribution of a gas and stars, their kinematics, the excitation state of the gas (e.g. turbulence, radiative heating, etc.), and the characteristics of the stellar population (e.g. age, mass, etc.), because these properties change significantly with galactocentric distance, as it can also be seen in this thesis, and global estimates conceal the important small scale information. Many studies have been conducted for the local universe (z < 0.01) due to the limited spatial resolution of the telescopes in the last decades. With the advance of more sophisticated instruments and facilities, more distant objects can be observed at scales comparable to the local galaxy sample observations. In the first part of my thesis, I present the results from SMA observations of molecular gas at sub-kiloparsec (kpc) resolution of three active galaxies from the LLQSO sample, which covers a redshift range of $z \sim 0.01$ - 0.06. I find the gas in the centers of these galaxies to be severely impacted, most likely by large scale dynamics and/or star formation.

Nevertheless, the galaxy, whose SMBH and environment can be observed at the highest angular resolution, will always be our own galaxy, the Milky Way. The centers of galaxies are believed to run frequently (every ~ 100 Myrs) through active periods that may last few 10 Myrs (e.g. Combes 2001,and therein) and indeed, evidences are accumulating that our currently faint Milky Way's SMBH, Sgr A*, has been in a remarkably higher accretion activity state in the past than is seen what is seen today. The proximity of our GC allows us to analyse what can happen on sub-parsec (pc) around a SMBH to shut down or to restart nuclear activity and star formation. In the second part of my thesis, I analysed ALMA observations of the inner 5 pc of our Galaxy showing this region at the higher angular scales in the millimeter emission. The matter in this region is known to stall in a molecular gas and dust ring with 1.5 pc in radius and from there is transported via streamers towards the center. These streamers are visible in dust and ionized gas emission. Surprisingly, there is also molecular gas in the immediate vicinity of the SMBH (< 0.04 pc) and I find it to be higher excited than the gas in the ring indicating a strong feedback from the nuclear stellar cluster and the SMBH, and/or turbulence, and tidal shear. This probably infalling cloud might be involved in a past, recent or upcoming feeding event.

This thesis is structured as followed: In this chapter I introduce the two relevant science cases, active galactic nuclei and the Galactic Center, and some general scientific terminology. Chapter 2 deals with the three extragalactic sources and chapter 3 with the GC seen with ALMA. This is followed by a summary and outlook in chapter 4.

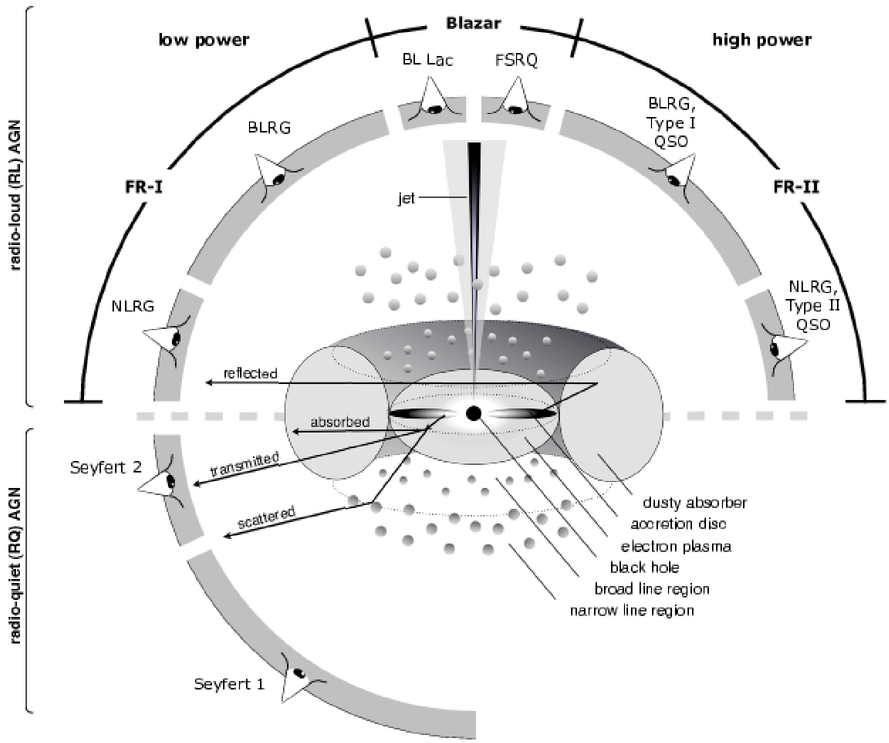

Figure 1.2: *Schematic model of an AGN in the unified scheme. Taken from Beckmann and Shrader (2012).*

1.1 Active Galactic Nuclei

The basic properties of active galactic nuclei (AGN) are a high - and potentially variable - luminosity, a strong non-thermal flat spectral energy distribution (SED) throughout most of the spectrum (from radio to γ-rays regime), highly excited permitted and forbidden emission lines, large line widths, and - in some cases - a jet. Such a high energy output from such a small region, i.e. the very centers of galaxies, cannot be generated by ordinary stellar processes (Fabian 1979). Instead, only the release of gravitational energy, i.e. the accretion of matter onto a BH, gives the needed efficiencies (Rees 1984).

1.1.1 AGN composition

The current model of an AGN is depicted in Fig. 1.2. The central SMBH is surrounded by an accretion disk in which the infalling matter loses energy and angular momentum by friction. Towards the inside the disk reaches temperatures of a few 10^5 K resulting in an excess emission mainly in the optical, UV and soft X-rays (Big Blue bump; Frank *et al.* 2002; King 2008). At a distance of 10 - 100 lightdays the accretion disk turns into the broad line region (BLR). These clouds of very dense (electron density: $n_e = 10^{11}$ cm^{-3}; Ferland *et al.* 1992) dust-free and highly ionized gas, traced in e.g. the hydrogen (e.g. Lyα, Hβ, Hα), the helium (e.g. HeII), and the carbon lines (e.g. CIV), move at high velocities (corresponding to the full width at half maximum (FWHM) of the emission lines) of 1000 - 20000 km s^{-1} (Netzer 2015) due to roughly Keplerian rotation around the SMBH and turbulence (cloud collision or outflow). This configuration is surrounded by a likely torus-shaped association of obscuring dust clouds - the dust torus - with dimensions of 0.1 - 10 pc (Netzer 2015). Its inner edge is expected to be defined by the dust sublimation temperature of $\sim$ 1500 K. It is heated by the UV-radiation from the accretion disk and the BLR and re-emits in the IR (50 - 1000 K; IR bump; Wilkes 2004). Perpendicular to the torus and delineated by it, the bi-conical narrow line region (NLR) can extend from 10 pc up to a few kpc. The low-density clouds ($n_e = 10^2$ - 10^4 cm^{-3}; Peterson 1997) in this region, move at velocities of 300 - 1000 km s^{-1} (Netzer 2015). Apart from the emission line species mentioned above, they also show forbidden (low density) emission lines, such as [OII], [OIII], [NII], or [OI]. Their relative line ratios depend on the impact/corresponding energies of the ionization process.

1.1.2 AGN unified model

As indicated in Fig. 1.2, the spectral differences concerning broad line emission of the AGN types can be explained by the viewing angle (Antonucci 1993; Urry and Padovani 1995; Urry 2003; Heckman and Best 2014): In the case of type 1 AGN, the line of sight (LOS) is closer to a face-on view onto the dust torus and emission from both, BLR and NLR, is observed. A type 2 AGN is the case when looking rather egde-on onto the system, so that the BLR is hidden behind the dust clumps of the torus and remains undetected. This unification based on source geometry is corroborated by the detection of BLR emission in polarized light scattered from dust above the plane of the torus (Krolik and Kallman 1987; Wilkes *et al.* 1995). Furthermore, AGN can be sub-divided into radio-loud, e.g. radiogalaxy, quasar, Fanaroff-Riley I & II, and radio-quiet, depending on the presence for a prominent extended jet structure in the radio and occasionally X- to γ-ray regime. In the case of blazars, we are looking straight into the jet (face-on) so that the emission lines in the optical to X-ray range are outshone by the relativisticly boosted jet radiation. Finally, AGN are categorized by the power of their SMBH, i.e. by luminosity and the high energy SED. The quasi stellar objects (QSOs) and their radio loud counterparts, the quasi stellar radio sources (quasars), are the brightest objects in the universe with luminosities of up to 10^{13} - 10^{15} $L_\odot$ = 100 - 10000 $L_{\rm host}$. The first objects discovered were believed to be a new class of stars ("quasi-stellar") until, with advance of the telescope design, their host galaxies were detected. quasi stellar objects (QSOs) are predominantly found in elliptical galaxies and at higher redshifts, i.e. around z= 2 - 3 (Peterson 1997), hinting at a relation to the galaxy interactions (Sanders *et al.* 1987,e.g.). The less powerful and mostly radio-quiet siblings of quasi stellar objects (QSOs) are located in Seyfert galaxies, with SMBH masses and luminosities about a 100 times less than for a typical QSO. Seyfert nuclei reside in spiral galaxies which implies the existence of mechanisms for sustaining a matter transport to the center without destroying the galactic disk. It was the bimodality of the Seyfert spectral characteristics that evoked the idea of the unified model, and it was further substantiated by the detection of the missing link between them in polarized light. low ionisation nuclear emission region galaxies (LINERs) are even less luminous, probably more scaled-down version of an AGN than Seyferts nuclei (Netzer 2009) and show moderately excited, neutral and weakly ionized gas emission lines (O, OI, NI [OI] or [SII]) which could be due to photoionization or shock waves propagating through gaseous matter (Heckman 1980; Ho *et al.* 1993). Seyferts make up about 10% and LINERs about 30% of the luminous galaxy population (Heckman 1980).

1.1.3 The Host Galaxy

The tight correlation between the SMBH mass and the bulge mass in almost all galaxies indicates a nearly simultaneous growth of both. It depends on a variety of processes like mergers (Di Matteo *et al.* 2005), jet-AGN outflow feedback (Silk and Rees 1998), or the radiation pressure by a starburst in the bulge. However, Narrow-line Seyfert 1 galaxies (NLS1s) for example, seem not to follow SMBH mass and the bulge mass relation (Mathur 2011; Orban de Xivry *et al.* 2011a) as the growth of their bulges seems to precede the growth of their SMBHs (Kawaguchi *et al.* 2008). How exactly these components influence each other is not well understood. Starburst (bulge growth) seem to precede AGN growth phases due to feedback from supernovae (SN) and winds of young massive stars (Wild *et al.* 2010). An AGN might be important for ULIRGs and their far-infared (FIR) emission and a ULIRG phase is expected to result in the formation of a QSO (Downes and Solomon 1998). In order to understand the relations between the involved components, the evolutionary sequences and the gas supply of starburst and AGN, the investigation of the galaxies in terms of structure, star formation, gas content, chemistry, interactions is essential (Shlosman 1990; Hopkins and Quataert 2010). Especially the starburst and AGN component needs to be separated from the host galaxies which is complicated by the strong AGN emission and requires high spatial resolution. The large amount of molecular gas suggests that the host galaxies cannot be quiescent. Its distribution and density need to be studied and and compared between all AGN accessible to high resolutions on a few kpc to sub-pc scale as a statistical base to get insight in into the fueling process. At least for the nearby QSOs the necessary resolution can be achieved by the current interferometers in the sub-mm regime which contains several diagnostic molecular lines (Helfer *et al.* 2003; Iono *et al.* 2005; Krips *et al.* 2007b) and allows for the investigation of possible circumnuclear molecular gas reservoirs, their distribution and dynamics. At higher redshifts ($z \geq 1$), extended mergers, lenses and a few un-lensed galaxies can still give insight in the crude distribution of neutral atomic and molecular gas (Greve *et al.* 2005) and complete the picture of galaxy evolution from the local universe to high redshifts.

1.1.3.1 ULIRGs

Ultra Luminous Infrared Galaxies stand out by their high IR excess with $L_{\mathrm{IR}[8-1000\mu\mathrm{m}]} \leq 10^{13} L_{\odot}$ (Rieke and Low 1972). Dust highly obscures the MIR, optical, UV, X-ray emission and re-emits the energy from the source of emission, that is either a strong nuclear starburst or an AGN (Sanders 1999), or a mixture, in the infrared. Obviously, a large amount of molecular gas is available in the central kpc to feed the source and high density gas has been traced in compact regions around the nucleus (Gao and Solomon 2004b). About 15 - 25% of the ULIRGs show features of an AGN $\sim 15-20\%$ (Nardini *et al.* 2008) and most of the ULIRGs are interacting with other galaxies or are even merging (Farrah *et al.* 2001). Similarities between ULIRGs and QSOs, especially their similar space densities (Soifer *et al.* 1986), indicate a significant importance of ULIRGs in AGN evolution. It is believed that in the case of an interaction or merger of two gas rich galaxies a large amount of gas is stripped of from its orbits. It sinks towards the galaxies' centers and triggers at a certain amount a burst in star formation that provides the major contribution to the FIR luminosity for about 10^8 years. When the merging nuclei reach projected separations less than 1 kpc, the AGN contribution begins to dominate the spectrum (Veilleux *et al.* 2009). By SN and later the increasing power of the central engine the dust is blown away dust and reveals a QSO. However, there are ULRIGs that do not show the assumed behavior such as fully merged ULIRGs that are not dominated by the AGN radiation or still are enshrouded in a dust envelope. Other ULIRGs have not merged yet, but already harbor a strong AGN. Obviously, there are different ways for a merger to evolve to an AGN (Veilleux *et al.* 2009).

1.1.4 The low-luminosity QSO (LLQSO) Sample

We selected a large, representative sample of low-luminosity quasi stellar object (LLQSO) from the Hamburg/ESO QSO survey (Wisotzki *et al.* 2000) with the goal to explore the signatures of internal or external triggers of the (circum-) nuclear activity (i.e., star formation and accretion onto the SMBH) and their importance in LLQSOs. In this context, we intend to study the link of the population of LLQSOs to the two regimes of local low-luminosity active galactic nuclei (LLAGN) and higher-redshift and powerful QSOs, that are in our case represented by the NUGA sample (García-Burillo *et al.* 2003; Haan *et al.* 2009; Casasola *et al.* 2011b; García-Burillo and Combes 2012) and the Palomar Green (PG) QSO sample (Evans *et al.* 2001, 2006; Scoville *et al.* 2003), respectively. Our study covers not only the volume from the local to the nearby Universe, but also the part of the AGN activity sequence, that can be studied in detail, to higher activity levels. The sample comprises 99 sources ($B_J \leq 17.3$) with a redshift of $z \leq 0.06$ (Fig. 2, Bertram *et al.* 2007) so that near-infared (NIR) diagnostic lines (e.g. the stellar CO(2–0) band head in the K-band) can be used to probe the stellar kinematics and to estimate the SMBH masses for all sample objects (e.g. Gaffney *et al.* 1995; Fischer *et al.* 2006; Busch *et al.* 2015). In addition, the sub-kiloparsec scale is still accessible with current facilities, so that it is possible to separate the starburst and the AGN component in extragalactic objects from the faint contribution of the host galaxy as well as to determine the properties of the interstellar medium and star formation in the inner 1 kpc of the QSO host galaxies. We observed about 40% of the LLQSO sample in the CO(1–0) and (2–1) transition with the IRAM 30 m telescope and a detection rate of 70%. 44% of the CO detected galaxies were also detected in the H I line transition with the Effelsberg 100 m telescope. These studies (Bertram *et al.* 2007; König *et al.* 2009) yielded that the hosts of

LLQSOs are rich in molecular and atomic gas with $M_{\mathrm{H}_2} \approx 5 \times 10^9 M_\odot$ and $M_{\mathrm{H\,I}} \approx 10^{10} M_\odot$. However, their global star-forming properties are different from those of local Seyfert and non-active galaxies as well as higher-z QSOs. We argue that these differences might result from the compactness and opacity of the gas taking part in the ongoing star formation. With ULIRGs and quiescent galaxies marking the two extremes, corresponding to maximum and minimum fractions of molecular gas participating in star formation, respectively, our objects fill the region between the two extremes.

Our NIR subsamples reveal most of the galaxies to be disk dominated and a high fraction (44% and 86 % respectively) of the sample displays a bar structure. In addition, several galaxies show rings or signs of interactions hinting at secular evolution as well as mergers as AGN activity trigger (Fischer *et al.* 2006; Busch *et al.* 2014). We also tested the blackhole masses and bulge luminosities and find the subsample to be off the M_{BH} - L_{bulge} - relation for inactive galaxies (Busch *et al.* 2014) which might be attributed to star formation in the bulges of active galaxies. Signs of ongoing star formation have been found for several sample members (Fischer *et al.* 2006; Bertram *et al.* 2007; Scharwächter *et al.* 2011; Busch *et al.* 2015). Interferometric work on ULIRGs and QSOs revealed that the gas reservoirs are often concentrated within 1 kpc of the nucleus (cf. Bertram *et al.* 2007,and references therein). Up to now, we were able to resolve a gas ring structure in the host of I Zw 1 (Staguhn *et al.* 2004,CO(1–0), $r \sim 1.2$ kpc) HE 2211–3903 (Scharwächter *et al.* 2011,optical emission lines, $r \sim 6$ kpc) and HE 1029–1831 (Busch *et al.* 2015,NIR emission lines, $r \sim 240$ pc). The latter we have already mapped and analyzed with the Institut de Radio Astronomie Millimétrique (IRAM) Plateau de Bure Interferometer (PdBI) and the Berkeley-Illinois-Maryland Association (BIMA) observatory (Krips *et al.* 2007a).

1.2 The Galactic Center

Our Milky Way is a barred spiral galaxy of type SBb/SBc (Churchwell 2006; Kormendy 2001) and, with a distance of 8.5 kpc from the solar system, its center is the closest galactic nucleus available. Our next neighbour, the Andromeda galaxy (M31), resides at a distance of 780 kpc to us (Holland 1998) and the next AGN, Centaurus A, is even 5 times further away than M31 (Harris *et al.* 2010). This makes the GC the highest spatially resolvable galactic nucleus in the universe and a unique laboratory in which the general physics for nuclei of similar galaxies can be studied. In the optical and UV wavelength domain, the GC is obscured by large gas and dust lanes in the galactic plane which makes it only observable in the radio, infrared and X-ray regime. The inner few pc region consists of the CND, the central cavity, the nuclear stellar cluster and the radio and infrared source Sgr A* which is associated with a SMBH of mass of about $4 \times 10^6 M_\odot$ (Eckart and Genzel 1996, 1997; Eckart *et al.* 2002; Schödel *et al.* 2002a; Eisenhauer *et al.* 2003; Ghez *et al.* 2000, 2005, 2008; Gillessen *et al.* 2009a).

1.2.1 The Interstellar Medium

According to its structure in the radio domain, Sagittarius A complex can be subdivided into the components Sgr A East and Sgr A West. Due to its non-thermal radiation features and its shell-like structure Sgr A East is likely to be a supernova remnant (Maeda *et al.* 2002; Ekers *et al.* 1983). The western part of Sgr A East surrounds the Sgr A West and the CND in projection. This spiral structured source, therefore also called the minispiral, is dominated by thermal radiation and has a flat spectrum. It connects the CND to the center of nuclear stellar cluster. The CND is an assemblage of clumpy molecular clouds and dust filaments with a mass of the order of $10^4 M_\odot$ and extends over a region of 1.5 - 7 pc from the center (see Fig. 1.3). With densities of 10^4 - 10^7 cm^3 and temperatures of 100 - 500 K the neutral gas and warm dust orbit the nucleus with a velocity of about 100 km s^{-1} in a circular rotation pattern (Guesten *et al.* 1987). Due to the geometrical projection, the CND has a lobed structure with emission concentrated in the northern and southern bow. Dust heated by the far-UV and hence photo-dissociating radiation of the nuclear stellar cluster could be an explanation for the limb brightening of the torus. The CND might be fed by gas infalling from molecular clouds at distances larger than 10 pc and itself seems to supply Sgr A West with interstellar matter.

Via three streamers in Sgr A West, the Northern Arm, the Western Arc and the extended/Eastern Bar, ionized gas of a few 10 $M_\odot$ spirals towards the very center at velocities of 100 - 200 km s^{-1} (Lacy *et al.* 1982). Aside from acceleration, the material is heated by strong winds and far-UV radiation of the central stellar cluster. According to the emission in the HII regions the gas reaches electron temperatures of about 7000 - 40000 K, depending on the distance to Sgr A* (Roberts *et al.* 1991) and has a high thermal flux density at cm wavelengths.

The streamers are visible in radio, infrared and dust emission and are organized in three

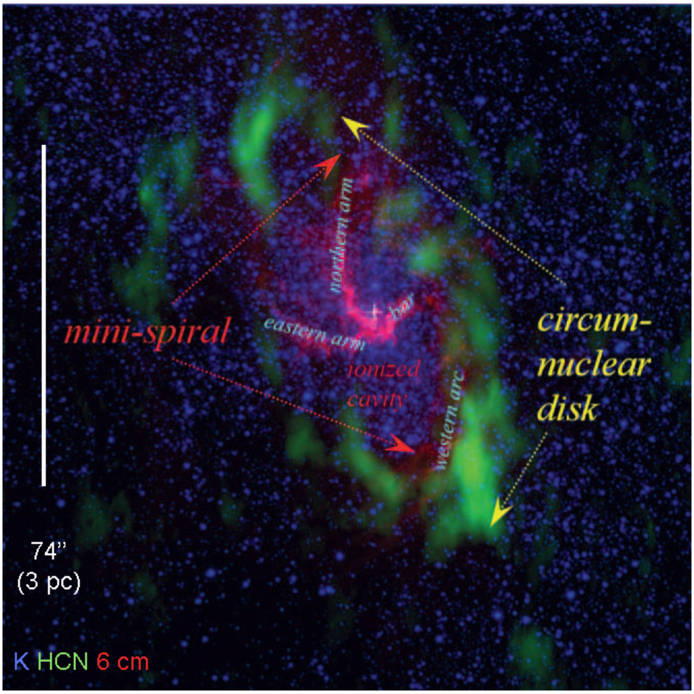

Figure 1.3: The inner few pc of the Milky Way with the CND and the minispiral at different wavelengths. The cross marks the position of the compact radio source Sgr A. 6 cm denotes the 6 cm radio continuum emission; HCN the HCN(1-0) radio emission; and K the NIR K-band emission at 2.2 μm (Genzel et al. 2010b)*

planes with different angles and rotational parameters (Vollmer and Duschl 2000; Zhao *et al.* 2009, 2010) as depicted in Figure 1.4. This structure, the minispiral, forms the brightest part of Sgr A West and apart from that the central cavity is comparably devoid of interstellar matter. While the CND configuration is assumed to be stable for several 10^6 years, the minispiral is rather a short-lived (infalling) structure with a dynamical time scale of about 10^4 years.

1.2.2 The Stellar Cluster

The GC harbors many bright sources (Fig. 1.5) that are visible mostly in NIR due to photospheric emission of the stars and in the mid-infared (MIR) due to extended gas/dust features of the ISM in this area (Becklin and Neugebauer 1968; Low *et al.* 1969). They form an extremely dense cluster with a supermassive black hole at the dynamical center (Fig 1.3). For distances larger than 0.5 pc from the center the cluster is nearly isothermal, on scales shorter than 6″ the number density flattens out to a cusp which is consistent with the predictions for the stellar distribution around a SMBH. It can be described by a broken-power law derived from the measured projected density with power-law indices of $\Gamma_{cusp} = 0.19 \pm 0.05$ for the cusp, and $\Gamma_{outer} = 0.75 \pm 0.1$ for the outer part of the cluster and a break radius of

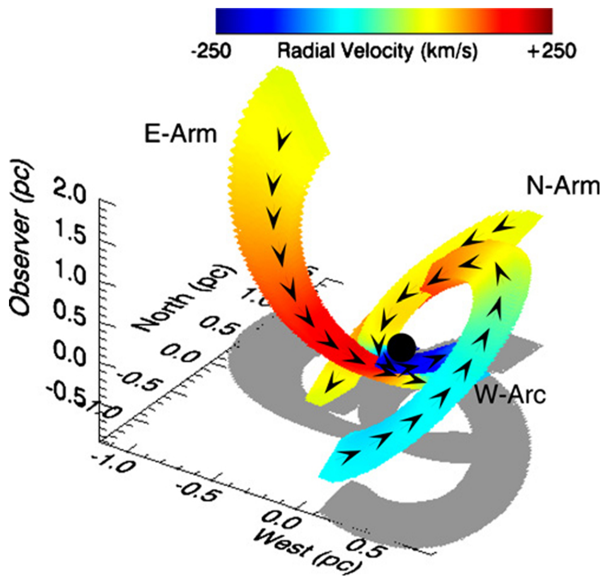

Figure 1.4: *The kinematics of Sgr A West as discussed by* Zhao et al. *(2010). The image gives an impression of the three-dimensional alignment of the streamers and their projection onto the sky-plane (grey). The arrows indicate the direction of the flows, the colors the radial velocity. The black sphere in the middle marks the position of Sgr A**

$R_{\rm break} = (6.0 \pm 1.0)'' = (0.22 \pm 0.04)$ pc (Schödel *et al.* 2007).

There is a significantly lower number of late-type stars in central few arcseconds but a larger number of early type stars (Krabbe *et al.* 1995; Paumard *et al.* 2001; Genzel *et al.* 2003b; Moultaka *et al.* 2005; Mužić *et al.* 2008). The early-type stars, also referred to as He-stars, are massive, hot blue supergiants like OB stars, Wolf-Rayet (WR) stars and luminous blue variables. Due to their surface temperatures of around 20 000 - 30 000 K, they are able to ionize Helium (Ott *et al.* 1999) and they produce strong interstellar winds with velocities up to 1000 km s^{-1} and heavy mass losses of 10^{-5} - $10^{-4} M_\odot/yr$ (Krabbe *et al.* 1991; Najarro *et al.* 1997). Many of them are interacting with the ISM in the GC which becomes visible in bow-shock sources (Tanner *et al.* 2002; Moultaka *et al.* 2004b). Their spectra can be considered as a convolution of their continuum emission with the absorption features of the surrounding dust. About two dozen of them dominate the luminosity in the central few arcseconds, for example IRS 13 and 16. Many of them are obviously witnesses of a star formation period about 10^6 - 10^7 years ago. Sources like IRS 1W, 3, 9, 10W, 21 could also be heavy mass losing stars (Becklin *et al.* 1978; Krabbe *et al.* 1991) or dust enshrouded young stellar objects (Krabbe *et al.* 1995; Clénet *et al.* 2001).

The late-type stars are intermediate-bright giants (Krabbe *et al.* 1995; Maness *et al.* 2007) or supergiants at the top of the asymptotic giant branch which seem to originate from another star forming period 10^8 years ago. The strength of the CO absorption which traces these stars drops towards the center. The reason might be that there is a higher concentration of

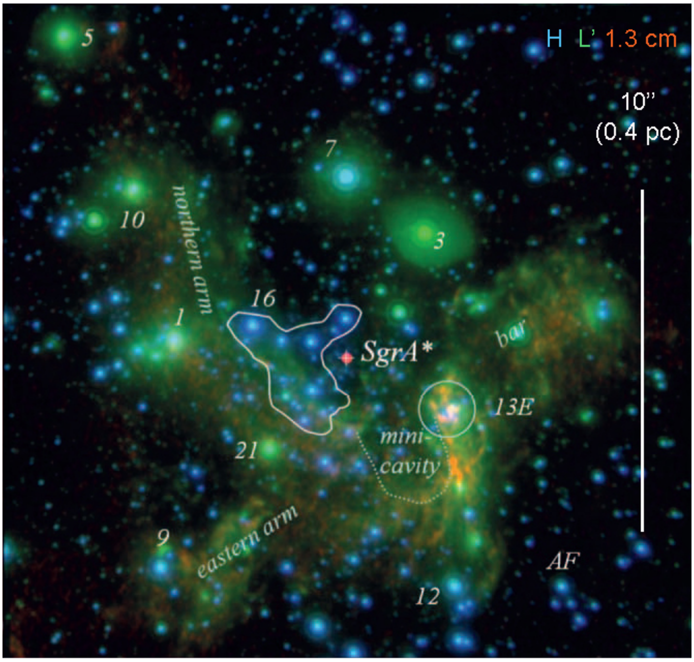

Figure 1.5: *The inner few pc of the Milky way with the minispiral and the nuclear stellar cluster at different wavelengths. The cross marks the position of the compact radio source Sgr A*. 1.3 cm denotes 1.3 cm radio continuum emission; L' the NIR L'-band emission at 3.8 µm (Genzel* et al. *2010b)*

early type stars, maybe because the envelopes are destroyed by collisions in the dense stellar cluster (Lacy *et al.* 1982; Sellgren *et al.* 1990) or that the CO absorption features are diluted by luminous blue stars in the central arcseconds (Eckart *et al.* 1995; Haller *et al.* 1996). In a region very close to the SMBH, about 1″ in radius, lies the so called S-cluster. Due to the acceleration by the dynamical center Sgr A* the S-stars reach orbital velocities of about 1000 km s^{-1} (Eckart *et al.* 1999; Ghez *et al.* 2003; Eisenhauer *et al.* 2005) and from their proper motions the mass of Sgr A* can be estimated (Ghez 2004; Eckart *et al.* 2005b; Schödel *et al.* 2009). According to spectroscopic observations they are possibly OB main sequence stars (Eckart *et al.* 1999; Ghez *et al.* 2003) and therefore likely to be young.

Star formation in the vicinity of a SMBH is still not understood. On the one hand, strong tidal forces are expected to inhibit star formation, according to the standard theories of stellar evolution (Thornley *et al.* 1997; Eckart *et al.* 2005b). On the other hand, if the young stars formed at greater distances, they could not have sunk towards the very center via dynamical friction within their expected life time. Possible explanations for the presence of young stars are, for example, events of stellar mergers or the infall and dissolution of massive young clusters bound by their total mass or by an intermediate mass black hole (IMBH). Nayakshin *et al.* (2007) found in simulations a possibility for stars to form at the fragmenting inner parts of a gaseous disk around Sgr A* but the formation of larger clusters could not be explained. Additionally, it has to be taken into account that on the one hand the densities of the ISM at the GC is too low for star formation, but on the other hand star formation could be triggered by shocks and collisions. Obviously, star formation in such a violent and complex environment like a galactic nucleus cannot be described by existing theories of stellar evolution and forms a special chapter in star formation theories that needs to be studied.

If star formation is still present at the GC, there should be even younger stars than the early-type ones and they might be still embedded. Such young stellar object (YSO) are pre-main sequence stars, like protostars, Herbig Ae/Be objects or T-Tauri stars. They exhibit a strong IR excess of their spectra due to heated dust grains close to the stellar surface. Possible YSO candidates in the GC region are the IRS 13N sources.

1.2.3 Sgr A*

The compact radio source Sgr A* is the dynamical center of the nuclear stellar cluster. The (non-) Keplerian orbits of the S-stars not only constrain its mass which is estimated to be about $3.6 \times 10^6 M_\odot$, but also its maximum size. With a radius of less than 2.4×10^{13} cm ≈ 2 AU the source can only be explained by a SMBH (Schödel *et al.* 2003). It is visible at all times in radio (Falcke *et al.* 1998; Falcke and Markoff 2000) with a luminosity of about 2×10^{34} erg s^1 which corresponds to 1.1 Jy at 2 cm wavelength (Eckart *et al.* 2005a). Sgr A* shows a flat to inverted radio spectrum (Falcke *et al.* 1998; Falcke and Markoff 2000; Yusef-Zadeh *et al.* 2006) with a spectral index of about $\alpha = 0.5$ for 110 - 230 GHz (Kunneriath *et al.* 2011; García-Marín *et al.* 2011) that peaks in the sub-mm (sub-mm bump) and drops off sharply towards the IR domain (Fig. 1.6). From the IR to the X-ray regime its quiescent state luminosity is very low (Baganoff 2003; Sabha *et al.* 2010; Dodds-Eden *et al.* 2010) and rather visible in its flaring high activity states at which emission bursts let the luminosity increase within minutes by a factor of 10 (IR) to 100 (X-ray) (Baganoff *et al.* 2001; Baganoff 2003; Genzel *et al.* 2003a; Eckart *et al.* 2004a, 2006). The short variability timescales indicate emission from a region close to the event horizon, maybe within about 10 Schwarzschild-radii ($R_{\text{Schwarzschild}} = 2$ GM / c^2) of the SMBH, and therefore could give information on the properties of the SMBH, such as its spin. Very long baseline interferometry (VLBI) observations at 1.3 mm wavelength already displayed the source structure on event horizon scales (Doeleman *et al.* 2008). To detect the shadow cast by the event horizon due to gravitational deflection of light closeby or even the event horizon itself would be the final proof for Sgr A* being a SMBH.

The Quiescent State Even though a large amount of gas and dust is available for accretion Sgr A* radiates at all frequencies far below the Eddington limit ($L \propto 10^7 L_{\text{Edd}}$) which is given by the balance of gravity and radiation pressure. This makes it the most under-luminous BH that is observable at the moment. Actually, its luminosity is even lower than expected from its low accretion rate of less than $10^{-7} M_\odot$ yr^1 (Eckart *et al.* 2005a). The conversion efficiency of thermal energy of a plasma into radiation energy amounts only to 5×10^{-6} (Narayan

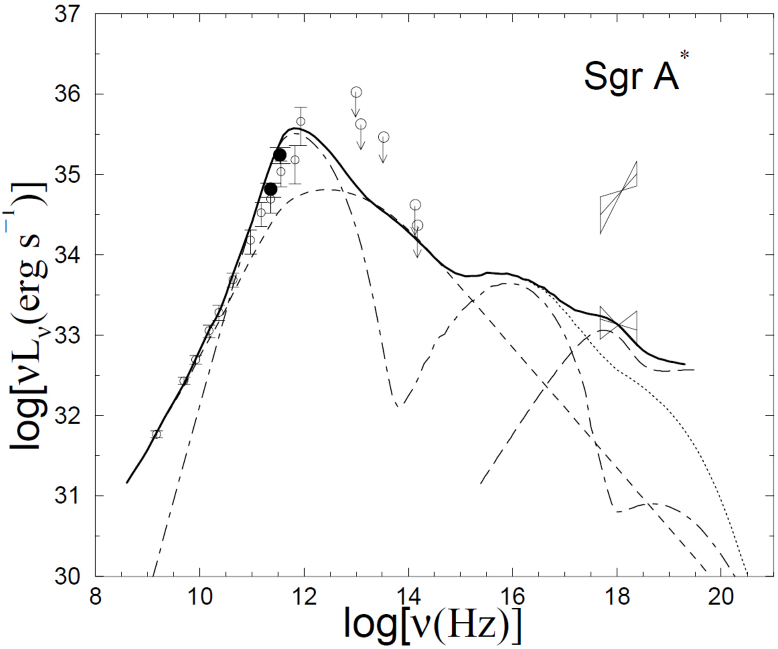

Figure 1.6: *Spectral energy distribution of the quiescent emission from Sgr A* (solid line). The dot-dashed line indicates the Synchrotron and SSC emission of thermal electrons, the dashed the Synchrotron emission for non-thermal electrons. The total Synchrotron as inverse Compton emission is represented by the dotted line and the Bremsstrahlung in the X-ray domain by the long-dashed line (Yuan* et al. *2003).*

et al. 1998) compared to the 10% usually assumed for a high density accretion in a thin disk (Shakura and Sunyaev 1973). The weak quiescent and strong flare emission cannot be explained by standard accretion disk models with a low accretion rate. Obviously, the radiation efficiency plays an important role. An example for an Radiatively Inefficient Accretion Flow (RIAF; Melia and Falcke 2001) is an Advection Dominated Accretion Flow model (ADAF; Narayan and Yi 1995; Yuan *et al.* 2003) The gravitational energy is transformed into thermal energy and transported towards the central BH. In this plasma, the electrons and protons are assumed to have different temperatures, as the electrons can cool more efficiently via radiation due to the fact that they are 2000 times less massive than the protons. At the same time this mass difference makes the protons radiate inefficiently. In addition, they cannot cool sufficiently via collisions with electrons due to the low density. Therefore, they stay very hot and transport the largest fraction of the thermal energy beyond the event horizon. As long as the free-fall time scale of the plasma is shorter than the cooling time scale, this scenario explains the low radiative efficiency. Still, for the low mass accretion rate the densities of an ADAF are too high. This effect can be incorporated into the model in the form of strong winds due to the radiation pressure that drive the the gas away from the disk. In this Advection Dominated

Inflow-Outflow Solution (ADIOS; Blandford and Begelman 1999), only a small fraction of the gas reaches the event horizon. The current model that describes the SED of Sgr A* the best is a combination of an ADAF and a jet model (Yuan *et al.* 2002). A small fraction of the material is ejected as a short, luminous jet close to the BH and can reach a higher electron temperature than possible in an ADAF alone. Its strong Synchrotron Self-Compton (SSC) radiation can then dominate the Bremsstrahlung from the ADAF. With this model the SED (Fig. 1.6) of the quiescent state can be reconstructed: The radio to IR radiations is likely to be synchrotron emission from the accretion disk and a short mildly relativistic, optically thick jet (Falcke and Markoff 2000), the sub-mm bump can be explained to be due to relativistic thermal electrons in the innermost hot, thick ADAF (Narayan and Yi 1995; Yuan *et al.* 2003; Dexter *et al.* 2010). In the IR regime, the radiation might also be produced by inverse Compton up-scattering of the synchrotron photons. This SSC radiation distribution then reaches out to the X-ray domain. Another X-ray component could arise from Bremsstrahlung of a cooler electron population in the disk and γ-ray emission is likely to come from high energy particle production (Baganoff 2004). The observation of the jet would support the ADAF-plus-jet model, but even if it existed it could not detected until now due to its low surface brightness (Markoff *et al.* 2007).

CHAPTER 2

Molecular gas and star formation in three nearby Seyfert galaxies

The goal of the low-luminosity quasi stellar object (LLQSO) sample is to investigate the signs of internal or external triggers for enhanced activity (i.e., star formation and accretion onto the SMBH) in the centers of galaxies and their frequency with respect to the nuclear activity. 40% of the LLQSO sample have been observed in the CO(1–0) and (2–1) transition (Krips *et al.* 2007a; Bertram *et al.* 2007). Among the most luminous of them, three Seyfert galaxies have been selected to for a follow-up study with the Submillimeter Array (SMA, Ho *et al.* 2004) at moderate spatial resolutions of $\sim 3''$ ($\sim$ 1 kpc). Two sources, HE 0433-1028 and HE 1108-2813, were observed in ^{12}CO(2–1) and ^{13}CO(2–1) and the third, HE 1029-1831, in ^{12}CO(3–2) and HCO^{+}(4–3) line emission. This chapter presents my results of these observations. For the analysis, I combine these new observations with our existing CO(1-0) and CO(2-1) data obtained with IRAM 30 m single dish (HE 0433-1028, HE1108-2813; Bertram *et al.* 2007) and IRAM PdBI data (HE 1029-1831; Krips *et al.* 2007a). Intriguingly, in all three galaxies the molecular gas accumulates at the center within a radius < 2 kpc and the gas kinematics indicate the presence of a decoupled central unresolved component. The $R_{21} = ^{12}$CO/^{13}CO(2–1) line luminosity ratios obtained for HE 0433-1028 and HE 1108-2813 are significantly enhanced with $R_{21} \gtrsim 20$ in the central region, indicating them to be warm and/or turbulent. Strikingly, also the ^{12}CO(3–2)/(1–0) line luminosity ratio in HE 1029-1831 suggests a higher excitation phase with $r_{31} \sim 1$, apart from the cold or diffuse gas phase implied by $r_{21} \sim 0.5$ for all three of them. From this, together with the LIRG typical infrared luminosities of $L_{\rm IR} \geq 10^{11} L_\odot$, I conclude that the emission in the centers of these Seyferts is strongly affected by diffuse gas due to violent star formation. Indeed, the centers of these galaxies seem to contain a circumnuclear starburst with minimum molecular gas mass and starformation rate (SFR) surface densities around Σ_{mol} = 70 - 540 $M_\odot$ pc^{-2} and $\Sigma_{\rm SFR}$ = 1.3 - 3.8 $M_\odot$ kpc^{-2}yr^{-1}. Therefore, the galaxies' ISM state is likely to be better described by a mass conversion factor typical for ULIRGs, as suggested by the dynamical and dust masses.

My work on these data shows how much information on the state of the molecular gas can already be obtained from these medium spatial resolutions, i.e. on 0.5 - 1 kpc-scales. With such simple observations the redshift range up to z ~ 0.1 could be efficiently tested.

The results of my work that I present in this chapter have been published recently in Astronomy & Astrophysics (A&A) under Moser *et al.* (2016a).

2.1 Introduction

The coevolutional growth of the SMBH and the host galaxy bulge (e.g. Hopkins *et al.* 2008) might be governed by an equilibrium between nuclear fueling and feedback, in which the mass rates of infalling material consumed by star formation and consumed by accretion onto the SMBH are more or less stable. Several mechanisms for the loss of gas angular momentum are known, from kpc-perturbations and mergers to secular evolution, but it is not clear how and on what scales they are efficient and how they relate to the host galaxy and AGN type (Hutchings and Neff 1992; Sanders *et al.* 1988; Kormendy and Kennicutt 2004; Schawinski *et al.* 2011; Kocevski *et al.* 2012; García-Burillo and Combes 2012; Storchi-Bergmann 2014).

To understand the phenomenom of feeding in all it facets and how it acts on the circumnuclear regions by changing the conditions for star formation, we have to investigate the gaseous material and its distribution in the host galaxies of AGN in detail (e.g. Helfer *et al.* 2003; Iono *et al.* 2005; Krips *et al.* 2007a; Bigiel *et al.* 2008; Leroy *et al.* 2008; Ford *et al.* 2013; Casasola *et al.* 2015). The study of gas dynamics and kinematics help to track down the processes of nuclear fueling and hence aid in constraining the fueling models. One important finding in the recent past is that depressions in the central gas/stellar velocity dispersion seem to be linked with intense central star formation activity and an enhanced central gas concentration (r $\lesssim$ 500 pc). This hints at a dynamically cold (compared to the bulge) nuclear structure (e.g. a disk) to be crucial for the fueling of nuclear star formation and the AGN (Falcón-Barroso *et al.* 2006; Hicks *et al.* 2013). The picture of galaxy evolution becomes less diluted, the more connections we find between the observations, also at different redshifts, and the various evolutionary scenarios.

The overall amount of cool molecular gas can be retrieved best by low-J CO transitions. However, for an inference of the gas properties and excitation state, also at high densities, the sources need to be observed in the emission of higher CO transitions or high density tracers (e.g. HCN, HCO^+), and their isotopologues. The basic tools to examine the ISM properties are the $R_{10,21}$ = ^{12}CO/^{13}CO(1–0) or (2–1) and the r_{31} = ^{12}CO(3–2)/(1–0) luminosity ratio. Galactic disk usually show values of $R_{10,21} \sim 5$ (e.g. Solomon *et al.* 1979) and $r_{31} \sim 0.4 - 0.6$ (Mauersberger *et al.* 1999; Israel 2005). With decreasing galactocentric distance the ratios rise up to $R_{10} > 20$ (turbulent and/or hot gas state, Devereux *et al.* 1994; Dumke *et al.* 2001; Muraoka *et al.* 2007; Papadopoulos *et al.* 2008; Iono *et al.* 2009; Papadopoulos *et al.* 2012a) and $r_{31} \gtrsim 1$ (very warm, dense gas, Hüttemeister *et al.* 2000; Sakamoto *et al.* 2007; Aalto 2007; Papadopoulos *et al.* 2008; Aalto *et al.* 2010; Costagliola *et al.* 2011) in (U)LIRGs. High values of r_{31} (up to 5) are also found in centers of normal galaxies, starbursts, and AGN (e.g. Devereux *et al.* 1994; Matsushita *et al.* 2004; Mao *et al.* 2010; Combes *et al.* 2013; García-Burillo *et al.* 2014). The presence of diffuse gas as well as of higher excitation phases affects the line luminosities significantly in starburst and (U)LIRGs and is evoked by the enhanced star formation activity (e.g. Hinz and Rieke 2006; Papadopoulos *et al.* 2012b,a; Bolatto *et al.* 2013; Kamenetzky *et al.* 2014; Shetty *et al.* 2014). Therefore, the basic assumptions typically made for the gas mass estimate do not hold under such conditions.

In the following, I present the results from an observation of CO emission in three galaxies (two in ^{12}CO(2–1) and ^{13}CO(2–1) and one in ^{12}CO(3–2) and HCO^{+}(4–3) with the SMA at a moderate angular resolution. The goal of this pilot study is the investigation of the morphology, kinematics and physical conditions of the ISM. These three galaxies belong to the LLQSO sample which comprises 99 nearby type-1 AGN from the Hamburg/ESO quasi-stellar object (QSO) survey (Wisotzki *et al.* 2000). The redshift cut-off of $z \leq 0.06$ (Fig. 2, Bertram *et al.* 2007) ensures that NIR diagnostic lines for the stellar and gaseous content are still accessible (e.g. Gaffney *et al.* 1995; Fischer *et al.* 2006; Busch *et al.* 2015). In terms of their optical luminosities (B_{J} magnitudes), the LLQSOs occupy the transition region between Seyferts and QSOs (Koehler *et al.* 1997). This sample is supposed to give insight into signs of internal or external mechanisms that can spur the (circum-) nuclear activity down to sub-kpc scales, their relevance for LLQSOs and how this population connects to local LLAGN and powerful QSOs at higher redshifts. Previous observations in the optical (Scharwächter *et al.* 2011; Tremou *et al.* 2015), in the NIR (Fischer *et al.* 2006; Busch *et al.* 2014, 2015), and in ^{12}CO(1–0), (2–1) and H I (Krips *et al.* 2007a; Bertram *et al.* 2007; König *et al.* 2009) imply that on-going circumnuclear star formation is likely to dominate the ISM characteristics and goes along with a large molecular gas reservoir. Characteristics like the activity level (e.g. B_{J} magnitude) and the FIR and CO luminosities are found to lie in between the ranges typical for local Seyfert/non-active galaxies and higher-z QSOs.

The three galaxies were selected for this follow-up study, because they are the rather luminous sources in CO emission from our ^{12}CO tested subsample (Krips *et al.* 2007a; Bertram *et al.* 2007). They have ^{12}CO(1–0) luminosities $L'_{\mathrm{CO}} > 0.9 \times 10^{9}$ K km s^{-1} pc^{2} hinting a very large gas reservoirs with masses of $M_{\mathrm{mol}} > 3.7 \times 10^{9} M_{\odot}$. Table 2.1 lists the molecular gas masses including helium obtained with standard cosmology with $H_0 = 70$, $\Omega_M = 0.3$ and $\Lambda_0 = 0.7$. Furthermore, they can be classified as LIRGs by their Infrared Astronomical Satellite (IRAS) based IR luminosities (8 - 1000μm) closely around $L_{\mathrm{IR}} = 10^{11} L_{\odot}$.

For HE 0433-1028 and HE 1108-2813 exist only single dish observations (Bertram *et al.* 2007). With their high ^{12}CO luminosities these targets are very suitable for interferometric follow-up studies with the SMA.

HE 0433-1028 is classified as a barred Seyfert 1 galaxy (Kewley *et al.* 2001) and has a redshift of z =0.03555 ± 0.00001 (Keel 1996). Balmer line widths of more than 3000 km s^{-1}

(Wang and Zhang 2007; Mullaney and Ward 2008) indicated it to fulfil the criteria of a Broad Line Seyfert 1 (BLS1), while the [OIII]λ5007/Hβ line ratio (Ryan *et al.* 2007; Mullaney and Ward 2008) is typical for NLS1s. The emission is dominated by the AGN component (Yuan *et al.* 2010). The galaxy's morphology and properties have not been further studied in the past.

HE 1029-1831 is a barred spiral galaxy and has a redshift of $z = 0.04026 \pm 0.00009$ (Kaldare *et al.* 2003). While its Balmer, Paα, and Brγ line widths of about 2000 km s^{-1} (optical and NIR; Nagao *et al.* 2001; Rodríguez-Ardila *et al.* 2000; Fischer *et al.* 2006) point at the a Narrow Line Seyfert 1 class, the optical line ratio diagnostics, Kewley *et al.* (2001) suggest it to be either an H II/borderline or an AGN/borderline galaxy. Furthermore, the NIR line and colour diagnostics are typical for a mixture of starburst and AGN excitation (Fischer *et al.* 2006; Yuan *et al.* 2010; Busch *et al.* 2015).

Its circumnuclear ring has two intense, but diminishing starburst regions with an intermediate-age stellar population of ~ 100 Myr in age. This population is likely to lower the mass-to-light ratio so that the galaxy follows the $M_{\rm BH}$–$M_{\rm bulge}$ relations but not the $M_{\rm BH}$–$L_{\rm bulge}$ relations of inactive galaxies (Busch *et al.* 2015), most likely due to the lower the mass-to-light ratio of the population. A FIR luminosity of $L_{\rm FIR} = 1.9 \times 10^{11}\ L_\odot$ classifying it as a LIRG and confirms active star formation(Fischer *et al.* 2006). It has an H I gas mass of $M_{\rm H\,I} = 6.6 \times 10^9 M_\odot$ (König *et al.* 2009). For this galaxy the cold gas morphology has been tested by IRAM PdBI and Berkeley-Illinois-Maryland Association (BIMA) observations (Krips *et al.* 2007a). In ^{12}CO, the emission is extended along the primary bar and shows a strong velocity gradient perpendicular to it which suggests a bar–driven inflow. Most of the molecular gas is cold and subthermally excited, as implied by the ^{12}CO (2–1)/(1–0) line ratio, except from the southern part of the bar emission (~4 kpc from the galactic nucleus, which might be a crossing point of bar end with spiral arm; Krips *et al.* 2007a).

HE 1108-2813 has a redshift of $z = 0.02401 \pm 0.00004$ (Theureau *et al.* 2005). It can be either classified as a Broad Line Seyfert 1 galaxy (Balmer broad line widths of about 5000 km s^{-1} Kewley *et al.* 2001; Crenshaw *et al.* 2003; Wang and Zhang 2007) or as Seyfert 1.5 galaxy based on the Balmer line peak ratio of the broad and narrow line components Kollatschny and Fricke (1983). Moreover, the nucleus displays a steep (negative) continuum slope towards the UV which goes along with the absence of higher ionization lines (e.g. C IV, C II]), but strong optical and UV Fe II]) multiplets.

The faint (dominant AGN component) barred and dusty grand design spiral (Yuan *et al.* 2010; Deo *et al.* 2006) of Hubble type SBc/d (Malkan *et al.* 1998) appears to be bulgeless (Orban de Xivry *et al.* 2011b). Strong dust features are visible in chaotic regions in the central kiloparsec and the bar as well as large scale lanes along the leading edges of the bar and in the spiral arms. The bar edges (Deo *et al.* 2006) show prominent star-forming regions.

In Section 2.2, I describe the observational setup, the calibration procedure and the mapping characteristics. In Section 2.3 I review the results from the observation, i.e. the CO

Table 2.1: *Properties of the three HE sources from literature (Credit: Moser et al. (2016a), reproduced with permission ©ESO.)*

object	RA (J2000)[1]	Dec. (J2000)[1]	z	$\log(M_{\rm BH}/M_\odot)$	$L_{\rm IR}$[8] $[10^{10} L_\odot]$	$M_{\rm mol}$[9] $[10^9 M_\odot]$
HE 0433-1028	$04^h36^m22.2^s$	−10°22′34″	0.03555 ± 0.00001[2]	6.9–8.3[5]	27	9.0
HE 1029-1831	$10^h31^m57.3^s$	−18°46′34″	0.04026 ± 0.00009[3]	6.7–7.4[6]	25	2 - 12
HE 1108-2813	$11^h10^m48.0^s$	−28°30′04″	0.02401 ± 0.00004[4]	6.5–7.8[7]	5	3.7

Notes. [(1)] values taken from NASA/IPAC Extragalactic Database (NED) [(2)] Keel (1996) [(3)] Kaldare *et al.* (2003) [(4)] Theureau *et al.* (2005) [(5)] Rao *et al.* (1992) (X-ray variability), Wang and Zhang (2007); Ryan *et al.* (2007) (optical lines) [(6)] Busch *et al.* (2015) (optical/NIR lines and stellar velocity dispersion) [(7)] Wang and Zhang (2007) (optical lines) [(8)] based on IRAS fluxes (NED) and formalism of Sanders and Mirabel (1996) for the 8-1000 micron range [(9)] Bertram *et al.* (2007) and Krips *et al.* (2007a)

Table 2.2: *Observational parameters (Credit: Moser et al. (2016a), reproduced with permission ©ESO.)*

object	phase tracking center RA (J2000)	Dec. (J2000)	Ant[1]	$\nu_{\rm CO\ rest}$ [GHz]	$t_{\rm total}$ [h]	FOV [″]	$\theta_{\rm beam}$ [″×″]	$rms_{\rm cont}$ [mJy beam^{-1}]	$rms_{5\ {\rm km\ s^{-1}}}$ [mJy beam^{-1}]	date
HE 0433-1028	$04^h36^m22.20^s$	−10°22′32.9996″	6	222.624	2.5	56	3.9 × 1.6	1.4	29 - 30[2]	June 2008
HE 1029-1831	$10^h31^m57.30^s$	−18°46′33.1965″	7	332.432	2.3	37	2.5 × 1.5	3.7	60[2] - 65	April 2007
HE 1108-2813	$11^h10^m48.00^s$	−28°30′02.9978″	8	225.132	5.0	55	4.6 × 3.0	0.9	17 - 23[2]	March 2008

Notes. [(1)] number of antennas [(2)] sideband containing the ^{12}CO emission line (given are lower sideband (left) and upper sideband (right) rms)

Table 2.3: *Calibrators (Credit: Moser* et al. *(2016a), reproduced with permission ©ESO.)*

object	bandpass	gain	flux
HE 0433-1028	3c454.3 (3c84)	0457-234	Uranus
HE 1029-1831	3c273	1058+015 1130-148	(Titan) 1130-148
HE 1108-2813	3c273 (3c84)	1037-295 1058+015	Titan Ganymede

emission spectra (2.3.1), the CO fluxes, gas masses and sizes (2.3.2) as well as the morphology and the kinematics (2.3.3) in all three galaxies. Moreover, I discuss a the dynamical mass estimate (2.3.4) and the dust properties (2.3.5). Section 2.4 deals with the star formation properties and Section 2.5 with the properties of the interstellar matter based on the obtained line ratios and the morphology. In Section 2.6, I recapitulate the results of my study.

2.2 Observation and data processing

The observations with the SMA in Hawaii were conducted in compact configuration between 2007 and 2008. For each target, one of the two 2 GHz - sidebands cover the ^{12}CO(2–1) or (3–2) line transition, respectively, (see Table 2.2), the other one the weaker emission lines of ^{13}CO(2-1) or HCO$^+$(4-3), respectively. Each sideband contains 24 partially overlapping spectral windows with a bandwidth of 10 MHz. The spectral windows comprise 128 channels with a resolution of 0.8125 MHz which translates to 1.10 km s^{-1} at 222.6 GHz and 0.73 km s^{-1} at 332.4 GHz. HE 0433-1028 and HE 1029-1831 were observed for ~ 2.5 hours in total and HE 1108-2813 was observed for ~ 5 hours in total. The field of view (FOV) is 56″ at 222.6 GHz and 37″ at 332.4 GHz. The spatial resolutions is between 1.5″ and 4.5″ (Table 2.2).

The observed calibrators can be seen in Table 2.3. The targest scans of a length of 20 - 30 min are enclosed with ~ 4 min scans on the gain calibrators. I calibrated the system temperatures with the SMA version of the Multichannel image reconstruction, image analysis, and display software package (SMA MIRIAD, Zhao 2013). Apart from this step, all data sets were processed with the Common Astronomy Software Application (CASA, Version 3.2/3.3, McMullin *et al.* 2007). The flux is corrected by the use of planets or their satellites as flux calibrators. For HE 1029-1831 I used the flux of the gain calibrator, because neither Titan nor 3c273 yielded reliable flux values. The corrected fluxes of all other calibrators correspond to the values listed in the Submillimeter Calibrator List of the SMA Observer Center [1] with 20% uncertainty.

[1] http://sma1.sma.hawaii.edu/smaoc.html

For image restoration with the best signal to noise ratio (S/N), I gave the visibilities a natural weighting. I computed image cubes with 256×256 pixels and a pixelscale of 0.2 $''$ pixel^{-1}. The velocities span a range from -200 to 200 km s^{-1} with a channel resolution of 5 km s^{-1}. The channel noise is less than 33 mJy at ^{12}CO(2–1) and 63 mJy at ^{12}CO(3–2) (see Table 2.5) and the continuum noise less than 1.5 mJy at 222 GHz and 3.9 mJy at 333 GHz (see Table 2.2). For deriving the moment maps, I clipped the HE 1108-2813 ^{12}CO(2–1) data cube at $3\sigma_{\text{rms-ch}}$, with $\sigma_{\text{rms-ch}}$ being the channel rms noise $\sigma_{\text{rms-ch}}$ in Jy beam^{-1}, and all other data cubes at $2\sigma_{\text{rms-ch}}$, because of a significant flux contribution below a $3\sigma_{\text{rms-ch}}$ level of 10% for ^{12}CO and up to 40% for ^{13}CO. All maps are primary beam corrected.

For undetected lines (non-detection) I use a value of 3 $\sigma_{\text{rms-int}}$ in Jy beam^{-1} km s^{-1} as an upper limit, where

$$\sigma_{\text{rms-int}} = \sigma_{\text{rms-ch}} \sqrt{v_{\text{FWZI}}\ v_{\text{ch}}} \tag{2.1}$$

with v_{FWZI} and v_{ch} as the full width of the line at zero intensity FWZI and the width of the channel in km s^{-1} (Ivison *et al.* 1996). Correspondingly, 3 times the continuum noise level $\sigma_{\text{rms-cont}}$ yields the upper limit of the continuum emission. The integrated flux uncertainty for extended emission depends on the zero level error and the noise error in the integrated area,

$$\Delta S_{\text{tot}} = \sigma_{\text{rms-int}}\, m \sqrt{1/n + 1/m} \tag{2.2}$$

where m and n are the integrated area and the rms tested area per beam area (Klein and Emerson 1981; Andernach 1999).

When applying a uniform weighting to the ^{12}CO visibilities, the larger baselines determine the spatial resolution on the cost of the sensitivity. In this way the gas distribution on smaller spatial scales becomes visible. Additionally, I applied a circular restoring beam, whose size is the geometric average of the uniformly weighted beam axes. The S/N in the observation of HE 1108-2813 is high enough, that I expect the CLEAN components to mimic the true brightness distribution very well. Therefore, I used only the minor axis size of the uniformly weighted beam for mapping this galaxy.

2.3 Results

I find the ^{12}CO emission to be well detected in all sources. While ^{13}CO is tentatively detected in HE 0433-1028 and HE 1108-2813, neither HCO^{+} line emission in HE 1029-1831 nor the continuum emission in all three galaxies are detected. Therefore I will give upper limits for the non-detections. When speaking of moments 0, 1 and 2 of an image cube I refer to the total/integrated flux, the velocity field and the velocity dispersion, respectively.

2.3.1 CO emission spectra

For retrieveing the spectra (Fig. 2.1), I used a region of the size of the beam and centered it on the peak of the integrated ^{12}CO emission.

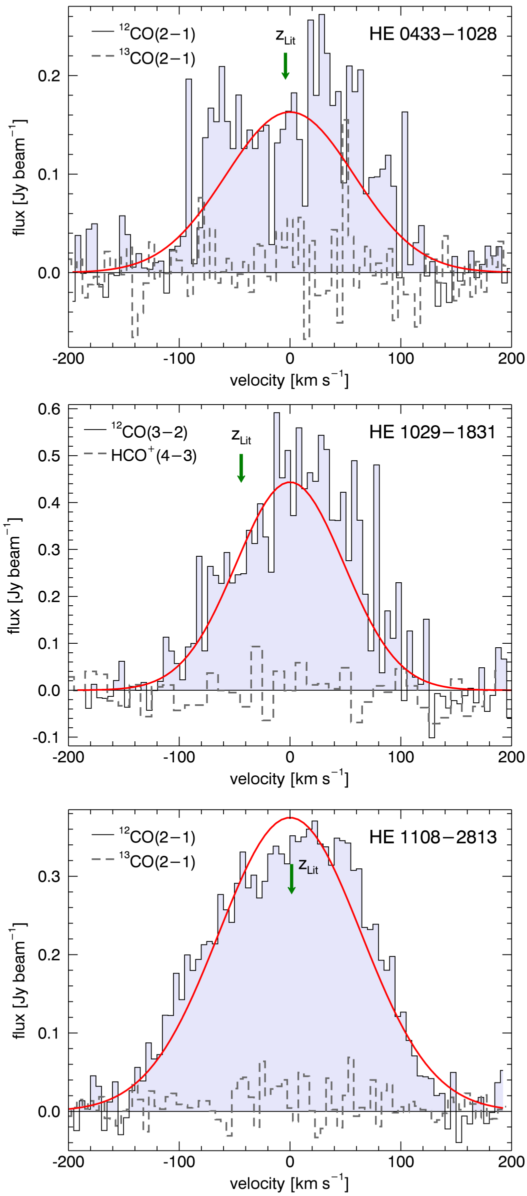

Figure 2.1: *^{12}CO spectra (solid black line) of the three sources obtained from a region with the size of the beam centered at the position of the integrated flux peak (velocity in LSR). The (green) arrows indicate the optical redshift from the literature (see Table 2.1). The parameters of the fitted Gaussian profile (solid red line) are given in Table 2.4 and 2.5. In addition, the ^{13}CO spectra of HE 0433-1028 and HE 1108-2813 from a beam-sized region at the position of the integrated ^{13}CO flux peak and a HCO^{+} spectrum (non-detection) of HE 1029-1831 at the position of the integrated ^{12}CO flux peak are shown (grey dashed line). (Credit: Moser et al. (2016a), reproduced with permission ©ESO.)*

The spectra of all galaxies display hints of skewness in the line profiles and there is an indications of a double horn profile in the case of HE 0433-1028. Nevertheless, fitting a Gaussian profile is sufficient for obtaining general characteristics of the ^{12}CO emission (see Table 2.4). As a consequence, the uncertainties in the Gaussian parameters are possibly larger by a factor of 5 to 10, i.e. a redshift error of 0.0001. The redshifts I derived from the fits correspond to the literature values (Table 2.1) within their uncertainties. The line widths (FWHM) cover a range of 115 - 150 km s^{-1}. The full width at zero intensity (FWZI) over the channel range where emission is detected (Table 2.5) are about 200 - 260 km s^{-1}. For HE 0433-1028, the FWZI matched the value measured by Bertram *et al.* (2007), but for HE 1029-1831 and HE 1108-2813 I find FWZIs that are larger by about 50 - 60 km s^{-1}. This difference can be attributed to flux resolved out by the interferometer.

The spectra (Fig. 2.1) around the ^{13}CO line frequency of HE 0433-1028 and HE 1108-2813 and of the HCO^{+} line frequency of HE 1029-1831 are extracted from a region with the size of the beam, centered on the integrated ^{13}CO emission peak in the case of the first two galaxies and on the integrated ^{12}CO flux peak for the latter. The ^{13}CO emission in HE 0433-1028 and HE 1108-2813 is faint but well above the rms-noise of $1\sigma_{\text{rms-ch}}$ (Table 2.2). For increasing the S/N, i.e. $1\sigma_{\text{rms-ch}}$ = 46 mJy beam^{-1}, for the HCO^{+} emission HE 1029-1831 I binned the data to 10 km s^{-1}-channels. However, the HCO^{+} emission in HE 1029-1831 remains undetected.

2.3.2 CO fluxes, gas masses and sizes

The Figures 2.2, 2.5 and 2.8 show the integrated flux maps, the velocity fields, the velocity dispersion maps and position-velocity (PV) diagrams I calculated from the ^{12}CO emission of the three galaxies. For HE 0433-1028 and HE 1108-2813, the ^{13}CO emission and the line luminosity ratios with the corresponding ^{12}CO emission are presented in Fig. 2.3 and 2.9, respectively. In the case of HE 1029-1831, I derived the line luminosity ratios of the three lowest ^{12}CO transitions which are given in Figure 2.6. The results from a 2D-Gauss Fit to the dominating ^{12}CO flux component are listed in Table 2.6, the integrated fluxes of all in this work detected lines in Table 2.5.

I find that the peak positions in the integrated flux are consistent with the phase tracking centers up to less than 0.5$''$ (Table 2.4), except for HE 0433-1028: here the peak is situated ~ 2$''$ towards south-east (Fig. 2.5). The total diameter of the detected gas content in HE 0433-1028, HE 1029-1831 and HE 1108-2813 is ~ 9$''$, 5$''$, 18$''$ (= 6.4, 4.0, 8.7 kpc) respectively (see Figures 2.2, 2.5 and 2.8).

By fitting an elliptical Gaussian component to the dominating central emission region in the uv-plane I find out that about 80 - 95 % of the total flux is located within a deconvolved source size of $d_{\text{FWHM}} \lesssim 0.7$ - 1.8 kpc (see Table 2.6).

The amount of flux missed by the interferometer in the case of HE 0433-1028 and HE 1108-2813 can be estimated from the IRAM 30m telescope data in Bertram *et al.* (2007). However, I found that the primary bars are larger than the 11.3$''$ ^{12}CO(2–1) beam of the IRAM 30m telescope. The primary bar of HE 0433-1028 is even larger than the 22.7$''$ ^{12}CO(1–0)

Table 2.4: *Position of the peak in integrated ^{12}CO flux and parameters of the Gaussian profile fitted to the spectra at that position (Credit: Moser* et al. *(2016a), reproduced with permission ©ESO.)*

object	^{12}CO transition	peak position [1] $\Delta\alpha$ [″]	$\Delta\delta$ [″]	S_{peak} [mJy beam^{-1}]	line center ν_{obs} [GHz]	line width σ [GHz]	$FWHM$ [km s^{-1}]	z
HE 0433-1028	2–1	1.70	-1.00	163 ± 13	222.621 ± 0.004	0.043 ± 0.003	137 ± 9	0.03556 ± 0.00002
HE 1029-1831	3–2	0.20	0.20	444 ± 28	332.363 ± 0.003	0.054 ± 0.003	115 ± 6	0.04041 ± 0.00001
HE 1108-2813	2–1	0.18	-0.41	375 ± 17	225.133 ± 0.002	0.048 ± 0.001	151 ± 4	0.02401 ± 0.00001

Notes. (1) offset relative phase tracking center

Table 2.5: *source fluxes, line ratios, luminosities and gas masses of the sources using the redshifts listed in Table 2.4 (Credit: Moser* et al. *(2016a), reproduced with permission ©ESO.)*

object	line	$FWZI_{im}$ [km s^{-1}]	S_{rms}	$S_{peak\ value}$ [Jy beam^{-1} km s^{-1}]	S_{tot} $(r \leq 10'')^{1}$ [Jy km s^{-1}]	$L'_{^{12}CO(X-Y)}$ [10^8 K km s^{-1} pc^2]	$\frac{^{12}CO(X-Y)}{^{12}CO(1-0)}$	$\frac{^{12}CO(X-Y)}{^{13}CO\ or\ HCO^+}$	$M_{mol}{}^{4}$ [$10^9 M_\odot$]
HE 0433-1028	^{12}CO(2–1)	195	0.9	33.2	56.6 ± 3.3	8.19	0.63^{2}		1.0 - 6.2
	^{13}CO(2–1)	150	0.8	3.8	3.2 ± 1.2		-	5 - 20	
HE 1029-1831	^{12}CO(3–2)	205	1.9	81.4	110.3 ± 6.1	9.17	1.00^{3}		0.7 - 4.5
	HCO^+(4–3)	~ 150	1.8	-	≤ 5.3			≥16	
HE 1108-2813	^{12}CO(2–1)	260	0.8	78.3	104.5 ± 3.1	6.84	0.65^{2}		0.9 - 5.5
	^{13}CO(2–1)	150	0.5	3.5	3.0 ± 0.7			5 - 30	

Notes. (1) flux errors do not include flux calibration error of 20% - 30% and are based on image noise only to demonstrate the data quality (2) based on single dish fluxes in Bertram *et al.* (2007) and corrected for source size and the adopted cosmology (3) based on line ratio map of PdBI data (Krips *et al.* 2007a) and my data in Fig.2.6 (4) total molecular mass in this observation (including Helium via a factor of 1.36) and covering a mass range corresponding to $\alpha_{CO} = 0.8$ - $4.8\ M_\odot$ (K km s^{-1} pc^2)$^{-1}$ for ULIRG and Galactic mass conversion (Downes and Solomon 1998; Solomon and Barrett 1991)

Table 2.6: *source distances, sizes (deconvolved Gaussian FWHM) and fractions f_{Gauss} of the total flux contained in a Gaussian of given size (Credit: Moser* et al. *(2016a), reproduced with permission ©ESO.)*

object	D_L[1] [Mpc]	scale[1] [kpc/″]	$d_{FWHM_1} \times d_{FWHM_2}$ [″ × ″]	[kpc × kpc]	PA [°]	f_{Gauss} [%]
HE 0433-1028	156.5	0.708	2.3 ± 0.2 × 2.5± 0.2	1.6 ± 0.1 × 1.8 ± 0.1	31	94
HE 1029-1831	178.4	0.799	1.3 ± 0.1 × 1.3± 0.2	1.1 ± 0.1 × 1.1 ± 0.2	- 25	96
HE 1108-2813	104.7	0.484	3.3 ± 0.1 × 1.4± 0.1	1.6 ± 0.1 × 0.7 ± 0.1	11	78

Notes. [(1)] obtained from Ned Wright's Cosmology Calculator Wright (2006) (http://www.astro.ucla.edu/~wright/CosmoCalc.html)

beam. Consequently the single dish fluxes have a high uncertainty. I developed a workaround to estimate the coupling of the extended sources with the single dish beam in order to correct the single dish fluxes. Since the emission is not homogeneous over the bar, but concentrated in the center, I define a weighted source size based on the knowledge from the Gaussian component source fit in Table 2.6:

$$\theta^2_{\text{wgt-src}} = (1 - f_{\text{Gauss}})\ \theta_{\text{bar}_1}\ \theta_{\text{bar}_2} + f_{\text{Gauss}}\ d_{\text{FWHM}_1}\ d_{\text{FWHM}_2} \tag{2.3}$$

with $\theta_{\text{bar}_{1,2}}$ and $d_{\text{FWHM}_{1,2}}$ denoting the major and minor axis of the bar and the fitted central component (Table 2.6). From optical images in Fig. 2.4 and 2.10 I estimate the bar sizes (major and minor axis) to be $29'' \times 13''$ and $17.5'' \times 6''$, respectively.

^{12}CO(2–1) emission traces cool gas. Therefore, I expect the emission to be distributed along the bar of HE 0433-1028 in a similar manner like HE 1108-2813. In this scenario, it is not detected in the bar of HE 0433-1028 only because of the 3 times lower S/N in this observation. Based on this, I apply the same flux fraction f_{Gauss} of the central component like in HE 1108-2813, i.e. 78% - contrary to the measurement in HE 0433-1028. The IRAM 30m fluxes (Bertram *et al.* 2007) fluxes are then corrected for the beam convolved source sizes

$$\theta^2_{\text{conv}} = \theta^2_{\text{wgt-src}} + \theta^2_{\text{beam}} \tag{2.4}$$

and the adopted cosmology. For HE 0433-1028, 61% (37% for $f_{\text{Gauss}} = 1$) of IRAM 30m ^{12}CO(2–1) flux is resolved out and for HE 1108-2813, 88% (103% for $f_{\text{Gauss}} = 1$) of the flux is recovered by the SMA. Still, the reduced flux obtained from the interferometer is not entirely due to the spatial filtering of diffuse gas emission, but also due to the S/N, especially for HE 0433-1028, as well as due to the flux calibration errors (20 - 30%). Since HE 1029-1831 has never be observed in ^{12}CO(3–2) before, I cannot constrain the missing flux. But since this transition traces a warmer and denser gas component, I expected the amount of missing flux to be low (< 10%).

I calculate the ^{12}CO(1–0) luminosities according to

$$L'_{\text{CO}} = 3.25 \times 10^7\ S_{\text{CO}} \Delta V\ D^2_{\text{L}}\ \nu^{-2}_{\text{obs}}\ (1+z)^{-3} \tag{2.5}$$

with the integrated flux $S_{\rm CO}\Delta V \equiv S_{\rm total}$ in Jy km s^{-1}, the luminosity distance in $D_{\rm L}$ in Mpc, the observed frequency $\nu_{\rm obs}$ in GHz and $L'_{\rm CO}$ in K km s^{-1} pc^2 (Solomon and Barrett 1991).

Since the gas masses that are determined from the ^{12}CO(1–0) transition luminosity, I need to obtain the global line (luminosity) ratios (see Table 2.5) first by

$$r_{21} = S_2/S_1 \cdot \nu_2^2/\nu_1^2 = I_2/I_1 \cdot \theta^2_{\rm conv_2}/\theta^2_{\rm conv_1}, \tag{2.6}$$

regarding the weighted source sizes $\theta_{\rm wgt\text{-}src}$ and adopted cosmology. The indices 1 and 2 refer to the two different line transitions from the ^{12}CO data from Bertram *et al.* (2007). All line ratio maps (Fig. 2.3, 2.6, and 2.9) that I show in this chapter are based on this formula. As a result, I find ^{12}CO(2–1)/(1–0) line ratios of $r_{21} \leq 0.65$ and suggests the emission to be almost subthermal in all three sources. A deviation from the adopted bar axis lengths of 1″ and from $f_{\rm Gauss}$ by 10 % , leads to uncertainty in the ratios of 0.15. Considering the extreme cases, where the single dish fluxes are solely given by either the central Gaussian component or, highly unlikely, the bar, this gives maximum ranges of $r_{21} = 0.45 - 1.00$ and $r_{21} = 0.58 - 0.86$ for HE 0433-1028 and HE 1108-2813, respectively. For HE 1029-1831, I combined the information of the PdBI data of Krips *et al.* (2007a) with my data to calculated the ^{12}CO(3–2)/(1–0) line ratio (see Section 2.3.3.2 and Fig. 2.6 for calculation and discussion). I find a $r_{31} \sim 1$ which points at the ^{12}CO(3–2) transition to be thermalized.

I derive the molecular gas masses (including Helium) using the ^{12}CO(X–Y)/(1–0) line ratio $r_{\rm X1}$ via

$$M_{\rm CO(X-Y)} = \frac{\alpha_{\rm CO(1-0)}}{r_{\rm X1}} L'_{\rm CO(X-Y)} \tag{2.7}$$

and obtain $(0.7 - 6.2) \times 10^9 M_\odot$. The conversion factor $\alpha_{\rm CO}$ depends on the gas conditions. For ULIRGs it is $\alpha_{\rm CO} = 0.8 M_\odot$ (K km s^{-1} pc^2)$^{-1}$ $\equiv \alpha_{\rm ULIRG}$ (Downes and Solomon 1998), and for the Milky Way $\alpha_{\rm CO} = 4.8 M_\odot$ (K km s^{-1} pc^2)$^{-1}$ $\equiv \alpha_{\rm MW}$ (Solomon and Barrett 1991). These factors will be discussed in section 2.5.4. Since the conditions and their acting scales are unknown, I use both values to calculate the masses.

I find strong differences between the masses of HE 1029-1831 obtained here and in the past: The ^{12}CO(3–2) data restores 41 % of the BIMA ^{12}CO(1–0) detected mass, 58 % of the PdBI ^{12}CO(1–0) mass, but 98 % of the PdBI ^{12}CO(2–1) mass, i.e. $M_{\rm CO(2-1)} = 4.5 \times 10^9 M_\odot$ ($\alpha_{\rm CO} = 4.8 M_\odot$ (K km s^{-1} pc^2)$^{-1}$) using the ^{12}CO(2–1) flux and the ^{12}CO(2–1)/(1–0) line ratio of ~ 0.5 in Krips *et al.* (2007a). When I compare this to the ^{12}CO(2–1) flux of ~ 93 Jy km s^{-1} observed with the Caltech Submillimeter Observatory (CSO) 10.4 m telescope (Monje *et al.* 2011), it appears that 73 % of the flux are resolved out by the PdBI. The corresponding mass is $18 \times 10^9 M_\odot$ ($\alpha_{\rm CO} = 4.8 M_\odot$ (K km s^{-1} pc^2)$^{-1}$), i.e. 1.6 $M_{\rm BIMA}$ for a ^{12}CO(2–1)/(1–0) line ratio of ~ 0.5. This indicates also that the BIMA might have resolved out 40 % of the flux. On the one hand, missing flux and sensitivity have a severe impact on the results. On the other hand, ^{12}CO(3–2) emission stems from the warmer and/or denser gas fraction that is accumulated the central region. This can also be seen in the source extent compared to the whole galaxy (Fig. 2.7). Consequently, the mass difference might be due to a mixture of excitational and spatial filtering effects.

While the gas masses of local galaxies are of the order of 10^8– few $10^9 M_\odot$ (e.g. Helfer *et al.* 2003; Israel 2009), intermediate redshift (z ~ 0.1 - 0.6) QSO hosts and ULIRGs show gas masses of a few 10^8– few $10^{10} M_\odot$ (Combes *et al.* 2011; Krips *et al.* 2012; Villar-Martín *et al.* 2013; Rodríguez *et al.* 2014). For a sample of sub-millimeter galaxies (z ~ 2) Tacconi *et al.* (2006) find masses between $10^{10} - 10^{11} M_\odot$.

With regard to the local galaxies, the masses of the three galaxies analysed here are rather large when using Galactic mass conversion, but they occupy rather the lower mass range when comparing to intermediate redshift QSOs and using ULIRG mass conversion.

2.3.3 Morphology and Kinematics

In this section I take a closer look at the morphology in ^{12}CO and ^{13}CO, the kinematics (velocity, velocity dispersion, and PV diagrams), and the isotopologue luminosity line ratios of the individual galaxies. In the case of HE 1029-1831, the luminosity line ratio are computed for the lower three ^{12}CO transitions. Furthermore, I compare the morphology of each galaxies with archive optical or NIR data. The velocity dispersions is very likely affected by beam smearing because one line of sight includes gas moving at different velocities, leading to a broadening of the observed line profile beyond the gas intrinsic dispersion. This effect intensifies with an inclination approaching edge-on view. Hence, the dispersion and maybe also the velocity map are not very precise.

2.3.3.1 HE 0433-1028

The molecular gas in HE 0433-1028 confined to a compact boxy region (Fig. 2.2). The irregular shape suggests a complex morphology which is mostly unresolved at the center. In the higher resolution obtained by weighting the visibilities uniformly, the complex morphology fragments into a central component and two east and west of it. The velocity field shows the dominant velocity range to be -50 to 55 km s^{-1} and seems to be tilted in the central region, i.e. gradient there is oriented at a position angle (PA) = 48° (from north to east), while the outskirts can be described by a PA ~ 0°. Such s-shaped iso-velocity lines hint at the presence of kinematically distinct feature, i.e. an inclined nuclear disk or bar. The dispersion peaks at the center with σ_v ~ 55 km s^{-1} and extends along the 0 km s^{-1} velocity-contour. It also reaches slightly to the south-west region of constant velocity (plateau). Towards the edge of the emission region the low S/N enhances the uncertainty in the dispersion.

The PV-cut along an intermediate velocity gradient of PA ~ 17° shows either a rigid-rotation component (assumed for our dynamical mass estimate) or two components (x-shape). As indicated by the velocity field, the central component, centered on 0″ ,seems to have a steeper gradient ranging from -100 to 100 km s^{-1}, while the east and west components indicated in the uniformly weighted image might have smaller gradients, from -2.5″ to 2.5″ and -40 to 50 km s^{-1}, for the east and west components indicated in the uniformly weighted image. Along the minor axis the PV-cut (PA ~ 107°) indicates a velocity range similar to that of the central velocity component in the x-shape case of the major axis PV-cut. Outliers

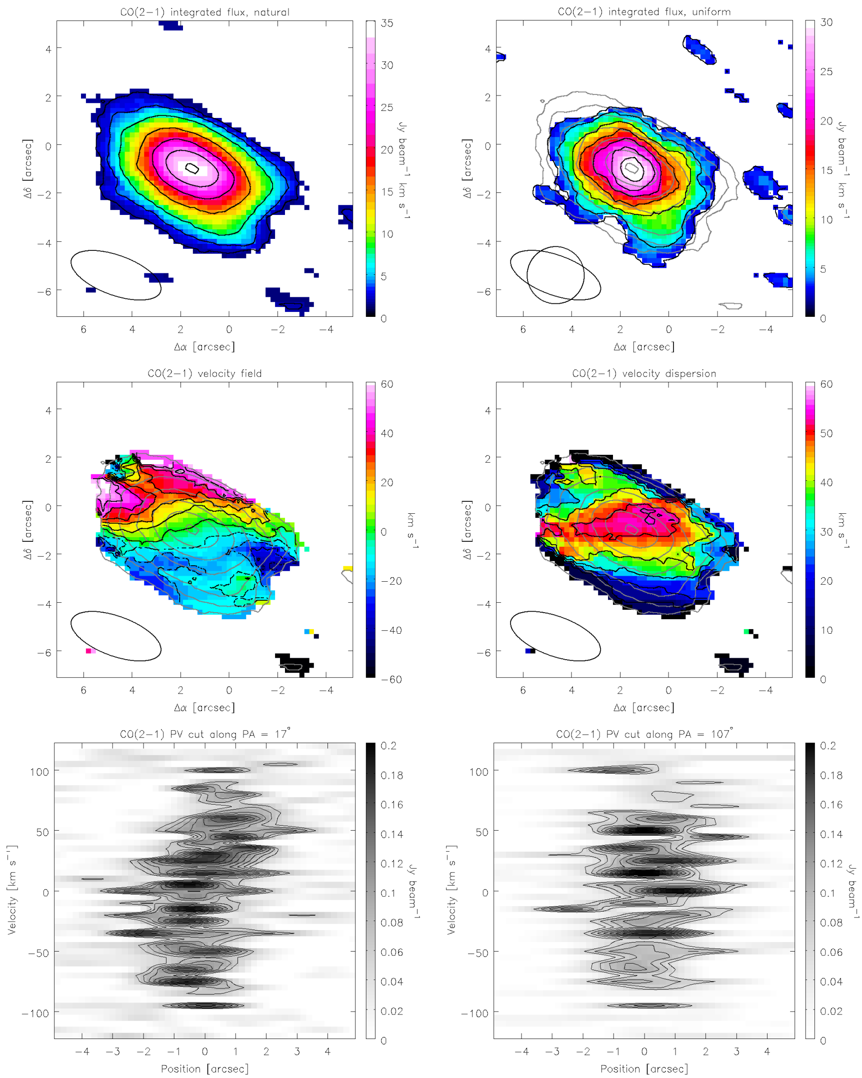

Figure 2.2: *HE 0433-1028:* Top panels: *the integrated* ^{12}*CO(2–1) flux image for natural weighting (*left*) and uniform weighting (*right*) obtained for a velocity range from -100 to +100 km s*$^{-1}$*. The beam sizes are* $3.9'' \times 1.6''$ *and* $2.35''$*, respectively. The contours are in steps of (2 (red), 4, 8, 16, 24, 32, 38)* $\times$ *1*$\sigma_{rms\text{-}int}$ *(= 0.9 Jy beam*$^{-1}$ *km s*$^{-1}$*) and (2 (red), 4, 8, 12, 16, 20, 24)* $\times$ *1*$\sigma_{rms\text{-}int}$ *(= 1.2 Jy beam*$^{-1}$ *km s*$^{-1}$*) , respectively.* Middle panels: *the corresponding iso-velocity (*left*) and velocity dispersion image (*right*) for natural weighting. The black contours are in steps of 10 km s*$^{-1}$ *from -50 to +50 km s*$^{-1}$ *and from 10 to 50 km s*$^{-1}$ *(additional contour at 53 km s*$^{-1}$*), respectively. The grey contours show the naturally weighted integrated* ^{12}*CO(2–1) flux.* Bottom panels: *the position velocity diagrams along the major (PA = 17°,* left*) and minor (PA = 107°,* right*) axis. (Credit: Moser* et al. *(2016a), reproduced with permission ©ESO.)*

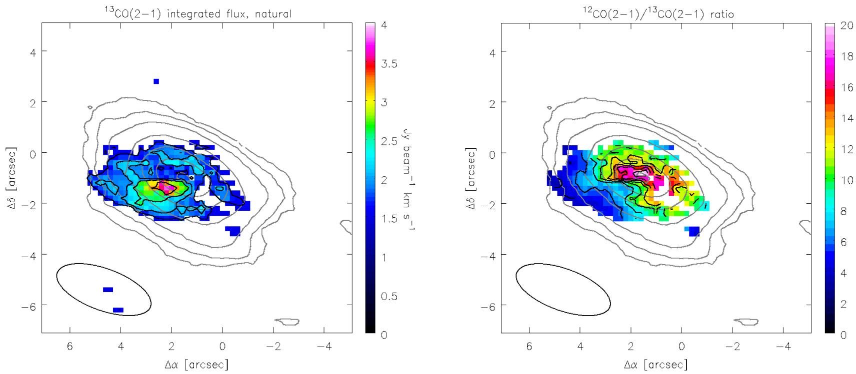

Figure 2.3: *HE 0433-1028:* Left: *the integrated* ^{13}*CO(2–1) flux image for natural weighting obtained for a velocity range from -75 to +75 km s*$^{-1}$*. Black contours are in steps of (2 (red), 2.5, 3, 4)* $\times$ *1*$\sigma_{rms\text{-}int}$ *(= 0.8 Jy beam*$^{-1}$ *km s*$^{-1}$*). The beam size is* $3.9'' \times 1.6''$*.* Right: *the* ^{12}*CO(2–1)/*^{13}*CO(2–1) luminosity ratio with black contours in steps of 2 from 4 to 18. The grey contours show the naturally weighted integrated* ^{12}*CO(2–1) flux as in Fig. 2.2. (Credit: Moser* et al. *(2016a), reproduced with permission ©ESO.)*

at lower velocities originate from from the edge of the emission region and are therefore uncertain due to a low S/N.

The SMA has tentatively detected ^{13}CO emission in the nuclear region (Fig. 2.3) which peaks somewhat off-center ($\sim 0.5''$, i.e. $< 0.5 \times \theta_{\rm minor}$) towards the south-east. There appears to be a dip in emission in the center, while there is more ^{13}CO emission towards the east than the west. The ^{12}CO/^{13}CO line ratio as low as 6 in the outskirts of the ^{12}CO emission in the east, steepens to 10 at a galactocentric distance of $< 2''$, and peaks with a value of 20 on the ^{12}CO maximum in the center. I revisit the ratios and their meaning later in section 2.5.1.

In order to understand the relation of the molecular gas to the stellar and dust distribution, I compare my data to NIR and optical images. The highest resolution image available for HE 0433-1028 is a V-band (550nm) image (Fig. 2.4) obtained with the ESO-Danish 1.54 m telescope (Hunt *et al.* 1999). Therein, the bar appears clumpy and the AGN emission strong. In order to intensify the contrast of the clumps in the bar and at the center, I first fit a Gaussian component to the dominating central component (AGN) and subtract it from the original image. In a second step, I smooth the resulting image and subtract it from the Gauss-subtracted image. This unsharp-masked image now shows bright bar tips and the dust lanes, that wind towards the nucleus and two bright peaks on opposing sides of the circumnuclear region. The latter could be star formation sites in a circumnuclear ring or a secondary bar at PA = -37° ± 5°. Simulations of Athanassoula and Misiriotis (2002,see their Fig. 11, middle panels) show, that a nuclear bar, which is misaligned with the global kinematical axes, seems to be slightly ahead of the twist in iso-velocity contours in the center. This matches the indications from the velocity distribution (s-shape) and the bar would be $\sim 5°$ ahead of the straight iso-velocity contours in the center. When comparing to the uniformly weighted ^{12}CO

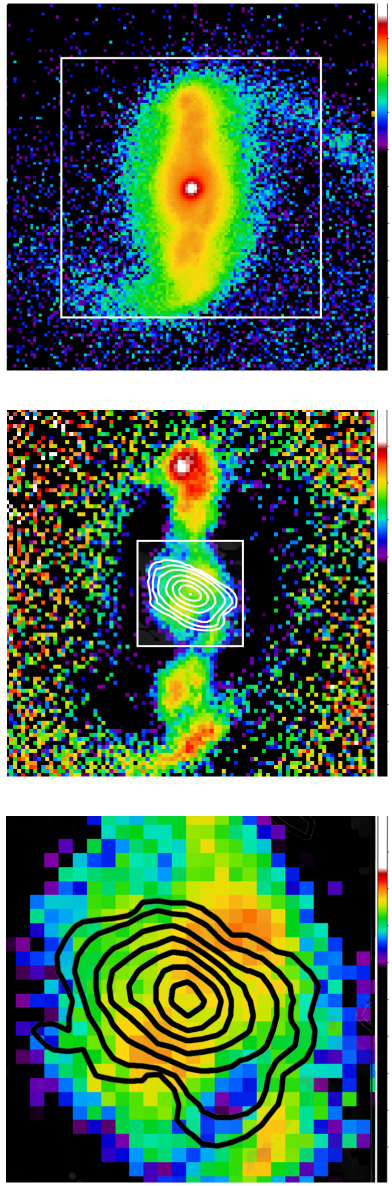

Figure 2.4: *HE 0433-1028:* Top: $50'' \times 50''$ *V-band image (ESO-Danish 1.54 m telescope, NED, arbitrary intensity units) of the galaxy, the box size is* $35'' \times 35''$. Middle: *zoomed into the box region of unsharp masked version of the image (arbitrary intensity units) overlayed with contours of naturally weighted integrated* ^{12}*CO(2–1) flux as in Fig. 2.2. Central region marked by box of size* $10'' \times 10''$. Bottom: *zoomed into inner* $10'' \times 10''$ *of unsharp masked image with contours of uniformly weighted integrated* ^{12}*CO(2–1) flux as in Fig. 2.2. (Credit: Moser* et al. *(2016a), reproduced with permission ©ESO.)*

data one can see that the molecular gas extends from the center out to the dust lane in the primary bar. The dust lanes seem to be heading to the two gas accumulations east and west of the center and seem tobe partly traced in ^{12}CO south-west of the center (see also red scaled region in Fig. 2.2, upper right panel). The angle of the alignment of the two clumps is PA = 74° ± 5°. At the same time these two regions correspond to the plateaus in the naturally weighted (imaging) iso-velocity map and local maxima in the dispersion (Fig. 2.2, middle). Obviously, kinematics behave here different from the central region.

2.3.3.2 HE 1029-1831

Since the ^{12}CO(3–2) line emission traces warmer and denser molecular gas, it is confined to the central region (see Fig. 2.5), i.e. within a radius 5 times smaller than the ^{12}CO(1–0) emission region observed by Krips *et al.* (2007a). In contrast to this, the ^{12}CO(1–0) and ^{12}CO(2–1) line emission from Krips *et al.* (2007a) appears to extend along the primary bar. Their ^{12}CO(2–1)/(1–0) line ratio of ~ 0.5 suggests subthermal excitation, except from a region in the south. My maps do not confirm the existence of this suspected high excitation component in the south (Krips *et al.* 2007a). Instead, they show a slight extension to the north-west (PA = -41° ± 5°). This asymmetry in the central region towards north-west becomes even more obvious when applying uniform weighting (PA = -44° ± 5°). Moreover, the peak position is shifted by 0.4″ (= 320 pc) toward the north-west. Both features imply the presence of a second component apart from the central one.

The dominating velocity components cover a range from -55 km s^{-1} to 70 km s^{-1} and the velocity gradient at the center is rather perpendicular to the primary bar PA = 115° ± 20° - in consistency with the study of Krips *et al.* (2007a, PA = 90°). However, the SMA is not a accurate as the PdBI data because of a lower sensitivity. The simulations by Krips *et al.* (2007a) suggest the velocity field to be induced by a bar potential and the velocity gradient by a bar-driven inflow. The velocity dispersion in the center is flat with $\sigma_{\rm v}$ ~ 50 km s^{-1} extends along the 0 km s^{-1}-contour (23° vs 24°) and the major axis. All in all, the ^{12}CO(3–2) emission represents rather the inner part of the bulge.

The PV diagrams match the previous results in Krips *et al.* (2007a). The minor axis PV-cut (PA = 0°) indicates a fast unresolved component with a velocity range of -100 to 100 km s^{-1}. The PV-cut along the major axis (PA = 90°) suggests an x-shape like for HE 0433-1028 and with this a kinematically distinct feature in the circumnuclear region. It has a steep component at offset 0″ ranging between -100 to 100 km s^{-1} and a shallower one from -1.5″ and -60 km s^{-1} to 1.5″ and 60 km s^{-1}.

The HCO$^+$(4–3) emission remains undetected in this observation. Instead I estimate a 3σ upper limit for the total flux. The rms in a 20 km s^{-1} channel is 33 mJy beam^{-1} and the line width is 150 km s^{-1}, similar to the ^{13}CO (2–1) emission line width for the other sources. These values yield an upper limit for the HCO$^+$(4–3) line flux of 5.3 Jy beam^{-1} km s^{-1}. With this, the ^{12}CO(3–2)/HCO$^+$(4–3) luminosity ratio at the peak position is > 16 as a lower limit.

For deriving the line ratios (see Fig. 2.6), one has to ensure, that the spatial scales considered are the same for the involved data sets. While it is the case for the ^{12}CO(2–1)/^{13}CO(2–1)

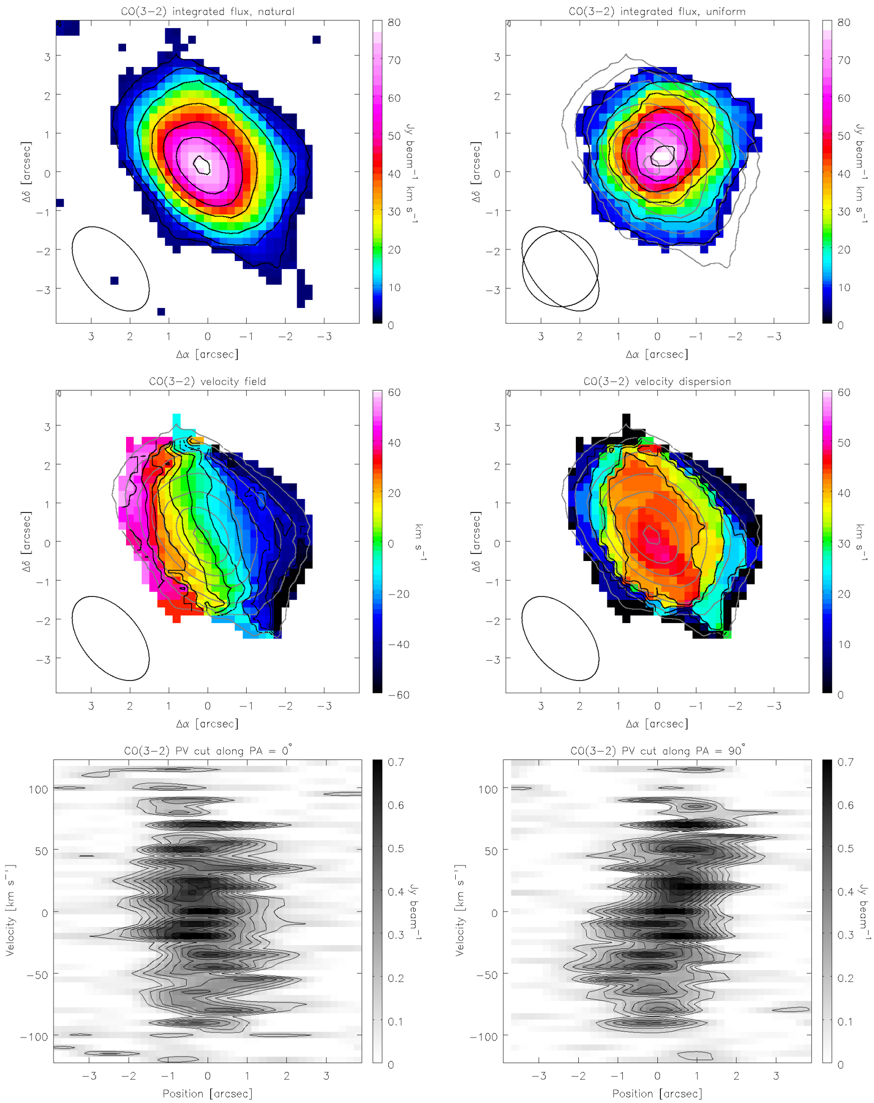

Figure 2.5: *HE 1029-1831:* Top panels: *the integrated ^{12}CO(3–2) flux image for natural weighting (*left*) and uniform weighting (*right*) obtained for a velocity range from -100 to +100 km s^{-1}. The beam sizes are 2.5″ × 1.5″ and 1.95″, respectively. The contours are in steps of (2 (red), 4, 8, 16, 24, 32, 40) × 1$\sigma_{rms\text{-}int}$ (= 1.9 Jy beam^{-1} km s^{-1}) and (2 (red), 4, 8, 12, 16, 20) × 1$\sigma_{rms\text{-}int}$ (= 3.7 Jy beam^{-1} km s^{-1}), respectively.* Middle panels: *the corresponding iso-velocity (*left*) and velocity dispersion image (*right*) for natural weighting. The black contours are in steps of 10 km s^{-1} from -50 to +50 km s^{-1} and from 10 to 50 km s^{-1}, respectively. The grey contours show the naturally weighted integrated ^{12}CO(3–2) flux.* Bottom panels: *the position velocity diagrams along the minor (PA = 0°, *left*) and major (PA = 90°, *right*) axis. (Credit: Moser* et al. *(2016a), reproduced with permission ©ESO.)*

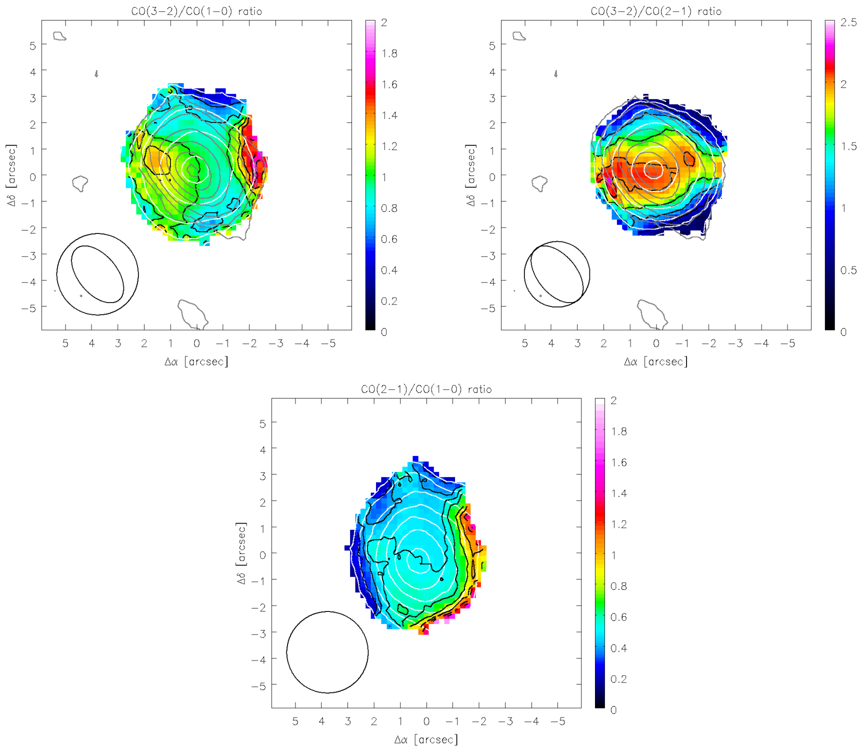

Figure 2.6: *HE 1029-1831:* Top left: *the* ^{12}*CO(3–2)/*^{12}*CO(1–0) luminosity ratio with black contours in steps of (4, 6, 8, 10, 12, 14, 16)* $\times$ *0.1. The white contours show the naturally weighted integrated*^{12}*CO(3–2) flux with contours of (4, 8, 16, 32, 48)* $\times$ *1*$\sigma_{rms\text{-}int}$ *(= 2.0 Jy beam*$^{-1}$ *km s*$^{-1}$*) for a beam size of* 3.1″. Top right: *the* ^{12}*CO(3–2)/*^{12}*CO(2–1) luminosity ratio with black contours in steps of (4, 8, 12, 16, 20)* $\times$ *0.1. The white contours show the naturally weighted integrated* ^{12}*CO(3–2) flux with contours of (2, 4, 8, 16, 32, 40)* $\times$ *1*$\sigma_{rms\text{-}int}$ *(= 2.2 Jy beam*$^{-1}$ *km s*$^{-1}$*) for a beam size of* 2.5″. Bottom: *the* ^{12}*CO(2–1)/*^{12}*CO(1–0) luminosity ratio with black contours in steps of (3, 4, 5, 6, 8, 10, 12, 14)* $\times$ *0.1. The white contours show the naturally weighted integrated* ^{12}*CO(2–1) flux with contours of (2, 4, 8, 12, 16, 20, 24)* $\times$ *1*$\sigma_{rms\text{-}int}$ *(= 0.9 Jy beam*$^{-1}$ *km s*$^{-1}$*) for a beam size of* 3.1″. *The grey contours show the naturally weighted integrated* ^{12}*CO(3–2) flux as in Fig. 2.5. (Credit:* Moser et al. (*2016a*)*, reproduced with permission ©ESO.)*

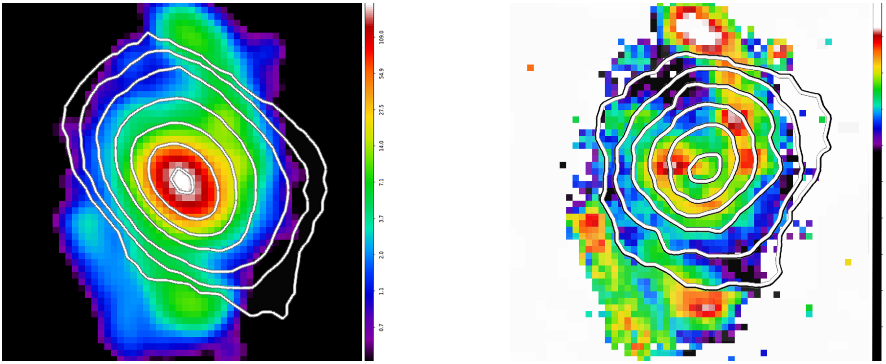

Figure 2.7: *HE 1029-1831:* Left: *7″ × 7″ SINFONI image (Busch* et al. *2015) of the integrated flux (arbitrary units) of the narrow Paα component of the galaxy overlayed with contours of naturally weighted integrated ^{12}CO(3–2) flux as in Fig. 2.5.* Right: *Corresponding equivalent width (arbitrary units) of the narrow Paα component with contours of uniformly weighted integrated ^{12}CO(3–2) flux as in Fig. 2.5. (Credit: Moser* et al. *(2016a), reproduced with permission ©ESO.)*

ratios (neighbouring spectral windows) in HE 0433-1028 and HE 1108-2813, it is not for the PdBI data. Therefore, I truncated the PdBI ^{12}CO (1–0) and (2–1) data of Krips *et al.* (2007a) to the uv-range of the SMA data, i.e. 14 - 120 kλ (15″-1.7″). Every line pair per ratio was imaged with a beam size set to the major axis length of the lower transition's beam. I enhanced the resolution of the ^{12}CO (1-0) image to 3.1″ by uniformly weighting the visibilities (compare natural weighting: 3.5″). As a result I find a ^{12}CO(3–2)/(1–0) line ratio of $\sim$ 1 in the center, 1.4 in the eastern and western regions and 0.6 in the northern and southern outskirts of emission. The ^{12}CO(3–2)/(2–1) line ratio is $\sim$ 2 in the center, 1.6 east and west and 0.6 north and south of the center. As consistency check I also derive the ^{12}CO(2–1)/(1–0) ratio at 3.1″ which appears as a beam smeared version of the results of Krips *et al.* (2007a). Since the beam size is relatively large the obtained maps provide rather global values that are likely dominated by the center (higher S/N). I discuss the line ratios in more detail in section 2.5.3.

The recent SINFONI data of the Paα emission and especially its equivalent width (Busch *et al.* 2015) show interesting details on the morphology of this galaxy (Fig. 2.7): It appears to have an actively star forming circumnuclear ring, but also the northern spiral arm in the bar shows two regions of bright (relative to the continuum) ionized gas emission. These clumps are the best explanation for the asymmetry to the north-west in the molecular gas in natural weighting and the shifted emission peak in the uniformly weighted image.

2.3.3.3 HE 1108-2813

The molecular gas distribution of HE 1108-2813 covers the primary bar and holds indications for a spiral arm pattern within it (Fig. 2.8). The bright nuclear component has an orientation of PA = -9° ± 5°. Since the beam is oriented at PA = -17° ± 1°, there has to be a non-circular component at positive PA. This assumptions is supported by the uniformly weighted image. The nuclear component extends along a PA = 20° ± 10°. Towards the tips of the bar the emission increases to Visible are also secondary maxima at the tips of the bar and the southern tip connects to the major spiral arm. Similar to the case of HE 0433-1028, the torsion of the iso-velocity lines in the central region suggests a kinematically different feature in the center, e.g. a nested bar or nuclear spiral/disk. The velocity dispersion reaches its maximum in the center (bulge turbulence) with $\sigma_{\mathrm{v}} \sim 50$ - 60 km s^{-1} and is elongated along PA = -31° ± 10°. Strikingly, turbulent regions in the primary bar, i.e. the shock fronts of the leading edges are not only visible in the uniformly weighted image, but also in the velocity dispersion with values of $\sigma_{\mathrm{v}} \sim 20$ - 25 km s^{-1}.

The PV-diagram along the major axis clearly outlines an x-shape. One part goes diogonal from about -6″ to 7″ and -100 to 80 km s^{-1} can be understood as a disk rotation curve. The vertical part around 0″ offset covers velocities from -125 to 120 km s^{-1}. The same feature can be seen in the minor axis PV-cut. In conclusion, the PV-diagram give another strong evidence for an unresolved and kinematically decoupled nuclear component in the center. I notice that the (projected) velocities in the circumnuclear region are larger than the disk velocities. This can be either due to a lower S/N towards the outskirts of the bar/disk or to nuclear component inclined at an angle different from the bar/disk inclination.

^{13}CO emission (Fig. 2.9) is contingently found in the nuclear region and peaks ∼ 0.7″ (i.e. $< 0.23 \times b_{\mathrm{min}}$) away from the center towards the south-west. At the ^{13}CO peak, the ^{12}CO/^{13}CO line ratio is 20 , at the ^{12}CO peak, it is 25, and it decreases at the (eastern) edges of the ^{13}CO emission (r ∼ 2″) to 5. In this way the behaviour of the ratio resembles the one found in HE 0433-1028.

The HST F606W image from Malkan *et al.* (1998) offers a high resolution view of this galaxy. However the AGN outshines the nuclear region and saturates the point spread function (PSF). I could enhance the image fidelity by subtracting a scaled and truncated PSF. For this, I used the Tiny Tim software (Krist *et al.* 2011) to generate the PSF for the pixel positions of the AGN region. I then scaled the PSF such that the flux of the diffraction spikes from the artifical PSF correspond the to background-subtracted flux of the real diffraction spikes and clipped the peak at a value given by the difference of the maximum counts and the background emission in the region. This procedure lowers the diffraction spikes efficiently except from some asymmetric artefacts in the PSF (negative spikes along the diagonals of the image).

When appliying unsharp-masking, a wealth of morphological details becomes obvious (Fig. 2.10). Two stretched patchy spiral arms form the leading edges of the primary bar and harbour several bright star forming spots. Dust lanes appear like a backbone of the spiral arms and curl off-center to connect to the central region. The image confirms the presence of a circumnuclear ring that seems to be actively forming stars. Such an accumulation of gas and stars is likely to mark the Inner Lindblad Resonance.

The compact star forming regions should constrain the ring diameter and can be fit by two possible ring shapes (solid and dashed lines in Fig. 2.10). The size of the solid circle

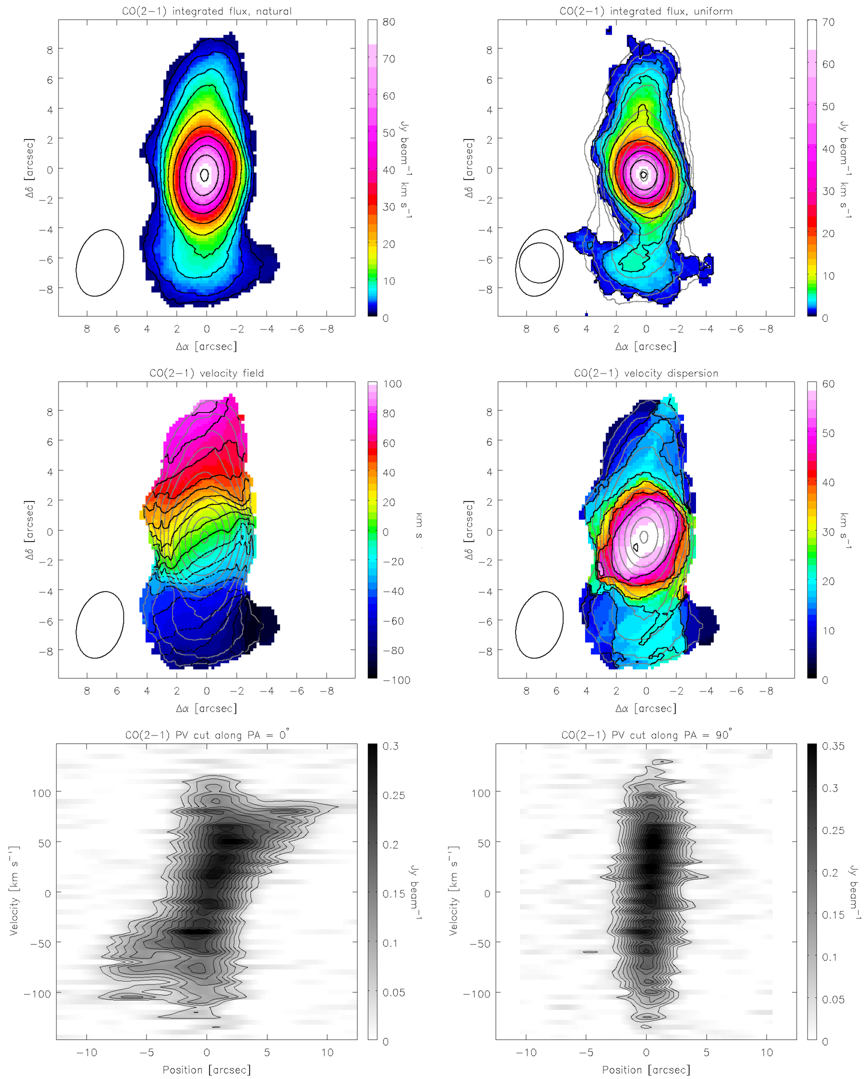

Figure 2.8: *HE 1108-2813:* Top panels: *the integrated ^{12}CO(2–1) flux image for natural weighting (*left*) and uniform weighting (*right*) obtained for a velocity range from -125 to +130 km s^{-1}. The beam sizes are* 4.5″ × 3.0″ *and* 2.68″*, respectively. The contours are in steps of (2 (red), 4, 8, 12, 20, 32, 48, 64, 80, 96) × 1$\sigma_{rms\text{-}int}$ (= 0.8 Jy beam^{-1} km s^{-1}) and (1 (red), 2, 4, 8, 16, 32, 48, 62) × 1$\sigma_{rms\text{-}int}$ (= 1.1 Jy beam^{-1} km s^{-1}), respectively.* Middle panels: *the corresponding iso-velocity (*left*) and velocity dispersion image (*right*) for natural weighting. The black contours are in steps of 10 km s^{-1} from -90 to +80 km s^{-1} and from 10 to 60 km s^{-1} (additional contour at 15 km s^{-1}), respectively. The grey contours show the naturally weighted integrated ^{12}CO(2–1) flux.* Bottom panels: *the position velocity diagrams along the major (PA = 0°,* left*) and minor (PA = 90°,* right*) axis. (Credit: Moser* et al. *(2016a), reproduced with permission ©ESO.)*

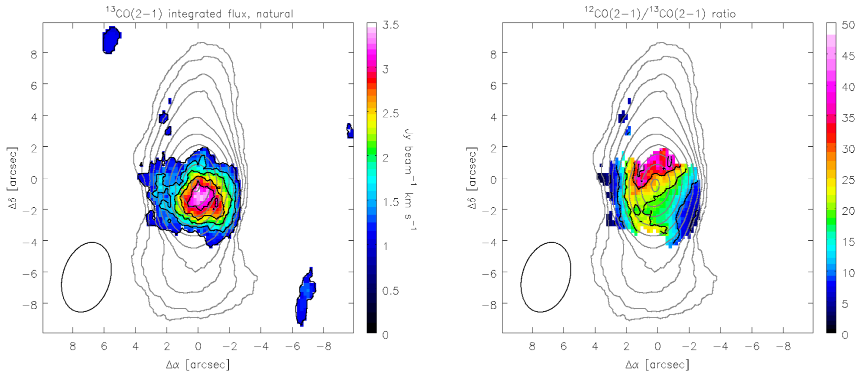

Figure 2.9: *HE 1108-2813:* Left: *the integrated* ^{13}*CO(2–1) flux image for natural weighting obtained for a velocity range from -75 to 75 km s*$^{-1}$. *Black contours are in steps of (2 (red), 3, 4, 5, 6)* $\times$ *1*$\sigma_{rms\text{-}int}$ *(= 0.5 Jy beam*$^{-1}$ *km s*$^{-1}$*). The beam size is* $4.5'' \times 3.0''$. Right: *the* ^{12}*CO(2–1)/*^{13}*CO(2–1) luminosity ratio with black contours in steps of 5, 10, 20, 30, 40. The grey contours show the naturally weighted integrated* ^{12}*CO(2–1) flux as in Fig. 2.8. (Credit: Moser* et al. *(2016a), reproduced with permission ©ESO.)*

is $2.0'' \times 2.2''$, i.e. 0.97 kpc $\times$ 1.07 kpc, and it concentric around the AGN. The dashed circle is slightly wider ($2.2'' \times 2.4''$, i.e. 1.07 kpc $\times$ 1.16 kpc) and shifted from on the AGN by $\sim$ 100 pc, i.e. $\Delta\alpha$ = 0.14″, $\Delta\delta$ = -0.14″. In bith cases, the scale match the minor axis diameter d_{FHWM} = 0.8 kpc of the fitted Gaussian component. The eastern and western star-forming clusters in the ring are close to the incoming the spiral arms suggesting the "string of pearls" model for circumnuclear star formation. The scenario for this is the following: In the moments that the gas flows from the bar spiral arm to the circumnuclear ring at the x_1–x_2 - orbit intersection region (see e.g. Fig. 15 in Regan and Teuben 2003), it is compressed by the local overdensity, which induces a very short-lived starburst. Once the overdensity is passed the the star formation activity declines Therefore, one can expect the cluster populations to be the older the further they moved away with the flow from the overdensity along the ring (Böker *et al.* 2008). To clarify the likelyhood of such a scenarios, the ages of the stellar populations have tobe tested. An alternative interpretation of the morphology could be that we are looking at a nuclear bar at a PA = -37° ± 10° whose tips - marked by the two opposing stellar clusters - might not be perfectly aligned. The orientation of the hypothetical bar is similar to the orientation central velocity dispersion field. Inside the circumnuclear ring, the artefacts from the image processing distorts the HST image here.

When comparing the optical image with the ^{12}CO emission it turns out that dust lanes the ^{12}CO spiral arm pattern closely. Moreover, the southern extension to the east is confirmed to be the southern galactic spiral arm. These correlations become even more evident when considering the uniformly weighted image. ^{13}CO(2–1) emitting gas accumulates at the overdensities/x_1–x_2 - orbit intersection regions, where the gas is cold and dense enough for this emission line. In contrast to this, ^{13}CO(2–1) is weak in the center, most likely because

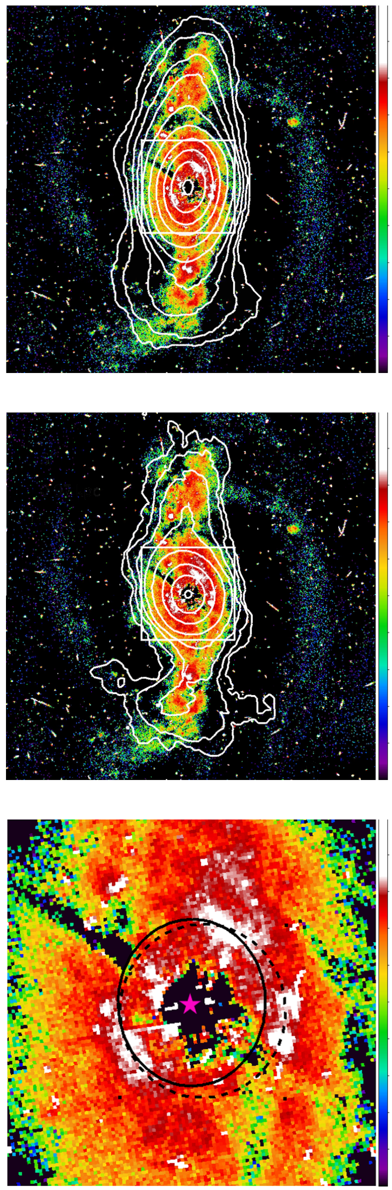

Figure 2.10: *HE 1108-2813:* Top: *20″ × 20″ of unsharp-masked HST image (F606, red, HST archive, arbitrary intensity units) of the galaxy overlayed with contours of naturally weighted integrated ^{12}CO(2–1) flux as in Fig. 2.8. The box size is 5″ × 5″.* Middle: *same as top, but with contours of uniformly weighted integrated ^{12}CO(2–1) flux as in Fig. 2.8.* Bottom: *zoomed into the box region of the image. The solid and dashed circles indicate possible circumnuclear ring configurations (see section 2.3.3.3). The magenta star denotes the AGN's position. (Credit: Moser* et al. *(2016a), reproduced with permission ©ESO.)*

the ISM is too hot and/or dense (compare Hüttemeister *et al.* 2000).

2.3.3.4 A note on the kinematics

In the previous sections I found all three galaxies evidences for an unresolved kinematically distinct component in their centers. In fact, they seem to be a feeding criterion in Seyfert galaxies: E.g. Dumas *et al.* (2007) discover based on a sample of matched pairs of active and inactive galaxies that Seyfert galaxies tend to display a higher perturbation of their central gas velocity fields (r < 500 pc) than inactive galaxies. These perturbations can come along in a large variety from wiggles along the gas kinematic minor axis to highly misaligned kinematic major axes of gas and stars. The latter case is so far unique to Seyferts. Furthermore, central depressions in velocity dispersion of gas/stars appear to correlate with a high concentration of gas ($r \lesssim 500$ pc) and a high star formation activity at the same location as the dispersion depression Falcón-Barroso *et al.* (2006); Hicks *et al.* (2013). These features are the property of a dynamically cold (compared to the bulge) nuclear structure (e.g. a disk). Such disks seem to be very efficient feeding agents for nuclear star formation and AGN activity.

2.3.4 Dynamical mass

The formalism for deriving the dynamical mass is given as

$$M_{\rm dyn}(r < R) = 2.325 \times 10^5 \; \alpha_M \; R \left(\frac{v(R)}{\sin i}\right)^2 \tag{2.8}$$

with the radius R of the enclosed mass in kpc, the projected velocity $v(R)$ in km s^{-1}, i the inclination of the galaxy and $M_{\rm dyn}$ in $M_\odot$ (Lequeux 1983). I adopted an intermediate value of 0.8 for the disk geometry factor α_M. Table 2.7 lists radii and corresponding velocities obtained from the PV diagrams as well as the inclinations, which are determined from the optical major and minor axis diameters (Hubble 1926; van den Bergh 1988), and resulting masses. The range of the dynamical masses of the three galaxies is $(1.5 - 6.7) \times 10^9 M_\odot$. The molecular gas masses correspond to 10 - 50% of the dynamical mass when adopting a ULIRG conversion factor, and 80 - 300% for the Galactic conversion factor.

The dynamical masses have a considerable uncertainty: First, except for HE 1108-2813, it cannot be excluded that the rotation curve was not full traced due to the low S/N towards the outskirts of the CO emission. It is very likely that the turn-over point from solid body to flat rotation has not been detected in the two other galaxies. The missed gas components make a considerable difference in the dynamical mass: For example, a distance and velocity variation of 25% and 13%, repectively, means dynamical mass uncertainty of $\sim$ 30% (HE 1029-1831). Second, the uncertainty in the inclination is high, because the assumption of a perfectly circular galactic disk may not hold. Typically gas masses make up about 10% (Young and Scoville 1991) of the dynamical masses in galaxies. For achieving this value, the inclinations would be 21 - 38° for a ULIRG conversion factor and 0° for a Galactic conversion factor (Table 2.7).

As a probe I derived the dynamical masses from the SMBH masses with the assumption that the bulge mass roughly corresponds to the dynamical masses. The three galaxies have SMBH masses of $M_{\mathrm{BH}} \sim 10^{7-8} M_\odot$, which translates into dynamical/bulge masses of $M_{\mathrm{dyn}} \sim (0.3 - 5.6) \times 10^{10} M_\odot$ (Sani *et al.* 2011; Kormendy and Ho 2013). The resulting bulge masses are more than 2.5 times larger the the gas dynamical mass, except from HE 1108-2813, where the bulge mass corresponds to 70% of the gas dynamical mass (Table 2.7). For HE 1029-1831 exists a 4 times larger dynamical mass value (than obtained from my data) of $M_{\mathrm{dyn}} = 6 \times 10^9 M_\odot$ based on stellar velocity dispersion (Busch *et al.* 2015).

Even though these bulge masses exceed the gas dynamical masses, most likely hinting at a detection issue, the molecular gas still correspond to 43 % of the bulge masses for a Galactic conversion factor α_{MW}. Propably, the majority of giant molecular clouds (GMCs) in these galaxies is not self-gravitating and hence, the Galactic conversion factor overestimates the gas masses (see Section 2.5).

2.3.5 Continuum Emission and Dust properties

Because emission in the 220 GHz and 330 GHz continuum was not detected, I estimated 3σ-upper limits based on the line-free channels (excluding the range of -200 km s^{-1} - +200 km s^{-1}; see Table 2.8).

Dust temperatures and masses can be estimated from the FIR SED. I used the fitting technique of Casey (2012, publicly available IDL-code) which fits a superposition of a modified single-temperature greybody component for the FIR (> 50 μm) and a power law component for the MIR (< 50 μm) to data sets. The greybody component describes the radiation from cold dust which heated by the star formation of the whole galaxy The power-law component can be understood as a superposition of several greybodies at different temperatures corresponding to hot dust heated to a varying extend by an AGN or an intense star forming regions. For each galaxy I found six AKARI/ASTRO-F satellite (AKARI) and four IRAS measurements, and for HE 0433-1028 further four Infrared Space Observatory (ISO) measurements. 3σ-upper limits for the sub-mm continuum emission give the sub-mm slope a rough lower limit. The results are shown in Figure 2.11 and Table 2.8.

The IR (8-1000 μm) and FIR (40-1000 μm) luminosities are about 10^{11} $L_\odot$ classifying them as LIRGs, except from HE 1108-2813. They are a factor of 1.3 smaller than the luminosities (Table 2.1) based on the IRAS fluxes (Sanders and Mirabel 1996). However, I regard the luminosities based on the SED fit as more accurate because it accounts for the individual slopes of the SED on both sides of the emission maximum. In contrast to this, the IRAS luminosities are estimated based on a template of a sample averaged SED.

The galaxies show intrinsic dust temperatures of $T_{\mathrm{fit}} \sim 58$ K, and peak dust temperatures $T_{\mathrm{peak}} \sim = 37$ K, which are given by Wien's displacement law for a single blackbody. I find the dust emissivity β to be in the range of typical values around 1.7 (Casey 2012,and references therein). Eventually, I obtain dust masses of $M_{\mathrm{dust}} = (1.6 - 4.4) \times 10^6$ $M_\odot$ from the extrapolated flux at 850 μm. A dust absorption coefficient of $\kappa = 0.15$ m^2 kg^{-1} (Weingartner

Table 2.7: *dynamical masses (Credit: Moser et al. (2016a), reproduced with permission ©ESO.)*

object	radius R [″]	radius R [kpc]	v [km/s]	i[1] [°]	M_{dyn} [$10^9 M_\odot$]	$M_{\mathrm{mol}}/M_{\mathrm{dyn}}$[2]	$i_{M_{\mathrm{mol}}=10\% M_{\mathrm{dyn}}}$[2] [°]	$M_{\mathrm{dyn\ (bulge)}}$[3] [$10^9 M_\odot$]
HE 0433-1028	1.0 ± 0.3	0.7 ± 0.2	100 ± 10	42	3.0 ± 0.8	0.3 - 2.1	21 - 8	14.5
HE 1029-1831	1.0 ± 0.3	0.8 ± 0.2	80 ± 10	53	1.5 ± 0.4	0.5 - 3.0	21 - 8	3.7
HE 1108-2813	6.0 ± 1.0	2.9 ± 0.5	80 ± 20	46	6.7 ± 2.0	0.1 - 0.8	38 - 15	4.7

Notes. [(1)] inclination based on major and minor axis values taken from NASA/IPAC Extragalactic Database (NED) [(2)] range given by ULIRG and Galactic mass conversion factor [(3)] bulge mass; average of the results of the M_{BH}-M_{bulge} relations given in Sani *et al.* (2011) and Kormendy and Ho (2013), derived from the average of the black hole mass range limits given in table 2.1.

Table 2.8: *dust properties derived from the MIR/FIR fit (Credit: Moser et al. (2016a), reproduced with permission ©ESO.)*

object	$S_{3\sigma\mathrm{cont}}$ [mJy beam^{-1}]	L_{IR} [$10^{11} L_\odot$]	L_{FIR} [$10^{11} L_\odot$]	T_{fit} [K]	T_{peak} [K]	β	M_{dust} [$10^6 M_\odot$]	$M_{\mathrm{mol}}/M_{\mathrm{dust}}$[1] [$10^2$]
HE 0433-1028	4.1 (220 GHz)	2.2 ± 0.1	1.1 ± 0.1	58 ± 1	38 ± 1	1.5 ± 0.1	4.4 ± 0.6	2.3 - 14.1
HE 1029-1831	11.1 (330 GHz)	2.0 ± 0.3	1.3 ± 0.2	58 ± 3	36 ± 3	1.7 ± 0.1	4.2 ± 0.6	1.8 - 10.7
HE 1108-2813	2.7 (220 GHz)	0.9 ± 0.1	0.6 ± 0.1	56 ± 2	35 ± 2	1.9 ± 0.1	1.6 ± 0.2	5.6 - 33.5

Notes. [(1)] range given by ULIRG and Galactic mass conversion factor

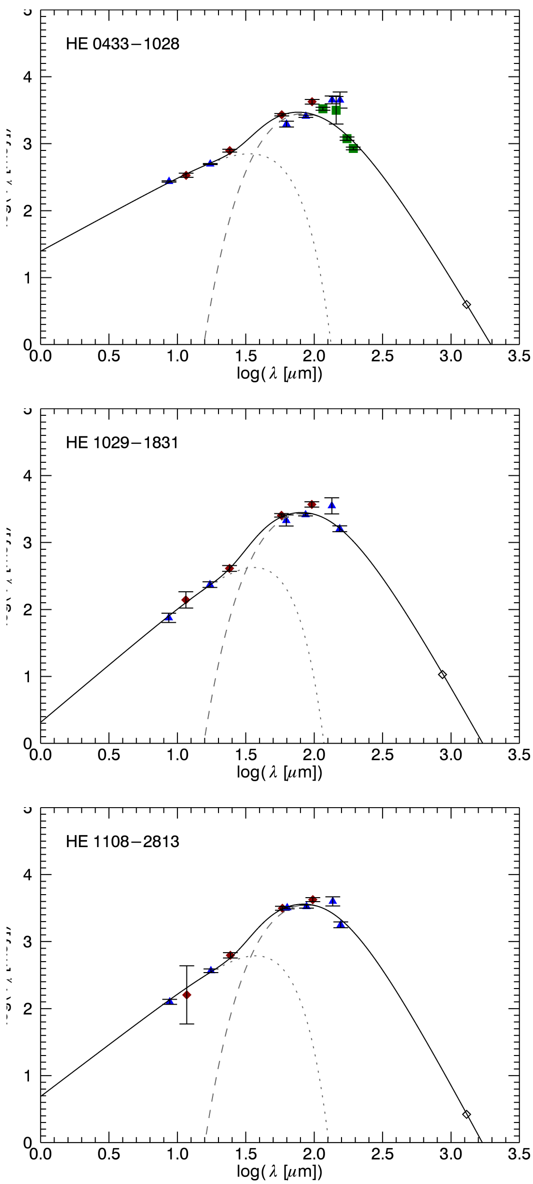

Figure 2.11: *SED fits to the IRAS (red diamonds), AKARI (blue triangles), and ISO data (green squares, only for HE 0433-1028 available) composed of a single dust temperature greybody component (grey dashed line) and a MIR power-law component (grey dotted line). The overall fit curve is shown as solid black line. White diamonds are SMA upper flux limits. (Credit: Moser* et al. *(2016a), reproduced with permission ©ESO.)*

and Draine 2001) is used. Omitting the sub-mm data upper limit data point yields even lower dust masses.

Based on the masses I determined in this work the gas to dust ratio in the three galaxies is about 1.8 - 5.6 larger than the standard ratio of 100 when assuming a ULIRG conversion factor, and 11 - 34 for a Galactic conversion factor. In fact, the gas-to-dust mass ratios in LIRGs/ULIRGs can be of the order of 200 - 350 (Sanders *et al.* 1991; Contini and Contini 2003; Seaquist *et al.* 2004; Wilson *et al.* 2008). In this light, the molecular gas in these three galaxies seems to be rather "ULIRG"-ish in terms of luminosity-mass conversion and gas-to-dust ratio.

Nevertheless, there are some caveats concerning the dust masses. First, I constrain the FIR emission at > 200 μm with only one data point and that a an upper limit. Second, this data point is based on an interferometric observation. It is possible that a significant amoung of flux has been resolved out. At this redshift range and spatial resolution the missing flux can make up to $\gtrsim$ 50% of the continuum flux (Wilson *et al.* 2008). Increasing the sub-mm fluxes by a factor of 2 doubles the dust masses in Table 2.8. Third, the emissivity is unknown (as well as the dust absorption coefficient, but this is less problematic for the sub-mm flux). Forth, the fit ignores the potential presence of another cold dust component at a different temperature. Therefore, this procedure can overestimated oder underestimate the FIR-to-sub-mm flux in the case of a more complex temperature structure.

Table 2.9: *SFRs and surface densities (Credit: Moser* et al. *(2016a), reproduced with permission ©ESO.)*

object	$SFR_{\rm IR}$	$SFR_{1.4\,\rm GHz}$	$\tau_{1.4\,\rm GHz\text{-}SFR}$ H$_2$+He	Σ_{mol} within $3 \times d_{\rm FWHM\,1,2}$	$\Sigma_{\rm SFR}$
	[$M_\odot$ yr^{-1}]		[Gyr]	[$M_\odot$ pc^{-2}]	[$M_\odot$ kpc^{-2}yr^{-1}]
HE 0433-1028	33	32	0.03 - 0.19	47 - 280	1.4
HE 1029-1831	31	25	0.03 - 0.18	92 - 553	3.1
HE 1108-2813	14	13	0.07 - 0.42	81 - 485	1.1

2.4 Star formation properties

The results from the previous sections, raise the suspicion that the Galactic luminosity-mass conversion factor strongly overestimates the gas masses. If a ULIRG conversion factor yields a better constraint, it implies a turbulent and heated medium as origin of the bulk of the gas emission. In the following I test if the galaxies display characterisitc of a starburst event.

The SFRs derived from $L_{\rm IR}$ (Table 2.8) using the calibration of 3.99×10^{-37} $M_\odot$ yr^{-1} W^{-1} from Panuzzo *et al.* (2003) are $\sim$ 30 $M_\odot$ yr^{-1} for the two more IR luminous galaxies and $SFR_{\rm IR}$ = 14 $M_\odot$ yr^{-1} for HE 1108-2813 (see Table 2.9). A FIR based SFR give reliable values only for starburst galaxies and dusty nuclear starbursts (Panuzzo *et al.* 2003). In this case, solely young stars heat the interstellar dust, which is optically thick.

But the dust in normal galaxies does not absorb all UV/visible emission from the young stars. Furthermore, a cooler, diffuse dust component emerges, the IR cirrus emission, which is due to more extended dust heated by the general stellar radiation field that comprises also visible radiation from older stellar populations (Kennicutt 1998a). An AGN emitting also in the FIR can be skew by AGN emission in the FIR.

As a second probe, I calculate the SFR based on the 1.4 GHz fluxes listed on the NASA/IPAC Extragalactic Database (NED) and a calibration of 6.35×10^{-22} $M_\odot$ yr^{-1} W^{-1} Hz from Murphy *et al.* (2011). Also here the AGN is likely contributing to the flux (Serjeant *et al.* 2002). I find the $SFR_{1.4\,\mathrm{GHz}}$ to be consistent with the SFR_{IR} up to within 1 $M_\odot$ yr^{-1} except for HE 1029-1831. The $SFR_{1.4\,\mathrm{GHz}}$ of the latter is 6 $M_\odot$ yr^{-1} less than the SFR_{IR}. For HE 1029-1831, Busch et al. (private communication) determined from the Brγ emission within a radius $r < 1''$ a SFR of $\sim$ 7 $M_\odot$yr^{-1}. While ionized hydrogen emission is thought to be dominated by stars younger than 10 Myr on average, the FIR emission traces age ranges up to 100 Myr (Kennicutt and Evans 2012). Regarding the different mean ages of the stellar populations contributing to the emission at a given wavelength range, the two corresponding SFR values seem compatible with each other.

The timescales (neglecting gas recycling) on which the reservoir of the given gas mass is consumed at the rate of $SFR_{1.4\,\mathrm{GHz}}$, is 30 - 420 Myr, depending on the conversion factor. The values in Table 2.8 are based on the observations presented here. IRAM 30m and BIMA gas masses (Bertram *et al.* 2007; Krips *et al.* 2007a) obtained with the here adopted cosmology and mass conversion factors, give a depletion timescale of τ_{SFR} $\sim$ 70 - 490 Myr for each of the three galaxies.

Another diagnostic property are surface densities. Since there is no information on the spatial extend of the FIR emission, I used for SFR surface density Σ_{SFR} the same parameters (size, gas mass fraction) of the Gaussian components fitted to the central bulk of ^{12}CO emission (Table 2.6). $3 \times d_{\mathrm{FWHM}\,1,2}$ gives conservative upper limit in CO and FIR emission. With this, the molecular gas mass surface density are $\sim$ 50 - 550 $M_\odot$ pc^{-2}, the SFR surface density are 1.1 - 3.1 $M_\odot$ kpc^{-2}yr^{-1}. For a minimum diameter of $d_{\mathrm{FWHM}\,1,2}$, the values rise by a factor of 9. The above mentioned Brγ-SFR for HE 1029-1831 translates into a $\Sigma_{\mathrm{SFR}} \gtrsim$ of 3.6 $M_\odot$ kpc^{-2}yr^{-1} matching my result. According the overview given in Kennicutt (1998a), the central regions of With the values, the three galaxies a confirmed to harbour a circumnuclear starburst with SFR time scales $\tau_{\mathrm{SFR}} \lesssim 1$ Gyr, a gas surface density $\Sigma_{\mathrm{mol}} \gtrsim 100$ $M_\odot$ pc^{-2} and a SFR surface density $\Sigma_{\mathrm{SFR}} \gtrsim 1$ $M_\odot$ kpc^{-2}yr^{-1} (criteria by Kennicutt 1998a).

When applying a surface diameter of $2 \times d_{\mathrm{FWHM}\,1,2}$ and the conversion factors used in the comparison samples, I find the three galaxies located right within the starburst sample of Kennicutt (1998b) as it can be seen in Figure 2.12. Furthermore, this region seems to mark also the transition between the SFGs and SMGs by Genzel *et al.* (2010a) at z = 1 - 2.5 and z = 1 - 3.5, respectively.

Rescaling the depletion times in Table 2.9 to an $\alpha_{\mathrm{CO}} = 3.2$ $M_\odot$ (K km s^{-1} pc^2)$^{-1}$ yields $\log \tau_{\mathrm{SFR}}$ = 8.1 - 8.4. For a stellar mass $M_\star$ of about 90 % M_{dyn} for HE 1108-2813, and 90 % $M_{\mathrm{dyn\,(bulge)}}$ for the other two sources (see Table 2.7), the specific star formation rate

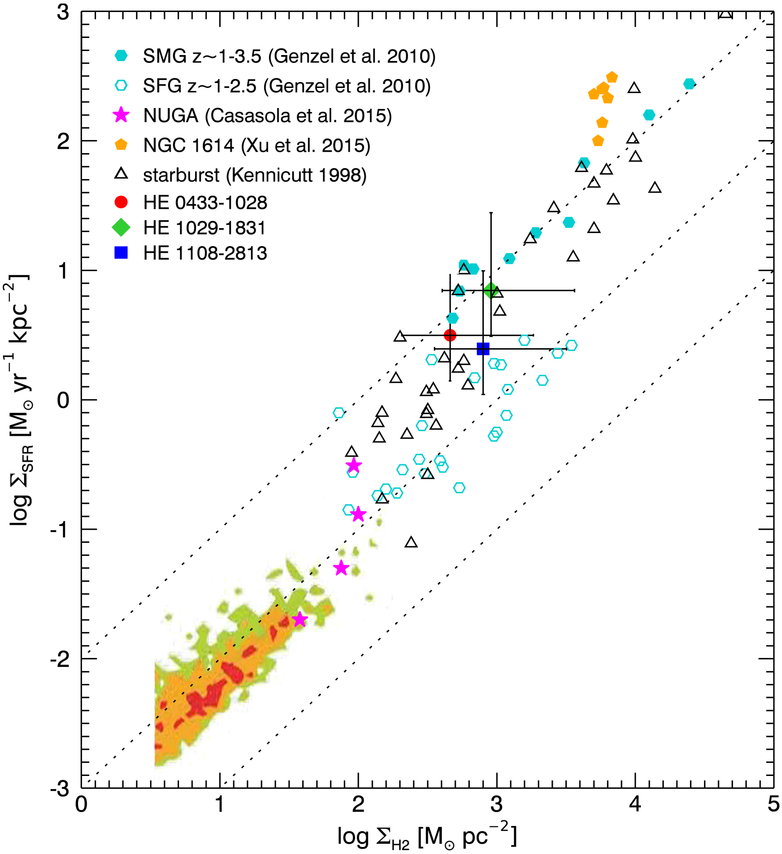

Figure 2.12: *Σ_{SFR} vs. Σ_{H_2} for the galaxies of my thesis compared to other analyses. I use a common α_{CO} = 3.5 $M_\odot$ (K km s^{-1} pc^2)$^{-1}$ for all data shown in this plot, i.e. a Galactic value with the exclusion of helium. The surface densities of the galaxies discussed in this thesis are rescaled to a surface with a 2 × $d_{FWHM\ 1,2}$ diameter and the error bar ends denote the lower and upper limit given by a surface diameter of 3 × $d_{FWHM\ 1,2}$ (and a ULIRG conversion factor in the case of Σ_{H_2} of $\alpha_{CO\ ULIRG}$ = 0.6 $M_\odot$ (K km s^{-1} pc^2)$^{-1}$ excluding helium) and of one $d_{FWHM\ 1,2}$, respectively. The green/orange/red colored patch shows the data of 7 nearby spiral galaxies from Bigiel* et al. *(2008,Fig. 9) sampled at a resolution of 750 pc. The yellow pentagons represent data from star-forming knots in the LIRG NGC 1614 from Xu* et al. *(2015) at a resolution of 100 pc. The open black triangles are disk-averaged measurements from nearby starburst galaxies from Kennicutt (1998b). The open and closed cyan circles show measurements from SFGs and SMGs from Genzel* et al. *(2010a) at z = 1 - 2.5 and z = 1 - 3.5, respectively. The magenta stars denote the average values for CO(2-1) based measuremnts at a 200 pc resolution for each of the 4 LLAGN in Casasola* et al. *(2015,Table 4). The diagonal dashed lines from top to bottom correspond to a depletion time τ_{SFR} of 0.1, 1 and 10 Gyr.*

($sSFR = SFR/M_\star$) is log($sSFR$) = - (8.8 - 8.1). With such timescales and rates, the three galaxies are located in the middle of the transition region from LIRGs to ULIRG, and SFGs (z > 1) to SMGs (z > 2) in Saintonge *et al.* (Figure 9 of 2011). Assuming ULIRG conditions ($\alpha_{\mathrm{CO\,ULIRG}} = 1\ M_\odot$ (K km s^{-1} pc^2)$^{-1}$ (Saintonge *et al.* 2011, Fig. 9)), they are relocated 0.5 dex downwards into the ULIRG and SMG regime.

However, for the extreme situation that the ratio of the gas mass and SFR surface diameter is 3 or 1/3, maximum variation of the depletion time is ~ 1 dex. Without further constraints on the size, one has to expect the galaxies to belong to the (U)LIRG/starburst group with $\tau_{\mathrm{SFR}} \lesssim 0.1$ Gyr as well as the local/distant normal star-forming galaxies group with $\tau_{\mathrm{SFR}} \gtrsim 1$ Gyr .

In general, the LLQSOs from our CO-tested subsample cover in a L_{FIR} vs. L'_{CO} plot a region between the Seyfert galaxies and LIRGs/QSOs regime and not the nearby galaxies regime which could be represented by the sample of Bigiel *et al.* (2008). The difference L_{FIR} between the active and quiescent galaxy regimes is about 1 dex, so that LLQSOs and nearby galaxies cannot follow the same linear relation.

2.5 Properties of the interstellar matter

The ^{12}CO(2–1)/(1–0) ratio is $r_{21} \sim 0.5$ in all three galaxies. Two galaxies show a ^{12}CO/^{13}CO(2–1) ratio of $R_{21} \gtrsim 20$ in the very center, the other one has a ^{12}CO(3–2)/(1–0) and ^{12}CO(3–2)/(2–1) ratio of $r_{31} \sim 1$ and $r_{32} \sim 2$, respectively. The upper limit for the ^{12}CO(3–2)/HCO$^+$(4–3) ratio in the same galaxy is 16.

2.5.1 ^{12}CO/^{13}CO(2–1) ratio

The Milky Way has a ^{12}CO/^{13}CO(1–0) ratio of $R_{10} \sim 5-8$ which indicates cool ($T_{\mathrm{k}} \leq 20$ K) GMCs as origin (Solomon *et al.* 1979; Polk *et al.* 1988; Oka *et al.* 1998,and ref. therein). With decreasing distance to the center the ratio increases to $R_{10}, R_{21} \sim 10$ in the centers of local spirals (Sawada *et al.* 2001; Meier *et al.* 2000; Mao *et al.* 2000; Sakamoto *et al.* 2006, 2007,and ref. therein), and nearby bright IR galaxies (Tan *et al.* 2011), $R_{10} \sim 10-15$ in the centers of starburst galaxies (Aalto 2007), and $R_{10} > 20$ in luminous mergers (Casoli *et al.* 1992; Aalto *et al.* 1991, 2010; Costagliola *et al.* 2011), with extreme outliers of $R_{10} \sim 40$ (e.g. Hüttemeister *et al.* 2000). That the ratio depends strongly on the star forming activity (Milky Way to mergers) indicates the significance of the impact of the feeding and feedback of star formation onto the ISM properties.

In local thermal equilibrium (LTE) the opacity of an emission line depends on the temperature T_{k}, the abundance ratio $[CO/H_2]$, the density $n_{\mathrm{H_2}}$ and the velocity gradient dv/dr, i.e.

$$\tau \propto \frac{1-e^{-E_{ul}/k_B T_{\mathrm{k}}}}{T_{\mathrm{k}}} \left[\frac{CO}{H_2}\right] \frac{n_{\mathrm{H_2}}}{(dv/dr)} \propto \frac{1-e^{-E_{ul}/k_B T_{\mathrm{k}}}}{T_{\mathrm{k}}} \frac{N_{\mathrm{CO}}}{dv}, \tag{2.9}$$

with N_{CO} the ^{12}CO column density and dv the line width.

The line ratio is high, when the ratio of the optical depths τ of the ^{12}CO and ^{13}CO line emission is high. This can be accomplished by a temperature gradient (Paglione *et al.* 2001; Bolatto *et al.* 2013). With increasing kinetic temperature T_k and sufficient density ($n_{H_2} \sim n_{crit^{12}CO(2-1)}$) the lower levels become depopulated which results in a decrease of the optical depth (Aalto *et al.* 1995; Paglione *et al.* 2001; Aalto 2007; Costagliola *et al.* 2011,and ref. therein). Since the intensity of the ^{13}CO line is a steeper function of the excitation temperature than the ^{12}CO intensity, $\tau_{^{12}CO}/\tau_{^{13}CO}$, and with it R_{21}, increase with temperature (radiative trapping; Wilson *et al.* 1999; Goto *et al.* 2003).

Furthermore, gas dynamics can change the opacity of the gas: Cloud collisions in the deep potential well and differential rotation (friction), tidal disruption, or stellar winds put a significant fraction of the molecular gas in a diffuse and gravitationally unbound state (Hüttemeister *et al.* 2000; Costagliola *et al.* 2011). Such turbulences increase the ^{12}CO line width and with it the gas velocity gradient. When considering equation 2.9 it becomes clear that the optical depth decreases remarkably towards low densities ($n_{H_2} \leq 10^3$ cm^{-3}) and the diffuse gas is difficult to detect, especially in the rarer isotopologues like ^{13}CO (Hüttemeister *et al.* 2000; Sakamoto *et al.* 2007; Costagliola *et al.* 2011). In contrast to the ISM properties mentioned above, significant abundance changes due to e.g. stellar processing (Young and Sanders 1986) or isotope-selective photodissociation are, if at all, of minor importance (see e.g. Paglione *et al.* 2001; Davis 2014).

Another impact on the line ratios comes from the technical side which is beam filling. Assume a dense cloud of CO gas that is surrounded by an envelope of more diffuse gas. ^{12}CO will trace most of both components, but ^{13}CO will only be visible when its opacity is high enough, i.e. in the dense core. While the ^{12}CO is likely to fill the whole telescope beam, the ^{13}CO emission from a few cores, that are small compared to the beam size, will be averaged over the whole beam (Sakamoto *et al.* 2007).

In summary, high ^{12}CO/^{13}CO ratio in the two lowest line transitions (R_{10} and R_{21} behave similar depending on the excitation Papadopoulos *et al.* 2012a) are due to a mixture of emission from a warm, dense, and probalby compact and from a diffuse gas component (Aalto *et al.* 1995; Paglione *et al.* 2001; Aalto 2007; Bolatto *et al.* 2013). These are the conditions typically found in the centers of galaxies which are governed by warmer GMCs and turbulence (Hüttemeister *et al.* 2000; Paglione *et al.* 2001; Costagliola *et al.* 2011).

With this background information I interpret the ^{13}CO(2–1) observations of HE 0433-1028 and HE 1108-2813 the following: The ^{13}CO(2–1) emission peaks in both galaxies are detected off-center from the ^{12}CO(2–1) peak, rather to one side of center. Their positions correspond to the x_1 and x_2 orbit crowding region where the bar interacts with the circumnuclear ring: While moving inwards along the bar, the molecular gas is increasingly compressed by the shock fronts at the bar leading edges. The gas inflow stalls at the connection points between the bar spiral arms and the circumnuclear ring. The orientation of these two gas accumulations is perpendicular to the bar and can usually be observed in ^{12}CO emission (Kenney *et al.* 1992; Kohno *et al.* 1999), and higher density tracers (see cartoons in Meier and Turner 2005, 2012). They are also indicated in my data. Due to the increased amount of non-diffuse, denser gas, these x_1-x_2 intersection regions are also visible in ^{13}CO emission (for a suitable beam size and sensitivity). The fact that the gas accumulations are not equally bright in both sides of the center indicates that the conditions in these regions are not necessarily identical but might depend on e.g. variations of the gas flow from the bar spiral arms (see cartoons in Meier and Turner 2005).

In HE 0433-1028, the ^{13}CO peak has a ^{12}CO/^{13}CO(2–1) ratio of $R_{21} \sim 7$, marking a cool gas phase. On the side opposite of the center, it is $R_{21} \sim 12$, hinting at the presence of turbulences and heating, as also indicated in the velocity dispersion map in Fig. 2.2. In the very center, i.e. on the ^{12}CO peak, the ratio climbs to $R_{21} \sim 20$. This region must be strongly heated by the nuclear activity which depopulated the lower ^{13}CO transition levels. In contrast to this, the ^{12}CO/^{13}CO(2–1) ratio in HE 1108-2813 is generally high with $R_{21} \sim 20$ at the ^{13}CO peak, $R_{21} \sim 25$ at the center (^{12}CO peak), and $R_{21} \gtrsim 30$ opposite of it. From this I conclude that diffuse gas in combination with a rising temperature gradient towards the center stongly affects the ISM state in the center of this galaxy. The bar edgeds in both galaxies show quiescent Galactic values of $R_{21} \sim 5$.

For these regions one has to bear in mind that the ^{13}CO emission in both galaxies is close to the detection limit implying a high uncertainty.

2.5.2 ^{12}CO(3–2)/HCO$^+$(4–3)

There are only few observations of the ^{12}CO(3–2)/HCO$^+$(4-3) line ratio reported in the literature. Wilson *et al.* (2008) determine an average ratio 19 ± 9 for their (U)LIRG sample. I obtain a lower limit of ^{12}CO(3–2)/HCO$^+$(4–3) ratio > 16. Obviously, the sensitivity of the SMA observations was too low to detect HCO$^+$(4–3). The presence of a very dense gas ($n_{\mathrm{crit}} \sim 6.5 \times 10^6$ cm^{-3}) remains unproved.

2.5.3 ^{12}CO $J + 1 \leq 3$ ratios

Nearby galaxies show a ^{12}CO(3–2)/(1–0) ratio of $r_{31} \sim 0.6$ (Mauersberger *et al.* 1999; Israel 2005). Since the ^{12}CO(3–2) emission increases in the presence of star-forming regions, the ^{12}CO(3–2)/(1–0) ratio rises towards the center (Dumke *et al.* 2001), and display usually a ratio of $r_{31} \sim 1$ in the central kiloparsecs of galaxies with enhanced central star formation or starburst galaxies (Devereux *et al.* 1994; Dumke *et al.* 2001; Muraoka *et al.* 2007; Papadopoulos *et al.* 2008; Iono *et al.* 2009).

In a study of LIRGs with $z \leq 0.1$, Papadopoulos *et al.* (2012a) find the ^{12}CO spectral line energy distributions (SLEDs) of the low J-levels to span a wide range from low excitation phases with $r_{21}, r_{32} < 1$, to high excitation phases with $r_{21}, r_{32} \geq 1$. In addition, they find the higher J-levels in some low excitations phase galaxies to reverse the decreasing sequence of line ratios, i.e. $r_{43} \geq r_{32}$ and $r_{32} \leq r_{21} \leq 1$, implying the onset of an even higher excitation phase with a well-excited and optically thin global ^{12}CO SLED. According to them the onset can even be at the $J + 1 = 3$ level with $r_{32} \geq r_{21}$ and $r_{21} \leq 0.6 - 1$, which is exactly the case for HE 1029-1831 with ratios of $r_{32} \sim 2$ and $r_{21} \sim 0.5$.

The ^{12}CO(3–2) line thermalizes at densities $n_{\rm crit} \sim$ few 10^4 cm^{-3}. At these densities, the opacity (Eq. 2.9) can only stay low/thin for kinetic temperatures of $T_{\rm k} \geq 100$ K and high gas turbulence.

A line ratio of ^{12}CO(2–1)/(1–0) ratio $r_{21} < 0.6$ (and maybe $r_{32} < 0.3$) implies the presence of a subthermal low excitation phase. This applies to two cases: Either the gas is cold ($T_{\rm k} \leq 20$ K) and self-gravitating like quiescent Galactic GMCs, or the gas is warm ($T_{\rm k} \gtrsim 30$ K), non-virialized, and diffuse with $n_{\rm H_2} \lesssim 10^3$ cm^{-3} like in envelopes and intercloud gas in ULIRGs (Hüttemeister *et al.* 2000; Papadopoulos *et al.* 2012a,and ref. therein). As shown in the previous section (Sec. 2.5.1), the corresponding ^{13}CO transitions aid in differentiating between these two phases. A ratio of $R_{10}, R_{21} \gtrsim 15$ indicates starburst and/or merger conditions, i.e. a high amount of warm and diffuse gas.

These diagnostics round off the picture of the three galaxies I disuss here: First, their $r_{21} \lesssim 0.6$ points at a subthermal gas phase. Second, for two of them I find evidence of a large fraction of diffuse gas in the central kpc by the ^{12}CO/^{13}CO ratio. Third, in the other galaxy, a high excitation phase with $r_{32} \sim 2$ appears to be overtaking low excitation phase ($r_{21} \sim 0.5$). This goes well along with the potential starburst I find in all three galaxy centers (see Sec. 2.4) which is in the case of HE 1029-1831 confirmed by NIR data (Busch *et al.* 2015).

Based on the tight correlation of $L_{\rm FIR}$, which is very similar for all three galaxies, and $L_{\rm CO}$ ($L_{\rm CO(3–2)}$ in particular: tracing warmer denser, potentially star-forming gas; Iono *et al.* 2009; Wilson *et al.* 2012) and on the assumption of starburst to dominate the FIR emission, I expect the two galaxies probed in ^{13}CO to show a ^{12}CO(3–2)/(2–1) ratio of $r_{32} \gtrsim 1$ in the circumnuclear region similar to HE 1029-1831. In the opposite direction, I expect the ^{12}CO/^{13}CO (R_{21}) in HE 1029-1831 to indicate warm and diffuse gas like in (U)LIRGs.

To raise the temperature and density and to stir up the molecular gas on the spatial and excitational scales observed in (U)LIRGs, spatially confined star formation regions are not efficient enough and a large scale heating source is required. The best candidates so far are AGN, cosmic rays (CRs) and turbulence (Papadopoulos *et al.* 2012b,a). Already the Galactic center of the Milky Way - a normal galaxy - shows evidence that the molecular gas heating is controlled by the CRs and turbulence (e.g. Yusef-Zadeh *et al.* 2007; Goicoechea *et al.* 2013).

2.5.4 $\alpha_{\rm CO}$ - factor and diffuse gas

Because of the importance for my disucssion of the molecular content in the three observed AGN, I give a brief introduction on how to derive molecular gas masses in galaxies, and the difficulties therein. Usually, the mass of the molecular gas in a region is derived from ^{12}CO(1–0) molecular line emission, because it is detectable best due to a high abundance and a low excitation energy and critical density. The idea of the luminosity-to-mass conversion factor $\alpha_{\rm CO}$ is to "count clouds" in the telescope beam:

When the GMCs are virialized, their luminosity is proportional to their mass and they do not overlap along the line of sight and in velocity (optically thin ensemble; Bolatto *et al.* 2013). In this case, the factor depends on the density $n_{\rm H_2}$ and temperature of the gas, i.e.

$\alpha_{\rm CO} \propto \frac{n_{\rm H_2}}{T_B} = \frac{n_{\rm H_2}}{f_b T_{ex}}$ with $T_{\rm B}$ the brightness temperature, $f_{\rm b}$ the beam filling factor and $T_{\rm ex}$ the excitation temperature. For high densities and opacities is $T_{\rm ex} \approx T_{\rm kin}$. Assuming that denser clouds potentially form stars, which then results in an increase of the temperature, the Galactic value for $\alpha_{\rm CO}$ of 4.3 - 4.8 $M_\odot$ (K km s^{-1} pc^2)$^{-1}$ (Bolatto *et al.* 2013; Solomon and Barrett 1991,respectively) is comparably robust.

However, there are conditions under which the conversion factor is not constant. In low metallicity environments, it rises due to the low abundance of ^{12}CO and therefore reduced self-shielding against photodissociating radiation (Casey *et al.* 2014,ref therein.). Even more striking is the variation of $\alpha_{\rm CO}$ with galactic radius. In the centers of local galaxies $\alpha_{\rm CO}$ is on average lower by a factor of 2 than in the disk and the central $\alpha_{\rm CO}$ of some of these galaxies 5-10 times lower than in the center of the Milky Way (Sandstrom *et al.* 2013). The conversion factor appears to be interrelated with the molecular gas density and the SFR surface density (Casey *et al.* 2014).

In addition, ^{12}CO/^{13}CO and ^{12}CO/C^{18}O correlate with these two quantities, but ^{13}CO/C^{18}O not. This suggests a dependency from the properties of the ISM traced by the ^{12}CO emission such as temperature and turbulence level (Davis 2014). Indeed, the $\alpha_{\rm CO}$ anticorrelates with the ^{12}CO/^{13}CO ratios which rise towards the centers of galaxies (Paglione *et al.* 2001). Consequently, a low $\alpha_{\rm CO}$ value seems to share the same mechanism, i.e. diffuse gas, as high ^{12}CO/^{13}CO ratios (see Sect. 2.5.1. How does the diffuse gas fraction influence the mass estimate? Evidence is found that e.g. within M33, the Milky Way and M51 roughly $\sim$ 50 % of the ^{12}CO luminosity can emerge from diffuse gas, or at least gas with densities $\lesssim 10^4$ cm^{-3} (Solomon and Rivolo 1989; Rosolowsky *et al.* 2007; Hughes *et al.* 2013; Schinnerer *et al.* 2013; Pety *et al.* 2013). Wilson and Walker (1994) determined a lower limit for the contribution of diffuse gas in M33 of $\gtrsim$ 30%.

Obviously the diffuse molecular gas is also widespread in terms of the scale height of galaxies and the linewith of ^{12}CO and the H I (tracing atomic gas) are similar, indicating a diffuse thick molecular disk similar in extend as the H I disk, making up a single dynamical component (Dame and Thaddeus 1994; Caldú-Primo *et al.* 2013).

Consequently, a standard conversion factor is not applicable for regions with high SFR surface density, because the basic assumption of self-gravitating gas is violated: A standard $\alpha_{\rm CO}$ of 4.3 - 4.8 $M_\odot$ (K km s^{-1} pc^2)$^{-1}$ (Bolatto *et al.* 2013; Solomon and Barrett 1991,respectively) overestimates the gas mass for the churned up ISM in (U)LIRGs by a factor of $\sim$ 6 (Downes and Solomon 1998; Papadopoulos *et al.* 2012b).

However, Papadopoulos *et al.* (2012b) obtained Galactic-like values for the conversion factor in ULIRGs based on HCN and high-J ^{12}CO lines tracing far higher densities the the low-J ^{12}CO transitions. This supports the suggestion deduced from past observations that, due to the high turbulence, about half of the gas mass in ULIRGs resides at higher densities, i.e. $n_{H_2} \geq 10^4$ cm^{-3} (Solomon *et al.* 1992; Gao and Solomon 2004a). As well as the subthermal line ratios r_{21} and r_{32}, this can be explained by a two-excitation-phase model: A diffuse, unbound gas component significantly contributes to the low-J ^{12}CO emission and results in a low $\alpha_{\rm CO}$. The actual molecular mass is potentially dominated by a dense, bound gas component detectable in high-J ^{12}CO or heavy rotor molecules (HCN, CS, HCO^+), so that the gas content is represented by a high α_{CO}.

Therefore, high density tracers are mandatory, not only to constrain the ISM excitation state but also to improve the molecular gas mass estimate. Possible degeneracies of the gas state from radiative transfer modeling can be overcome by rare isotopologues (e.g. ^{13}C) of the mentioned high density tracers.

In addition, LIRGs and less perturbed galaxies tend to have a large reservoir of cold, star formation quiescent gas in their gas-rich disk extending beyond (up to ~ 3 kpc) their central starburst region (~ 1-2 kpc). Papadopoulos *et al.* (2012b) find that in this case the global ^{12}CO SLED is dominated by the central starburst, due to the low ^{12}CO(1–0) brightness of the extended cold gas component, which yields a lower molecular gas mass.

In this section I discussed the complications for constraining the mass conversion factor and other gas properties due to the different density phases that can be present within in the same source.

In general, observations of low-J ^{12}CO and ^{13}CO lines and dust continuum emission at sufficiently high spatial resolution assist in tracing the ISM properties and with it the α_{CO} gradient. In this way, the cold gas content can be discriminated from the central star-forming gas component.

For HE 0433-1028 and HE 1108-2813, ^{12}CO/^{13}CO line ratio distribution vaguely traces the starburst region and the cold disk. Based on this, I conclude that the center is characterized by a rather low, starburst/ULIRG-like α_{CO}, whereas the material in the primary bar is represented by a higher, Milky Way (MW) like α_{CO}. Adopting 20% of the ^{12}CO luminosity to come from the primary bar with an $\alpha_{CO\,MW} = 4.8\ M_\odot$ (K km s^{-1} pc^2)$^{-1}$ and 80% from the central region (Gaussian component fit for HE 1108-2813, Table 2.6) with an $\alpha_{CO\,ULIRG}$ = 0.8 $M_\odot$ (K km s^{-1} pc^2)$^{-1}$, I determine a global value of $\alpha_{CO} = 2\ \alpha_{CO\,ULIRG} = 1.6\ M_\odot$ (K km s^{-1} pc^2)$^{-1}$ for the conversion factor in these three galaxies.

The diffuse gas in the observed galaxies does not only affect the ^{12}CO/^{13}CO ratio but also the FWZI: The zero intensity line width measured in this observation is lower than for the single dish obseravations. Such discrepancies have also been found by Caldú-Primo *et al.* (2015), where the interferometric line widths are 20 - 40 % less than the single dish widths.

2.6 Summary and Conclusions

Three Seyfert galaxies from the LLQSO sample have been observed with the SMA in Hawaii at a resolution of 1.5″ - 4.5″. HE 0433-1028 and HE 1108-2813 were observed in the ^{12}CO(2–1) and ^{13}CO(2–1) transition, and HE 1029-1831 in ^{12}CO(3–2) and HCO^+(4–3) transition. In the following I summarize my results and conclusions:

Morphology: Most of the detected molecular gas, i.e. > 80% is restricted to a region with a diameter < 1.8 kpc in (i.e. the FWHM of the 2D-Gauss-fit to the central emission component). The gas distribution reaches slightly along the primary bar, but not beyond its edges - at the sensitivity given by the observations. For HE 1108-2813, the ^{12}CO(2–1) emission covers the whole bar and outlines even the spiral arms within it. All three galaxies hold hints that the central emission component stretched towards the incoming dust lanes in the leading edges of the bar. In this way the gas extensions are likely to mark the x_1 and x_2 orbit intersections, where the inflowing gas and dust pile-up. This is corroborated by the detection of ^{13}CO in these locations. No HCO$^+$(4–3) emission has been detected in HE 1029-1831.

Kinematics: Along the kinematical major axis, the velocities rise steeply. There are signs of an unresolved central component reaching velocities $\geq$ 100 km s^{-1} on both kinematical axes. Only for HE 1108-2813, the sensitivity is high enough to trace the rotation curve up to the bar tips. The prominent x-shape in the PV-cut along the velocity gradient is a strong cue for a kinematically decoupled component, e.g. a nuclear disk.

Masses: The dynamical masses are $M_{\rm dyn} = (1.5 - 6.7) \times 10^9 M_\odot$, while the molecular gas masses are $M_{\rm mol} = (0.7 - 6.2) \times 10^9 M_\odot$ and accord to $10 - 50$ % $M_{\rm dyn}$ and $80 - 300$ % $M_{\rm dyn}$ for ULIRG and for Milky Way mass conversion, respectively. However, the uncertainy in $M_{\rm dyn}$ is high due to a low S/N along the primary bar and a low accuracy of the inclination. Only for HE 1108-2813, a reasonable dynamical mass with $M_{\rm dyn} > M_{\rm mol}$ was measured. For the dust masses I derived an upper limit of $M_{\rm dust}$ = (1.6 - 4.4) $\times$ 10^6 $M_\odot$. The resulting gas-to-dust ratios are $M_{\rm mol}/M_{\rm dust}$ = 180 - 350 (ULIRG conversion factor) and 1100 - 3400 (Milky Way conversion factor).

Star formation: I determined star formation rates of SFR = 14 - 33 $M_\odot$ yr^{-1} which translates into upper limit consumption time scales of $\tau_{\rm SFR}$ = 70 - 490 Myr. Combining this property with the found minimum gas mass surface densities of Σ_{mol} = 50 - 550 $M_\odot$ pc^{-2} and SFR surface densities of $\Sigma_{\rm SFR}$ = 1.1 - 3.1 $M_\odot$ kpc^{-2}yr^{-1}, I conclude that the three galaxies harbor a circumnuclear starburst.

Excitation: The ^{13}CO emission very likely marks the overdensities at the x_1 and x_2 intersection. Asymmetries in the brightness of the opposing emission regions attributed to excitation differences and/or beam filling. While the ^{12}CO/^{13}CO(2–1)-ratio in the ^{13}CO peak of HE 0433-1028 indicated quiescent gas with $R_{21} \sim 7$ it increases $R_{21} \sim 20$ at the nucleus most likely generated by higher temperatures and stronger turbulence as in a starbursts. HE 1108-2813 shows the same behavior, but with a higher offset resulting in $R_{21} \sim 20$ at the ^{13}CO peak and $R_{21} \sim 25$ in the nucleus. The gas appears even more diffuse/hot elsewhere ($R_{21} \gtrsim 30$). At the edges of the bar the ratio takes Galactic values. Also the ^{12}CO(3–2)/(1–0)-ratio in HE 1029-1831 of $r_{31} \sim 1$ suggests a high star formation activity as in the inner kiloparsecs of galaxies and for starburst galaxies. Remarkably, the galaxy also displays ratios of $r_{32} \sim 2$ and $r_{21} \sim 0.5$ signifying the ^{12}CO(3–2) transition to be thermalized whereas the ^{12}CO(2–1) transition is only subthermally excited. Obviously, there are two ISM phases coexisting (higher excited vs. cold or diffuse).

Recapitulating the information from all three galaxies lead to the following conclusion: The $r_{21} \lesssim 0.65$ ratio is low in all three galaxies which could be either ascribed to cold virialized or diffuse non-virialized gas. Two galaxies show hints for a diffuse gas phase interpretation. Due to the similar FIR luminosities and the strong central star forming activity, I can expect their $L_{CO(3-2)}$ to be similar ($L_{FIR} - L_{CO(3-2)}$ - correlation) as well as their central r_{31} and r_{32} (due to similar $L_{CO(1-0)}$). Conversely, I suspect HE 1029-1831 to display large R_{21} and R_{10} and with this the presence of a diffuse gas state. The mass-to-luminosity ratio α_{CO} is highly unconstrained, since there no more detailed information on the gas excitation. However, I can make out tendencies for a given region based on my maps, because the conversion factor anticorrelates with the ^{12}CO/^{13}CO(2–1)-ratio. A large fraction of the gas is confined to region with high R_{21} suggestive of a low ULIRG-typical α_{CO} therefore the average α_{CO} for the galaxies might be in the middle between ULIRG- and Milky Way-like values. The dynamical and dust masses I derived seem to support a low conversion factor, but are relatively uncertain (SNR).

Outlook: The SMA data can give us a first ideas of the distribution, the kinematics, and the excitation state of the molecular gas in these three galaxies. My study shows very well, what plethora of data on nearby (z ~ 0.01 - 0.06) galaxies can already be gathered at 0.5 - 1 kpc-scales. Such observations provide information on basic parameters in the scope of evolution studies and, hence, need to be tracked - additional to single dish data. In order to constrain the ISM phases better, higher CO transitions and high density tracers (HCN, HCO$^+$, etc.) at several transitions are crucial. In addition, higher resolution observation are mandatory to follow the matter transport to the nucleus and the distribution of the ISM states. ALMA can resolve spatial scales around 100 pc and less (e.g. $0.1'' \lesssim 80$ pc for the three galaxies) so that we can directly compare our results to local samples such as the NUGA sample observed both with the IRAM PdBI (García-Burillo *et al.* 2003; Combes *et al.* 2004; Hunt *et al.* 2008; Casasola *et al.* 2008; Haan *et al.* 2009; Casasola *et al.* 2010, 2011a; García-Burillo and Combes 2012) and with ALMA (e.g. Combes *et al.* 2013, 2014; García-Burillo *et al.* 2014). In addition, with information on the ionized gas, the hot molecular gas, the stellar component and the supermassive black hole (e.g. Smajić *et al.* 2014; Busch *et al.* 2015; Smajić *et al.* 2015), observations at comparable scales in the NIR complete the analysis. Most important, we need to conduct these studies for a larger fraction of our sample in order to yield representative results.

CHAPTER 3

GAS AND DUST IN THE VICINITY OF SGR A*

The central few parsec (~3 light years) is a region of extreme conditions not only in terms of intense IR to ultraviolet (UV) radiation from the NSC and X-ray emission from a population of stellar remnants and the SMBH, Sgr A*, but especially in terms of turbulence and shocks due to stellar winds and tidal shear. Furthermore it comprises several overlapping molecular and ionized structures that can be studied in term of feeding inflow and star formation potential. Its proximity makes the GC a unique laboratory for our understanding of galactic nuclei and galaxy evolution on the smallest accessible scales.

In this chapter, I present serendipitous detections of line emission towards Sgr A* and its environment with the Atacama Large Millimeter/submillimeter Array (ALMA) in band 3, 6, and 7. This up to now highest resolution (<0.75″) view of the GC in the sub-mm domain shows molecular gas at projected distances $\lesssim 1''$ from the SMBH. Among the highlights are: the very first 340 GHz map of the minispiral, the very first and highly resolved detection of sub-mm molecular emission in the immediate vicinity of the SMBH, and the highly resolved structures of CND features, especially of a region comprising a methanol class I maser closest to the SMBH.

The emission in H39α and of the 100 GHz continuum imply a uniform electron temperature around $T_e \sim 6000$ K for the minispiral. Sgr A* has a spectral index ($S \propto \nu^{\alpha}$) of $\alpha \sim 0.5$ at 100 - 250 GHz and $\alpha \sim 0.0$ at 230 - 340 GHz. The spectral indices of the luminous objects in the inner minispiral tend to -0.1 indication Bremsstrahlung emission, while the minispiral exterior shows the growing importance of the dust component with increasing frequency.

From the detected species, the clumpy molecular gas distribution is represented best by the CS emission. Further species detected are $H^{13}CO^+$, HC_3N, SiO, SO, C_2H, CH_3OH, ^{13}CS and N_2H^+. Most of the emission can be found at positive velocities and in a region limited by the sources IRS 3 and 7, the minispiral Bar, and the minispiral Northern Arm that I termed central association of clouds (CA). For some few regions in the field, the molecular emission appears at velocities of up to 200 km s^{-1}.

At certain negative velocities ranges, the radio recombination line (RRL) emission partly overlaps with the molecular line emission regions, but a clear relation to the minispiral is not obvious. Probably, the CA is an infalling group of clouds composed of denser cloud cores and diffuse gas. I calculated three times higher CS/X (X: any other observed molecule) ratios for the CA than for the CND which hints at a combination of higher excitation - by a temperature gradient and/or IR-pumping - and abundance enhancement due to UV- and/or X-ray emission. Assuming the nuclear stellar cluster as the cause, CA must be closer to the center than the CND is to the center.

Within the CND itself, I discerned two interesting regions: The first region emits in lines of all molecular species and higher energy levels observed in this and earlier studies. Furthermore, it harbours a methanol class I maser. The second region shows line ratios similar to the CA. Beyond the CND, I discover that the largest accumulations of traditionally quiescent gas tracer N_2H^+ match the largest IR dark clouds in the field. The previously detected methanol class I masers in these IRDCs coincide with the methanol emission observed by ALMA. I conclude, that all of these special regions should be investigated in more detail in the context of hot/cold core and extreme PDR/XDR chemistry and consequent star formation in the central few parsecs.

The results of my work that I present in this chapter have been accepted for publication in A&A as Moser *et al.* (2016b).

3.1 Introduction

The center of our Milky Way is a very intriguing and complex region of extreme conditions. Its proximity makes the GC a unique laboratory for studying the interplay of a SMBH with its environment on the smallest accessible scales. Sgr A* is embedded into nuclear stellar cluster NSC consisting mostly of massive stars (e.g., Serabyn and Lacy 1985; Krabbe *et al.* 1991). The SMBH's location is also the focal point of three infalling streamers of ionized gas that build up the so called minispiral or Sgr A West (e.g., Lo and Claussen 1983; Roberts and Goss 1993; Zhao *et al.* 2009). In addition to thermal emission of ionized gas, the minispiral is radiating emission of hot dust ($T \sim 200$ K, Gezari *et al.* 1985; Cotera *et al.* 1999; Viehmann *et al.* 2006; Lau *et al.* 2013). The streamers are crossed by several NSC stars so that they produce bowshocks and some stars even appear to be embedded into the streamers. Many of the NSC stars are remarkably young ($\sim 10^6$ yr) which points at in situ formation and cannot be explained by the current understanding of star formation in such environments (e.g., Nayakshin *et al.* 2007). The minispiral structure is surrounded by the CND of molecular gas and dust with an extent from 1.5 pc to about 2.5 pc (e.g., Guesten *et al.* 1987; Jackson *et al.* 1993; Marr *et al.* 1993; Yusef-Zadeh *et al.* 2001; Wright *et al.* 2001; Christopher *et al.* 2005). Two of the minispiral arms coincide in velocity and space with a large fraction of the

CND and thus seem to represent the inner ionized edge of it. The CND seems to be fed by molecular gas streamers, especially in the south and the west, from larger cloud associations that are part of the GMCs - M-0.02-0.07 (50 km s^{-1}-cloud) and M-0.13-0.08 (20 km s^{-1}-cloud), in the east and south of the CND (Coil and Ho 1999, 2000; Liu *et al.* 2012).

Previous observations of gas in the GC at larger scales (e.g., Guesten *et al.* 1987; Jackson *et al.* 1993; Marr *et al.* 1993; Yusef-Zadeh *et al.* 2001; Wright *et al.* 2001; Christopher *et al.* 2005) showed no molecular gas in the central cavity inside the CND, but only neutral and ionized gas. In contrast to this, CO, H_2CO, H_3^+ and OH absorption studies (Geballe *et al.* 1989; Goto *et al.* 2014; Karlsson *et al.* 2003, 2015) as well as high resolution maps of CN and high energy transitions of HCN and CS, and near-infrared (NIR) transitions of H_2 (Montero-Castaño *et al.* 2009; Martín *et al.* 2012; Ciurlo *et al.* 2016) hint at the presence of a diffuse or clumpy gas phase towards the cavity. Furthermore, a widespread distribution of water and CO ice has been detected within the minispiral (Moultaka *et al.* 2004a, 2005, 2015a,b).

The new and revolutionary telescope ALMA provides the spatial resolution and sensitivity needed for the investigation of the gas and dust content in the GC. In its very first observation of the GC, i.e., in Cycle 0, I found serendipitous detection of line emission in the central parsec up to within 1″ (∼ 0.04 pc) around Sgr A* in projection. These archive data provide angular resolutions down to ≲0.5″, but mostly ∼0.75″, which corresponds to about 28 mpc or 5775 AU at a distance to the Galactic Center of 8±0.3kpc (Schödel *et al.* 2002b; Eisenhauer *et al.* 2003; Horrobin *et al.* 2004; Ghez *et al.* 2008; Gillessen *et al.* 2009c,b). This so far highest angular resolution view on the GC in the sub-mm domain comprises the very first 340 GHz map of the minispiral, the very first and highly resolved detection of cool molecular gas emission very close to Sgr A*, and the highly resolved structures of CND features, especially of a region containing a methanol class I maser that is the closest one to Sgr A*.

This chapter has the following structure: Section 3.2 describes the observations, the calibration and the imaging of the line and continuum emission data. Section 3.3 deals with the results and data analysis: Sections 3.3.1 and 3.3.2 cover the results and analysis of radio continuum and radio recombination lines, respectively, Sections 3.3.3 and 3.3.4 of the molecular gas emission in the outerÂ and inner region (i.e. beyond and within the central 40″ of the GC), respectively, and Section 3.3.5 of the molecular gas kinematics. Within Section 3.4 I discuss the continuum spectral index and electron temperature distribution in Section 3.4.1 and 3.4.2, respectively. Furthermore, the discussion of the emission towards some of the most prominent stellar sources in the NSC and the molecular line ratios in the central few parsecs including molecular excitation and abundances are covered in Section 3.4.3 and 3.4.4, respectively. Section 3.5 deals with the general nature of the molecular gas in the GC and focuses on the IRDCs and methanol masers in Section 3.5.1, the high velocity clouds in Section 3.5.2, and the origin of the molecular gas in cavity in Section 3.5.3. I summarize my findings in Section 3.6. Additional images and tables are given in the appendices A.1 - A.5.

Table 3.1: *Observational parameters (Credit: Moser et al. (2016b), reproduced with permission ©ESO.)*

band	ν_c [GHz]	t_{total} [min]	FOV [″]	$FOV10$ [″]	$\theta_{beam\text{-}c}$ [″×″]	v_{ch} [km s^{-1}]	$peak_c$ [mJy beam^{-1}]	rms_c	rms_{ch}
3	100	18	59.2	98.4	1.83×1.51	46.88	2.42	0.50	0.53
6	250	18	22.8	37.9	0.72×0.57	18.75	4.13	0.21	1.00
7	340	27	16.7	27.9	0.49×0.41	13.79	4.26	0.27	1.60

Notes. ν_c is the central frequency, t_{total} the target integration time, FOV the average field of view, $FOV10$ the average field of view at the 10% primary beam power level ($\Delta FOV = \Delta FOV10 = 10\%$), $\theta_{beam\text{-}c}$ the continuum beam size, v_{ch} the average channel resolution, $peak_c$ the peak (Sgr A*) flux density of the continuum, rms_c the noise σ of the continuum, and rms_{ch} the average noise σ of the channel.

3.2 ALMA observations and data reduction

Being one of the most complex regions in the Milky Way, a detailed study of the GC necessitates high sensitivity and angular resolution which now are accessible thanks to ALMA. The data that I analyse in this chapter were taken on 18 May 2012 with ALMA under the project 2011.0.00887.S (PI: Heino Falcke) in a quasi-simultaneous monitoring campaign in Band 3, 6, and 7 alternatingly. Table 3.1 summarizes the the observational properties per band.

3.2.1 Observation

The Band 3, 6, and 7 receivers were tuned to central frequencies around 100, 250, and 340 GHz, respectively. The correlator was set to Time Division Mode comprising 128 channels of 15.625 MHz width yielding a total bandwidth of ~ 2 GHz per spectral window. This corresponds to a velocity resolution of ~ 50, 20, and 15 km s^{-1}, respectively. Each band has four spectral windows so that te total effective bandwidth is ~ 8 GHz. The observations were conducted for a single pointing on Sgr A* ($17^h45^m40\overset{s}{.}040$, $-29\overset{\circ}{.}00\overset{\prime}{.}28\overset{\prime\prime}{.}118$, J2000), giving a field of view (FOV) of ~ 60, 23, and 17″, respectively, and in the most extended array configuration (in Cycle 0) with baselines ranging from 36 to 400 m. This translates into angular resolutions of about 1.5″, 0.7″, and 0.5″, respectively, and maximum recoverable scales of < 10″, < 4″ and < 3″, respectively. The overall execution time is 7.5 h and the total integration time on target and per band is ~ 20 min. With 19 antennas and a large range of hour angles covered, the uv-plane is marvellously sampled.

3.2.2 Data calibration

For my study I used calibrated data which is available at the ALMA archive together with the reduction scripts for the Common Astronomy Software Application (CASAv3.4; McMullin *et al.* 2007) that have been used to produce them. The inaccuracy in the flux calibration in band 3, 6, and 7 is less than 17%, 9%, and 10%, respectively. I found the data to require

Table 3.2: *Overview of the properties of the lines detected with ALMA (Credit: Moser et al. (2016b), reproduced with permission ©ESO.)*

molecule	transition	physical			technical			
		ν [GHz]	E_u [K]	$n_{crit}(100\ K)$ [cm^{-3}]	θ_{beam} [$'' \times ''$]	$\sigma_{ch\text{-}rms}$ [mJy beam^{-1}]	n_{clip}	v_{int} [km s^{-1}]
^{13}CS	2–1	92.494	6.66	3.3×10^5	1.93×1.57	0.52	3	-130 - 130
N_2H^+	1–0	93.174	4.47	2.0×10^5	1.93×1.57	0.53	4	-150 - 100
H51β		93.607			1.93×1.57	0.54	3	-370 - 340
CH_3OH-A	8_0–7_1	95.169	83.50	7.9×10^5	1.89×1.55	0.52	3	-120 - 130
H49β		105.302			1.72×1.44	0.54	3	-350 - 320
H39α		106.737			1.75×1.48	0.62	3	-440 - 400
CS	5–4	244.936	35.30	5.4×10^6	0.76×0.59	0.91	5	-150 - 200
HC_3N	27–26	245.606	165.03		0.76×0.59	0.87	3	-70 - 100
H36β		260.033			0.70×0.55	1.10	3	-330 - 340
$H^{13}CO^+$	3–2	260.255	24.98	3.3×10^6	0.70×0.55	1.10	3	-80 - 110
SiO	6–5	260.518	43.76	8.3×10^6	0.70×0.55	0.90	4	-150 - 210
SO $^3\Sigma$	6_7–5_6	261.844	47.60	3.7×10^6	0.70×0.56	1.00	4	-80 - 100
C_2H	$3_{3.5,4}$–$2_{2.5,3}$	262.004	25.15	6.3×10^6				
C_2H	$3_{3.5,3}$–$2_{2.5,2}$	262.006	25.15	6.5×10^6				
C_2H	$3_{2.5,3}$–$2_{1.5,2}$	262.065	25.16	6.7×10^6	0.70×0.56	1.00	4	-190 - 80
C_2H	$3_{2.5,2}$–$2_{1.5,1}$	262.067	25.16	6.9×10^6				
H33β		335.207			0.50×0.42	1.28	5	-390 - 100
CH_3OH-E	7_{-1}–6_{-1}	338.345	70.60	1.3×10^6	0.50×0.42	1.28	3	-80 - 100
CH_3OH-A	7_0–6_0	338.409	65.00	1.4×10^6				
SiO	8–7	347.331	75.02	2.0×10^7	0.48×0.41	1.90	4	-150 - 200

Notes. Listed are the frequencies ν; upper state energies E_u; critical densities n_{crit} in the two-level approximation for given kinetic temperature based on data from the Leiden Atomic and Molecular Database (LAMDA; Schöier *et al.* 2005,http://home.strw.leidenuniv.nl/~moldata/); beam sizes θ_{beam}, channel noise $\sigma_{ch\text{-}rms}$, and noise clipping level from $n_{clip}\sigma_{ch\text{-}rms}$ per line cube; velocity range v_{int} over which the integrated flux maps were obained.

further reduction and calibration step which I conducted in Common Astronomy Software Application (CASA)v.4.3 - as well as the imaging and analysis.

Apart from flagging residual noisy data, I applied an finely-stepped and careful self-calibration procedure on phase and on amplitude - despite the flux variability of Sgr A*. This flux variability generates bright sidelobes in the time-integrated image that outshine the fainter extended emission I am interested in. If I self-calibrate the data on the phase only, the dynamic range (DR) improves only by a factor of 1.7, 6.4, and 6.2 at 100, 250, and 340 GHz, respectively. With a subsequent self-calibration on amplitude and eventually on amplitude and phase together, the DR increases by a factor of 11.4, 31.9, and 57.7, respectively, compared to the non-self-calibrated data. With this procedure, I was able to enhance the DR drastically, i.e. to 4500, 7600, and 11200, respectively, resulting - aside from the loss in astrometric accuracy and time resolution information - in an overall data quality sufficient for my purpose.

I subtracted the continuum information from the uv-data to obtain the information from the comparably faint emission lines only. In the following section I describe the procedures for the extraction of the line and continuum images.

3.2.3 Line and continuum imaging

The continuum subtraction revealed that a large number of lines is detected above the 3 - 5 σ noise level in the different bands (see Table 3.2). In the following, I lead through the process of image creation and the general quality of the data. Furthermore, I point out the features and caveats for some frequency ranges such as line overlaps and artefacts, which influence the line and channel selection and need to be kept in mind for the interpretation of the images.

I produced the line and continuum for a natural uv-weighting with a pixel size of 0.15, 0.075, and 0.05 $''$, respectively, and an image size of 768×768 pixels which corresponds to twice the FOV. The continuum was created by using the line-free channels. For the setup of image cubes I used the natural channel size and frequency setup of the corresponding spectral window. The noise root mean square (rms) is 0.5, 0.2, and 0.3 mJy beam^{-1} for the continuum, and 0.5, 1.0, and 1.6 mJy beam^{-1} for a channel. To avoid the inclusion of dilution effects and noise, I clipped all line (cube channels) and continuum data at $\geq 3\sigma$ (see Table 3.2). From the clipped cubes I made 0th and 1st order moment maps, i.e. integrated flux and velocity field, by using the CASA task `immoments`. In the last step, I corrected the integrated flux and the continuum maps for the primary beam attenuation out to a primary beam level of 10%. Eventhough the sensitivity of the primary beam and with it the accuracy of the corrected fluxes decrease with increasing distance from the pointing center, several bright features are detected outside the traditional definition of the FOV. I therefore decided to extend the map to the field given by the 10% power full width of the primary beam (FOV10) (see Table 3.1).

As the most prominent ionized gas emission structure in the central parsecs, the minispiral is well detected in the 100, 250, and 340 GHz continuum (Fig. 3.2) and in the Hα and β RRL emission in band 3 (Fig. 3.3). The H49β line partly overlaps with faint H61δ line emission offset by about -300 km s^{-1} and the H49β line is slightly blended by faint H58γ line emission offset by about -500 km s^{-1}. The H36β line in band 6 is weaker and restricted to compact structures. Moreover, the $H^{13}CO^+$ line emission covers a similar frequency range so that its emission is visible in the integrated H36β map and vice versa. The weak H33β line in band 7 shows reliable detections only towards IRS 1, 2 and 13.

The RRL emission covers a velocity range from -400 to 400 km s^{-1}. The molecular emission lines in band 3 appears from -150 to 150 km s^{-1} corresponding to the entire CND velocity range. In band 6 and 7, the velocity range for the molecular emission lines is narrower, i.e., from -80 (-100) km s^{-1} to 80 (100) km s^{-1}, because of the smaller FOV. CS and SiO are an exception and extends to velocities up to 200 km s^{-1}. SiO is already visible at -160 km s^{-1}.

The integrated emission images of the lines are shown in Figures 3.4 and 3.5. In the case of N_2H^+ and C_2H a few channels around the line peaks in the image cubes are affected by strong ring shaped sidelobe artefacts around the position of Sgr A*. Consequently, the ring shaped structures in the inner 12$''$ of the N_2H^+ emission is doubtful and the emission of C_2H that is blending with the sidelobes should to be treated with caution. In band 6 and 7, several lines presumably show artefacts of an imperfect/insufficient continuum subtraction at the position of Sgr A*.

3.2.4 Obtaining spectral and spatial properties of the sources

I setup catalogues for all clumps with significant molecular gas emission and listed therein the positions, source sizes, fluxes, and spectral features for all the molecular emission lines they are appearing in (see Tables A.2 and A.3 - A.5). Furthermore, I compared the continuum images to images in the IR (Mužić *et al.* 2007; Viehmann *et al.* 2006,finding charts therein) and cm-regime (Zhao *et al.* 2009,finding charts therein) and searched for counterpart sources to obtain their positions, source sizes, and fluxes (see Table A.1) from my data. I determined the spectral properties for a subset of IR sources in the central 10$''$ (see Fig. A.6). For obtaining positions, sizes and contained fluxes I used the CASAv4.3 task `imfit` to fit a 2D-Gaussian to the untapered, naturally weighted (and integrated) image. To obtain the spectra I centered a beamsized aperture as given in Table 3.2 on the mean position of each clump averaged on all emission lines. I fitted the spectra with the MPFIT module in Python[1]. The emission lines often extend over 2 - 3 channels only so that the spectral line fit is of limited precision or can even fails despite a 3σ detection of a line. For such cases, I give an estimate of the uncertainties and/or the parameters.

I derived the continuum spectral index maps, integrated line flux to continuum ratio maps and line luminosity ratios of certain molecules on channel basis (Table A.7) which I discuss in section 3.4. Basically, the ratios between different ALMA bands need to be computed for the same uv-coverage. Unfortunately, clipping the uv-planes to the same ranges leads to distortions and flux losses of up to 50 % even when dropping large baselines only. Therefore, the images are uv-tapered only and cleaned with the same beam size per ratio. Because of

[1] https://code.google.com/archive/p/astrolibpy/downloads

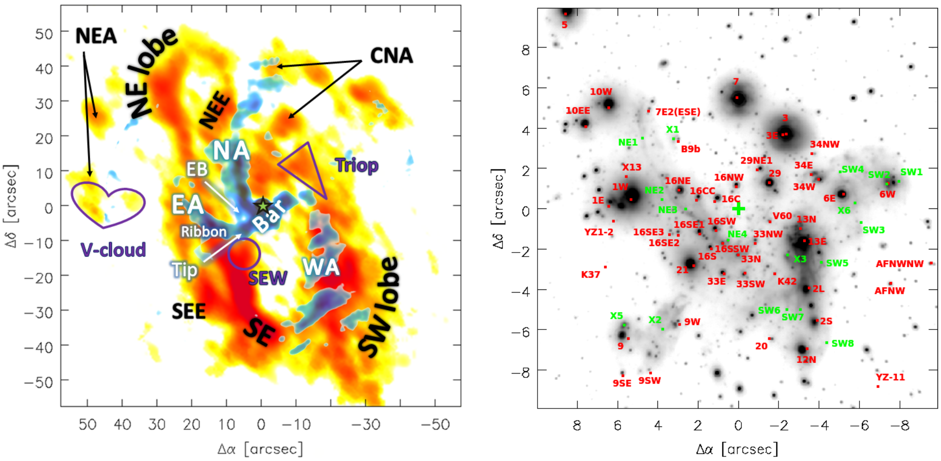

Figure 3.1: *Left: Overview of the structures in the inner 4.8 pc of the GC. Shown in orange: CND (CN(2–1),* Martín et al. 2012*); blue: minispiral (100 GHz continuum, this work); and green star: Sgr A*. The abbreviations are as follows: NE lobe for northeastern lobe, SW lobe for southwestern lobe, SE for southern extension, NEE for northeastern extension, CNA for CND-northern Arm, NEA for northeastern arm, NA for northern arm, WA for western arc, EA for eastern arm, and EB for eastern bridge. The new defined regions are southern extension west, (SEW) southern extension east (SEE), Triop, and V-cloud. Right: Overview of the stars and filaments* Paumard et al. *(2006);* Viehmann et al. *(2006);* Mužić et al. *(2007) mentioned in this work, demonstrated for the inner 20″ (0.8 pc) on a Very Large Telescope (VLT/NACO) NIR L' (3.8 μm) emission map (Sabha, private communication, here: arbitrary units). (Credit:* Moser et al. *(2016b), reproduced with permission ©ESO.)*

the missing flux which it resolved out in the higher band data, ratios between a higher and a lower band only give lower limit, whereas ratios within the same band will be very accurate due to a similar uv-plane coverage and the same flux calibration. Within the same band, the ratios are only affected by the cleaning procedure and by the binning of the channels to the same grid because of an unreliable interpolation in uv-plane regions with a low S/N and/or sparse sampling. For purpose of discovering trends in the molecular line ratios from region to region it is sufficient to interpret the channel based molecular line ratios as rough values and drop the uncertainties because the channel S/N is less than for the total bandwidth.

3.3 Results and Analysis

This section deals with the main results of the ALMA continuum and line emission data. The complex GC region comprises several prominent features and objects. Therefore, Figure 3.1 is an essential finding chart for the names of the features that I use here. I refer to the CND-nomenclature of Christopher *et al.* (2005) and Martín *et al.* (2012). The brightest regions in the CND are the NE and SW lobe. The SE denotes the southeast side of the CND. The

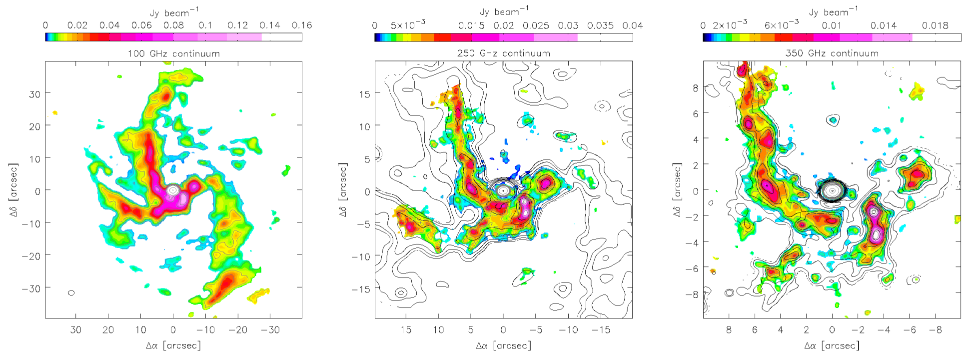

Figure 3.2: *Continuum emission images of the inner $\lesssim$ 3 pc. From left to right: central 80″ at 100 GHz, central 40″ at 250 GHz with 100 GHz contours of [6, 12, 24, 48, 96, 144, 192, 384, 1920, 4800] $\times\, \sigma$ (= 0.5 mJy beam^{-1}), and central 20″ at 340 GHz with 250 GHz contours of [6, 12, 24, 36, 48, 72, 96, 144, 192, 1920, 19200] $\times\, \sigma$ (= 0.21 mJy beam^{-1}). The beam sizes are 1.8″ × 1.5″, 0.7″ × 0.6″, and 0.5″ × 0.4″, respectively. (Credit: Moser* et al. *(2016b), reproduced with permission ©ESO.)*

NEE agrees with the eastern edge of the NA of the minispiral, whereas the CNA is located at the western side of the NA. The NEA lies east of the CND. In addition, I specify a few more regions that are subject of this chapter: The V-cloud resides south of the NEA with its eastern edge coinciding with the southern tip of the latter. East of the middle part of the SE is the large cloud Southern Extension East (SEE) and northwestern tip of the SE I named Southern Extension West (SEW). West of the central pc at southern end of the CNA, the *triop* is situated.

For the minispiral features, I follow the nomenclature of Paumard *et al.* (2004). The minispiral emission is dominated by the so-called Bar which stretches from the west to the south of the SMBH. The NA appears in the north aligned with the NEE, the WA is at the inner edge of the SW CND Lobe and the EA moves from the east towards the center. The latter consists of the Ribbon representing the largest part of the EA, the Tip, a bright region between the Bar and the Ribbon, and the EB, a vertical apparent connection between the Ribbon and the NA. The inner 10″ around Sgr A* can be best described and discussed by using the IRS sources as reference points (Fig. 3.1).

3.3.1 Continuum

The continuum emission of the minispiral at 100, 250, and 340 GHz is well detected at (see Fig. 3.2). At 100 GHz, the continuum emission outlines well the minispiral arms in terms of their total extent and brightest features within them. The spatial resolution is similar to the resolution of the data of e.g. Lo and Claussen (1983) at 6 cm (VLA). The most prominent emission feature besides Sgr A* is the IRS2L/13 complex and the ridge in the IRS 16/21/33 region which are both part of the Bar (see Fig.3.1 for orientation). Moreover, the sources IRS

1W , 5, 6, 7, 8, and 9 can be recognized.

However, I discovered some discrepancies between the 100 GHz and the 6 cm map: At 100 GHz, ALMA has detected a southeast extension at the eastern end of the EA to a faint cloud slightly to the south ($\Delta\alpha \sim 17''$, $\Delta\delta \sim -15''$) between a CND clump east of the eastern end of the EA and the northern tip of the CND SE. This cloud (peak flux ~ 10 mJy/beam) can barely be seen in the low frequency (≤ 20 GHz) observations, except from a putatively detected extension (e.g., Lo and Claussen 1983; Roberts and Goss 1993; Zhao *et al.* 2009). Instead, it can be found in the 1.3 mm map of Kunneriath *et al.* (2012a) and the extension towards it is prominent in the MIR - both facts that indicate a dusty nature of this cloud.

At 250 GHz, the extended gas in the minispiral is traced and the brightest minispiral structures begin to resolve, i.e. in the NA: the filaments X1, NE 1, 3, and 4; in the Bar: SW 6, 7, 8 (S of IRS 2L), 3 (W of IRS 13); and in the Tip: X2 (filament nomenclature: Mužić *et al.* 2007). At the edges of the radio continuum emission the dusty features X5 (Tip, north of IRS 9), SW 2, 4, and X6 (IRS 6 region) can be found. At this resolution (~0.75″), the IRS 13 cluster and IRS 2L appear as own sources each. A substructure in the ridge in the IRS 16/21/33 region hints at the filament NE4 and IRS 21. Further sources that become visible are IRS 5 in the NA (bowshock to the northeast), sources east (most eastern: IRS 17) of it (IRS 5S, 5SE1, 5SE2, 17), the sources IRS 10W, 16NE, 16C, VISIR 60/K 22 (Viehmann *et al.* 2006; Zhao *et al.* 2009) - the last two are close to Sgr A*-, and K 42 (Zhao *et al.* 2009) at the heart of the minicavity. Comparing IRS 7 in the 100 GHz map to the 250 GHz map, a positional shift of < 0.5″ to the S(W) is evident. Either the star or bowshock head overlaps with the tail at the lower resolution at 100 GHz or the excitation conditions in the head differ from the ones in the tail.

The 340 GHz data traces thanks to its high resolution of ~0.5″ the compact structures as known in the MIR and in the radio (compare Viehmann *et al.* 2006; Zhao *et al.* 2009) in detail. Further filaments that can be seen at 340 GHz are X3 and SW5, southeast and southwest of IRS 13, respectively. In addition, the IRS 13 cluster starts to resolve into the 13N and 13E clusters.

3.3.2 Radio recombination lines

In Figure 3.3 I present the emission of the strongest RRLs in the ALMA data, in Fig. A.1 the weaker RRLs. The bright H39α emission strongly resembles the distribution of the 100 GHz continuum, except from the low sensitivity edge of the FOV10. There, IRS 8 ($\Delta\alpha \sim 3''$, $\Delta\delta \sim 28''$) and the southern end of the WA are barely detected. The faint continuum clump at the southern end of the EA is not detected at this sensitivity level.

This following part of this section deals with the comparison of the overall brightness distributions in the RRL emission and in the radio continuum, and to the results of H92α, H30α and Ne II data of Zhao *et al.* (2009, 2010) and Irons *et al.* (2012), respectively. In contrast to my data the integrated H92α brightness (Zhao *et al.* 2009) in the region around IRS 21, 16SW, 33 becomes fainter towards Sgr A* and reaches its maximum south of IRS 33 (see Fig.3.1 for orientation). The EA becomes comparably fainter towards its middle and

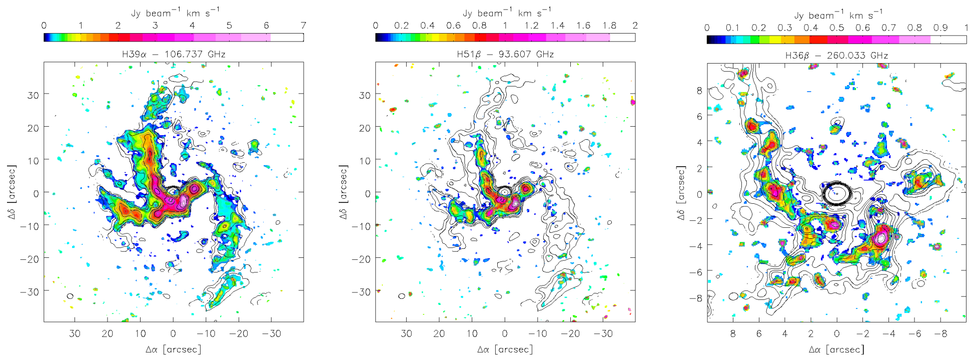

Figure 3.3: *Recombination line (RRL) emission images of the inner $\lesssim$ 3 pc. From left to right: H39α and H51β in the central 80″, both with the 100 GHz continuum contours as in Fig. 3.2, and H36β overlayed with the 250 GHz contours as in Fig. 3.2. H49β and H33β can be seen in Fig. A.1. The beam sizes are 1.9″ × 1.6″, 1.8″ × 1.4″, and 0.7″ × 0.6″, respectively. (Credit: Moser* et al. *(2016b), reproduced with permission ©ESO.)*

its eastern end is brighter than the Tip. The Ne II brightness (Irons *et al.* 2012) in the region enclosed by IRS 13, 21, and 33 is lower than at IRS 1W and 2L. This can be explained by a different excitation behaviour of the Ne ion, but the H30α brightness in Zhao *et al.* (2010) behaves similar.

On the one hand, the ALMA RRL cubes could be affected by their low spectral resolution of ~ 50 km s^{-1} as indicated by the minor differences between the H49β and H51β maps. Opacity changes - if significant at all at 100 GHz - or deviations from LTE within these two very close transitions can be ruled out and an instrumental bias might be at play. While the spatial resolution of the Zhao *et al.* (2009, 2010) and Irons *et al.* (2012) data is comparable to my data, the higher spectral resolution is with ~ 15 km s^{-1} and ~ 4 km s^{-1}, respectively, much higher so that the minispiral clumps can be expected to be traced better. On the other hand, in all of the three RRLs around 100 GHz, the region to the south(west) of Sgr A* is the second brightest. It is possible that the RRL emission brightness distributions is caused by the different velocity ranges used for integration: I use a range for the H39α emission of -400 to 400 km s^{-1}, Irons *et al.* (2012) integrate from -339 - 299 km s^{-1} and Zhao *et al.* (2010) from -360 - 345 km s^{-1}, even though there is faint emission at extremer negative velocities as also implied by Brγ, Fe III, and He I emission presented in Steiner *et al.* (2013) and the Ne II data cube of Irons *et al.* (2012,link on online journal page), both detecting ionized gas up to -380 km s^{-1}.

In the ALMA band 6, the H36β emission traces mostly structures along the minispiral filaments that have a high S/N and for the H33β data in band 7 only the IRS 2L and 13 region are reliably detected.

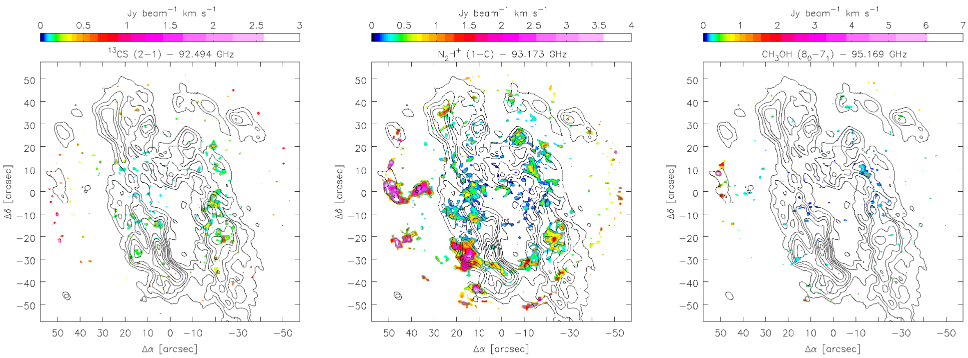

Figure 3.4: *Molecular line emission images of the inner 120″ (4.8 pc). From left to right: ^{13}CS(2–1), N_2H^+(1–0), and CH_3OH(8–7) at a resolution of 1.9″ × 1.6″ (see Table 3.2). The contours at the levels [8, 16, 24, 32, 48, 64, 80, 96, 112] × σ (= 1.9 Jy beam^{-1} km s^{-1}) show CN(2–1) emission of the CND at a resolution of 4.0″ × 2.6″ for orientation (compare Fig. 3.1; CN data: Martín* et al. *2012). (Credit: Moser* et al. *(2016b), reproduced with permission ©ESO.)*

3.3.3 Molecular gas in the outer regions

In band 3, the FOV10 covers the entire CND and regions beyond it and I term distances with $r > 40''$ from Sgr A* as outer regions. In Fig. 3.4 I compare the emission of ^{13}CS, N_2H^+, and CH_3OH(8–7) to the CN data of Martín *et al.* (2012). The N_2H^+ line emission is brighter and more widespread than the ^{13}CS and CH_3OH(8–7) line emission. The ^{13}CS line emission is mainly found at the west side of the CND and in the SEW and SEE regions (see Fig.3.1 for orientation). The brightest N_2H^+ line emission stems from the SEE and in the V-cloud outside of the CND which itself shows several N_2H^+ patches especially towards local peaks in CN emission. This matches the lower resolution ($\theta_{\text{beam}} \sim 8''$) N_2H^+ and CH_3OH(2–1) data of Moser *et al.* (2014, 2017), as well as H_2CO distribution in Martín *et al.* (2012). The V-cloud has been only barely traced in any other molecule in the past (compare Christopher *et al.* 2005; Montero-Castaño *et al.* 2009; Martín *et al.* 2012). In contrast to H_2CO the N_2H^+ emission is faint in the northern clump of the eastern extension (nomenclature: Christopher *et al.* 2005; Martín *et al.* 2012). CH_3OH(8–7) line emission is detected in CND regions near the center - especially in the western CND - , in the SEE, and along the part of the NEA that overlaps with the V-cloud. This goes well along with the CH_3OH(2–1) emission reported in Moser *et al.* (2014, 2017) is brighter in the eastern part of the V-cloud than the western part.

The brightest peak in the V-cloud matches a 36 GHz and 44 GHz class I methanol maser source reported in Yusef-Zadeh *et al.* (2001); Sjouwerman *et al.* (2010); Pihlström *et al.* (2011) and the pointy shape and high brightness in the ALMA data suggest the CH_3OH(8–7) emission to be stimulated as well. The clouds to the north and south of it correspond to peaks in N_2H^+ emission and the fourth methanol clump further south is located at a minimum of N_2H^+ emission at the V-cloud edge. Sjouwerman *et al.* (2010) found a second 36 GHz maser

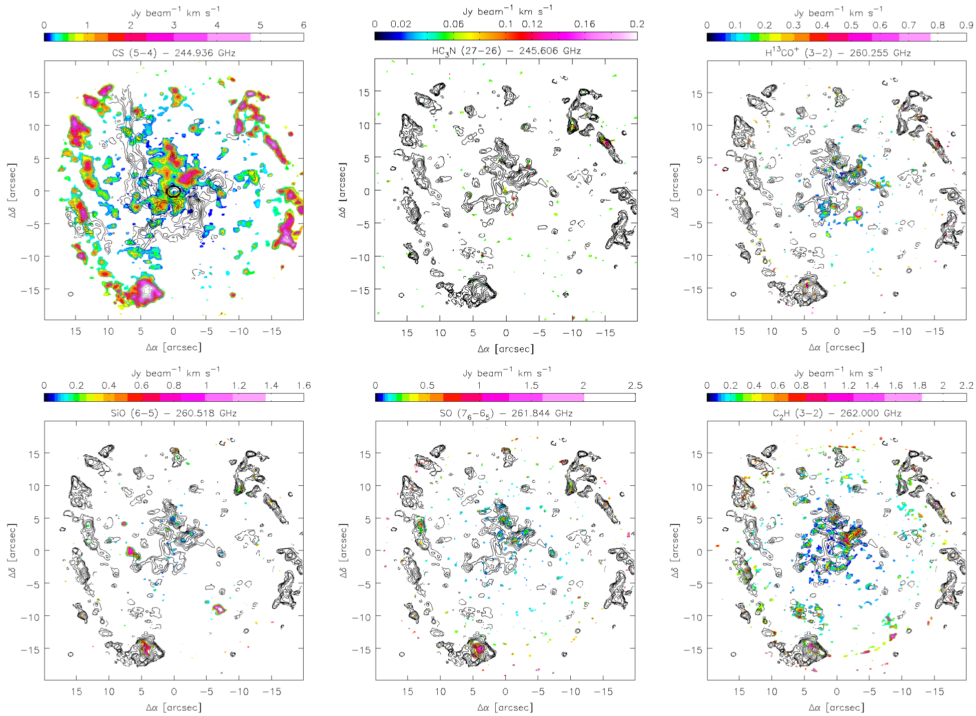

Figure 3.5: *Molecular line emission images of the inner 40″ (1.6 pc) at a resolution of about 0.7″ × 0.6″. Top row (from left to right): CS(5–4), with 250 GHz contours as in Fig. 3.2, HC_3N(27–26), and $H^{13}CO^+$(3–2). Bottom row (from left to right): SiO(6–5), SO(7–6), and C_2H(3–2). The contours show the CS(5–4) emission at the levels of [4, 8, 12, 18, 24, 30, 36, 48, 60, 72, 84] × σ (= 0.08 Jy beam^{-1} km s^{-1}) for comparison (see also Fig. A.3). Zooms into the inner 20″, the triop (15″ northwest of Sgr A*), and the SEW clumps (15″ south(east) of Sgr A*) can be found in Figs. A.5 and A.4, A.6, and A.7, respectively. (Credit: Moser* et al. *(2016b), reproduced with permission ©ESO.)*

in region that is not detected in this CH_3OH(8–7) data. The location of the CH_3OH(8–7) line emission in the SEE cloud corresponds to a 36 GHz maser (Sjouwerman *et al.* 2010), but compared to the luminous point source in the V-cloud, the CH_3OH(8–7) emission is faint and spread out.

3.3.4 Molecular gas in the inner 40 arcseconds

Here I outline and discuss the distribution of the different molecular emission lines detected in this ALMA observation and compare them to the brightest line of them in the central region, i.e. CS(5-4). The images of the integrated emission of the lines are shown in Fig. 3.5. The CS line emission is bright, clumpy, and widely spread over the entire region. Its emission is prominent in the CND, i.e. east and west of the center in the band 6 FOV10,

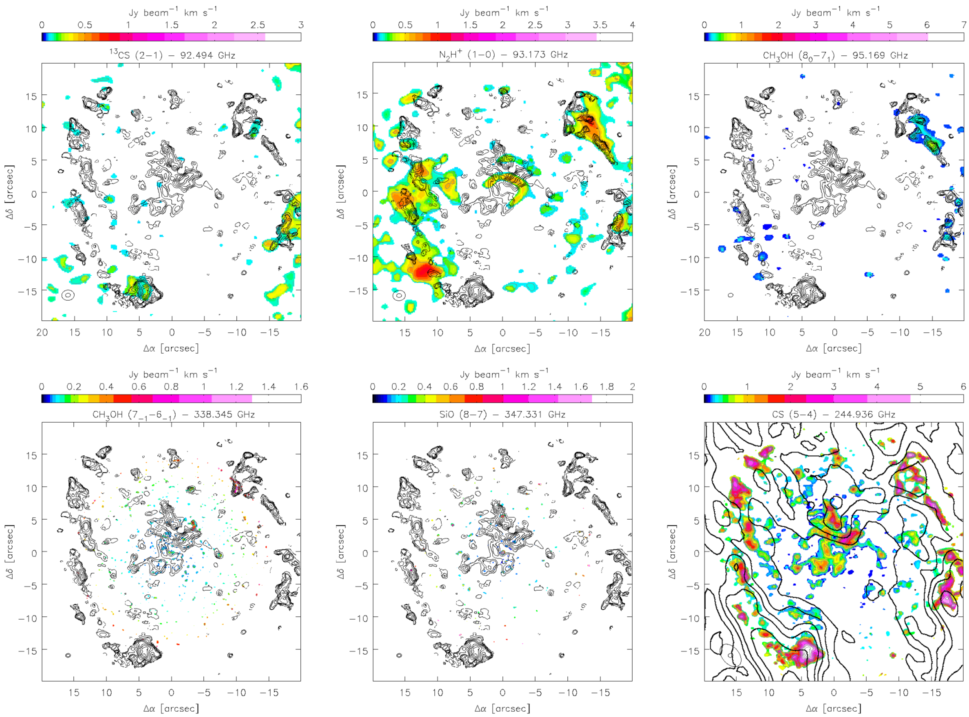

Figure 3.5 (Cont.): *Molecular line emission images of the inner 40″ (1.6 pc) at a resolution of about 0.7″ × 0.6″. Top row (from left to right): ^{13}CS(2–1), N_2H^+(1–0), and CH_3OH(8–7) as in Fig. 3.4, but zoomed in. Bottom row (from left to right): CH_3OH(7–6) and SiO(8–7), both at resolutions of 0.5″ × 0.5″, and CS(5–4) as before. The contours show the CS(5–4) emission at the levels of [4, 8, 12, 18, 24, 30, 36, 48, 60, 72, 84] × σ (= 0.08 Jy beam^{-1} km s^{-1}) for comparison. except from bottom right image, which is overlayed with the CN(2–1) emission as in Fig. 3.4. The inner rim of the CND is detected (cf. Fig. 3.1) toward the edge of the FOV10 of the band 6 and 7 emission lines. (Credit: Moser* et al. (*2016b), reproduced with permission ©ESO.)*

especially towards the inner edges of the CND. On the eastern side, the CS emission appears to be aligned with the eastern edge of the extended emission of the minispiral NA (e.g. at 100 GHz) and intersected by the EA (e.g. at 250 GHz). The maximum in emission maximum resides in the SEW (compare Fig.3.1). On the western side, the emission is bright in the *triop* and in the northwestern ridge of the minispiral WA. There the CS emission is cutoff to the south by the FOV10. The strong CS peaks in the inner pc as well as the CND are also the location of the emission from $H^{13}CO^+$, SiO, SO, and C_2H, which are fainter than CS in general. Emission of ^{13}CS, N_2H^+, and CH_3OH(8–7) appear to reside rather in the CND, but the sensitivity to different size scales in the ALMA bands 3 and 6 as a reason for this cannot be ruled out.

3.3.4.1 Triop

This feature in the western CND reminded me of a crustacean shrimp due to its unusual triangular shape so that I named it *triop*. This structure is detected in all molecular emission lines in my ALMA data (see also Fig. A.6). One can group the substructures of the *triop* into the head, i.e. the extended northeastern part of the *triop*, and the tail, i.e. the thin southwestern part. The side facing the NSC shines brightest in most of the molecular emission lines, especially in the middle of the tail and in the southeast clump in the head being nearest to the center. The tail center is the emission maximum of the triop for all the ALMA detected molecules, except from ^{13}CS and N_2H^+, which have their maximum towards the center of the *triop*. Remarkably, the *triop* has been detected in all molecules of earlier observations (e.g., Guesten *et al.* 1987; Jackson *et al.* 1993; Marr *et al.* 1993; Yusef-Zadeh *et al.* 2001; Wright *et al.* 2001; Christopher *et al.* 2005; Montero-Castaño *et al.* 2009; Martín *et al.* 2012). Among them are density and PDR tracers like HCO^+, HCN, CN, but also highly UV-sensitive species like HC_3N. In these previous studies, *triop* appears to be oval or triangular because of the lower angular resolution. In contrast to this, ALMA has now revealed its underlying filamentary structure. In addition, the tail center of the *triop* harbours the so far closest class I methanol maser emission at 44 GHz to the center, matching the peak in CH_3OH(8–7) emission and possibly implying an early phase of star formation (Yusef-Zadeh *et al.* 2001; Sjouwerman *et al.* 2010).

3.3.4.2 Southern extension west

The SEW cloud at the western fork of the northern tip of the SE is the brightest and largest cloud in the CS emission and detected in all band 6 molecules, except from HC_3N. No N_2H^+ and CH_3OH(8–7) is traced in this observation for this cloud. Together with previous studies (compare Christopher *et al.* 2005; Montero-Castaño *et al.* 2009; Martín *et al.* 2012) this suggests the SEW to be less shielded from UV-radiation than the *triop*. The SEW has a diameter in the CS emission of 4″. It appears as a double core in north-south direction and shows an extension from the northwestern end to the southwest. It seems to be a front perpendicular to the direction to Sgr A* (see also Fig. A.7). The C_2H emission extends to the northern CS peak and the C_2H emission peak is 1″ west of the CS maximum. The SO emission follows the distribution of CS but is more extended over the CS cores to the east. East of the SO and C_2H peak and marginally east of the southern CS maximum, but still on the northern CS maximum lies the SiO peak and extends to the north and east and to another SiO peak at the southern CS maximum. The $H^{13}CO^+$ emission is most distant from the front facing the center and peaks between the northern CS and SiO peak from where it stretches to the northeast similar to SiO. Two more $H^{13}CO^+$ clumps are located 1″ east and west of the southern CS core. The eastern clump corresponds to the eastern edge of the SO emission and the western to the southern rigde of the C_2H peak. Bright ^{13}CS emission is detected at the CS peaks and at the northeastern edge of the SEW. However, the difference in angular scales in band 3 and 6 need to be considered. The layered structure of the emission regions of the different molecular lines perpendicular to the direction to Sgr A* and the NSC could hint at a stratification of the emission.

3.3.4.3 The central 20 arcseconds

The most extraordinary aspect of the ALMA data is the detection of CS emission within a (projected) radius of < 8″ around Sgr A* (see also Figs. A.3, A.3, and A.5). This central association (CA) of clouds is spreads over the region where NA cosses the bar of the minispiral to the region north of Sgr A* where it seems to be limited by the inner rim of the bar and the NA facing the SMBH. The northern part can be separated into two features, both containing two to three clumps. One feature is located 2″ northwest from Sgr A* and extends parallel to the bar towards the northwest with a length of about 3″ (SE-NW cloud) and the other feature stretches from 4″ north of Sgr A* northwards over 4″ with a small bend to the east (NS cloud). The center of the NS cloud corresponds the ionized emission from IRS 7 visible in the continuum emission images.

Southeast of Sgr A*, the CS emission comprises two clumps, one extending a triangular area constrained by the IRS 16 southern cluster, IRS 16 SE2 and 16SE3 (35), and IRS 21, the other following the minicavity's eastern inner rim. These clumps are partially detected in C_2H emission, which corrupted by a sidelobe in this region. Further to the south, CS emission is present around IRS 9 in the EA. Moreover, CS and C_2H are detected in tiny clumps directly north and south of IRS 1W. CS emission shows also up along the EB, connecting the NA with the EA (see MIR images in Fig. 3.6), as well as $H^{13}CO^+$, SiO, SO, and C_2H. Apart from the features mentioned, the CS emission appears to shun the minispiral inner region such as IRS 13 to IRS 2.

The SE-NW cloud consists of two prominent clumps detected in all band 6 emission lines, one in the IRS 29 region, the other in the southwest of IRS 3. From the latter position, the CS emission show faint extensions towards IRS 3 itself and to the northwestern edge of the IRS 3 dust shell. Strikingly, this northwestern edge is well detected in HC_3N and CH_3OH(7–6), which both are not present elsewhere in the central 12″, and marginally detected in $H^{13}CO^+$. Obviously, there is a change in the ISM conditions compared to the other CS detected region.

The southern end of the NS cloud lies almost between IRS 3 and 7, the middle clump southwest IRS 7, and the third clump northeast of IRS 7, but not along its tail (MIR image).

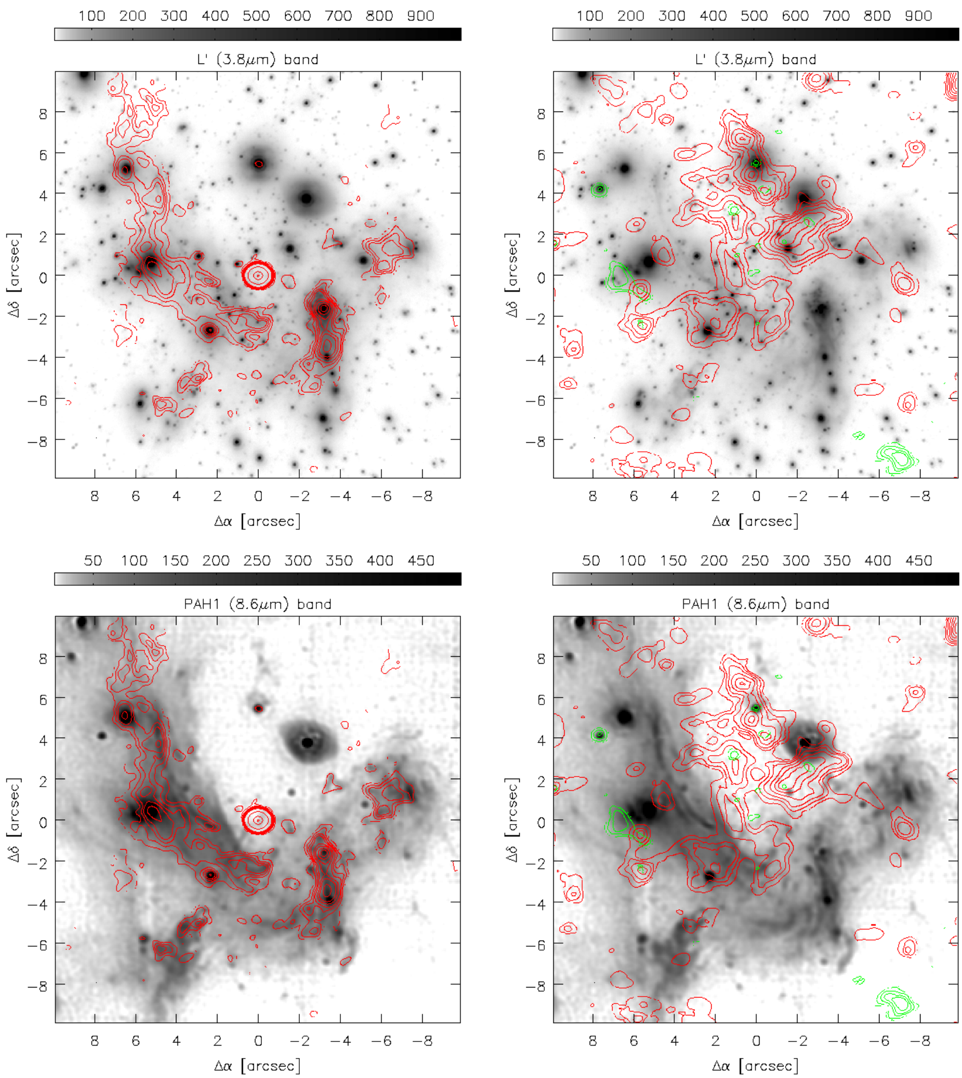

Figure 3.6: *Molecular gas and continuum emission maps in the inner 20″ compared to the NIR VLT/NACO L' (3.8 μm) emission (top, Sabha, private communication) and the MIR VLT/VISIR PAH (8.6 μm) emission images (bottom,* Sabha et al. 2016*) in arbitrary units. The left side shows the 340 GHz continuum in red contours of [6, 12, 18, 24, 36, 48, 72, 96, 960, 9600, 17280] $\times\, \sigma$ (= 0.24 mJy beam^{-1}). The right side shows CS(5–4) in red contours as in Fig. 3.5 and SiO(6–5) in green contours of [2, 4, 8, 12, 16] $\times\, \sigma$ (= 0.08 Jy beam^{-1} km s^{-1}). (Credit:* Moser et al. (2016b)*, reproduced with permission ©ESO.)*

These clumps have counterparts in $H^{13}CO^+$, SiO, SO, and C_2H. Between IRS 16CC and IRS 7, a further clump is detected in all band 6 lines. In addition, emission of CS, SiO, SO, C_2H, and CH_3OH(7–6) show up in a clump at the southwestern ridge of the Bar, i.e. south of IRS 6E and 6W.

Aside from the peculiar behaviour of HC_3N and CH_3OH(7–6) close to IRS 3, SiO exhibits a curious deviation from the CS detected gas morphology: Yusef-Zadeh *et al.* (2013) first reported two high velocity SiO clumps southeast of IRS 1W and southwest of IRS 12 - named clump 1 & 2 and clump 11; YZ1-2 and YZ11 hereafter. ALMA detected both in SiO(6–5) emission, whereas only YZ1-2 is detected in SiO(8–7). At similar velocities only faint CS emission clumps northeast of IRS 1W and south of IRS 21 are visible. In addition, the SiO maser stars IRS 7 and IRS 10EE (Reid *et al.* 2007; Li *et al.* 2010) are detected both ALMA SiO transitions at the corresponding position and velocities (see Fig. 3.7). SiO emission from IRS 10EE was also reported as clump 3 (YZ3) in Yusef-Zadeh *et al.* (2013).

3.3.5 Kinematics in the inner 40 arcseconds

In this section, I outline the kinematics in a main velocity range of about -100 km s^{-1} to +100 km s^{-1} and at higher velocities of up to +200 km s^{-1}. High velocity features are most likely due to either to outflows or cloud collisions, or to the proximity (<10″ or 0.4 pc) to the dynamical center. Figure 3.7 shows the channels maps between -140 km s^{-1} and 200 (220) km s^{-1} for CS and SiO in comparison to H36β, so that cloud complexes can be identified and the motion of the molecular and ionized gas becomes visible. The channel velocities given in the channel image corners are the channel lower edges and the channel width is 20 km s^{-1}. The spectral properties of the regions are listed in the Tables A.3 - A.5, and A.6.

3.3.5.1 Main velocity range

Due to the FOV10 in band 6, the velocity range of the CND clouds detected is of about -100 km s^{-1} and +100 km s^{-1} in the inner 40″. Nevertheless, IRS 7 shows SiO emission from channel -140 km s^{-1} to -100 km s^{-1}, so that I let Fig. 3.7 start at -140 km s^{-1}.

Regarding the low velocity resolution, spectral SiO properties of IRS 7 consistent with the findings of Reid *et al.* (2007) reporting a velocity of -114 km s^{-1} and a line width of 5-10 km s^{-1}. In the mentioned velocity range, the H36β appears in the western end of the bar between IRS 6E and 6W and towards IRS 21 where it is elongated in northsouth orientation. Between channel -80 to -40 km s^{-1} the first CS emission (r ~ 2″) clumps show up in the NA, i.e. between the EA/IRS21 and IRS 1W, between IRS 1W, 10 and probably 5, and south of IRS 7. From -40 to 0 km s^{-1}, the extended CS cloud in the NA south and east of Sgr A* arises. It reaches from IRS 1W to the eastern edge of the minicavity and is as wide as the NA in that region. Furthermore, IRS 10EE radiates SiO emission around the reported velocity of -27 km s^{-1} and line width of 5 - 10 km s^{-1} (Reid *et al.* 2007; Li *et al.* 2010). Between -80 to 0 km s^{-1}, the RRL emission shifts northeast from IRS 21 to IRS 1W and is mostly found at the northeastern edge of the large CS cloud or within it. In the same channel range, the SEW

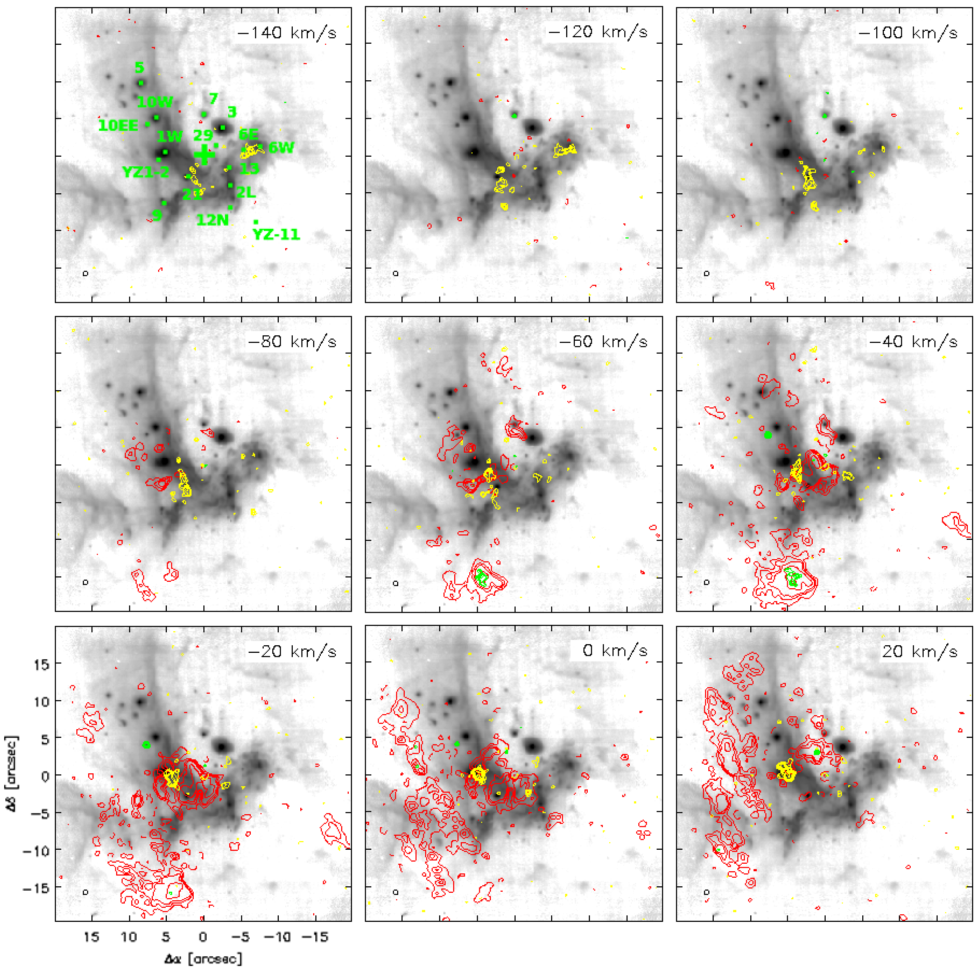

Figure 3.7: *Velocity distribution maps from -140 to 20 km s^{-1} in the inner 40″ overlayed onto the MIR (8.6 μm) PAH image from Fig 3.6. Red contours show the CS(5–4) emission at the levels [4, 8, 12, 24, 48, -3, -45] × σ (= 0.91 mJy beam^{-1}), green contours the SiO(6–5) emission at [4, 5, 6, 7, 8, 10, 12, 14, -4] × σ (= 0.94 mJy beam^{-1}), and yellow contours represent the H36β emission at [3, 4, 5, 6, 8, 10, -3, -6] × σ (= 1.05 mJy beam^{-1}) for comparison to the RRL emission. Green numbers denote the IRS sources and the green cross Sgr A*. (Credit:* Moser et al. *(*2016b*), reproduced with permission ©ESO.)*

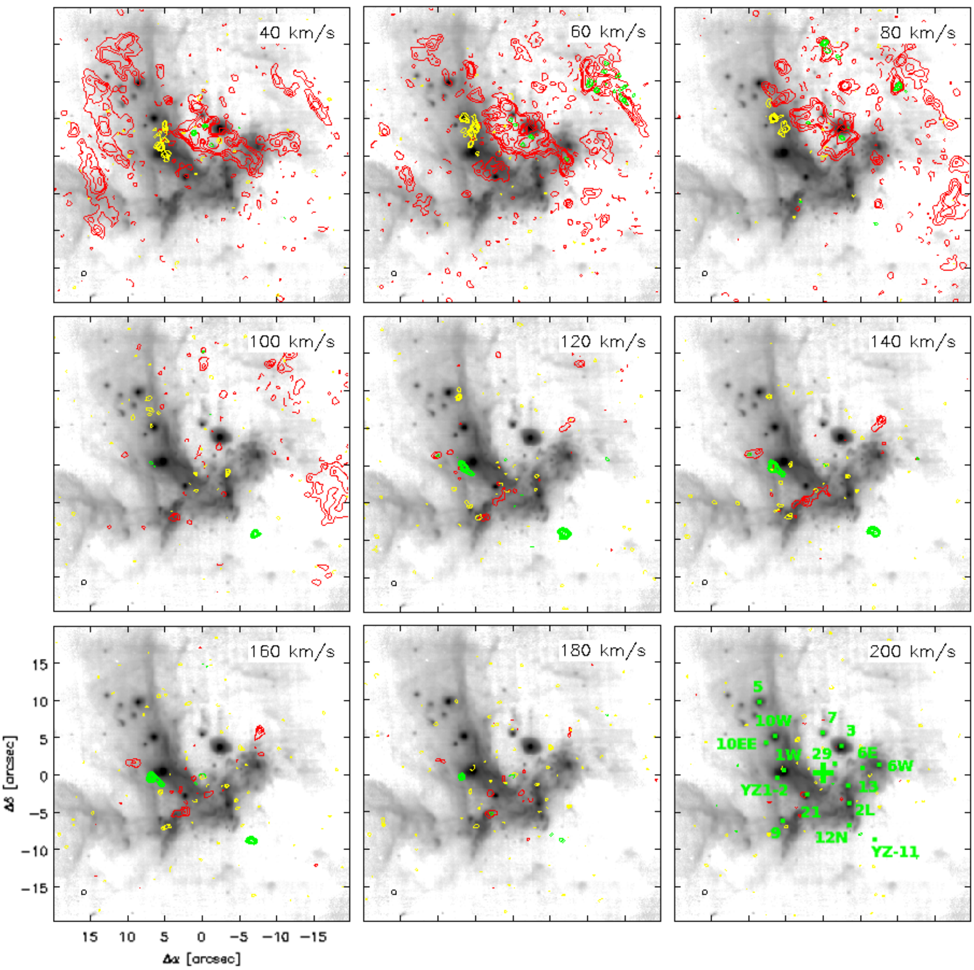

Figure 3.7 (Cont.): *Velocity distribution from 40 to 200 km s^{-1} in the inner 40″ overlayed onto the MIR (8.6 µm) PAH image from Fig 3.6. Red contours show the CS(5–4) emission at the levels [4, 8, 12, 24, 48, -3, -45] × σ (= 0.91 mJy beam^{-1}), green contours the SiO(6–5) emission at [4, 5, 6, 7, 8, 10, 12, 14, -4] × σ (= 0.94 mJy beam^{-1}), and yellow contours represent the H36β emission at [3, 4, 5, 6, 8, 10, -3, -6] × σ (= 1.05 mJy beam^{-1}) for comparison to the RRL emission. Green numbers denote the IRS sources and the green cross Sgr A*. (Credit: Moser et al. (2016b), reproduced with permission ©ESO.)*

emerges in CS and SiO emission and peaks around -40 km s^{-1}. Channels -40 and -20 km s^{-1} show faint putative connection between the large central CS clump south of Sgr A* and the SEW.

From channel -20 km s^{-1} onwards the CS emission moves from the SEW into the eastern CND, crosses the EA and proceeds northwards along the NA until the channel of 60 km s^{-1}. Furthermore, tiny CS clumps appear nearby or at the dusty sources east of IRS 5 (Perger *et al.* 2008) and IRS 5 itself between velocities of 20 and 60 km s^{-1}. While the CS emission within the minispiral decreases to few faint clump for channels above 0 km s^{-1}, the bulk of the molecular gas between 20 and 100 km s^{-1} resides within a region constrained by the NA, the Bar, IRS 3, and 7. From this region, a filament extends to the southwest crossing the Bar, i.e. to the southeast of IRS 6W, and a group of small clumps between the southwest of the Bar and the WA at velocities of 40 to 80 km s^{-1}. The SiO emission peaks coincide with several CS peaks in the central pc and channel range. The RRL emission progresses further northwards to IRS 5 and does not coincide with the CS emission anymore but seems to follow it. However, large scale RRL emission might exist but could be resolved out in band 6. From 40 to 80 km s^{-1}, NA edge between IRS 1W and 10W seem to closely delineate the CS emission.

The *triop* is visible in CS from 20 to 120 km s^{-1}, or 40 to 80 km s^{-1} for the fainter lines. Its emission proceeds from the southwest to the northeast and reaches its maximum around 60 km s^{-1}. 15″ north of Sgr A*, a larger clump peaks at 80 km s^{-1}. This clump as well as the main clumps in the *triop* are also prominent in SiO emission. Moreover, a cloud south of *triop*, southwest of the Bar, and seemingly within the WA or CND pups up at 80 to 100 km s^{-1}.

3.3.5.2 High velocities

Beyond the -100 to 100 km s^{-1} velocity range of the CND between the lobes, I make out several clumps with high velocities in a region of less than ~10″ around Sgr A*: The first group of sources are the two SiO clumps YZ11 and YZ1-2 mentioned before. They appear from 80 to 200 km s^{-1} and 100 to 180 km s^{-1}, respectively, and peak around 140 to 160 km s^{-1} matching the findings of Yusef-Zadeh *et al.* (2013). The second remarkable group consists of three CS emitting clumps: One feature spans from IRS 9/the Tip past IRS 21 to the minicavity's eastern rim between 80 to 200 km s^{-1}, the second one appears 5″ north of IRS 6W between 120 to 180 km s^{-1}, and the last one coincides with faint SiO emission 5″ northeast of YZ1-2 between 100 to 180 km s^{-1}. At velocities higher than 100 km s^{-1}, the sensitivity of H36β cube channels drops and the RRL emission is found in weak, small clumps only. It is well detected in the Tip above 100 km s^{-1}, as expected from other ionized gas emission studies (e.g. Ne II cube of Irons *et al.* 2012), where it coincides with the CS emission around 120 and 140 km s^{-1}.

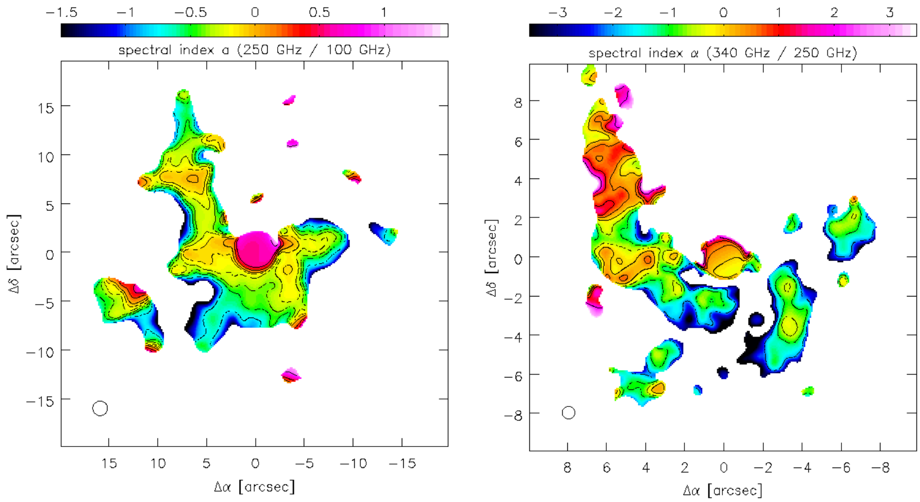

Figure 3.8: *Images of the continuum spectral index distribution in the inner $\lesssim$ 1.6 pc. Left: Between 100 and 250 GHz (inner 40″) tapered to a resolution of 1.5″ with contours of [-0.75, -0.5, -0.375, -0.25, -0.125, 0, 0.25, 0.5, 1, 1.5]. Right: Between 250 and 340 GHz (inner 20″) tapered to a resolution of 0.65″ with contours of [-2,-1, -0.5, 0, 0.5, 1, 2]. Maps on the uncertainties can be found in Fig. A.8. (Credit: Moser* et al. *(2016b), reproduced with permission ©ESO.)*

3.4 Discussion

This section first deals with the spectral index of the (sub-) mm continuum emission in the central 40″ and the electron temperature of the ionized gas. I then continue with a study of the relation between the stars and the gas. In the last part of this section I discuss the trends in the molecular line ratios depending on their location in the GC and their probable causes.

3.4.1 Continuum spectral index

I calculated maps of the spectral indices (see Fig. 3.8) between 100, 250, and 340 GHz following a power law with $S_\nu \propto \nu^\alpha$, where α is the spectral index. These are based on tapered continuum images (same resolution) that have been clipped at a 5σ level prior to primary beam correction. The corresponding uncertainties introduced by the S/N and the flux calibration uncertainties are shown in the Appendix in Fig. A.8. In regions of high S/N, flux calibration errors dominate the uncertainty of the spectral index (see Sect. 3.2.2).

In the 100 to 250 GHz range, Sgr A* has an inverted spectrum with $\alpha_{100-250} \sim 0.58 \pm 0.21$ due synchrotron emission from the accretion disk. My result agrees with the $\alpha_{100-230} \sim 0.5$ reported by Kunneriath *et al.* (2012a,b) and is in concordance with the findings of Falcke *et al.* (1998), i.e. $\alpha_{100-150} \sim 0.76$ and $\alpha_{43-100} \sim 0.52$ in the 3 - 2 mm and 7 - 3 mm range, respectively.

Uncertainties introduced from the uv-coverage can be ruled out, because Sgr A* is at point source and detected with a high S/N. Consequently, the spectral index of Sgr A* is plausible but it could be impacted by a variability of flux density depending on the frequency (Kunneriath *et al.* 2012a). Nevertheless, my result matches the spectral trend in this frequency domain. This holds also for the 340 GHz regime, where Sgr A* is detected with a high S/N and shows a flat $\alpha_{250-340} = 0.17 \pm 0.45$. The result is in agreement with the $\alpha_{230-690} \sim -0.13$ given by Marrone *et al.* (2006b) and the $\alpha_{217-355} = -0.06 \pm 0.26$ by Bower *et al.* (2015), where the latter hints at the emission at these frequencies to change from the optically thick to the optically thin regime. SMA observations at 345 GHz and 690 GHz suggest the overall spectrum of Sgr A* to peak around 345 GHz (Marrone *et al.* 2006b,a; Marrone 2006) and Eckart *et al.* (2012) find synchrotron turnover frequencies in the range 300 - 400 GHz for the majority of their synchrotron and SSC models.

The spectral indices derived here for the minispiral should be considered as lower limits, because flux at large angular scales, that could be detected in the lower frequency band, is resolved out in the higher frequency band of these ALMA data. For the inner 10″ around Sgr A*, the minispiral displays negative spectral indices between 100 and 250 GHz, as it was also observed by Kunneriath *et al.* (2012b). In the regions IRS 13, 2L, 6, 1W, and 10W, $\alpha_{100-250}$ approaches ~ -0.1, implying free-free thermal bremsstrahlung emission. Since these sources are luminous and compact, they dominate the emission compared to the diffuse gas and their flux measurements are barely affected by beam filling factor and resolution effects. The case might be different for the filaments in the the Tip and south and west of Sgr A* in the Bar which are not very bright compared to the embedding diffuser emission gas.

The drop of the spectral index to ~ -0.4 and even less, i.e. ~ -0.7 in the Tip, could be explained by resolved out 250 GHz flux. Similarly steep values can be found towards the compact sources in the spectral index map of Kunneriath *et al.* (2012b) obtained from Combined Array for Research in Millimeter-wave Astronomy (CARMA) observation, but these values are likely affected by the lower spatial resolution which mixes faint extended emission into the flux and a uv-coverage which is inferior compared to ALMA. Going down to angular resolutions such as the ALMA data discussed here, the spectral index of point source can be expected to depend only on the point source fluxes. The spectral indices become positive in the Ribbon of the EA with $\alpha_{100-250} \gtrsim 0.1$, towards the region south of IRS 5 ($\Delta\delta \sim 7''$ from Sgr A*) and in the IRS 1 to IRS 16NW region of the NA with $\alpha_{100-250} \gtrsim 0$, and in a few single clouds in the field with $\alpha_{100-250} \gtrsim 0.5$. Obviously, a dust component begins to add significantly to the continuum emission at frequencies $\gtrsim$ 230 GHz (see also Kunneriath *et al.* 2012a).

Between 250 and 340 GHz, a spectral index of $\alpha_{250-340} \gtrsim 0$ is reached in the entire NA down to the south of IRS 1W, emphasizing the trend of the growing importance of dust emission with increasing frequency. The Tip and the Bar have an $\alpha_{250-340} \sim -1 - 0$ and only the brightest sources reach an $\alpha_{250-340} \sim -0.3$. Apart from angular filtering effects the 340 GHz data suffers from a lower S/N. Large scale emission, though detectable by the uv-coverage of the 340 GHz observation, might be too weak to be detected at this noise level. As a consequence the spectral indices show extremer values than for the 100 - 250 GHz range.

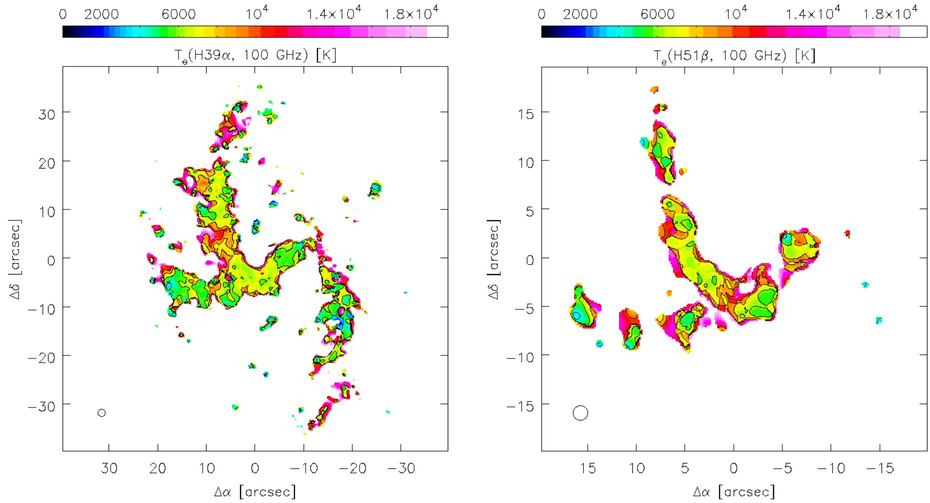

Figure 3.9: *Images of the electron temperature distribution in the inner $\lesssim$ 1.6 pc. Left: Based on H39α (inner 40″) and tapered to a resolution of 1.5″ with contours of [4, 6, 8, 10] × 1000 K. Right: Same as top, but based on H51β (inner 20″). Maps on the uncertainties can be found in Fig. A.9. (Credit: Moser* et al. *(2016b), reproduced with permission ©ESO.)*

3.4.2 Electron temperature

The electron temperature give information on the strength and location and with this the potential cause of the ionization in the GC. Based on the formula given in Zhao *et al.* (2010) I calculate the LTE electron temperature from the H39α and the continuum emission. For this I need to assume the RRL and continuum emission to be optically thin and in LTE. The resulting electron temperature maps in Figure 3.9 are based on tapered (same resolution) continuum map and RRL cube that have been clipped at 3σ before primary beam correction. Instead of $S_L \Delta V_{FWHM}$ I used the integrated flux $\int S_L dV$, because of the high uncertainty in the line width due to the low spectral resolution. Furthermore, a correction factor for the power-law approximation at 100 GHz was applied, i.e. $\alpha(\nu = 100\text{ GHz}, T_e \sim 10^4\text{ K}) \sim 0.904$ (Mezger and Henderson 1967).

I find the LTE electron temperature to be comparably uniform for the entire minispiral with a $T_e \sim 6000$ K. The electron temperature rises to 7000 K in the NA and towards the central region of the Bar, and 9000 K around IRS 1W and 10W, and decreases to 5000 K in the western Bar, the WA, and the EA. Towards the edges of the ionized emission, the S/N drops significantly, so that the resulting temperatures are not reliable. Observations of H76α, H92α, H30α RRL emission by Schwarz *et al.* (1989), Roberts and Goss (1993), Roberts *et al.* (1996), and Zhao *et al.* (2010) yield temperatures of ∼ 7000 K, especially in the arms and are consistent with the temperature range of 6000 ± 1000 K from this ALMA observation.

The T_e outliers in the IRS 1W to 10W region could be a product of H39α flux smoothed out in the wide frequency channels as mentioned in Section 3.3.2. As a probe, I computed the electron temperature based on the H51β line (Fig. 3.9) which has a higher S/N than the H49β line. I scale the Hβ flux to the Hα flux using an LTE Hα/Hβ ratio of 3.55 (e.g., Gordon and Walmsley 1990). As a result the IRS 1W to 10W region shows a $T_e \sim 6000$ K. Apart from this difference, the electron temperature in all other regions in the minispiral corresponds to the Hα based values.

However, Zhao *et al.* (2010) obtain $T_e > 10000$ K towards the center of the Bar, i.e. the region between IRS 21, 16, and 33. H51β temperature map may show hints for such a trend but not as far in the NA as in the data of Zhao *et al.* (2010). Instead, I suspect a low S/N in this region to produce these high temperatures in my maps as it is also visible towards the edges of the minispiral. In fact, there is a very broad (in velocity) but weak ionized gas component near to and within the minicavity (spectra/line cube in Roberts *et al.* 1996; Zhao *et al.* 2010; Irons *et al.* 2012) which is picked up in the ALMA H39α data but not in the H51β data due to the line's weaker intensity. The H39α data gives a $T_e = 6500 \pm 500$ K throughout this region, which is in agreement with the ~ 6850 K found by Roberts *et al.* (1996).

Because of the low spectral resolution of my RRL line cubes, I can expect the ALMA data to recover the electron temperature well only for regions with a single velocity component, such as the minispiral arms. However, for more complex regions, where the minispiral arms and/or unassigned velocity components overlap in projection, my data shows discrepancies compared to earlier studies.

3.4.3 Stellar sources

This section is dedicated to the question on a connection between molecular and ionized gas as well as to the stars. For this, I compare the line centers of the sources (see Table 3.3). However, there are not many matches despite allowing a generous velocity offset of 70 km s^{-1} between two features.

The ionized gas LOS velocity obtained from the H39α and H36β data accord with the stellar velocities for the IRS 1W, 1E, 7, 9SW, 9SE, 10W, 13W, 13E2, 16NE, 33N, 34E, 34NW, W11b, and W13b within the offset range (see Figs. 3.1 and A.11). For these sources, the stellar motion could be connected to the extended gas motion, but it cannot be ruled out that the true stellar IR spectra are possibly outshone by the bright ionized gas emission in the IR of the surrounding material in some cases.

The comparison between the CS traced molecular gas velocities and stellar velocities yields only two matches: IRS 3E and W13b. These results seem to rule out that the molecular gas could have been produced in and expelled from the stellar atmospheres, despite the many O/B and Wolf-Rayet (WR) stars in the NSC. Nevertheless, the initial velocity information of the molecular gas – and with that a hint on its origin – could have been lost in the turbulence generated by the collision of the winds from all the stars in the region.

The ionized and molecular gas show similar velocities in the Bar/NA region of the minispiral, i.e. in IRS 5, 6E, 16SSW, 16CC, 16SE2, 33SW, 33NW, 33N, W13b, W10b, W7b, and W14b from my selection (see also Sect. 3.3.5) which is also discussed in Section 3.5.3.

Table 3.3: *The gas radial velocities in RRL and CS emission at the position of the nuclear cluster stars, their stellar radial velocities and spectral type (Credit: Moser et al. (2016b), reproduced with permission ©ESO.)*

sources	gas radial velocity v_g [km s^{-1}]			stellar radial velocity v_s [km s^{-1}]	type
	H39α	H36β	CS(5–4)		
IRS 1W[P06]	32	5	-	35[P06]	Be?
IRS 1E[P06]	34	-	-	18[P14]	B1-3 I
IRS 2L[V06]	-251, 22	-284	-	-	-
IRS 2S[V06]	-237	-289	-	107[G00]	L
IRS 3[V06]	-	-	61	-	E
IRS 3E[P06]	-	-	63	107[P06]	WC5/6
IRS 4[V06]	175	-	-20	-	-
IRS 5[V06]	125	-	66	-	-
IRS 6W[V06]	-128	-147	-	-150[G00]	E
IRS 6E[V06]	-134	-67, 21	28, 99	-	-
IRS 7[V06]	-110	-118	-130[SiO] , -53	-114[R07]	L
IRS 7E2(ESE)[P06]	102	-	-	-80[P06]	Ofpe/WN9
IRS 9[V06]	173	-	-	-342[R07]	-
IRS 9N[V06]	170	160	-	-110[G00]	-
IRS 9W[P06]	-70, 300	-	-	140[P06]	WN8
IRS 9SW[P06]	202	-	-	180[P06]	WC9
IRS 9SE[P06]	198	-	-31	130[P06]	WC9
IRS 10W[V06]	91	65	-	7[G00]	-
IRS 10EE[V06]	102	-	-31[SiO]	-55[G00] , -27[R07,L10]	L
IRS 12N[V06]	-207	-	-	-96[G00] , -63[R07,L10]	L
IRS 13E[V06]	-200, -40	-	-	45[G00]	E
IRS 13W[V06]	-220, -30	-	-	-74[G00]	L
IRS 13Nη[V06]	-40	-33	-	40[P06]	B V/III
IRS 13E1[P06]	-200, -30	-45	-	71[P06]	B0-1 I
IRS 13E4[P06]	-180, -30	-	-	56[P06]	WC9
IRS 13E2[P06]	-200, -30	-55	-	-2[P14]	WN8
IRS 16NW[P06]	-	-	46	-30[G00] , -44[P06] , 17[P14]	Ofpe/WN9
IRS 16C[P06]	-	-	-41	125[P06] , 186[P14]	Ofpe/WN9
IRS 16SW[P06]	-130	-155	-36	320[P06] , 460[P14]	Ofpe/WN9
IRS 16SSW[P06]	-157	-222, 37	-36, 45	206[P06] , 221[F15]	O8-9.5 I
IRS 16CC[P06]	-52	-	-41	241[P06] , 145[P14] , 256[F15]	O9.5-B0.5 I
IRS 16NE[P06]	-19	-	-	17[G00] , -10[P06] , 53[P14]	Ofpe/WN9
IRS 16SSE2[P06]	-122	-137	-34	286[P06] ,	B0-0.5 I
IRS 16SSE1[P06]	-117	-133	-33	216[P06] , 229[F15]	O8.5-9.5 I
IRS 16SE1[P06]	-93	-30	-	450[G00] , 366[P06]	WC8/9
IRS 16S[P06]	-128	-155	-34	100[P06] , 123[P14] , 149[F15]	B0.5-1 I
IRS 16SE2[P06]	-40	-72	-38	327[P06]	WN5/6

Table 3.3: *Continued.*

sources	gas radial velocity v_g [km s^{-1}] H39α	H36β	CS(5–4)	stellar radial velocity v_s [km s^{-1}]	type
IRS 16SE3[P06]	-30	-54	-	281[P06]	O8.5-9.5 I
IRS 17[V06]	-	-	16	185[G00], 73[R07]	L
IRS 20[V06]	-199	-	-	17[G00]	L
IRS 21[V06]	-84	-96	-9	-	-
IRS 29NE1[P06]	-	-	46	-130[G00], -99[P14]	WC8/9
IRS 29[P06]	-	-	46	-190[P06]	WC9
IRS 33SW[V06]	-220, 29	-	-27, 138	-	-
IRS 33NW[V06]	-300, 18	-312	-30	-	-
IRS 33N[P06]	-235, 19	-295	-29	68[P06], 93[P14], 105[F15]	B0.5-1 I
IRS 33E[P06]	-150	-167	-	160[G00], 170[P06], 214[P14]	Ofpe/WN9
IRS 34E[P06]	-200, -30	-	63	-154[P06]	O9-9.5 I
IRS 34W[P06]	-180, -50	-	40	-215[G00], -290[P06], -184[P14]	Ofpe/WN9
IRS 34NW[P06]	-248	-200	55	-150[P06]	WN7
AFNW[P06]	-	74	-	150[G00], 70[P06]	WN8
AFNWNW[P06]	-	84	-	30[P06]	WN7
W11b[P06]	-295, 22	-	-34	-364[P06]	OB
W13b[P06]	-301, 20	-	-33	-24[P06]	OB I?
W10b[P06]	27	-	-30	-434[P06]	O8-9.5 III/I
W7b[P06]	31	-	79	-344[P06]	O9-9.5 III?
W14b[P06]	11	-	-26	-224[P06]	O8.5-9.5 I?
B9b[P06]	145	130	3	-150[P06]	WC9

Notes. Spectra were obtained from a beam sized aperture centered on the source position (see Table A.6, and Fig. 3.1 and A.11 for details). References for the source positions and velocities are [P06] Paumard *et al.* (2006), [V06] Viehmann *et al.* (2006), [P14] Pfuhl *et al.* (2014), [G00] Genzel *et al.* (2000), [R07] Reid *et al.* (2007), [L10] Li *et al.* (2010), and [F15] Feldmeier-Krause *et al.* (2015) . The spectral type is taken from Paumard *et al.* (2006), except from the classes E and L that are denoting the early-type and late-type stars as given in Genzel *et al.* (2000). [SiO] velocities from SiO(6–5) emission of SiO maser stars.

In the following, I describe the line and continuum emission towards the most famous IRS sources.

IRS 1W This dust embedded bowshock star (NIR; Sanchez-Bermudez *et al.* 2014) is located at the lower end of the minispiral NA near the region where the NA meets the Bar. CS(5-4) and RRL emission are detected around its radial velocity of 20 km s^{-1} and the integrated CS(5-4) emission maps show two clumps northwest and southeast IRS 1W. In general, the velocity pattern is consistent with that of the NA. Southeast of the source, the gas velocity is between 0 km s^{-1} to 15 km s^{-1}. At 15 km s^{-1} to 30 km s^{-1} the emission knot separates into a northwest and southeast component and avoids the exact position of IRS 1W. Between

30 km s^{-1} to 45 km s^{-1} only the northwest component is visible. Probably, a combination of absorption and excitation is at work here.

In the 340 GHz and 250 GHz continuum, the emission maximum is positioned on the bright ridge of the minispiral about 0.2″ to 0.3″ southwest from IRS 1W and reaches 8 mJy beam^{-1} and ~13 mJy beam^{-1}, respectively. At 100 GHz, IRS 1W is heavily blended by the minispiral because of the lower resolution. The emission at IRS 1W has a bright peak of ~34 mJy beam^{-1} and spreads towards the southwest along 0.5″ to 1″.

IRS 2L Zhao *et al.* (e.g., 2010) find IRS 2L to have a RRL velocity of about -270 km s^{-1} which matches the H36β line peak at -280 km s^{-1} in this ALMA data. The region is avoided by the molecular gas emission. A definite line identification at the position of IRS 2L is not possible and the emission is blended with RRL line flux from ionized gas north of IRS 2L (e.g. IRS 13E). IRS 2L has a 340 GHz and 250 GHz continuum flux peak of 19 mJy beam^{-1} and 27 mJy beam^{-1}, respectively. The 100 GHz continuum flux is about ~100 mJy beam^{-1} towards IRS 2L.

IRS 3 This dust-enshrouded star is confirmed to be composed of an extended shell and a central compact source (Very Large Telescope Interferometer (VLTI) observations in the NIR; Pott *et al.* 2008b) and has an unknown radial velocity. ALMA has detected CS(5–4) and a C_2H(3–2) line emission at 60 km s^{-1} and less well-defined RRL emission at 80 km s^{-1} at the position of the central star. The molecular gas is related to a bright bar spreading about 1″ to the north and south with line emission also toward IRS 7. Furthermore, there is a suspicious clumps 2″ west of IRS 3 covering 2″ in north-south direction. It is connected to the northwest end of the SE-NW cloud in CS(5–4) and $H^{13}CO^{+}$(3–2) emission at around 50 to 80 km s^{-1} and shows the only prominent peak of CH_3OH(7–6) and HC_3N(27–26) emission in the entire CA. The H36β line emission appears at a velocity of about -200 km s^{-1} as a luminous bar expanding about 1″ to southwest.

The weak 340 GHz continuum emission peaks at IRS 3 at 1.4 mJy beam^{-1} and shows a faint extended feature to the south and west. There is a ridge of 250 GHz continuum emission spanning between IRS 3 and IRS 7 with a peak brightness of 1.5 mJy beam^{-1}. In addition, an unresolved source of ~ 2 mJy beam^{-1} (peak) is visible at the position of IRS 3. At 100 GHz, no significant continuum emission is detected around or at IRS 3.

IRS 5 This dust embedded bowshock star has a RRL radial velocity os 110 km s^{-1} (e.g., Zhao *et al.* 2010; Sanchez-Bermudez *et al.* 2014). There is no bright line or continuum emission originating from this source. Nearby RRL emission appears in the NA about 1.3" to the west and IRS 5S and 5SE1 in the southwest are visible in continuum emission (see also Table A.1).

IRS 6 The IRS 6E and IRS 6W region shines up at RRL velocities of about -120 km s^{-1}. The continuum and RRL emission do not appear towards two sources themselves but is spread in the void between them as filaments (K13, K14, K17, K19; Zhao *et al.* 2009). About 1″ north of IRS 6E CS(5–4) emission appears at about 40 km s^{-1} and prolongs 3″ to the southwest, where also SiO(6–5), SO(7–6), and CH_3OH(7–6) show a local peak at about 60 km s^{-1}.

IRS 7 This bowshock source (e.g., Zhao *et al.* 2009) shows - given the channel sizes - a velocity centroid at about -120 km s^{-1} in the extended RRL emission as well as spatially unresolved maser emission in SiO(6–5), and somewhat brighter in SiO(8–7) (compare with Reid *et al.* 2007). The emission of the CS(5–4) and C_2H(3–2) lines have both peaks at -50 km s^{-1} and +50 km s^{-1} in this region. A comparison to the integrated CS(5–4) line emission reveals that IRS 7 is embedded in the NS ridge which has its maximum about 0.5″ south-southeast of IRS 7. About 0.2″ to the south, unresolved C_2H(3–2) line emission appears.

IRS 7 is detected as a point source the 340 GHz and 250 GHz continuum emission with 2 mJy $beam^{-1}$ and 2.8 mJy $beam^{-1}$ peak flux density, respectively. The 100 GHz continuum shows a 1.5″ to 2″ long tail (compare e.g. Serabyn *et al.* 1991; Yusef-Zadeh and Morris 1991; Zhao *et al.* 2009) which peaks 0.65" north of the stellar position at 1.6 mJy $beam^{-1}$. The peak flux density towards IRS 7 itself is 1 mJy $beam^{-1}$.

IRS 9 Reid *et al.* (2007) find IRS 9 to have a stellar radial velocity of -340 km s^{-1} . Apart from weak CS(5-4) line emission around 0 km s^{-1} there is no line emission visible at the position of IRS 9. Furthermore, IRS 9 shows no continuum above 1 mJy $beam^{-1}$ at 100 GHz to 340 GHz. Only dusty source IRS 9N (X5 in Mužić *et al.* 2007) 0.3″ to the north has a faint counterparts at 340 GHz and 250 GHz with peaks a 2.5 mJy $beam^{-1}$ and ~5 mJy $beam^{-1}$, respectively.

IRS 10 The radial stellar velocity for IRS 10W is about 10 km s^{-1}. The ALMA observations show the RRL H36β line to peak at the source at about 70 km s^{-1}. IRS 10W appears as only marginally extended continuum source at 340 GHz and 250 GHz with peak flux densities of ~7 mJy $beam^{-1}$ and ~8 mJy $beam^{-1}$, respectively. At 100 GHz, its continuum emission is mixed with the extended minispiral emission and has a total peak flux density of ~50 mJy $beam^{-1}$.

In the southeast, IRS 10EE pops up in the masing SiO lines around -30 km s^{-1} (compare with Reid *et al.* 2007; Li *et al.* 2010) and in the H36β emission as a bright compact component at 70 km s^{-1} within the NA stream. Apart from the ones mentioned, no other line or continuum emission can be seen towards IRS 10EE.

IRS 12N The NIR source IRS 12N has a stellar radial velocity of about -60 km s^{-1}. No prominent continuum or line emission towards it is detected in the ALMA data.

IRS 13E The compact cluster IRS 13E (Eckart *et al.* 2013) has a diameter of 0.5″ and a radial velocity around 45 km s^{-1} (Paumard *et al.* 2006). The RRL H36β line emission shows two ~75 km s^{-1} broad components at -190 km s^{-1} and -40 km s^{-1}. In fact, the peak of the RRL H36β emission in this region is at -300 km s^{-1} and located about 0.5″ north of IRS 2L, i.e. between it and IRS 13E, coinciding with a faint NIR L-band source. In addition, there is a velocity component at -160 km s^{-1} right at IRS 13E and two components at -60 km s^{-1} and -43 km s^{-1} in the general IRS 13 (E+N) region. These finding are reproduced by the H39α RRL considering the lower angular resolution. No molecular gas emission is detected.

The center of the IRS 13E cluster coincides with peaks in flux density of 23 mJy $beam^{-1}$, ~30 mJy $beam^{-1}$, and 110 mJy $beam^{-1}$ in the 340 GHz, 250 GHz, and 100 GHz continuum emission, respectively.

IRS 13N The 0.3″ diameter stellar cluster north of IRS 13E (Eckart *et al.* 2004b, 2013) has an IR radial velocity of about 40 km s^{-1} (Paumard *et al.* 2006). It is rather inconspicuous in its line emission. CS(5-4) line emission emerges around 90 km s^{-1} but might not related to the source. The H39α line displays emission at velocities from -90 till -170 km s^{-1} and at 44 km s^{-1}, while the H36β line is visible at the southern edge of the cluster in a velocity range of -43 km s^{-1} to -60 km s^{-1}.

At 340 GHz, the spatial resolution is high enough to resolve the IRS 13N cluster as an own entity but still attached to IRS 13E. The 340 GHz and 250 GHz continuum flux densities of IRS 13N peak at 7.5 mJy $beam^{-1}$ and 18 mJy $beam^{-1}$, respectively, and IRS 13N shows a diffuse component extending ~0.5″ to the northwest. At 100 GHz, IRS 13N cannot be separated from the IRS 13E cluster.

IRS 16NE Pfuhl *et al.* (2014) report for IRS 16NE a stellar radial velocity of 50 km s^{-1} . ALMA traced a 100 km s^{-1} broad H33β line component peaking at a velocity of -30 km s^{-1} and -80 km s^{-1} at the position of IRS 16NE. 0.5″ to the east, the H36β line emission reaches its local maximum at -80 km s^{-1}. In general, RRL emission emerges between -100 km s^{-1} to +100 km s^{-1} east of source which seems to integrated into the minispiral flow. Molecular line emission appears in the range of -40 km s^{-1} until -10 km s^{-1} 0.5″ east of the source. Apart from that, IRS 16NE shows no other emission lines.

In continuum emission, IRS 16NE clearly detected as a point source with ~5 mJy $beam^{-1}$ and ~4 mJy $beam^{-1}$ at 340 GHz and 250 GHz, respectively. In band 3, the source cannot be resolved and the region is dominated by the minispiral emission.

IRS 16SW The radial velocity of IRS 16SW is about 460 km s^{-1} (Pfuhl *et al.* 2014). Faint CS(5-4) line emission is detected at -40 km s^{-1} and the integrated flux reveals IRS 16SW to be located in a 0.5″ wide valley between two CS(5-4) line emitting regions. The continuum is tentatively detected at 340 GHz and 250 GHz with flux densities of 1 mJy $beam^{-1}$ and 2.5 mJy $beam^{-1}$, respectively.

IRS 21 This dust-enshrouded star (Sanchez-Bermudez *et al.* 2014) resides in the Bar of the minispiral. The H36β line emission peaks at -96 km s^{-1} corresponding to the gas motion in the minispiral (e.g., Zhao *et al.* 2010) and additional RRL emission appears north and south of IRS 21. At velocities from -40 to 60 km s^{-1}, widespread CS(5-4) emission emerges towards the source position. In the 340 GHz and 250 GHz continuum, IRS 21 is discernible as a compact source on the ridge of the minispiral and peaks ~0.1″ to the northwest at flux densities of 7 mJy $beam^{-1}$ and 10 mJy $beam^{-1}$, respectively. The 100 GHz continuum emission towards the source is dominated by the minispiral due to the lower angular resolution and becomes brighter towards the northwest.

IRS 29 The two main sources IRS 29 and IRS 29NE of this complex show radial velocities of -190 km s^{-1} (Paumard *et al.* 2006) and -100 km s^{-1} (Pfuhl *et al.* 2014), respectively. CS(5-4) and C_2H(3-2) line emission at 50 km s^{-1} is detected at their positions. In fact, the molecular emission is part of the SE-NW cloud south of IRS 3 whose ridge passes between IRS 29 and IRS 29NE 0.4″ northeast of IRS 29. No continuum emission is detected.

IRS 33 Located west and southwest of IRS 16SW is the IRS 33 group with its most prominent members IRS 33NW, N, (S)E, and SW. For IRS 33N and 33E the radial velocities are measured to be ~100 km s^{-1} and 214 km s^{-1}, respectively (Pfuhl *et al.* 2014; Feldmeier-Krause *et al.* 2015). The sources IRS 33SW, N, and NW lie along the ridge of an elongated molecular gas cloud detected in CS(5-4) line emission at -30 km s^{-1} and not associated with the sources. In contrast to this, the position of IRS 33E shows no prominent molecular line emission. Hydrogen RRL emission from the minispiral transits 0.1″ south of IRS 33N at -330 km s^{-1}. The continuum emission shows no IRS source detection but the extended minispiral features in this region.

3.4.4 The molecular line ratios

The first hints on molecular excitation and abundance can be obtained from molecular line ratios. For all regions specified in Sect. 3.2.4 (see description of computation therein), I derived the molecular line ratios for different molecules (see Table A.7). As a summary, I grouped the ratios by regions with similar values and arranged them depending on the overall trend of the CS ratios (see Table 3.4).

As a result I find that all CS/X (X: any other observed molecule) ratios rise steeply towards the center and the SEW clump. There, they are more than 3 times higher compared to the *triop* and presumably CND-related material further out of the center. These findings are reminiscent of the trend visible in the CS(7-6)/HCN(4-3) intensity ratio map of Montero-Castaño *et al.* (2009): The luminosity ratio, which corresponds in this case to intensity ratio because of the similar frequencies observed, is about 10 times higher around Sgr A* than in the CND. An enhancement of the ratios by a factor of 1.5 in the CA and the SEW clump can also be seen for C_2H/X and SO/X (see Table 3.4). Concerning ratios with C_2H, the C_2H flux suffers from strong sidelobe artefacts in the channels -20 and 0 km s^{-1}. Moreover, the C_2H emission stems mainly from two fine structure lines that might happen to overlapp in the same channel and location but denote different velocities. Each of the effects can produce

Table 3.4: *Molecular line ratio trends on larger regional scales (Credit: Moser et al. (2016b), reproduced with permission ©ESO.)*

Ratio	Regions								
	center	edge	mHVC	Triop	SEW	CND N&E	CND W	V-cloud	SEE
CS / C_2H	5 - 7 [5,12,20]	2 - 4	-	1 - 2	5 - 7 [SEW2]	1 - 3 [CND-10]	-	-	-
CS / SO	5 - 15 [4]	2	2 - 3	2 - 4 [T1]	5 - 8	2 - 4	-	-	-
CS / $H^{13}CO^+$	5 - 16	5	-	2 - 4	8 - 14	-	-	-	-
CS / SiO	5 - 17	-	2	3 - 5 [T9]	7 - 9	2 - 5	-	-	-
CS / HC_3N	6 - 9	3	-	6 - 7 [T4]	-	-	-	-	-
CS / CH_3OH(7–6)	4 - 11	4	-	-	-	-	-	-	-
C_2H / SO	1.3 - 2.1	1.2	-	1.5	1.0 - 1.6	-	-	-	-
C_2H / $H^{13}CO^+$	1.8 - 3.0 [3]	-	-	1.5	2.1 - 2.6	-	-	-	-
C_2H / SiO	2.2 - 2.6 [14]	-	-	-	1.1 - 1.9	-	-	-	-
SO / SiO	1.0 - 2.4	-	-	1.1	1.2 - 1.7	1.4	-	-	-
SO / $H^{13}CO^+$	0.7 - 1.9	-	-	1.2	1.7 - 2.3	-	-	-	-
SiO / $H^{13}CO^+$	0.6 - 1.7	-	-	1.2	1.6	-	-	-	-
$H^{13}CO^+$ / HC_3N	1.3 - 1.9	-	-	1.6	-	-	-	-	-
$H^{13}CO^+$ / CH_3OH(7–6)	1.0 - 1.6	0.7	-	-	-	-	-	-	-
CS / N_2H^+	-	-	-	2 - 4	-	1 - 7	2 - 8	-	-
CS / CH_3OH(8–7)	-	-	-	4 - 8	-	8	10 - 15	-	-
CS / ^{13}CS	-	-	-	5 - 7	28 - 33	4 - 8	8 - 13	-	-
N_2H^+ / $H^{13}CO^+$	-	-	-	0.6 - 1.3	-	1 - 2	0.8	-	-
N_2H^+ / CH_3OH(8–7)	-	-	-	1.3 - 2.5	-	2.3	1.3 - 2.1	1.0 - 1.7	4.0
N_2H^+ / ^{13}CS	-	-	-	2.3 - 2.5	-	1.9 - 3.2	1.0 - 1.6	-	3.9
^{13}CS / CH_3OH(8–7)	-	-	-	0.8	-	-	1.1 - 1.7	-	-

Notes. Ratios are obtained from a beam-sized aperture of 0.65″ centered onto the average position of all integrated emission line peaks in the corresponding region. For ratios with N_2H^+, CH_3OH(8–7), and ^{13}CS a beam-sized aperture of 1.5″ is used. SiO refers to the J = 6–5 transition of SiO. The regions comprise the following clumps (see Fig. A.10) listed in the Table A.5 in the Appendix: center: the bulk of the CA, clumps 1 - 16, 20; edge: edge of the CA, clumps 19, 21, 22; mHVC: high velocity molecular clouds, clumps 24 - 27; *Triop*: clumps T1 - T11; SEW: clumps SEW1 - SEW4; CND N&E: northern and eastern edge of the CND, clumps SEW8 - SEW13, CND1 - CND10; CND W: western CND, clumps CND-W1 - CND-W3; V-cloud: clumps V1 - V12; SEE: clumps SEB1 - SEB6. [(annotations)] regions that do not fall into the range of ratios an overestimate of the line flux. In contrast to the ratios above, the SiO(6–5)/$H^{13}CO^+$ ratio barely changes or -if at all - slightly drops towards the center.

There are several effects that could lead to the above described line emission behaviour: The strong IR to UV radiation from the NSC and the X-ray emission from a population of stellar remnants and the SMBH (e.g., Serabyn and Lacy 1985; Krabbe *et al.* 1991; Baganoff *et al.* 2003; Perez *et al.* 2015; Mori *et al.* 2015) pose extreme conditions to the ISM in the GC. Moreover, gravitational shear and winds from the NSC and the SMBH affect this region where the three minispiral streamers meet and interact. The resulting kinematics will produce magnetic fields in the ionized gas and shocks on all scales, severely impacting the ISM. Assuming the CA to be very close to the center, possibly an infalling CND clump, one can expect the stellar winds from the NSC to drive away a large portion of the gas to reduce the cloud to its densest cores and a diffuse intercloud medium. Consequently, the resulting density, temperature and overall chemistry structure in such an environment is very complex.

3.4.4.1 Excitation

In this section I speculate on possible relations between the gas properties and conditions in the central region and the observed molecular line ratios - and with this - the molecular excitation in the central region.

Among the molecules whose transition is detected in band 6, $H^{13}CO^+$ has the lowest upper state energy of $E_u/k_B \sim 25$ K and critical density of $n_c \sim 3 \times 10^6$ cm^{-3}. C_2H has the E_u/k_B, but requires twice the density of $H^{13}CO^+$ for thermalization. The critical density of the CS transition, which shows the brightest emission of all molecules in the center, is a bit lower than the former's, but the upper state energy is 35 K. The next higher upper state temperatures of $\sim$ 45 K have the SO and SiO transitions in band 6. SO requires densities similar to $H^{13}CO^+$, but SiO requires 8×10^6 cm^{-3}, which is one of the highest in band 6. A few regions have conditions ideal for high excitation transitions such as CH_3OH with an E_u/k_B of 70 and 80 K and critical densities of 0.6 - 1 $\times 10^6$ cm^{-3} and SiO with an E_u/k_B 75 K and a critical density of 2×10^7 cm^{-3}, which is the highest of the sample. The highest upper state energy of 165 K has the transition of HC_3N, which found in the same regions as the former two molecule.

The similar critical densities around 5×10^6 cm^{-3} suggest that the excitation of CS, C_2H, and $H^{13}CO^+$ might be governed by the temperature. In fact, Goto *et al.* (2014) obtained for a cloud towards IRS 3 a temperature of $T_k = (300 \pm 50)$ K and a density of $n_{H_2} \geq 10^4$ cm^{-3} from non-LTE radiation transfer models of H_3^+ and CO. This result fits well into the scenario of a small filling factor ensemble consisting of irradiated dense clouds/clumps (Goicoechea *et al.* 2013). While the kinetic gas temperature in the minispiral can be expected to be of the order of its dust temperatures of T_d = 150 - 300 K based on MIR/FIR dust observations (Gezari *et al.* 1985; Cotera *et al.* 1999; Lau *et al.* 2013) or higher, the clumps in the CND, especially in the SW lobe, are estimated to have temperatures and densities of $T_k \sim$ 100 - 500 K, $n_{H_2} \sim 10^{4.5}$ - $10^{6.5}$ cm^{-3} and T_d = 50 - 90 K (Mills *et al.* 2013; Requena-Torres *et al.* 2012; Lau *et al.* 2013).

Moreover, radiative trapping could be at work, if CS is abundant enough, letting the transition reach an apparent thermalization at densities up to 25 times lower than the critical density (Shirley 2015). Amo-Baladrón *et al.* (2011) determined abundance ratios in the GC of CS/$H^{13}CO^+$ ∼ 25-70 and SiO/$H^{13}CO^+$ ∼ 2-3. Therefore, $H^{13}CO^+$ emission is likely to be weak. Hints on the inner, denser cloud material could be given by SiO and SO based on their excitation but also their abundance.

In addition, the level population can be affected by IR pumping. In this case, the IR emission excites the lowest vibrational levels, which then decay to purely rotational states. In this way, higher levels become populated than predicted for the gas collisional excitation rate. Among the molecules Carroll and Goldsmith (1981) studied in this context, CS can be pumped most efficiently, followed by SiO and HCN with decreasing efficiency. The minimum dust temperature required for the IR pumping of CS is $T_\mathrm{d} \geq 114$ K. Consequently, pumping cannot take place further away from a dust embedded star ($L \sim 10^5 L_\odot$) than $r \lesssim 0.04$ pc = 1″. The neighbourhood of Sgr A* contains several dust embedded sources with dust temperatures > 200 K, i.e. IRS 1W, 3, 6, 7, 21, 29 (Gezari *et al.* 1985; Tanner *et al.* 2002, 2005; Moultaka *et al.* 2004a; Viehmann *et al.* 2006; Pott *et al.* 2008a,b), which appear to be surrounded by or embedded in CS emission. Furthermore, the inner r ∼ 5″ of the minispiral provides dust temperatures of $T_\mathrm{d} = 120 - 150$ K and the region between IRS 3 and 7 $T_\mathrm{d} = 105 - 135$ K (19μm/37μm colour temperature map; Lau *et al.* 2013). In a scenario where the molecular gas enshrouds and permeates the NSC and the minispiral, it becomes very likely that the hot dust impacts the CS SLED by IR pumping.

The existence of vibrationally excited HCN in a dense, shielded region in the SW lobe of the CND has already been proven by Mills *et al.* (2013). A stellar heating origin cannot be identified from the NIR Hubble Space Telescope (HST)-NICMOS images - it might be highly extincted. Obviously, the conditions are adequate for the populating the vibrational states of HCN in this clump. Therefore, they can be expected to be perfect in the center. This is supported by the difficulties of Goto *et al.* (2014) to simulate the CO SLED measured towards IRS 1W and IRS 3 based on radiative transfer. They proposed that IR pumping might skew the level population. However, (ro-)vibrational transitions from several molecular species (CS, HCN, SiO) need to be observed in this region to assess the importance of this effect.

3.4.4.2 Abundance

The edges of PDRs and diffuse ISM provide a high abundance of ionized sulphur in the gas phase, so that CS is the most abundant S-bearing species in these regions (PDR shell tracer, e.g. Lepp *et al.* 1988; Lucas and Liszt 2002; Goicoechea *et al.* 2006). In contrast to this, the CS abundance is low in dense clouds (e.g., Bergin *et al.* 2001; Di Francesco *et al.* 2002), because there, sulphur is bound in the progenitor molecules which are frozen out onto grains (Charnley 1997; van der Tak *et al.* 2003). Furthermore, X-ray emission increases the abundances of CS and SO in the gas phase as chemical modelling shows (Benz *et al.* 2007). Nevertheless, SO and SiO seems to be constant in the luminosity ratios over the entire central few pc. One interpretation could be that X-rays and/or IR pumping do not have a significant impact on the abundances and/or SLED, the other could be that there is an additional effect depleting these species compared to CS.

The photodissociation rates of SiO, SO, and CH_3OH indicate that these molecules are sensitive to UV radiation, only surpassed by HC_3N. In contrast, $H^{13}CO^+$ survives in a very strong UV-field and has a $\gtrsim$2 magnitudes lower photodissociation rate coefficient than the former molecules. C_2H and CS lie in between, but are rather as UV-sensitive as SiO, SO, and CH_3OH. The integrated emission maps show the emission of the UV-sensitive molecules to be constrained to the CS peaks. Apart from an excitation effects, this might imply a shielding effect of the gas layers from the UV-radiation.

The formation of CS, SO, SiO, CH_3OH is closely connected to grains: CH_3OH and the progenitors of CS and SO form on grains and grains are often composed of silicates (i.e. SiO) among others. These molecules or their progenitors pass into the gas phase either via evaporation at a molecule specific temperature or via sputtering by shocks. SiO is commonly used as a shock indicator, but the abundance raise of the other molecules can also hint at higher temperatures. An example could be the region west of IRS 3 which emits brightly in HC_3N and CH_3OH, moderately in $H^{13}CO^+$, but weakly in CS. The absence of SiO implies that shock chemistry is unlikely here. Instead, the region seems to be shielded from UV-radiation and warm enough for these molecules to exist in the gas phase so that their excitation and/or abundance enhancement can be attributed to a higher temperature in this region.

3.5 Nature of the molecular gas

3.5.1 Infrared dark clouds and methanol masers

In Figure 3.10 I overlayed a NIR HST NICMOS image with the map of the integrated N_2H^+ line emission. It reveals that the V-cloud and the SEE are consistent with large IRDCs of dust that are in the foreground of the GC and absorb the NIR radiation. This agreement fits well to the picture of IRDC: The main destruction path for N_2H^+ is the reaction with CO. N_2H^+ is expected to be abundant especially at temperatures of $T_k \lesssim 25$ K, when most of the CO is frozen out onto dust grains (Vasyunina *et al.* 2012). These temperatures are typical for IRDCs. The lack of bright emission from other molecules (see Sect. 3.3.3) indicates a depletion of them from the gas phase like in the case of CO and that these regions must be considerably colder than the CND. At the same time, the gas cannot be colder than $T_k \sim 15$ K (Vasyunina *et al.* 2012), because else the progenitor molecule N_2 freezes out and N_2H^+ cannot be formed. However, the relation between N_2H^+ emission and IRDCs is not always tight: For example, the IR dark clumps $\sim 30''$ north of Sgr A* display no N_2H^+ emission and the N_2H^+ line emission region $10''$ east of Sgr A* has no NIR absorbing dust counterpart. This suggests a complex interplay of cloud structure, irradiation, and from this, excitation, and abundance evolution.

The velocity of the V-cloud peaks at ~ 60 km s^{-1} in the east and ~ 0 km s^{-1} in the west, the velocity of the SEE at ~ 10 km s^{-1}. The line FWHMs are ~ 20 km s^{-1} (Martín *et al.* 2012). The ALMA data reproduces this behaviour taking the low spectral resolution into

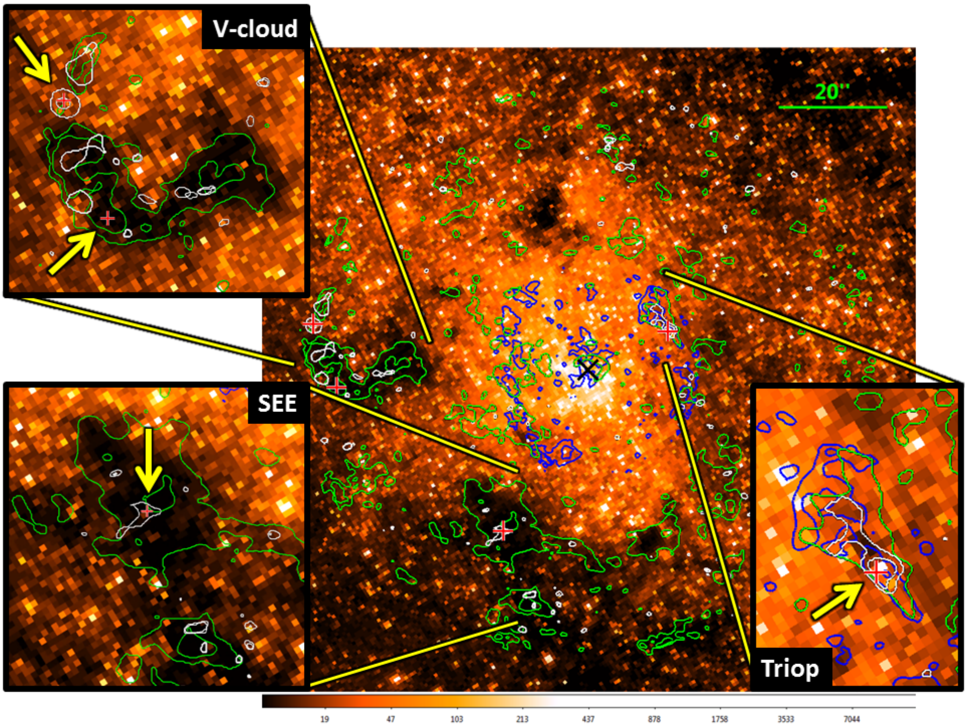

Figure 3.10: *Schematic view on the central $\lesssim$ 5pc. N_2H^+(1–0) is indicated by green contours of [4, 32] $\times\sigma$ (= 0.07 Jy beam^{-1} km s^{-1}), CS(5–4) shown as blue contours of [8, 48] $\times$ σ (= 0.08 Jy beam^{-1} km s^{-1}), and CH_3OH(8–7) indicated by white contours of [3, 6, 96] $\times$ σ (= 0.06 Jy beam^{-1} km s^{-1}) on a NIR HST NICMOS (1.87 μm) image (HST archive). Red crosses in the triop, SEE, and the V cloud show the class I methanol masers (see text) and the black cross Sgr A*. (Credit: Moser* et al. *(2016b), reproduced with permission ©ESO.)*

account. In terms of location and velocity, the two clouds match the 20 km s^{-1}- and 50 km s^{-1}-GMCs in the southeast and the east of the GC. They are more likely to be linked to them than to the CND, which shows only weak N_2H^+ emission.

The V-cloud and the SEE and the tiny dark cloud at the heart of the *triop* show class I CH_3OH maser emission at 36 and 44 GHz (see Section 3.3.3). Furthermore, the CH_3OH(8–7) transition, which can also be excited to maser emission (95 GHz class I maser, (e.g., Voronkov *et al.* 2012,and references therein), is detected towards the 36 GHz maser in the SEE, and the two 44 GHz masers in the *triop* and in the eastern edge of the V-cloud, where the CH_3OH(8–7) emission in the former two is much weaker and more extended than in the latter. The line widths of masers is typically very narrow with $\sim 1-2$ km s^{-1} (Yusef-Zadeh *et al.* 2001; Sjouwerman *et al.* 2010; Pihlström *et al.* 2011). Consequently, these ALMA observations discussed here cannot be used to test the maser activity in the CH_3OH(8–7) transition due to the low spectral resolution. However, the suspiciously bright point source

CH_3OH(8–7) emission at the 44 GHz masers in the V-cloud is best explained by 95 GHz class I maser activity. It is assumed that the pumping is achieved by collisions and shocks for class I methanol masers and in by FIR-radiation from star-forming regions for class II methanol masers. Class I masers at 36, 44 and - typically fainter - 95 GHz often occur at the same time, which hints at a common ISM and common excitation conditions for all three transitions (e.g., Fontani *et al.* 2010; McEwen *et al.* 2014; Kang *et al.* 2015). Optimal masing conditions for the 36 GHz and 44 GHz maser line emission together are $T_\mathrm{k} \gtrsim 50$ K and $n \sim 10^5 - 10^6$ cm^{-1} (from modelling of the methanol maser transitions; McEwen *et al.* 2014). The 44 GHz maser occurs in denser (and warmer) gas than the 36 GHz masers in the case of star-forming regions and vice versa in the case of supernova remnants (SNR; Pratap *et al.* 2008).

The cause of the shock triggered maser emission in the GC is not clear. On the one hand, the maser regions in the eastern rim of the V-cloud and the SEE coincide with strong and widespread SiO line emission only outmatched by the CND SW lobe. Such a large shock region could be generated by an impact of the supernova remnant (SNR) Sgr A East shell on the 20 km s^{-1} and 50 km s^{-1} - GMCs (Sato and Tsuboi 2008; Martín *et al.* 2012; Moser *et al.* 2014, 2017). On the other hand, small-scale shocks can be produced by outflows from YSOs. The V-cloud, the SEE, and the *triop* are cold and dense enough to form stars as the detection of N_2H^+ suggests and the 36 (SEE) and 44 GHz (V-cloud, *triop*) masers in these regions appear to lie within $r < 0.5''$ from a star or weak NIR source in projection. In conclusion, more line emission studies are required to analyse and understand the conditions and their causes in these regions.

3.5.2 High velocity clouds

In this section I discuss clouds with velocities extremer than the main CND range, i.e. -100 to 100 km s^{-1} which I termed high velocity clouds (see Sect. 3.3.5). For the two SiO(5–4) detected clumps YZ1-2 and YZ1, Yusef-Zadeh *et al.* (2013) obtained a velocity and width of $v \sim 148$ km s^{-1} and FWHM ~ 47 km s^{-1}, and $v \sim 136$ km s^{-1} and FWHM ~ 56 km s^{-1}, respectively. They propose them to be highly embedded protostellar outflows with $n_{\mathrm{H}_2} \sim 10^5 - 10^6$ cm^{-3} and $T_\mathrm{k} \sim 100 - 200$ K based on line transition modelling. The significantly higher spatial resolution reveals the SiO clumps YZ1-2 and YZ11 as elongated structures pointing at each other (see Fig. 3.6). On the one hand, the constellation resembles a double lobed outflow structure from an invisible source between the two SiO clumps, but the high but similar velocities do not support this scenario. They might be the single-sided outflow lobes originating from two independent sources as Yusef-Zadeh *et al.* (2013) suggested.

On the other hand, YZ1-2 has an filamentary/elongated shape that resembles a boundary outlining the NA edge. In this region, the EB, i.e., the vertical minispiral filament connecting the NA with the EA, and the NA meet with opposite proper motions: The x- and y-velocity components of the NA and the EB are $v_\alpha \sim$ -188 km s^{-1} and $v_\delta \sim$ -560 km s^{-1}, and $v_\alpha \sim 32$ km s^{-1} and $v_\delta \sim 360$ km s^{-1}, respectively (clumps X13 and K37, respectively, in Zhao *et al.* 2009). Furthermore, the radial velocities of the EB range from ~ 40 to 140 km s^{-1} and it

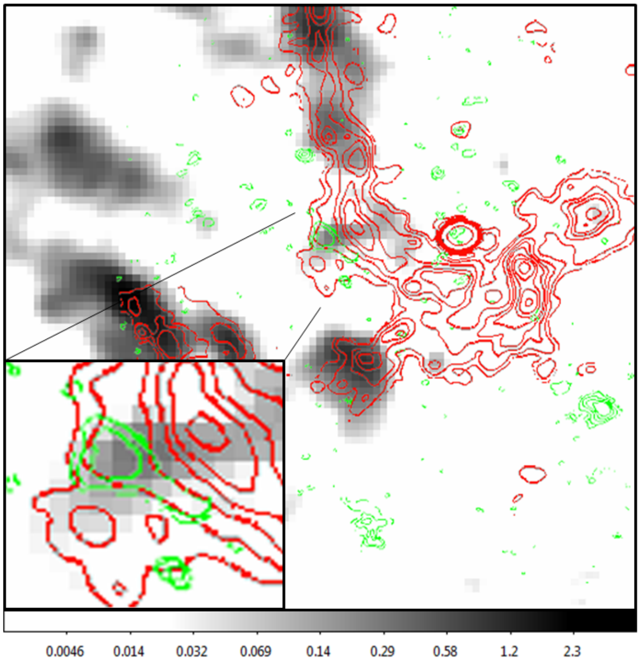

Figure 3.11: *130 km s^{-1} channel image of the Ne II line emission cube from Irons* et al. *(2012). Ionized emission appears at the high velocity SiO cloud YZ1-2 southwest of IRS 1W (arbitrary units). SiO(6–5) emission is shown in green contours as in Fig. 3.5 and the 250 GHz continuum in red contours as in Fig. 3.2. (Credit: Moser* et al. *(2016b), reproduced with permission ©ESO.)*

shows an emission component at 130 km s^{-1} right at the hypothetical boundary. The radial velocities of the NA are ~ 20 km s^{-1} (Fig. 3.11). The length of YZ1-2 roughly corresponds to the thickness of the main filament of the EB which looks like a link between the Tip and IRS 1W and comprises the K37 source from Zhao *et al.* (2009). At these high velocities, a frontal impact of the NA streamer and the EB filament can be expected to degrade the dust grains and molecules. Instead, if the two streamers scratched past each other, it could induce shock velocities in the cloud layers further inwards of the clouds that are suitable to sputter the grains and release or produce gas-phase SiO.

In the neighbourhood of the SiO clumps YZ1-2 and YZ11, I found three further clumps, which are detected in CS emission at similar velocities. The most eastern one appears to be related to YZ1-2, because there is weak CS emission at the SiO peak and brighter CS emitting clump 5″ northeast of YZ1-2, which also shows faint SiO emission in the same channels. This elongation of YZ1-2 to the northeast is also visible in the SiO data of Yusef-Zadeh *et al.* (2013). The southern CS clump lies between the minicavity and the Tip and the western CS clump north of IRS 6 in the Bar. Both are stretched and parallely aligned to each other. The southern CS clump coincides with ionized gas emission in the same channel, whereas for the western clump no other emission is detected, just as for the YZ11 cloud. Finding several clumps - maybe even with inclusion of the SiO clumps - within a radius of 10″ that roughly agree in velocities and line FWHM could imply a common origin. They might be the denser remains of an infalling and tidally disrupted cloud. Zhao *et al.* (1995); Karlsson *et al.* (2003); Donovan *et al.* (2006) suggested a similar scenario for the high negative velocity cloud detected in e.g. OH absorption and NH_3 emission around -180 km s^{-1}. However, earlier observations of Wright *et al.* (2001); Martín *et al.* (2012) give no information on a diffuser, extended counterpart to the ALMA HVC. Only the channel maps of Christopher *et al.* (2005) might show tentative detection of it.

3.5.3 Origin of the molecular gas in the central 20 arcseconds

In this section, I elaborate on the relation of the CA to other features in the GC. The region of the NSC containing young and hot He-stars and the SMBH Sgr A* poses such extreme conditions, that one expects molecules to dissociate into ionized elements. Nevertheless, molecular gas or even ice seems to have survived in the GC as it is suggested by past studies. For example, deep CO absorption has been detected towards IRS 3 and 7 (Geballe *et al.* 1989) and water and CO ice absorption have been found in the minispiral and towards the mass losing stars. This is possible because the crossing timescale of a freshly infalling or orbiting gas cloud through the NSC is shorter than the evaporation time scale and the dissociation time scale for the case that the cloud is shielded (Moultaka *et al.* 2004a, 2005, 2015a,b). Further hints on molecular gas extending towards Sgr A* are visible the CN (channel) map of Martín *et al.* (2012) and in the HCN(4–3) and CS(7–6) maps of Montero-Castaño *et al.* (2009). Goicoechea *et al.* (2013) conducted an extensive line study of the GC including CO transitions from J=4–3 to J=24–23 and assert that the line fluxes can be reproduced by either a single component with a temperature $T_{\rm k} > 1000$ K and a density $n_{\rm H_2} \leq 10^4$ cm^{-3} or by several comparably compact components with a lower temperature and a higher density, where the latter case is corroborated by the ALMA observations presented here.

Observations of H_2O ice, hydrocarbons, CO ice, and gaseous CO give details on the distribution of molecular gas and ices in the central minispiral region (NIR and MIR data; Moultaka *et al.* 2015a,b): The H_2O ice absorption is widespread in the entire minispiral region, whereas the gaseous CO and hydrocarbons absorption prevail in the dust filaments and the stars (CO). However, each of these species reaches high optical depths towards IRS 3, 7, 29 and the western part of the Bar. In contrast, solid CO absorption is confined to the dusty filaments between IRS 1W and the minicavity, IRS 21 and the IRS 2L region, and probably to IRS 3, 7, and 29. Most likely these regions are shielded enough to reach temperatures of T < 25 K so that CO can freeze out (Vasyunina *et al.* 2012).

The high optical depth gas and ice regions around IRS 3, 7, 29 and the western Bar show strong IR absorption by dust grains: Spectra of IRS 3 and IRS 7 have silicate absorption features and the corresponding dust grains seems to be of interstellar origin instead of being produced in the atmospheres of IRS 3 and IRS 7 (Pott *et al.* 2008b,a). The MIR images of Viehmann *et al.* (2006) reveal a silicate dust veil within the same region as the high optical depth molecular gas and ice. The SiO molecule detected in this region might stem from this veil and was released to gas phase by shocks, evaporation, UV radiation, or X-rays. The CS emission is cospatial with the IR ice, gas and dust absorption structures around IRS 3, 7, and 29, and part of the western Bar at positive velocities. Despite their high mass-loss, there is no clear evidence that the CA gas is mainly produced in the circumstellar envelope of, e.g., IRS 3 and IRS 7, because the distribution peaks of the gas and ice and do not match the positions of IRS sources, except from a CS peak on IRS 29. Instead, the CS gas seems to share a common origin with silicate dust, which needs to further investigated. The blueshifted part of the CS emission overlaps with the strong IR CO gas and ice absorption features in the dusty region between the minicavity, IRS 21, and IRS 1W, but not with the absorption region around IRS 2L. On the one hand, the agreement of the molecular gas emission and the minispiral RRL emission in position and velocity, i.e. around -40 to 0 km s^{-1}, be explained by a molecular cloud with an ionized outer layer or an interaction of a - not yet ionized - molecular gas streamer with the NA. On the other hand, the fact that the CS emission is not consistent with all IR ice and gas absorption regions in the minispiral rather negates a relation between them.

Regarding the kinematics, the strong absorption features in the higher transition levels of H_3^+ and CO in the NIR, that Goto *et al.* (2014) studied, peak for IRS 3 at about 50 and 60 km s^{-1}, respectively. A fainter absorption feature occurs around 45 km s^{-1}, which is, in fact, the only velocity component seen in the spectra towards IRS 1. This is consistent with the 50 km s^{-1} determined by Geballe *et al.* (1989) for the same sources, given the lower spectroscopic and spatial resolution. What is more, the observed line absorption towards IRS 1 appears from 0 to 40 km s^{-1} and the broad absorption in the range of 0 to 60 km s^{-1} is not only seen towards IRS 3, but also IRS 6 and 7, which is confirmed by the ALMA CS emission channel maps (Fig. 3.7). A further measurement comes from Martín *et al.* (2012): the clump 18, which corresponds in extent to the positive velocity CS emission outlined by Sgr A*, IRS 3, and 7, velocity peak at 46 km s^{-1} and an integrated emission peak towards IRS 7. In addition, this region has a second component at -77 km s^{-1} which is in agreement with the lower excitation CO absorption at -72 km s^{-1} around IRS 1, IRS 3, and IRS 16NE (Goto *et al.* 2014) and the molecular gas emission at or close to these sources in the -80 to -40 km s^{-1} channels of the ALMA band 6 data.

I suggest, that the H_3^+ and CO absorption, the sub-mm molecular gas emission, and - potentially - the silicate dust absorption happen in the same cloud which seem to be in front of or embed IRS 3 and 7. Its LOS position within the GC is unclear, and the only orientation from up to date data could be the LOS distance of IRS 3 and 7 to Sgr A* which are barely constrained. If the molecular gas is not produced in the atmospheres of the evolved stars in the NSC, as my results and discussion suggest, the CA cloud could be related to the CND instead: Goto *et al.* (2014) have shown that the CND velocities of the *triop* region correspond to the range of the positive velocity bulk of CA suggesting it to be an extension of the CND.

Another structure the CA could be related to is a streamer detected in OH absorption and so far unnoticed in other molecular lines (Karlsson *et al.* 2003, 2015).

It appears between -30 to 70 km s^{-1} and extends from the center to the southwest. The "head" peaks northwest from Sgr A* at 50 km s^{-1} and the "tail" beyond the SW lobe at $\sim$

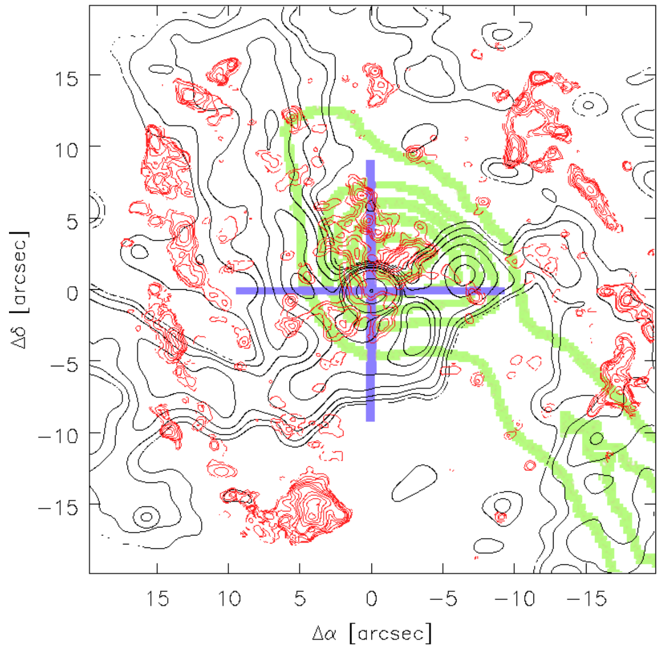

Figure 3.12: *Schematic view on the OH streamer in OH emission at 50 km s^{-1} in green contours with lowest level at~ 90 mJy beam^{-1} (~ 3.5σ) and steps of 1σ from Karlsson* et al. *(2015). Black contours show the 100 GHz continuum emission as in Fig. 3.2, red contours indicate the CS(5–4) emission as in Fig. 3.5, and the blue cross indicates Sgr A*. The shape of the streamer head resembles the distribution of the CS clumps. (Credit: Moser* et al. *(2016b), reproduced with permission ©ESO.)*

70 km s^{-1}. It is tentatively visible in the CS(1–0) channel maps of Liu *et al.* (2012) and (Karlsson *et al.* 2015) discover its denser part in form of a single clumps in the CN data of Martín *et al.* (2012). The CS emission detected by ALMA shows as thin and short extension across the western Bar along the streamer (Fig. 3.12). The distributions of the OH absorption of the head and the CS emission are centered on Sgr A* within -30 and 15 km s^{-1} and show an wide extension to the southeast at ~0 km s^{-1}.

These agreements suggest that the two molecular species trace different aspects of the very same source - at least for the redshifted line part. The 1665 and 1667 MHz transitions of OH can already be excited in diffuse gas. If the source is a tidally stretched cloud, the high density tracers (e.g. HCN, HCO$^+$, CS) would only be tentative visible towards a few high density clumps so that the streamer tail is not obvious from their emission. The CS emission towards the OH-streamer head implies a higher density than in the tail. An interpretation could be that the head represents the dense core of the infalling cloud, or a compression region due to the stellar winds and collisions with the other gas streamers, or a combination of both. SiO emission peaks towards the CS emission peaks within the region between Sgr A*, IRS 3, and 7, might hint at such shocks, but could also be produced by the strong X-ray and UV radiation field.

The CA gas at negative velocities might indicate that the OH-streamer is on an orbit so that the orientation, the eccentricity, and the periapse distance of the orbit would determine the excitation and ionization properties of the gas. On the one hand, an interaction of the streamer with the NA resulting in a gas entrainment by the NA might give a reason for the agreement in projected location and velocity of the molecular and ionized gas. On the other hand, the NA does not show any SiO emission at negative velocities except towards the SiO maser stars. The peaks in CS emission integrated over positive velocities in the center are twice as bright as in the peaks of CS emission integrated over negative velocities. If the SiO emission behaves in the same fashion, its emission peak would be below the rms level of this observation. If the streamer gas is not dragged along the NA flow after the impact onto the NA, it could have slowed down to settle in a disk providing material to the central 10″ (0.4 pc) and maybe to the counterclockwise disk (Paumard *et al.* 2006; Bartko *et al.* 2009, 2010; Lu *et al.* 2009).

The questions on the links between the sources and the kinematics and dynamics in the GC make proper motion studies of the streamer and CA gas absolutely essential. Zhao *et al.* (2009, 2010), for example, collected RRL data within an epoch of ~ 15 yr and was able to reproduce the minispiral streamers as Keplerian orbits around Sgr A*. A similar campaign is necessary to finally obtain a 3D model of the molecular gas in the CND and the cavity.

3.6 Summary

I have presented ALMA Cycle 0 observations of Sgr A* and its environment in band 3, 6, and 7 corresponding to 100, 250, and 340 GHz. They have a velocity resolution of 15-50 km s^{-1} and a for this region unprecedented angular resolution of 0.5 - 1.5″. Apart from the continuum emission in all three bands, I identified 11 molecular line transitions and 5 RRL transitions and several interesting regions and features. In the following, I summarize my main results:

Continuum and RRL emission: The 100 GHz continuum and the H39α emission trace the minispiral in its overall extent and indicate a relatively uniform electron temperature around $T_e \sim 6000$ K. At 250 and 340 GHz, the continuum emission outlines the minispiral filaments and IRS sources at a resolution < 0.75″ for the first time in the sub-mm domain. Sgr A* has a spectral index of ~ 0.5 at 100 - 250 GHz and ~ 0.0 at 230 - 340 GHz. Towards the compact and high S/N sources in the GC I find a spectral index of about -0.1 indicating Bremsstrahlung emission. In the NA and EA, the dust emission contributes to the continuum emission as suggested by the positive spectral index.

Molecular line emission: For first time, it is possible to detect and resolve sub-mm molecular line emission in the inner 20″ of the GC. ALMA has revealed a CA of CS line emitting clumps whose emission bulk resides at positive velocities in a region outlined by the Bar, the

NA, and the sources IRS 3 and 7. At certain negative velocities ranges, the RRL emission partly overlaps with molecular gas emission form the CA, but a clear relation to the minispiral cannot be seen. Fainter molecular emission, such as from SO, SiO, $H^{13}CO^+$, is detected rather towards the CS emission peaks only.

My results and previous OH absorption studies suggest the CA to be an infalling cloud composed of denser cloud cores surrounded by diffuse gas. I calculated three times higher CS/X (X: any other observed molecule) ratios for the CA than for the CND which hints at a combination of higher excitation - by a temperature gradient and/or IR-pumping - and abundance enhancement due to UV- and/or X-ray emission. Assuming the nuclear stellar cluster as the cause, CA must be closer to the center than the CND is to the center. Furthermore, I discovered emission at unexpectedly high velocities. I identified few SiO and CS clumps appearing in a range of 100 to 200 km s^{-1}. Previous studies suggested the SiO clumps to be protostellar outflows from YSOs. However, the similar velocities and widths could imply a relations between SiO and CS clumps, such as being the remnants of a tidally disrupted cloud.

Within the CND itself, I discerned two interesting regions: The *triop* is lies in the CND to the northwest of Sgr A*. It emits in lines of almost all molecular species and higher energy levels observed in this and earlier studies. ALMA has resolved its filamentary structure for the first time. Furthermore, it contains a methanol class I maser and emission of high upper state energies transition, such as HC_3N(26–25) with $T_u \sim 160$ K. Apparently, conditions typical for hot core chemistry and early stages of star formation are met here. The SEW at the northwestern tip of the CND SE has CS/X ratios significantly higher than the CND, but slightly lower than the center. The emission from different molecules is aligned in a apparently layered structure perpendicular to the direction to the SMBH. It could be due to an impact of the radiation and/or the stellar winds from the NSC. Beyond the CND region, I discovered that the largest accumulations of traditionally quiescent gas tracer N_2H^+ match the largest IR dark clouds in the field. The previously detected methanol class I masers in these IRDCs coincide with the methanol emission observed by ALMA and are probably excited by large scale shocks from the shell of the SNR Sgr A East.

IRDCs are cradles for stars and the N_2H^+ detected IRDC presented here could be ideal candidates for harbouring prestellar cores and with this for the investigation of the earliest stages of star formation in such a turbulent environment as the GC.

Outlook: ALMA has revealed a compilation of intriguing regions with characteristics different from an average CND cloud and which are worthwhile becoming subject to dedicated studies. The line ratios I obtained prove a trend to more extreme conditions for the molecular gas emission the close it is to the center in projection. The density and temperature structure of the gas clouds in such a violent region is complicated and requires observations of multiple transitions per tracer molecule (e.g. density, PDR, etc.) comprising a wide range of J-levels to sample the molecule specific excitation ladder. Such a study should also include vibrationally excited CS, SiO or HCN transitions to assess the importance of IR-pumping for the level populations. Atomic line emission should be detectable towards the transition regions from molecular to ionized gas and can help give orientation on the relations between the features and their gas state. For a robust line modelling, a much higher spectral resolution than given in this ALMA data is necessary. In order to understand the arrangement, kinematics, and distances of the molecular and neutral gas clouds to Sgr A*, it is essential to follow the gas proper motions over decades. The warmer *triop* and the colder IRDCs seem to provide good conditions for hydrocarbons as the detection of CH_3OH, HC_3N and H_2CO imply. Follow-up observations of more complex hydrocarbons - and possibly deuterated species - will help to assess the density and temperature dependent core chemistry and might shed light on the mystery of (recent) star formation in the turbulent and molecule dissociating GC. Eventhough, the data was taken by ALMA in early science Cycle 0, the high capabilities of the array are already outstanding. ALMA full array observations will usher the GC research in a new era.

CHAPTER 4

Summary and Outlook

I have analyzed the molcular gas content of theree Seyfert galaxies and in the center auf the Milky Way.

The results from my study on the Seyfert galaxies The majority of the molecular gas is concentrated within less than 1.8 kpc and all three objects show indications of a kinematically decoupled central unresolved molecular-gas component. Apart from giving ranges and limits for the gas, dust, and dynamical masses, I find these galaxies to have peculiar ^{12}CO/^{13}CO(2–1) > 20 and ^{12}CO(3–2)/(1–0) ~ 1 line ratios at their centers, similar to starbursts and (ultra)luminous infrared galaxies ((U)LIRGs), implying higher temperatures and stronger turbulence. These results are confirmed by LIRG typical infrared luminosities and starburst typical surface densities of gas and star formation rate (SFR) that I derive from my CO masses and the publicly available mid-infrared data. I conclude that the interstellar medium in the centers of these LIRG Seyferts is strongly affected by violent star formation resulting in a non-negligible amount of diffuse gas.

The results from my study on the GC The ALMA data needed post-standardcalibration-flagging and an additional sophisticated procedure of self-calibration on phase and amplitude before imaging in order to remove residual side lobe artefacts due to the flux variability of Sgr A*. After a detailed inspection, the ALMA archive data turn out to be quite sensational in several ways. First, I obtain the very first 340 GHz continuum image of the minispiral, i.e. the ionized gas and dust streamers that seem to connect the CND to the center. Second, it is at a resolution of 0.5″ - the highest for this feature in this wavelength regime - and clumps, stars and filaments are partly resolved. Third, I present the very first high resolution images

(<0.7″ at 250/340 GHz) of molecular line emission in the immediate vicinity of Sgr A* (<0.04 pc) and the nuclear stellar cluster, proving that the central cavity is not devoid of molecular gas. Mapping of this specific distribution in the sub-mm this clearly is a novelty that has not been reported before. Fourth, this central association of molecular gas seems to be higher excited than the gas in the CND indicating a strong feedback from the NSC and the SMBH, and/or turbulence, and tidal shear. This probably infalling cloud might be involved in a past, recent or upcoming feeding event. Fifth, I find regions showing emission from methanol lines that require upper state energies 70 K. They are coinciding with Class I methanol masers that might indicate early stages of star formation. Therefore, the ALMA data confirms the presence of warm molecular gas.

General outlook In both datasets, I dealt with molecular gas components that are the opposite of quiescent and virialized. They seem to be quite common in AGN and are able to dominate the centers or even the whole galaxy. We need molecular gas emission data of further galaxies of our LLQSO sample to enlarge our statistical basis. For the investigation of the distribution and the kinematics a CO transition is sufficient, but for determining the excitation of the molecular gas, several CO transitions, their isotopologues, and maybe a higher density tracer such as HCN are mandatory. The closest and brightest LLQSOs could be tested for polarized emission.

The ALMA data has shown a large variety of information and revealed a compilation of intriguing regions with properties different from an average CND cloud and which deserve further investigation. In contrast to the LIRG Seyferts I analysed, the excitation extremes seen in the ALMA data act on small scales - i.e. a clumplet in a confined region. More observations at same scales or higher and at higher excitation levels are needed to understand the physics dominating the clumps as well as their fate within this "gas-hostile" environment of the SMBH also with respect to star formation.

ALMA is the perfect instrument for continuing the two projects.

APPENDIX

A

Appendix for Chapter 3

A.1 Additional images

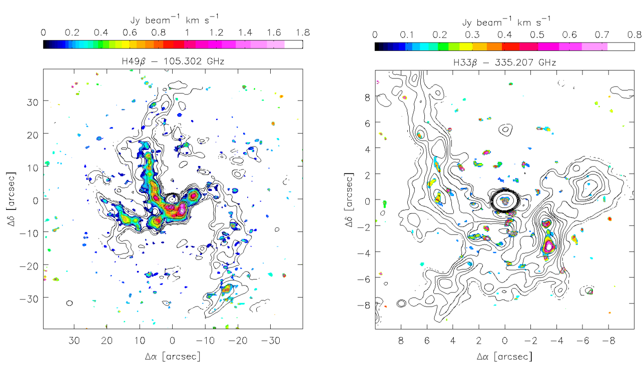

Figure A.1: *Recombination line (RRL) emission images of the inner $\lesssim 3$ pc. Left: H49β with the 100 GHz continuum contours as in Fig. 3.2. Right: H33β with the 250 GHz continuum contours as in Fig. 3.2. (Credit: Moser* et al. *(2016b), reproduced with permission ©ESO.)*

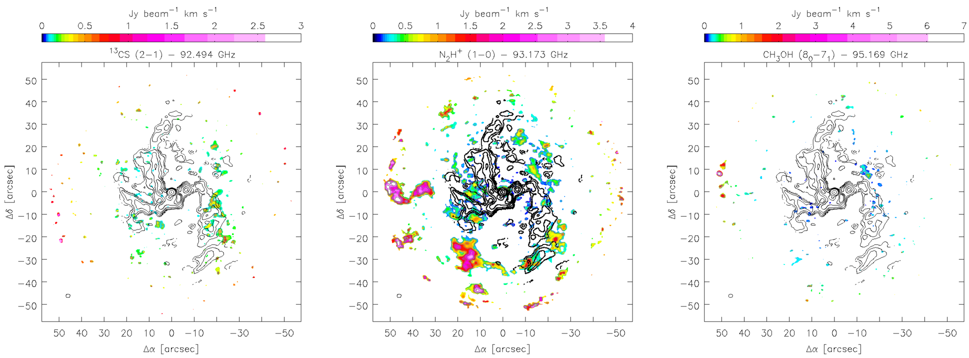

__Figure A.2:__ Molecular line emission images of the inner 120″ (4.8 pc) from left to right: ^{13}CS(2–1), N_2H^+(1–0), and CH_3OH(8–7). The contours at the levels of [6, 12, 24, 48, 96, 144, 192, 384, 1920, 4800]×σ (= 0.5 mJy beam^{-1}) show the 100 GHz continuum emission. (Credit: Moser et al. (2016b), reproduced with permission ©ESO.)

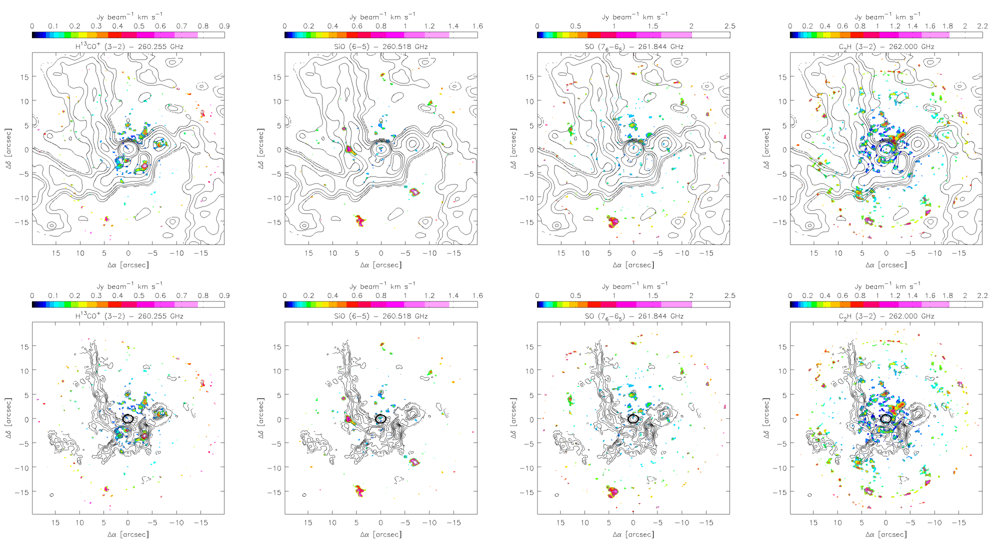

__Figure A.3:__ Molecular line emission images of the inner 40″ (1.6 pc) compared to the 100 GHz (top) and 250 GHz (bottom) continuum emission (as in Fig. 3.2): From left to right: $H^{13}CO^+$(3–2), SiO(6–5), SO(7–6), and C_2H(3–2) as in Fig. 3.5. (Credit: Moser et al. (2016b), reproduced with permission ©ESO.)

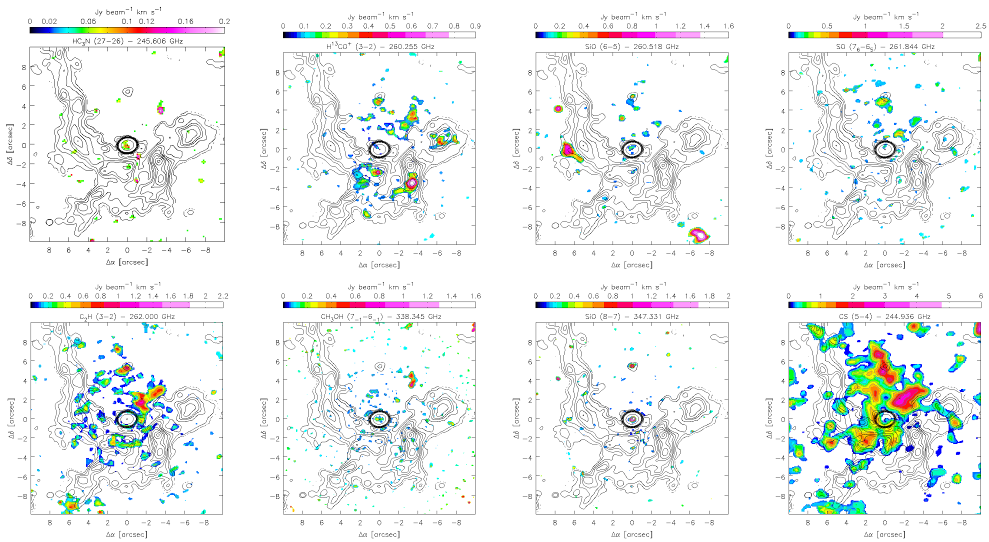

Figure A.4: *Molecular line emission images of the inner 20″ (as in Fig. 3.5) compared to the 250 GHz continuum emission in contours (as in Fig. 3.2). Top row (from left to right): HC_3N(27–26), $H^{13}CO^+$(3–2), SiO(6–5), and SO(7–6). Bottom row (from left to right): C_2H(3–2), CH_3OH(7–6), SiO(8–7), and CS(5–4). (Credit: Moser et al. (2016b), reproduced with permission ©ESO.)*

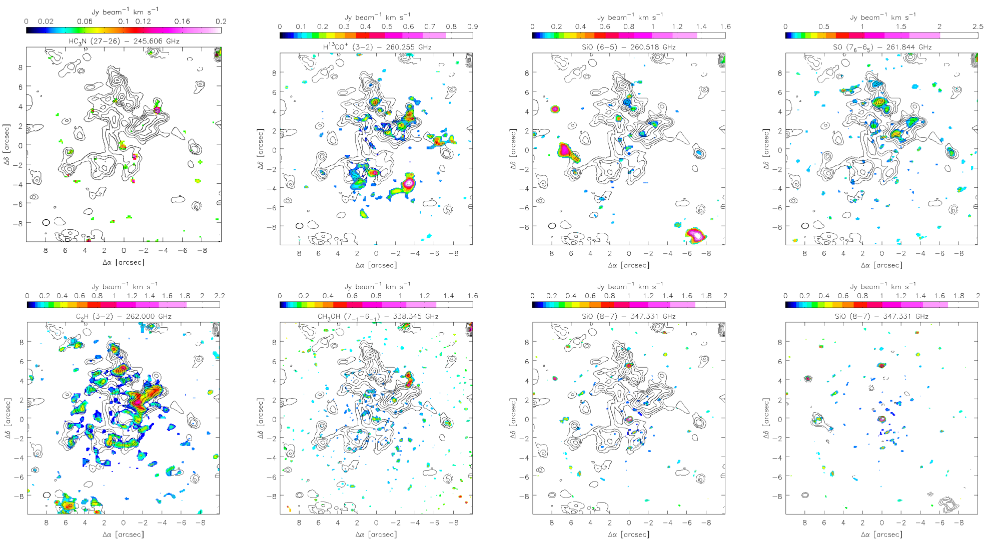

Figure A.5: *Molecular line emission images of the inner 20″ (as in Fig. 3.5) compared to the CS(5–4) emission in contours (as in Fig. 3.5). Top row (from left to right): HC_3N(27–26), $H^{13}CO^+$(3–2), SiO(6–5), and SO(7–6). Bottom row (from left to right): C_2H(3–2), CH_3OH(7–6), and two times SiO(8–7). The image at the bottom right corner shows SiO(6–5) contours at [2, 4, 8, 12, 16]×σ (= 0.08 Jy beam^{-1} km s^{-1}) for comparison. (Credit:* Moser et al. *(*2016b*), reproduced with permission ©ESO.)*

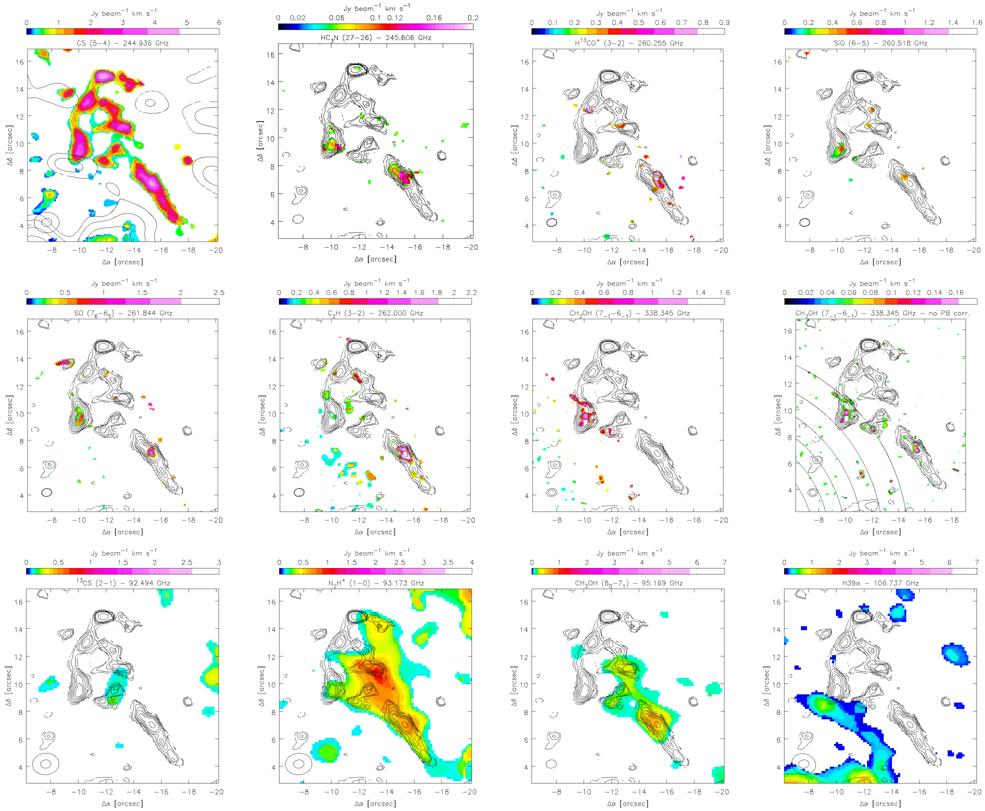

Figure A.6: *Triop in the light of molecular line, RRL and continuum emission: Top row (from left to right): CS(5–4), HC_3N(27–26), $H^{13}CO^+$(3–2), and SiO(6–5) (all as in Fig. 3.5). Middle row (from left to right): SO(7–6), C_2H(3–2), and CH_3OH(7–6) (all as in Fig. 3.5), and CH_3OH(7–6) when not corrected for primary beam (PB) with PB contours of 10% (outmost ring segment) to 60% (lower left corner), to show the full extend of the emission within the triop. Bottom (from left to right): ^{13}CS(2–1), N_2H^+(1–0), and CH_3OH(8–7) (all as in Fig. 3.4), and H39α (all as in Fig. 3.3). Contours show the CS(5–4) emission (as in Fig. 3.5), except from the top outer left, which shows contours of the 100 GHz continuum emission as in Fig. 3.2. (Credit:* Moser et al. (2016b)*, reproduced with permission ©ESO.)*

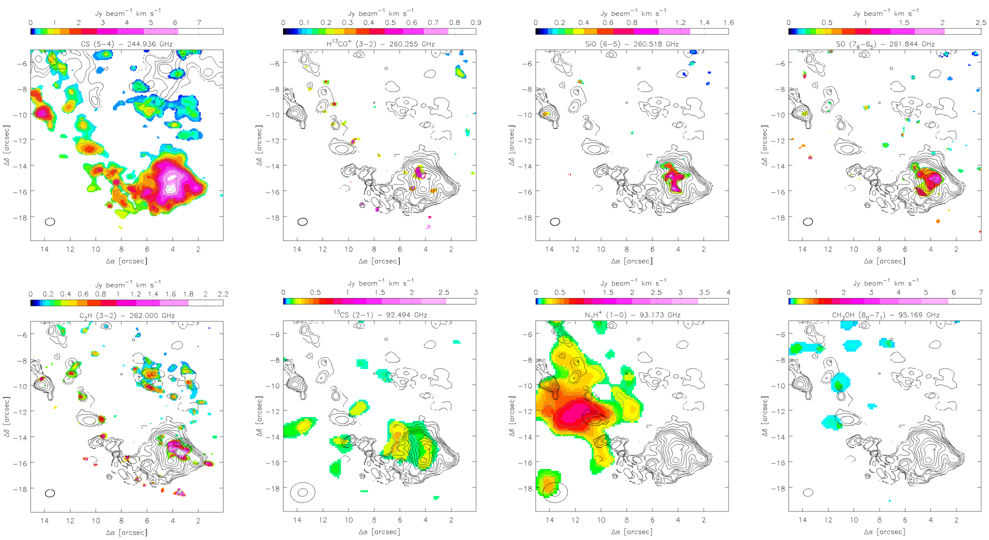

Figure A.7: *SEW cloud in the light of molecular line and continuum emission: Top row (from left to right): CS(5–4), $H^{13}CO^+$(3–2), SiO(6–5), and SO(7–6) (all as in Fig. 3.5). Bottom - from left to right: C_2H(3–2) (as in Fig. 3.5), and ^{13}CS(2–1), N_2H^+(1–0), and CH_3OH(8–7) (all three as in Fig. 3.4). Contours show the CS(5–4) emission (as in Fig. 3.5), except from the top outer left, which shows contours of the 250 GHz continuum emission as in Fig. 3.2. (Credit: Moser* et al. *(2016b), reproduced with permission ©ESO.)*

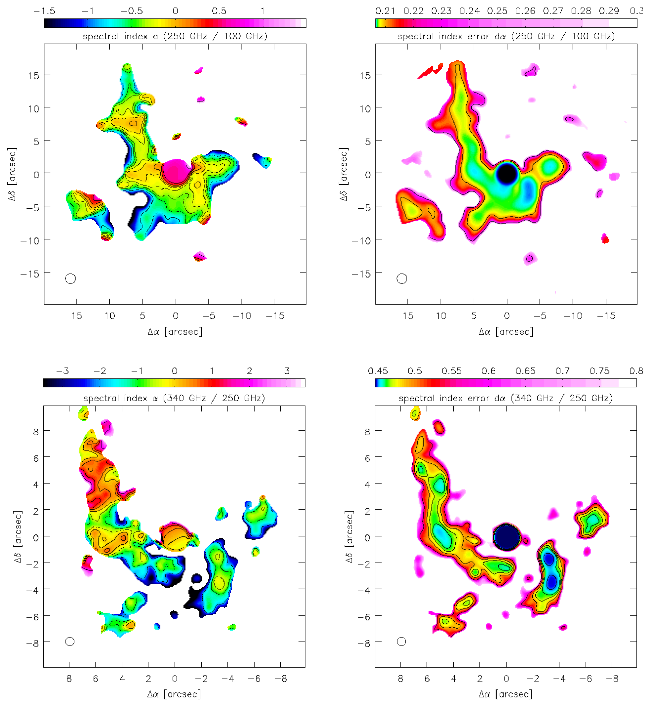

__Figure A.8:__ Continuum emission images of the inner $\lesssim$ 3 pc. Top: Between 100 and 250 GHz (inner 40″) tapered to a resolution of 1.5″. From left to right: Spectral index with contours of [-0.75, -0.5, -0.375, -0.25, -0.125, 0, 0.25, 0.5, 1, 1.5], error of the spectral index with contours of [2.068, 2.073, 2.1, 2.4] $\times$ 0.1, and spectral index overlayed with error contours. Bottom: Between 250 and 340 GHz (inner 20″) tapered to a resolution of 0.65″. From left to right: Spectral index with contours of [-2,-1, -0.5, 0, 0.5, 1, 2], error of the spectral index with contours of [4.6, 4.7, 4.9, 5.5] $\times$ 0.1, and spectral index overlayed with error contours. (Credit: Moser et al. *(2016b), reproduced with permission ©ESO.)*

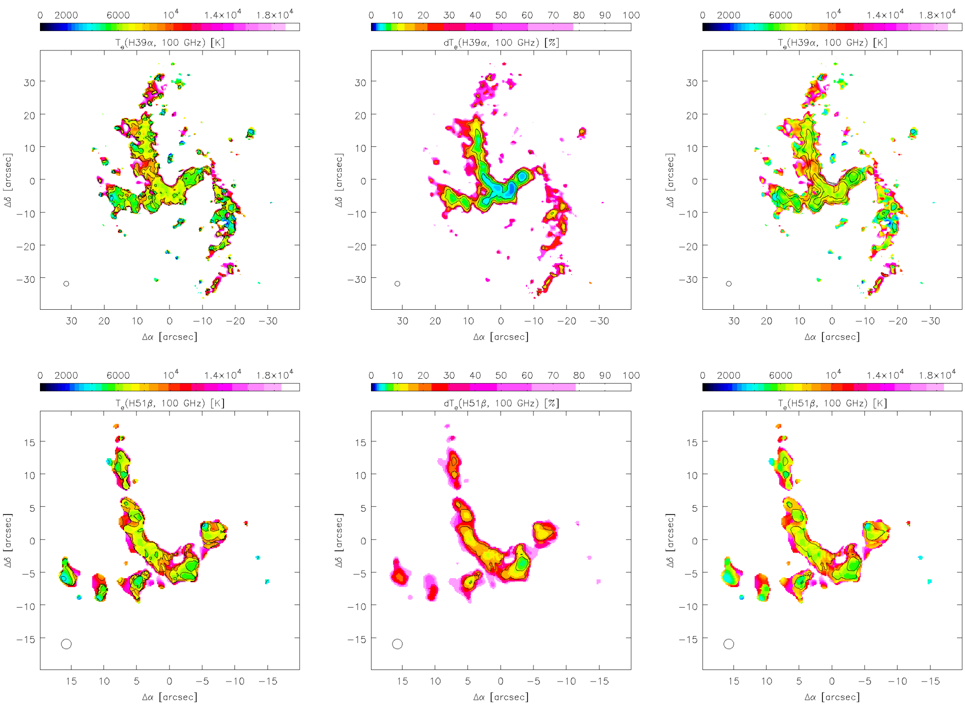

Figure A.9: *Images of the electron temperature distribution in the inner $\lesssim$ 1.6 pc. Top: Based on H39α (inner 40″) and tapered to a resolution of 1.5″. From left to right: T_e with contours of [4,6,8,10] × 1000 K, ΔT_e with contours of 5, 10, and 20%, and T_e overlayed with ΔT_e contours. Bottom: Based on H51β (inner 20″) and tapered to a resolution of 1.5″. From left to right: T_e with contours of [4,6,8,10] × 1000 K, ΔT_e with contours of 5, 10, and 20%, and T_e overlayed with ΔT_e contours. (Credit: Moser* et al. *(2016b), reproduced with permission ©ESO.)*

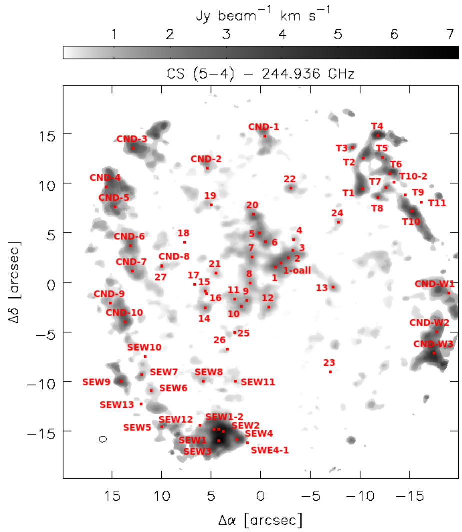

Figure A.10: *Finding charts for the clumps in the inner 40″ (1.6 pc) based on the CS(5–4) emission. (Credit: Moser* et al. *(2016b), reproduced with permission ©ESO.)*

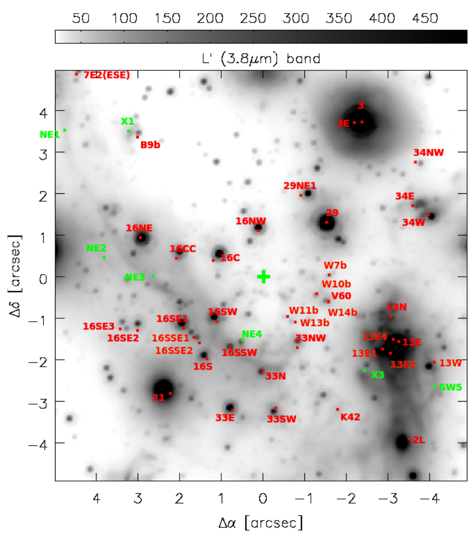

Figure A.11: *Finding charts for the stars and filaments Paumard* et al. *(2006); Viehmann* et al. *(2006); Mužić* et al. *(2007) mentioned in this work, demonstrated for the inner 10″ (0.4 pc) on a NIR L' (3.8 µm) emission image (Sabha, private communication, here: arbitrary units). (Credit: Moser* et al. *(2016b), reproduced with permission ©ESO.)*

A.2 Source positions and fluxes

Table A.1: *Results of 2D Gauss fits to the continuum sources: Source positions are relative to $17^h40^m00.00^s$ and $-29°00'00.00''$(J2000). (Credit: Moser* et al. *(2016b), reproduced with permission ©ESO.)*

region	band	peak position		deconvolved size			flux			
		R.A.	Dec.	d_{maj}	d_{min}	PA	S_{peak}	S_{int}	S_{base}	
	[GHz]	[^{s}]	[$''$]	[$''$]	[$''$]	[°]	[mJy beam^{-1}]	[mJy]	[mJy beam^{-1}]	
3	250^n	39.866 ± 0.003	24.538 ± 0.042	0.87 ± 0.19	0.70 ± 0.22	25 ± 72	1.5 ± 0.1	3.77 ± 0.49	0.01 ± 0.01	
	250^u	39.857 ± 0.005	24.516 ± 0.060	0.58 ± 0.15	0.56 ± 0.14	45 ± 354	1.6 ± 0.4	1.96 ± 0.79	−0.02 ± 0.03	c
	340^n	39.867 ± 0.003	24.496 ± 0.030	0.47 ± 0.90	0.37 ± 0.55	50 ± 25	1.4 ± 0.2	1.22 ± 0.38	−0.27 ± 0.02	
5S	250^n	40.753 ± 0.005	20.434 ± 0.059	1.12 ± 0.19	0.60 ± 0.06	46 ± 7	2.2 ± 0.3	3.57 ± 0.73	1.64 ± 0.06	
	250^u	40.763 ± 0.003	20.231 ± 0.033	0.53 ± 0.88	0.50 ± 0.76	69 ± 82	3.7 ± 0.6	3.70 ± 1.00	0.85 ± 0.07	c
	340^n	40.744 ± 0.002	20.538 ± 0.020	0.49 ± 0.11	0.27 ± 0.13	58 ± 29	4.9 ± 0.4	8.40 ± 1.10	−1.09 ± 0.39	
5SE1/X7	100^u	40.834 ± 0.006	20.960 ± 0.054	0.90 ± 0.35	0.58 ± 0.50	99 ± 84	6.5 ± 0.7	8.90 ± 1.60	5.94 ± 0.73	
	250^n	40.857 ± 0.004	21.022 ± 0.053	0.75 ± 0.19	0.26 ± 0.26	29 ± 22	5.2 ± 0.7	9.00 ± 1.80	0.86 ± 0.07	
	250^u	40.852 ± 0.003	21.148 ± 0.052	0.80 ± 0.15	0.49 ± 0.61	38 ± 10	4.7 ± 0.7	7.10 ± 1.70	0.65 ± 0.05	
	340^n	40.861 ± 0.003	21.121 ± 0.027	0.48 ± 0.17	0.14 ± 0.14	60 ± 31	6.4 ± 0.9	9.70 ± 2.00	−0.67 ± 0.17	
16NE	250^n	40.267 ± 0.002	27.343 ± 0.024	0.56 ± 0.13	0.39 ± 0.28	20 ± 58	6.1 ± 0.4	9.60 ± 1.00	−0.32 ± 0.03	
	250^u	40.261 ± 0.000	27.324 ± 0.001	0.50 ± 0.01	0.38 ± 0.01	110 ± 2	6.5 ± 0.0	11.12 ± 0.06	−1.78 ± 3.81	
	340^n	40.261 ± 0.000	27.243 ± 0.003	0.29 ± 0.02	0.20 ± 0.03	136 ± 12	5.2 ± 0.1	6.70 ± 0.14	−0.85 ± 1.00	
16SW	250^u	40.137 ± 0.002	29.050 ± 0.023	0.56 ± 0.13	0.27 ± 0.20	50 ± 23	2.2 ± 0.2	3.65 ± 0.48	0.54 ± 0.40	
	340^n	40.138 ± 0.003	29.092 ± 0.028	0.62 ± 0.11	0.35 ± 0.36	57 ± 7	1.0 ± 0.1	1.09 ± 0.26	0.13 ± 0.03	
16SE2	250^u	40.253 ± 0.002	29.505 ± 0.025	0.78 ± 0.11	0.69 ± 0.11	45 ± 52	6.5 ± 0.4	19.90 ± 1.70	0.13 ± 1.77	20

Notes. Annotations: Sources without a letter before the number denote IRS sources. K and X sources are taken from Zhao *et al.* (2009), V sources from Viehmann *et al.* (2006), and SW, NE, and MX sources from Mužić *et al.* (2007). Sources with A (ALMA) are detected for the first time with this observation. u and n stand for "uniform" and "natural" weighting of the data, c for "convolved source size" (deconvolution not possible), d for "devoured" (hidden in Gauss wings from neighboring strong sources), numbers in the last column for the percentage of deviation or overestimate from the real source size and shape (also affecting integrated fluxes) estimated by visual inspection. These deviations are due to either overlapping of multiple sources, deviation from 2D Gaussian distribution, or very weak sources in a diffuse background. For details on the procedure see Sect. 3.2.4.

Table A.1: *Continued. Results of 2D Gauss fits to the continuum sources: Source positions are relative to 17^{h}40^{m}00.00^s and −29°00′00.00″(J2000). (Credit: Moser* et al. *(2016b), reproduced with permission ©ESO.)*

region	band	peak position		deconvolved size			flux			
		R.A.	Dec.	d_{maj}	d_{min}	PA	S_{peak}	S_{int}	S_{base}	
	[GHz]	[^{s}]	[″]	[″]	[″]	[°]	[mJy beam^{-1}]	[mJy]	[mJy beam^{-1}]	
	340^n	40.253 ± 0.001	29.442 ± 0.016	0.78 ± 0.06	0.39 ± 0.05	49 ± 5	4.7 ± 0.2	12.42 ± 0.81	0.44 ± 0.06	20
20	250^n	39.905 ± 0.002	34.618 ± 0.020	1.12 ± 0.08	0.62 ± 0.06	129 ± 6	5.7 ± 0.3	15.90 ± 0.95	0.16 ± 0.04	
	250^u	39.903 ± 0.006	34.690 ± 0.038	0.89 ± 0.24	0.35 ± 0.17	108 ± 14	3.4 ± 0.5	7.80 ± 1.70	−0.15 ± 0.08	
34SW	250^n	39.742 ± 0.004	26.627 ± 0.025	0.91 ± 0.13	0.53 ± 0.05	73 ± 6	2.3 ± 0.3	2.68 ± 0.51	2.64 ± 0.17	c
	250^u	39.737 ± 0.005	26.592 ± 0.023	0.75 ± 0.14	0.43 ± 0.05	80 ± 8	2.6 ± 0.4	3.18 ± 0.78	0.97 ± 0.09	c
	340^n	39.738 ± 0.003	26.561 ± 0.016	0.73 ± 0.10	0.35 ± 0.07	86 ± 8	3.2 ± 0.3	7.40 ± 0.82	−1.47 ± 0.08	
35	250^u	40.299 ± 0.002	29.947 ± 0.018	1.02 ± 0.07	0.66 ± 0.06	58 ± 8	5.9 ± 0.3	21.70 ± 1.30	0.17 ± 0.28	30
	340^n	40.288 ± 0.003	30.034 ± 0.025	0.91 ± 0.12	0.43 ± 0.08	65 ± 8	3.8 ± 0.3	11.60 ± 1.30	0.62 ± 0.04	40
A1	250^n	40.575 ± 0.002	29.639 ± 0.023	0.68 ± 0.92	0.49 ± 0.24	28 ± 10	2.1 ± 0.1	3.29 ± 0.31	1.75 ± 0.04	20
	250^u	40.579 ± 0.010	29.723 ± 0.122	0.95 ± 0.50	0.45 ± 0.35	44 ± 28	2.2 ± 0.7	6.30 ± 2.50	0.54 ± 0.03	
	340^n	40.547 ± 0.001	29.867 ± 0.010	0.73 ± 0.04	0.47 ± 0.03	144 ± 5	2.4 ± 0.1	6.57 ± 0.26	−0.21 ± 0.17	
AF/AHH	250^n	39.545 ± 0.001	35.111 ± 0.011	0.38 ± 0.91	0.32 ± 0.11	108 ± 88	3.7 ± 0.2	4.82 ± 0.33	−0.12 ± 0.22	
	250^u	39.541 ± 0.001	35.150 ± 0.013	0.58 ± 0.43	0.45 ± 0.25	60 ± 8	3.2 ± 0.2	3.23 ± 0.36	−0.01 ± 0.07	
	340^n	39.546 ± 0.003	35.041 ± 0.023	0.36 ± 0.15	0.16 ± 0.13	68 ± 68	4.0 ± 0.5	5.40 ± 1.10	−1.68 ± 0.12	c
K1	100^u	40.189 ± 0.009	0.416 ± 0.148	2.37 ± 0.49	0.63 ± 0.41	146 ± 8	13.8 ± 1.8	35.20 ± 6.30	8.98 ± 0.28	
K2	100^u	40.570 ± 0.000	16.323 ± 0.009	2.74 ± 0.02	0.90 ± 0.02	5 ± 0	28.7 ± 0.2	93.46 ± 0.75	4.99 ± 7.29	
	250^u	40.567 ± 0.002	16.193 ± 0.085	1.83 ± 0.21	0.34 ± 0.11	173 ± 2	5.9 ± 0.5	28.10 ± 3.00	4.29 ± 0.42	

Notes. Annotations: Sources without a letter before the number denote IRS sources. K and X sources are taken from Zhao *et al.* (2009), V sources from Viehmann *et al.* (2006), and SW, NE, and MX sources from Mužić *et al.* (2007). Sources with A (ALMA) are detected for the first time with this observation. u and n stand for "uniform" and "natural" weighting of the data, c for "convolved source size" (deconvolution not possible), d for "devoured" (hidden in Gauss wings from neighboring strong sources), numbers in the last column for the percentage of deviation or overestimate from the real source size and shape (also affecting integrated fluxes) estimated by visual inspection. These deviations are due to either overlapping of multiple sources, deviation from 2D Gaussian distribution, or very weak sources in a diffuse background. For details on the procedure see Sect. 3.2.4.

Table A.1: *Continued. Results of 2D Gauss fits to the continuum sources: Source positions are relative to 17^{h}40^{m}00.00^s and −29°00′00.00″(J2000). (Credit: Moser* et al. *(2016b), reproduced with permission ©ESO.)*

region	band	peak position		deconvolved size			flux			
		R.A.	Dec.	d_{maj}	d_{min}	PA	S_{peak}	S_{int}	S_{base}	
	[GHz]	[^{s}]	[″]	[″]	[″]	[°]	[mJy beam^{-1}]	[mJy]	[mJy beam^{-1}]	
K3	100^u	40.584 ± 0.001	18.411 ± 0.010	1.29 ± 0.03	0.63 ± 0.04	177 ± 3	14.1 ± 0.2	24.07 ± 0.45	16.40 ± 0.39	
	250^n	40.572 ± 0.001	18.754 ± 0.035	1.19 ± 0.10	0.42 ± 0.09	171 ± 4	7.7 ± 0.4	20.50 ± 1.50	3.19 ± 0.16	
	250^u	40.571 ± 0.002	18.719 ± 0.066	1.07 ± 0.19	0.22 ± 0.14	165 ± 6	6.6 ± 0.8	17.50 ± 2.70	1.66 ± 0.11	20
	340^n	40.576 ± 0.002	19.011 ± 0.019	0.39 ± 0.11	0.31 ± 0.15	35 ± 74	5.2 ± 0.4	8.50 ± 1.00	3.94 ± 0.44	
K8/10W	100^u	40.520 ± 0.000	23.030 ± 0.005	1.63 ± 0.02	0.85 ± 0.02	41 ± 1	19.9 ± 0.1	41.79 ± 0.40	14.48 ± 37.54	20
	250^n	40.532 ± 0.001	23.057 ± 0.012	0.79 ± 0.04	0.23 ± 0.08	18 ± 4	7.6 ± 0.2	13.63 ± 0.53	4.59 ± 0.80	
	250^u	40.535 ± 0.001	23.105 ± 0.014	1.07 ± 0.05	0.55 ± 0.03	38 ± 3	10.1 ± 0.3	35.10 ± 1.30	−0.75 ± 2.07	
	340^n	40.535 ± 0.001	23.043 ± 0.011	0.79 ± 0.03	0.45 ± 0.03	12 ± 3	7.1 ± 0.2	20.48 ± 0.70	2.37 ± 0.21	
K10	250^n	39.618 ± 0.001	25.675 ± 0.009	0.58 ± 0.06	0.51 ± 0.06	142 ± 36	5.2 ± 0.1	9.02 ± 0.35	0.91 ± 1.82	
	250^u	39.620 ± 0.000	25.662 ± 0.002	0.43 ± 0.01	0.21 ± 0.02	31 ± 3	3.5 ± 0.0	4.99 ± 0.06	0.86 ± 0.29	
	340^n	39.617 ± 0.003	25.648 ± 0.021	0.46 ± 0.15	0.21 ± 0.17	101 ± 60	2.8 ± 0.3	4.25 ± 0.78	−0.33 ± 0.02	
K13	250^u	39.584 ± 0.004	26.886 ± 0.024	1.28 ± 0.13	0.60 ± 0.07	72 ± 5	8.7 ± 0.6	35.50 ± 3.10	0.40 ± 0.25	
	340^n	39.594 ± 0.003	26.862 ± 0.025	1.11 ± 0.10	0.58 ± 0.06	60 ± 6	6.9 ± 0.5	29.90 ± 2.40	−0.87 ± 0.08	
K14	100^u	39.541 ± 0.000	27.071 ± 0.005	1.52 ± 0.02	1.17 ± 0.02	138 ± 3	37.2 ± 0.3	84.12 ± 0.79	19.44 ± 1.47	
	250^n	39.535 ± 0.002	27.029 ± 0.022	1.12 ± 0.09	0.93 ± 0.07	113 ± 24	11.4 ± 0.5	40.20 ± 2.40	7.88 ± 0.41	
	250^u	39.532 ± 0.003	27.005 ± 0.029	1.05 ± 0.12	0.75 ± 0.08	99 ± 16	6.7 ± 0.5	27.00 ± 2.60	5.61 ± 0.20	
	340^n	39.539 ± 0.005	26.884 ± 0.040	0.83 ± 0.19	0.49 ± 0.14	72 ± 29	4.1 ± 0.6	12.50 ± 2.40	3.78 ± 0.10	

Notes. Annotations: Sources without a letter before the number denote IRS sources. K and X sources are taken from Zhao *et al.* (2009), V sources from Viehmann *et al.* (2006), and SW, NE, and MX sources from Mužić *et al.* (2007). Sources with A (ALMA) are detected for the first time with this observation. u and n stand for "uniform" and "natural" weighting of the data, c for "convolved source size" (deconvolution not possible), d for "devoured" (hidden in Gauss wings from neighboring strong sources), numbers in the last column for the percentage of deviation or overestimate from the real source size and shape (also affecting integrated fluxes) estimated by visual inspection. These deviations are due to either overlapping of multiple sources, deviation from 2D Gaussian distribution, or very weak sources in a diffuse background. For details on the procedure see Sect. 3.2.4.

Table A.1: *Continued. Results of 2D Gauss fits to the continuum sources: Source positions are relative to $17^h40^m00.00^s$ and $-29°00'00.00''$ (J2000). (Credit: Moser et al. (2016b), reproduced with permission ©ESO.)*

region	band	peak position		deconvolved size			flux			
		R.A.	Dec.	d_{maj}	d_{min}	PA	S_{peak}	S_{int}	S_{base}	
	[GHz]	[^{s}]	[$''$]	[$''$]	[$''$]	[°]	[mJy beam^{-1}]	[mJy]	[mJy beam^{-1}]	
K15	100^u	39.296 ± 0.011	27.496 ± 0.081	1.00 ± 0.52	0.51 ± 0.34	82 ± 87	8.7 ± 1.5	12.10 ± 3.40	0.63 ± 0.09	
	250^n	39.274 ± 0.004	27.631 ± 0.034	0.90 ± 0.18	0.47 ± 0.19	58 ± 21	3.3 ± 0.3	6.96 ± 0.97	−0.32 ± 0.16	
	250^u	39.282 ± 0.003	27.604 ± 0.045	0.76 ± 0.14	0.45 ± 0.05	44 ± 9	2.2 ± 0.3	2.91 ± 0.69	−0.12 ± 0.04	c
K16/1W	100^u	40.412 ± 0.003	27.889 ± 0.043	3.28 ± 0.14	1.34 ± 0.08	42 ± 2	42.8 ± 1.4	189.00 ± 7.50	9.77 ± 1.37	
	250^n	40.417 ± 0.004	27.877 ± 0.071	1.98 ± 0.21	0.61 ± 0.11	34 ± 4	12.7 ± 1.1	59.00 ± 5.90	6.14 ± 0.07	
	250^u	40.417 ± 0.004	27.912 ± 0.070	1.82 ± 0.21	0.54 ± 0.10	34 ± 3	9.5 ± 0.9	52.70 ± 5.60	3.77 ± 0.05	
	340^n	40.409 ± 0.005	28.098 ± 0.080	2.03 ± 0.23	0.73 ± 0.10	35 ± 4	7.2 ± 0.7	63.70 ± 6.90	2.54 ± 0.04	
K16/1W-2	100^u	40.415 ± 0.000	27.901 ± 0.003	1.84 ± 0.01	0.49 ± 0.01	37 ± 2	33.8 ± 0.3	26.67 ± 0.08	6.96 ± 5.84	
	250^n	40.425 ± 0.000	27.787 ± 0.005	1.17 ± 0.02	0.60 ± 0.01	38 ± 1	15.0 ± 0.1	43.80 ± 0.54	5.30 ± 1.11	
	250^u	40.424 ± 0.001	27.803 ± 0.008	1.04 ± 0.03	0.54 ± 0.02	40 ± 2	11.3 ± 0.2	37.78 ± 0.90	3.26 ± 1.05	
	340^n	40.428 ± 0.001	27.791 ± 0.016	1.10 ± 0.05	0.60 ± 0.03	43 ± 3	8.1 ± 0.3	35.40 ± 1.50	2.47 ± 0.87	
K17/MX6	250^n	39.558 ± 0.001	27.558 ± 0.015	1.78 ± 0.05	1.06 ± 0.03	127 ± 2	21.3 ± 0.5	120.90 ± 3.20	−3.54 ± 1.25	
	250^u	39.563 ± 0.002	27.645 ± 0.018	1.54 ± 0.07	0.93 ± 0.04	120 ± 3	15.8 ± 0.6	103.10 ± 4.10	−4.25 ± 1.04	
	340^n	39.568 ± 0.002	27.679 ± 0.024	1.01 ± 0.09	0.74 ± 0.07	117 ± 14	9.1 ± 0.6	42.90 ± 3.30	−1.53 ± 0.33	
K19	250^u	39.622 ± 0.003	28.091 ± 0.034	0.67 ± 0.15	0.60 ± 0.16	107 ± 70	4.5 ± 0.5	11.50 ± 1.70	−0.31 ± 0.07	
	340^n	39.631 ± 0.004	28.162 ± 0.034	0.58 ± 0.18	0.24 ± 0.14	124 ± 28	3.2 ± 0.5	5.80 ± 1.20	−0.72 ± 0.03	
K20/NE3	250^n	40.217 ± 0.000	28.536 ± 0.002	0.80 ± 0.01	0.50 ± 0.01	84 ± 1	4.9 ± 0.1	4.74 ± 0.12	4.51 ± 0.89	20, c

Notes. Annotations: Sources without a letter before the number denote IRS sources. K and X sources are taken from Zhao *et al.* (2009), V sources from Viehmann *et al.* (2006), and SW, NE, and MX sources from Mužić *et al.* (2007). Sources with A (ALMA) are detected for the first time with this observation. u and n stand for "uniform" and "natural" weighting of the data, c for "convolved source size" (deconvolution not possible), d for "devoured" (hidden in Gauss wings from neighboring strong sources), numbers in the last column for the percentage of deviation or overestimate from the real source size and shape (also affecting integrated fluxes) estimated by visual inspection. These deviations are due to either overlapping of multiple sources, deviation from 2D Gaussian distribution, or very weak sources in a diffuse background. For details on the procedure see Sect. 3.2.4.

Table A.1: *Continued. Results of 2D Gauss fits to the continuum sources: Source positions are relative to $17^h40^m00.00^s$ and $-29°00'00.00''$(J2000). (Credit: Moser* et al. *(2016b), reproduced with permission ©ESO.)*

region	band	peak position		deconvolved size			flux			
		R.A.	Dec.	d_{maj}	d_{min}	PA	S_{peak}	S_{int}	S_{base}	
	[GHz]	[^{s}]	[$''$]	[$''$]	[$''$]	[°]	[mJy beam^{-1}]	[mJy]	[mJy beam^{-1}]	
	250^u	40.215 ± 0.000	28.531 ± 0.002	0.48 ± 0.02	0.13 ± 0.03	70 ± 2	7.0 ± 0.1	9.71 ± 0.16	0.50 ± 1.00	
	340^n	40.224 ± 0.002	28.443 ± 0.014	0.63 ± 0.08	0.22 ± 0.08	61 ± 7	5.6 ± 0.3	10.44 ± 0.94	−0.18 ± 0.33	
K22/V60	250^n	39.939 ± 0.007	28.472 ± 0.082	0.70 ± 0.35	0.64 ± 0.60	171 ± 107	5.1 ± 1.1	10.80 ± 3.30	0.34 ± 0.13	
	250^u	39.927 ± 0.003	28.487 ± 0.048	0.96 ± 0.16	0.57 ± 0.13	149 ± 17	4.6 ± 0.5	14.80 ± 2.00	−1.26 ± 0.07	
	340^n	39.924 ± 0.003	28.490 ± 0.048	0.97 ± 0.14	0.66 ± 0.12	25 ± 18	3.9 ± 0.4	16.70 ± 2.20	−1.37 ± 0.06	
K25/33NW	340^n	39.988 ± 0.001	29.669 ± 0.009	0.97 ± 0.04	0.33 ± 0.02	131 ± 1	3.2 ± 0.1	9.38 ± 0.31	−1.59 ± 0.43	
K31/K27/K26	100^u	39.792 ± 0.001	30.014 ± 0.014	2.21 ± 0.04	1.47 ± 0.04	21 ± 2	107.7 ± 1.4	362.70 ± 6.10	−19.72 ± 18.42	
	250^n	39.793 ± 0.002	29.890 ± 0.023	0.87 ± 0.82	0.52 ± 0.92	21 ± 12	34.4 ± 1.8	76.90 ± 5.40	7.26 ± 0.77	
	250^u	39.793 ± 0.002	29.873 ± 0.027	0.74 ± 0.90	0.50 ± 0.90	18 ± 18	26.2 ± 1.9	66.00 ± 6.30	4.35 ± 0.47	
	340^n	39.793 ± 0.001	29.844 ± 0.024	0.65 ± 0.78	0.41 ± 0.75	15 ± 13	22.6 ± 1.6	55.10 ± 5.30	2.89 ± 0.18	
K32	250^u	39.889 ± 0.003	30.101 ± 0.045	0.58 ± 0.20	0.40 ± 0.22	14 ± 86	2.7 ± 0.4	5.30 ± 1.10	−0.70 ± 0.13	
K32	340^n	39.891 ± 0.001	30.156 ± 0.024	0.48 ± 0.06	0.42 ± 0.04	6 ± 32	1.4 ± 0.2	1.35 ± 0.26	−0.63 ± 0.07	c
K33	250^n	40.038 ± 0.001	30.536 ± 0.016	1.33 ± 0.06	1.10 ± 0.05	123 ± 12	18.7 ± 0.6	84.90 ± 3.00	−1.98 ± 0.98	
K33	250^u	40.033 ± 0.001	30.545 ± 0.006	0.53 ± 0.04	0.23 ± 0.03	107 ± 4	4.8 ± 0.1	7.40 ± 0.31	6.11 ± 0.66	
K33	340^n	40.030 ± 0.001	30.564 ± 0.011	0.91 ± 0.05	0.64 ± 0.03	108 ± 6	9.5 ± 0.3	37.10 ± 1.60	−1.85 ± 0.14	20
K36/21/K45/K28	100^u	40.105 ± 0.010	30.676 ± 0.065	2.57 ± 0.36	1.35 ± 0.21	83 ± 9	35.6 ± 3.4	124.00 ± 15.00	23.48 ± 1.17	c
	250^n	40.212 ± 0.003	30.841 ± 0.021	0.59 ± 0.13	0.41 ± 0.12	97 ± 68	9.8 ± 0.8	15.60 ± 1.90	5.45 ± 0.61	

Notes. Annotations: Sources without a letter before the number denote IRS sources. K and X sources are taken from Zhao *et al.* (2009), V sources from Viehmann *et al.* (2006), and SW, NE, and MX sources from Mužić *et al.* (2007). Sources with A (ALMA) are detected for the first time with this observation. u and n stand for "uniform" and "natural" weighting of the data, c for "convolved source size" (deconvolution not possible), d for "devoured" (hidden in Gauss wings from neighboring strong sources), numbers in the last column for the percentage of deviation or overestimate from the real source size and shape (also affecting integrated fluxes) estimated by visual inspection. These deviations are due to either overlapping of multiple sources, deviation from 2D Gaussian distribution, or very weak sources in a diffuse background. For details on the procedure see Sect. 3.2.4.

Table A.1: *Continued. Results of 2D Gauss fits to the continuum sources: Source positions are relative to $17^h40^m00.00^s$ and $-29°00'00.00''$(J2000). (Credit: Moser* et al. *(2016b), reproduced with permission ©ESO.)*

region	band	peak position		deconvolved size			flux			
		R.A.	Dec.	d_{maj}	d_{min}	PA	S_{peak}	S_{int}	S_{base}	
	[GHz]	[^{s}]	[$''$]	[$''$]	[$''$]	[°]	[mJy beam^{-1}]	[mJy]	[mJy beam^{-1}]	
	250^u	40.216 ± 0.004	30.853 ± 0.035	0.42 ± 0.23	0.25 ± 0.15	76 ± 79	8.2 ± 1.4	11.60 ± 3.10	3.08 ± 0.11	
	340^n	40.218 ± 0.002	30.849 ± 0.022	0.49 ± 0.76	0.40 ± 0.50	84 ± 25	7.0 ± 1.0	6.70 ± 1.70	2.14 ± 0.03	
K37/V39	100^u	40.541 ± 0.002	30.818 ± 0.071	2.52 ± 0.18	0.31 ± 0.19	178 ± 2	7.7 ± 0.4	19.90 ± 1.30	3.98 ± 0.30	
	250^n	40.541 ± 0.002	30.832 ± 0.024	1.06 ± 0.07	0.82 ± 0.08	5 ± 19	4.4 ± 0.2	14.20 ± 0.84	−1.43 ± 0.20	
	250^u	40.541 ± 0.002	30.912 ± 0.023	0.42 ± 0.15	0.30 ± 0.24	118 ± 72	2.9 ± 0.3	4.28 ± 0.66	−0.10 ± 0.09	
	340^n	40.537 ± 0.001	31.037 ± 0.008	0.54 ± 0.04	0.41 ± 0.04	57 ± 14	2.3 ± 0.1	4.94 ± 0.22	1.92 ± 3.15	
K40/33SW	340^n	40.020 ± 0.001	31.338 ± 0.011	0.64 ± 0.05	0.20 ± 0.05	133 ± 4	2.6 ± 0.1	4.91 ± 0.27	−0.26 ± 0.03	
K41	340^n	39.929 ± 0.002	31.265 ± 0.035	0.72 ± 0.12	0.34 ± 0.11	155 ± 11	2.8 ± 0.3	6.63 ± 0.88	−0.66 ± 0.05	
K42	250^n	39.910 ± 0.002	31.313 ± 0.015	0.78 ± 0.78	0.61 ± 0.63	89 ± 26	4.5 ± 0.2	9.67 ± 0.63	2.87 ± 0.27	
K42	250^u	39.907 ± 0.001	31.247 ± 0.013	0.59 ± 0.68	0.37 ± 0.76	50 ± 15	4.0 ± 0.2	7.69 ± 0.53	0.28 ± 0.12	
K42	340^n	39.907 ± 0.002	31.284 ± 0.024	0.60 ± 0.11	0.43 ± 0.10	57 ± 47	3.5 ± 0.3	8.04 ± 0.99	−0.72 ± 0.12	
K43/K46/2L	100^u	39.782 ± 0.002	31.554 ± 0.030	2.60 ± 0.08	1.51 ± 0.06	166 ± 3	108.1 ± 2.6	423.00 ± 12.00	−17.11 ± 18.30	d
	250^n	39.777 ± 0.002	31.601 ± 0.035	1.38 ± 0.09	0.68 ± 0.07	171 ± 4	31.2 ± 1.6	111.60 ± 7.10	4.96 ± 0.66	
	250^u	39.776 ± 0.002	31.598 ± 0.035	1.31 ± 0.09	0.67 ± 0.06	172 ± 4	22.2 ± 1.2	103.90 ± 6.80	2.09 ± 0.44	
	340^n	39.777 ± 0.001	31.622 ± 0.030	1.20 ± 0.08	0.70 ± 0.05	173 ± 5	19.0 ± 1.0	102.00 ± 6.20	0.77 ± 0.21	
K45	340^n	40.075 ± 0.005	31.520 ± 0.029	0.75 ± 0.20	0.31 ± 0.15	83 ± 15	4.1 ± 0.6	9.30 ± 2.00	−0.20 ± 0.05	
K47/SW6	250^u	39.845 ± 0.010	32.601 ± 0.068	0.90 ± 0.40	0.50 ± 0.36	79 ± 39	4.7 ± 1.2	13.00 ± 4.40	4.21 ± 0.19	

Notes. Annotations: Sources without a letter before the number denote IRS sources. K and X sources are taken from Zhao *et al.* (2009), V sources from Viehmann *et al.* (2006), and SW, NE, and MX sources from Mužić *et al.* (2007). Sources with A (ALMA) are detected for the first time with this observation. u and n stand for "uniform" and "natural" weighting of the data, c for "convolved source size" (deconvolution not possible), d for "devoured" (hidden in Gauss wings from neighboring strong sources), numbers in the last column for the percentage of deviation or overestimate from the real source size and shape (also affecting integrated fluxes) estimated by visual inspection. These deviations are due to either overlapping of multiple sources, deviation from 2D Gaussian distribution, or very weak sources in a diffuse background. For details on the procedure see Sect. 3.2.4.

Table A.1: *Continued. Results of 2D Gauss fits to the continuum sources: Source positions are relative to 17^{h}40^{m}00.00^s and −29°00′00.00″(J2000). (Credit: Moser et al. (2016b), reproduced with permission ©ESO.)*

region	band	peak position		deconvolved size			flux			
		R.A.	Dec.	d_{maj}	d_{min}	PA	S_{peak}	S_{int}	S_{base}	
	[GHz]	[^{s}]	[″]	[″]	[″]	[°]	[mJy beam^{-1}]	[mJy]	[mJy beam^{-1}]	
	340^n	39.842 ± 0.006	32.557 ± 0.093	0.67 ± 0.28	0.55 ± 0.32	1 ± 162	3.8 ± 1.0	10.80 ± 3.90	1.74 ± 0.08	
K48	340^n	40.253 ± 0.002	32.621 ± 0.015	0.60 ± 0.08	0.37 ± 0.06	99 ± 14	4.9 ± 0.3	10.32 ± 0.99	−1.05 ± 0.03	
K49	250^u	39.921 ± 0.000	33.143 ± 0.002	0.40 ± 0.02	0.09 ± 0.04	115 ± 3	2.2 ± 0.0	2.78 ± 0.06	3.83 ± 0.60	
	340^n	39.907 ± 0.004	33.153 ± 0.036	0.47 ± 0.23	0.42 ± 0.17	125 ± 50	2.5 ± 0.4	4.10 ± 1.00	0.58 ± 0.05	
K50	100^u	40.258 ± 0.001	33.160 ± 0.010	2.06 ± 0.05	0.40 ± 0.05	122 ± 1	20.2 ± 0.3	41.31 ± 0.80	20.40 ± 3.02	20
	250^n	40.263 ± 0.002	33.192 ± 0.016	0.83 ± 0.09	0.32 ± 0.09	128 ± 7	7.7 ± 0.4	13.82 ± 0.95	4.65 ± 0.95	
	250^u	40.263 ± 0.002	33.212 ± 0.022	0.74 ± 0.11	0.36 ± 0.09	123 ± 11	7.0 ± 0.5	14.70 ± 1.60	1.60 ± 1.07	
	340^n	40.264 ± 0.003	33.205 ± 0.026	0.68 ± 0.13	0.30 ± 0.12	119 ± 13	5.6 ± 0.6	12.10 ± 1.80	0.64 ± 0.74	
K51/V31	250^n	40.301 ± 0.001	33.359 ± 0.005	1.46 ± 0.03	0.44 ± 0.01	121 ± 1	9.0 ± 0.1	26.14 ± 0.40	1.95 ± 1.99	30
	250^u	40.308 ± 0.002	33.360 ± 0.011	1.06 ± 0.06	0.40 ± 0.03	115 ± 2	5.6 ± 0.2	15.82 ± 0.72	1.48 ± 0.98	40
	340^n	40.313 ± 0.000	33.385 ± 0.005	1.04 ± 0.01	0.41 ± 0.01	148 ± 1	6.1 ± 0.1	21.28 ± 0.27	−0.75 ± 0.40	
K52/2S	250^u	39.743 ± 0.002	33.488 ± 0.035	0.96 ± 0.99	0.31 ± 0.98	19 ± 5	4.3 ± 0.3	11.40 ± 1.10	2.09 ± 0.44	
K53/SW7	250^n	39.831 ± 0.001	33.582 ± 0.007	1.00 ± 0.04	0.65 ± 0.03	113 ± 4	10.1 ± 0.2	26.14 ± 0.69	1.51 ± 0.31	
	250^u	39.823 ± 0.003	33.544 ± 0.041	0.92 ± 0.15	0.54 ± 0.12	145 ± 16	7.6 ± 0.8	22.70 ± 2.90	−0.24 ± 0.48	
	340^n	39.828 ± 0.003	33.549 ± 0.039	0.72 ± 0.14	0.53 ± 0.13	148 ± 29	5.6 ± 0.6	16.50 ± 2.40	−0.48 ± 0.19	
K54	250^n	39.841 ± 0.005	33.579 ± 0.034	0.86 ± 0.23	0.40 ± 0.17	99 ± 23	4.3 ± 0.6	8.20 ± 1.50	6.55 ± 0.50	
	250^u	39.856 ± 0.007	33.655 ± 0.037	0.87 ± 0.22	0.38 ± 0.46	110 ± 5	2.9 ± 0.5	3.70 ± 1.10	3.62 ± 0.17	

Notes. Annotations: Sources without a letter before the number denote IRS sources. K and X sources are taken from Zhao *et al.* (2009), V sources from Viehmann *et al.* (2006), and SW, NE, and MX sources from Mužić *et al.* (2007). Sources with A (ALMA) are detected for the first time with this observation. u and n stand for "uniform" and "natural" weighting of the data, c for "convolved source size" (deconvolution not possible), d for "devoured" (hidden in Gauss wings from neighboring strong sources), numbers in the last column for the percentage of deviation or overestimate from the real source size and shape (also affecting integrated fluxes) estimated by visual inspection. These deviations are due to either overlapping of multiple sources, deviation from 2D Gaussian distribution, or very weak sources in a diffuse background. For details on the procedure see Sect. 3.2.4.

Table A.1: *Continued. Results of 2D Gauss fits to the continuum sources: Source positions are relative to $17^h40^m00.00^s$ and $-29°00'00.00''$ (J2000). (Credit: Moser* et al. *(2016b), reproduced with permission ©ESO.)*

region	band	peak position		deconvolved size			flux			
		R.A.	Dec.	d_{maj}	d_{min}	PA	S_{peak}	S_{int}	S_{base}	
	[GHz]	[^{s}]	[$''$]	[$''$]	[$''$]	[°]	[mJy beam^{-1}]	[mJy]	[mJy beam^{-1}]	
	340^n	39.846 ± 0.003	33.600 ± 0.032	0.76 ± 0.14	0.54 ± 0.11	111 ± 60	4.5 ± 0.5	13.60 ± 2.00	0.09 ± 0.18	c
K55	100^u	41.144 ± 0.011	33.663 ± 0.132	1.84 ± 0.56	0.57 ± 0.41	46 ± 19	16.9 ± 2.8	34.50 ± 8.20	12.16 ± 0.18	
	250^n	41.136 ± 0.004	33.765 ± 0.081	1.41 ± 0.23	0.80 ± 0.18	20 ± 13	10.8 ± 1.3	43.10 ± 6.40	5.29 ± 0.45	
	250^u	41.151 ± 0.002	33.750 ± 0.021	0.83 ± 0.10	0.29 ± 0.10	55 ± 6	13.4 ± 0.9	29.70 ± 2.80	2.44 ± 1.41	
K57/MX5/9N	250^n	40.463 ± 0.001	33.945 ± 0.009	1.06 ± 0.05	0.40 ± 0.04	62 ± 2	5.1 ± 0.1	11.58 ± 0.41	−0.04 ± 0.94	
	250^u	40.472 ± 0.002	33.887 ± 0.027	0.70 ± 0.12	0.37 ± 0.13	45 ± 17	4.9 ± 0.4	10.40 ± 1.30	−0.76 ± 0.23	
	340^n	40.469 ± 0.002	33.936 ± 0.010	0.87 ± 0.07	0.30 ± 0.04	79 ± 3	3.6 ± 0.2	9.24 ± 0.61	−0.61 ± 0.28	
K59	100^u	40.374 ± 0.002	34.561 ± 0.015	1.59 ± 0.07	1.14 ± 0.05	96 ± 6	22.3 ± 0.5	50.40 ± 1.70	19.87 ± 5.66	
	250^n	40.384 ± 0.004	34.591 ± 0.032	1.70 ± 0.12	1.23 ± 0.09	81 ± 10	15.2 ± 0.9	92.80 ± 6.00	−2.19 ± 3.74	
	250^u	40.392 ± 0.005	34.534 ± 0.038	0.56 ± 0.26	0.33 ± 0.17	76 ± 70	5.9 ± 1.0	10.30 ± 2.60	3.49 ± 0.20	
	340^n	40.392 ± 0.004	34.492 ± 0.029	0.59 ± 0.19	0.28 ± 0.19	79 ± 48	5.2 ± 0.8	9.80 ± 2.20	1.86 ± 0.08	
K60	250^n	40.131 ± 0.003	34.851 ± 0.031	0.51 ± 0.20	0.50 ± 0.31	47 ± 87	5.7 ± 0.6	9.30 ± 1.40	1.36 ± 0.25	
	250^u	40.134 ± 0.002	34.876 ± 0.013	0.61 ± 0.79	0.36 ± 0.73	70 ± 14	5.1 ± 0.3	9.71 ± 0.78	−0.30 ± 0.10	
	340^n	40.140 ± 0.002	34.973 ± 0.025	0.45 ± 0.13	0.28 ± 0.16	19 ± 38	3.6 ± 0.3	6.06 ± 0.85	−0.19 ± 0.04	
K63	250^n	40.477 ± 0.005	35.834 ± 0.038	0.84 ± 0.22	0.49 ± 0.18	109 ± 48	5.2 ± 0.6	10.50 ± 1.80	1.40 ± 0.14	
	250^u	40.479 ± 0.007	35.921 ± 0.033	0.67 ± 0.30	0.12 ± 0.17	100 ± 26	4.3 ± 0.8	6.90 ± 2.00	0.36 ± 0.06	
	340^n	40.466 ± 0.001	36.004 ± 0.014	0.63 ± 0.05	0.22 ± 0.06	27 ± 4	3.4 ± 0.1	6.60 ± 0.40	−0.42 ± 0.85	

Notes. Annotations: Sources without a letter before the number denote IRS sources. K and X sources are taken from Zhao *et al.* (2009), V sources from Viehmann *et al.* (2006), and SW, NE, and MX sources from Mužić *et al.* (2007). Sources with A (ALMA) are detected for the first time with this observation. u and n stand for "uniform" and "natural" weighting of the data, c for "convolved source size" (deconvolution not possible), d for "devoured" (hidden in Gauss wings from neighboring strong sources), numbers in the last column for the percentage of deviation or overestimate from the real source size and shape (also affecting integrated fluxes) estimated by visual inspection. These deviations are due to either overlapping of multiple sources, deviation from 2D Gaussian distribution, or very weak sources in a diffuse background. For details on the procedure see Sect. 3.2.4.

Table A.1: *Continued. Results of 2D Gauss fits to the continuum sources: Source positions are relative to 17^{h}40^{m}00.00^s and −29°00′00.00″(J2000). (Credit: Moser* et al. *(2016b), reproduced with permission ©ESO.)*

region	band	peak position		deconvolved size			flux			
		R.A.	Dec.	d_{maj}	d_{min}	PA	S_{peak}	S_{int}	S_{base}	
	[GHz]	[^{s}]	[″]	[″]	[″]	[°]	[mJy beam^{-1}]	[mJy]	[mJy beam^{-1}]	
K64	250^n	40.571 ± 0.003	35.979 ± 0.026	0.58 ± 0.16	0.42 ± 0.18	92 ± 87	4.0 ± 0.4	6.38 ± 0.91	0.33 ± 0.26	
	250^u	40.580 ± 0.001	35.962 ± 0.024	0.55 ± 0.57	0.42 ± 0.33	180 ± 12	4.6 ± 0.4	4.08 ± 0.68	−0.32 ± 0.05	c
	340^n	40.579 ± 0.002	35.900 ± 0.031	0.53 ± 0.07	0.44 ± 0.05	175 ± 26	2.1 ± 0.3	2.37 ± 0.49	0.50 ± 0.22	c
MX1	250^u	40.289 ± 0.003	24.853 ± 0.045	0.85 ± 0.18	0.23 ± 0.15	140 ± 10	1.9 ± 0.2	4.15 ± 0.68	−0.28 ± 0.07	
	340^n	40.290 ± 0.002	24.738 ± 0.028	0.63 ± 0.08	0.35 ± 0.03	149 ± 5	1.6 ± 0.1	1.70 ± 0.28	0.28 ± 0.01	c
SW3	250^n	39.565 ± 0.001	29.128 ± 0.013	1.06 ± 0.05	0.78 ± 0.05	132 ± 8	4.6 ± 0.1	13.95 ± 0.51	0.39 ± 1.81	20
	250^u	39.572 ± 0.004	29.201 ± 0.078	0.64 ± 0.25	0.15 ± 0.29	160 ± 23	2.4 ± 0.5	4.20 ± 1.30	0.33 ± 0.05	
	340^n	39.577 ± 0.001	29.285 ± 0.008	0.60 ± 0.03	0.26 ± 0.03	156 ± 4	3.5 ± 0.1	6.96 ± 0.26	0.26 ± 0.13	
V26	250^n	40.008 ± 0.004	20.547 ± 0.126	1.31 ± 0.35	0.32 ± 0.25	171 ± 10	1.3 ± 0.2	3.46 ± 0.82	−0.16 ± 0.03	
	250^u	40.019 ± 0.002	20.468 ± 0.042	0.85 ± 0.12	0.20 ± 0.12	11 ± 6	1.9 ± 0.2	4.15 ± 0.52	−0.81 ± 0.18	
	340^n	40.032 ± 0.002	20.023 ± 0.056	0.78 ± 0.16	0.27 ± 0.21	14 ± 10	2.1 ± 0.3	4.99 ± 0.90	−0.18 ± 0.04	
V32	250^u	40.367 ± 0.003	35.579 ± 0.020	0.58 ± 0.09	0.39 ± 0.04	69 ± 10	1.7 ± 0.2	1.47 ± 0.34	2.36 ± 0.07	c
	340^n	40.360 ± 0.001	35.786 ± 0.025	0.55 ± 0.07	0.30 ± 0.02	36 ± 4	1.1 ± 0.1	0.88 ± 0.16	1.47 ± 0.13	c
V37	250^u	40.536 ± 0.001	20.530 ± 0.012	0.48 ± 0.47	0.35 ± 0.70	4 ± 102	4.5 ± 0.2	7.50 ± 0.49	1.62 ± 0.21	
V63/16C	250^u	40.116 ± 0.011	27.574 ± 0.102	0.50 ± 0.36	0.40 ± 0.23	74 ± 103	2.2 ± 1.4	1.70 ± 2.10	0.33 ± 0.32	
	340^n	40.107 ± 0.009	27.633 ± 0.071	0.59 ± 0.35	0.37 ± 0.21	95 ± 45	2.6 ± 0.9	5.40 ± 2.60	−0.69 ± 0.20	c
X4	100^u	40.605 ± 0.002	13.282 ± 0.042	1.78 ± 0.12	0.49 ± 0.17	177 ± 4	8.9 ± 0.4	18.00 ± 1.10	13.39 ± 0.66	

Notes. Annotations: Sources without a letter before the number denote IRS sources. K and X sources are taken from Zhao *et al.* (2009), V sources from Viehmann *et al.* (2006), and SW, NE, and MX sources from Mužić *et al.* (2007). Sources with A (ALMA) are detected for the first time with this observation. u and n stand for "uniform" and "natural" weighting of the data, c for "convolved source size" (deconvolution not possible), d for "devoured" (hidden in Gauss wings from neighboring strong sources), numbers in the last column for the percentage of deviation or overestimate from the real source size and shape (also affecting integrated fluxes) estimated by visual inspection. These deviations are due to either overlapping of multiple sources, deviation from 2D Gaussian distribution, or very weak sources in a diffuse background. For details on the procedure see Sect. 3.2.4.

Table A.1: *Continued. Results of 2D Gauss fits to the continuum sources: Source positions are relative to $17^h40^m00.00^s$ and $-29°00'00.00''$ (J2000). (Credit:* *Moser* et al. *(2016b), reproduced with permission ©ESO.)*

region	band	peak position		deconvolved size			flux			
		R.A.	Dec.	$d_{\rm maj}$	$d_{\rm min}$	PA	$S_{\rm peak}$	$S_{\rm int}$	$S_{\rm base}$	
	[GHz]	[^{s}]	[$''$]	[$''$]	[$''$]	[°]	[mJy beam^{-1}]	[mJy]	[mJy beam^{-1}]	
X6	100^u	39.355 ± 0.008	19.715 ± 0.035	1.96 ± 0.26	0.99 ± 0.07	81 ± 4	8.3 ± 0.8	11.30 ± 1.80	−0.19 ± 0.04	c
	250^n	39.380 ± 0.007	19.678 ± 0.050	0.89 ± 0.31	0.51 ± 0.31	74 ± 65	4.3 ± 0.7	9.30 ± 2.10	−0.35 ± 0.02	
	250^u	39.394 ± 0.005	19.592 ± 0.067	0.85 ± 0.20	0.44 ± 0.06	139 ± 8	4.3 ± 0.8	6.20 ± 1.80	0.19 ± 0.05	c
X9/7	100^u	40.036 ± 0.001	22.495 ± 0.006	1.61 ± 0.02	1.52 ± 0.02	76 ± 13	9.8 ± 0.1	26.44 ± 0.25	−5.36 ± 2.12	
	250^n	40.034 ± 0.002	22.685 ± 0.016	0.66 ± 0.92	0.52 ± 0.88	118 ± 56	2.9 ± 0.2	5.35 ± 0.40	0.00 ± 0.24	
	250^u	40.031 ± 0.003	22.695 ± 0.023	0.42 ± 0.14	0.30 ± 0.23	114 ± 77	2.6 ± 0.3	3.87 ± 0.61	−0.05 ± 0.11	
	340^n	40.035 ± 0.002	22.734 ± 0.015	0.55 ± 0.98	0.26 ± 0.88	77 ± 13	1.9 ± 0.2	3.42 ± 0.41	−0.16 ± 0.03	
X11/NE1	100^u	40.437 ± 0.001	24.281 ± 0.019	2.12 ± 0.05	0.86 ± 0.04	10 ± 1	26.8 ± 0.4	69.60 ± 1.50	14.09 ± 7.16	20
	250^u	40.417 ± 0.002	24.306 ± 0.058	0.88 ± 0.16	0.30 ± 0.21	8 ± 10	5.9 ± 0.7	14.30 ± 2.40	4.17 ± 0.85	
	340^n	40.414 ± 0.003	24.422 ± 0.026	0.56 ± 0.11	0.47 ± 0.11	95 ± 82	4.3 ± 0.4	9.90 ± 1.40	4.74 ± 0.25	
X12/34NE	250^n	39.769 ± 0.002	26.286 ± 0.030	0.91 ± 0.93	0.59 ± 0.42	132 ± 7	4.0 ± 0.3	5.24 ± 0.72	0.41 ± 0.02	
	250^u	39.770 ± 0.002	26.242 ± 0.039	0.73 ± 0.10	0.52 ± 0.54	151 ± 12	3.2 ± 0.4	4.69 ± 0.87	0.00 ± 0.03	c
	340^n	39.770 ± 0.003	26.179 ± 0.066	0.79 ± 0.18	0.42 ± 0.57	149 ± 8	2.4 ± 0.4	3.90 ± 1.00	−0.17 ± 0.02	c
X13	250^u	40.448 ± 0.000	26.674 ± 0.007	0.72 ± 0.02	0.17 ± 0.04	168 ± 2	4.6 ± 0.1	8.78 ± 0.22	4.60 ± 0.43	
	340^n	40.456 ± 0.001	26.763 ± 0.011	0.75 ± 0.05	0.41 ± 0.04	127 ± 5	3.7 ± 0.1	9.81 ± 0.50	3.00 ± 0.30	
X17	250^n	41.264 ± 0.004	31.848 ± 0.112	0.96 ± 0.28	0.55 ± 0.97	19 ± 12	5.3 ± 1.2	6.80 ± 2.50	5.78 ± 0.08	
	250^u	41.258 ± 0.004	32.144 ± 0.088	0.93 ± 0.22	0.50 ± 0.77	23 ± 10	10.3 ± 2.0	18.60 ± 5.30	1.33 ± 0.12	c

Notes. Annotations: Sources without a letter before the number denote IRS sources. K and X sources are taken from Zhao *et al.* (2009), V sources from Viehmann *et al.* (2006), and SW, NE, and MX sources from Mužić *et al.* (2007). Sources with A (ALMA) are detected for the first time with this observation. u and n stand for "uniform" and "natural" weighting of the data, c for "convolved source size" (deconvolution not possible), d for "devoured" (hidden in Gauss wings from neighboring strong sources), numbers in the last column for the percentage of deviation or overestimate from the real source size and shape (also affecting integrated fluxes) estimated by visual inspection. These deviations are due to either overlapping of multiple sources, deviation from 2D Gaussian distribution, or very weak sources in a diffuse background. For details on the procedure see Sect. 3.2.4.

Table A.1: *Continued. Results of 2D Gauss fits to the continuum sources: Source positions are relative to $17^h40^m00.00^s$ and $-29°00'00.00''$(J2000). (Credit: Moser* et al. *(2016b), reproduced with permission ©ESO.)*

region	band	peak position		deconvolved size			flux			
		R.A.	Dec.	d_{maj}	d_{min}	PA	S_{peak}	S_{int}	S_{base}	
	[GHz]	[^{s}]	[$''$]	[$''$]	[$''$]	[°]	[mJy beam^{-1}]	[mJy]	[mJy beam^{-1}]	
X18/4	100^u	40.871 ± 0.004	34.391 ± 0.047	1.07 ± 0.27	0.73 ± 0.36	20 ± 57	12.4 ± 0.9	19.80 ± 2.20	9.26 ± 0.64	
	250^n	40.869 ± 0.000	33.919 ± 0.004	0.89 ± 0.02	0.27 ± 0.02	38 ± 1	6.0 ± 0.1	11.61 ± 0.17	1.50 ± 0.10	
	250^u	40.860 ± 0.004	34.351 ± 0.033	0.75 ± 0.15	0.53 ± 0.13	112 ± 83	3.8 ± 0.4	9.50 ± 1.40	1.62 ± 1.15	20
	340^n	40.841 ± 0.002	34.451 ± 0.013	0.59 ± 0.07	0.30 ± 0.06	62 ± 9	9.7 ± 0.6	19.00 ± 1.50	−2.61 ± 0.93	
X19	100^u	38.596 ± 0.002	35.919 ± 0.022	1.25 ± 0.12	1.13 ± 0.14	148 ± 51	5.5 ± 0.2	10.97 ± 0.50	5.97 ± 0.84	
X20/K66/V12	100^u	40.813 ± 0.002	36.727 ± 0.033	1.39 ± 0.13	0.96 ± 0.14	174 ± 17	18.3 ± 0.8	36.70 ± 2.20	−0.59 ± 0.05	
	250^n	40.810 ± 0.002	37.009 ± 0.052	1.25 ± 0.15	0.31 ± 0.20	17 ± 5	9.5 ± 0.8	24.80 ± 2.70	−0.15 ± 0.14	
	250^u	40.806 ± 0.004	37.057 ± 0.075	1.08 ± 0.23	0.29 ± 0.21	29 ± 8	8.8 ± 1.3	25.00 ± 4.70	−1.37 ± 0.27	
X23	100^u	38.564 ± 0.005	42.420 ± 0.107	2.83 ± 0.30	0.70 ± 0.23	156 ± 3	7.5 ± 0.6	22.90 ± 2.20	4.35 ± 0.14	
X24	100^u	39.339 ± 0.006	43.195 ± 0.069	0.98 ± 0.39	0.80 ± 0.43	44 ± 89	5.5 ± 0.7	8.50 ± 1.50	0.32 ± 0.12	
	250^n	39.328 ± 0.004	42.890 ± 0.062	0.65 ± 0.17	0.40 ± 0.06	146 ± 12	2.4 ± 0.5	1.50 ± 0.64	0.87 ± 0.29	c
X25	100^u	38.799 ± 0.004	57.291 ± 0.024	2.05 ± 0.14	0.82 ± 0.09	109 ± 3	10.0 ± 0.4	23.40 ± 1.30	11.18 ± 1.41	

Notes. Annotations: Sources without a letter before the number denote IRS sources. K and X sources are taken from Zhao *et al.* (2009), V sources from Viehmann *et al.* (2006), and SW, NE, and MX sources from Mužić *et al.* (2007). Sources with A (ALMA) are detected for the first time with this observation. u and n stand for "uniform" and "natural" weighting of the data, c for "convolved source size" (deconvolution not possible), d for "devoured" (hidden in Gauss wings from neighboring strong sources), numbers in the last column for the percentage of deviation or overestimate from the real source size and shape (affecting also integrated fluxes) estimated by visual inspection. These deviations are due to either overlapping of multiple sources, deviation from 2D Gaussian distribution, or very weak sources in a diffuse background. For details on the procedure see Sect. 3.2.4.

Table A.2: *Results of 2D Gauss fits to the molecular sources: Source positions are relative to 17^{h}40^{m}00.00^s and $-29°00'00.00''$(J2000). (Credit: Moser et al. (2016b), reproduced with permission ©ESO.)*

		peak position		convolved size			deconvolved size			flux		
region	line	R.A. [s]	Dec [”]	$d_{\mathrm{maj,c}}$ [”]	$d_{\mathrm{min,c}}$ [”]	PA_c [°]	$d_{\mathrm{maj,d}}$ [”]	$d_{\mathrm{min,d}}$ [”]	PA_d [°]	S_{int} [Jy km s^{-1}]	S_{peak} [Jy bm^{-1} km s^{-1}]	S_{off}
1-all	CS(5–4)^n	39.88 ± 0.01	-26.07 ± 0.10	2.6 ± 0.4	1.3 ± 0.2	127 ± 6	2.5 ± 0.4	1.1 ± 0.2	128 ± 7	16.30 ± 2.40	2.2 ± 0.29	0.55 ± 0.03
	H^{13}CO$^+$(3–2)^t	39.84 ± 0.02	-25.68 ± 0.16	1.0 ± 0.5	0.8 ± 0.4	112 ± 73	0.7 ± 0.6	0.4 ± 0.5	112 ± 73	0.30 ± 0.22	0.2 ± 0.09	0.08 ± 0.00
	SO(7–6)^n	39.93 ± 0.01	-26.59 ± 0.05	1.0 ± 0.3	0.4 ± 0.1	107 ± 6	-	-	-	0.55 ± 0.22	0.5 ± 0.11	0.13 ± 0.00
	CH$_3$OH(7–6)^n	39.90 ± 0.00	-26.28 ± 0.02	0.3 ± 0.1	0.3 ± 0.0	53 ± 55	-	-	-	0.11 ± 0.05	0.3 ± 0.05	0.07 ± 0.00
	SiO(8–7)^t	39.90 ± 0.00	-26.24 ± 0.25	1.0 ± 0.6	0.3 ± 0.0	1 ± 4	-	-	-	0.30 ± 0.24	0.4 ± 0.13	0.20 ± 0.02
1	CS(5–4)^n	39.92 ± 0.00	-26.39 ± 0.04	1.8 ± 0.1	1.3 ± 0.1	101 ± 7	1.7 ± 0.2	1.1 ± 0.1	102 ± 9	14.80 ± 1.20	2.9 ± 0.21	-0.08 ± 0.10
	SiO(6–5)^t	39.93 ± 0.01	-26.55 ± 0.05	0.8 ± 0.4	0.5 ± 0.1	90 ± 20	-	-	-	0.13 ± 0.09	0.1 ± 0.05	0.05 ± 0.02
	C$_2$H(3–2)^t	39.93 ± 0.01	-26.49 ± 0.07	2.2 ± 0.2	1.4 ± 0.1	48 ± 8	2.1 ± 0.2	1.2 ± 0.1	48 ± 8	13.30 ± 1.40	1.9 ± 0.17	-0.53 ± 0.44
2	H^{13}CO$^+$(3–2)^t	39.84 ± 0.01	-25.67 ± 0.08	0.6 ± 0.4	0.4 ± 0.2	78 ± 43	-	-	-	0.08 ± 0.09	0.1 ± 0.07	0.13 ± 0.01
	SiO(6–5)^t	39.84 ± 0.00	-25.59 ± 0.03	0.6 ± 0.1	0.3 ± 0.0	60 ± 6	-	-	-	0.17 ± 0.06	0.4 ± 0.05	0.08 ± 0.01
	SO(7–6)^n	39.81 ± 0.01	-25.45 ± 0.11	0.7 ± 0.3	0.4 ± 0.1	148 ± 19	-	-	-	0.17 ± 0.10	0.2 ± 0.06	0.08 ± 0.01
	C$_2$H(3–2)^t	39.81 ± 0.01	-25.51 ± 0.06	1.7 ± 0.2	0.8 ± 0.1	131 ± 4	1.6 ± 0.2	0.4 ± 0.1	131 ± 4	3.05 ± 0.38	1.0 ± 0.10	0.16 ± 0.06
3	HC$_3$N(27–26)^t	39.78 ± 0.00	-24.64 ± 0.04	0.8 ± 0.1	0.6 ± 0.1	15 ± 9	-	-	-	0.28 ± 0.05	0.2 ± 0.02	-0.03 ± 0.07
	H^{13}CO$^+$(3–2)^t	39.78 ± 0.01	-24.76 ± 0.15	0.9 ± 0.4	0.5 ± 0.1	166 ± 22	-	-	-	0.33 ± 0.19	0.3 ± 0.10	0.14 ± 0.01
	CH$_3$OH(7–6)^n	39.78 ± 0.00	-24.54 ± 0.02	0.9 ± 0.1	0.4 ± 0.0	153 ± 2	-	-	-	1.10 ± 0.10	0.7 ± 0.04	-0.01 ± 0.03
4	CS(5–4)^n	39.77 ± 0.00	-23.70 ± 0.02	0.8 ± 0.1	0.6 ± 0.0	57 ± 7	-	-	-	0.84 ± 0.10	0.8 ± 0.06	0.05 ± 0.01
	H^{13}CO$^+$(3–2)^t	39.78 ± 0.00	-23.69 ± 0.02	0.3 ± 0.0	0.3 ± 0.0	41 ± 53	-	-	-	0.05 ± 0.02	0.2 ± 0.03	0.09 ± 0.01
	C$_2$H(3–2)^t	39.84 ± 0.01	-23.66 ± 0.06	0.6 ± 0.2	0.3 ± 0.0	49 ± 8	-	-	-	0.15 ± 0.08	0.3 ± 0.06	0.14 ± 0.01
	CH$_3$OH(7–6)^n	39.79 ± 0.00	-23.68 ± 0.04	0.5 ± 0.1	0.4 ± 0.0	11 ± 16	-	-	-	0.42 ± 0.12	0.5 ± 0.08	0.09 ± 0.01
5	CS(5–4)^n	40.05 ± 0.00	-23.19 ± 0.09	1.1 ± 0.2	0.9 ± 0.2	12 ± 28	1.0 ± 0.3	0.5 ± 0.4	10 ± 28	3.88 ± 0.95	1.7 ± 0.31	0.81 ± 0.03

Notes. For details on the procedure see Sect. 3.2.4. A finding chart is provided in Fig. A.10 $^{(t)}$ tapered beam size, i.e. 0.65” in band 6 and 7, 1.5” in band 3 ; $^{(n)}$ natural beam size at the given frequency

Table A.2: *Continued. Results of 2D Gauss fits to the molecular sources: Source positions are relative to 17^{h}40^{m}00.00^s and −29°00′00.00″(J2000). (Credit: Moser et al. (2016b), reproduced with permission ©ESO.)*

region	line	peak position		convolved size			deconvolved size			flux		
		R.A. [s]	Dec ["]	$d_{\rm maj,c}$ ["]	$d_{\rm min,c}$ ["]	PA_c [°]	$d_{\rm maj,d}$ ["]	$d_{\rm min,d}$ ["]	PA_d [°]	$S_{\rm int}$ [Jy km s^{-1}]	$S_{\rm peak}$ [Jy bm^{-1} km s^{-1}]	$S_{\rm off}$ [Jy bm^{-1} km s^{-1}]
	$H^{13}CO^+$(3–2)^t	40.05 ± 0.00	-23.27 ± 0.04	0.8 ± 0.1	0.6 ± 0.1	129 ± 16	-	-	-	0.38 ± 0.09	0.4 ± 0.05	0.04 ± 0.03
	SiO(6–5)^t	40.04 ± 0.00	-22.68 ± 0.03	0.4 ± 0.1	0.3 ± 0.0	137 ± 19	-	-	-	0.10 ± 0.05	0.3 ± 0.05	0.11 ± 0.01
	SO(7–6)^n	40.06 ± 0.01	-23.26 ± 0.05	1.1 ± 0.2	0.6 ± 0.1	109 ± 10	0.8 ± 0.4	0.2 ± 0.2	112 ± 34	0.72 ± 0.20	0.4 ± 0.08	0.10 ± 0.01
	C_2H(3–2)^t	40.06 ± 0.01	-23.09 ± 0.06	1.5 ± 0.3	0.7 ± 0.1	120 ± 6	1.4 ± 0.3	0.4 ± 0.2	120 ± 6	3.28 ± 0.61	1.2 ± 0.17	0.22 ± 0.05
	CH_3OH(7–6)^t	40.07 ± 0.03	-23.33 ± 0.37	0.7 ± 1.2	0.5 ± 0.5	50 ± 129	-	-	-	0.04 ± 0.11	0.1 ± 0.08	0.11 ± 0.00
	SiO(8–7)^n	40.04 ± 0.00	-22.65 ± 0.02	0.4 ± 0.1	0.4 ± 0.0	82 ± 26	-	-	-	0.82 ± 0.24	1.0 ± 0.15	0.18 ± 0.01
6	CS(5–4)^t	40.00 ± 0.00	-24.00 ± 0.05	1.4 ± 0.1	1.2 ± 0.1	3 ± 40	1.2 ± 0.1	1.1 ± 0.1	3 ± 40	7.98 ± 0.85	2.0 ± 0.17	0.19 ± 0.36
	SiO(6–5)^t	40.00 ± 0.00	-23.93 ± 0.02	0.6 ± 0.1	0.4 ± 0.0	98 ± 7	-	-	-	0.16 ± 0.04	0.3 ± 0.03	0.03 ± 0.07
	SO(7–6)^n	40.00 ± 0.00	-24.08 ± 0.07	0.7 ± 0.2	0.4 ± 0.1	168 ± 9	-	-	-	0.23 ± 0.08	0.3 ± 0.06	0.07 ± 0.01
	C_2H(3–2)^t	40.01 ± 0.01	-23.70 ± 0.03	0.6 ± 0.2	0.3 ± 0.0	107 ± 9	-	-	-	0.17 ± 0.11	0.4 ± 0.09	0.11 ± 0.02
7	CS(5–4)^n	40.12 ± 0.01	-25.38 ± 0.15	1.9 ± 0.4	0.9 ± 0.1	14 ± 8	1.8 ± 0.4	0.6 ± 0.3	14 ± 8	4.20 ± 0.91	1.1 ± 0.19	0.47 ± 0.02
	SiO(6–5)^n	40.12 ± 0.00	-24.92 ± 0.01	0.4 ± 0.0	0.3 ± 0.0	135 ± 8	-	-	-	0.28 ± 0.05	0.7 ± 0.05	0.08 ± 0.01
	SO(7–6)^n	40.10 ± 0.01	-25.78 ± 0.33	1.2 ± 0.8	0.4 ± 0.1	23 ± 10	-	-	-	0.23 ± 0.19	0.2 ± 0.08	0.11 ± 0.01
	C_2H(3–2)^t	40.09 ± 0.01	-25.53 ± 0.02	1.3 ± 0.3	0.4 ± 0.0	94 ± 2	-	-	-	0.95 ± 0.25	0.8 ± 0.11	0.13 ± 0.01
	CH_3OH(7–6)^t	40.12 ± 0.00	-25.83 ± 0.05	0.4 ± 0.2	0.2 ± 0.0	50 ± 7	-	-	-	0.04 ± 0.04	0.2 ± 0.04	0.11 ± 0.00
8	CS(5–4)^t	40.12 ± 0.00	-28.12 ± 0.06	1.7 ± 0.2	0.9 ± 0.1	13 ± 3	1.6 ± 0.2	0.6 ± 0.1	13 ± 3	2.84 ± 0.27	0.8 ± 0.06	0.75 ± 0.18
9	CS(5–4)^t	40.15 ± 0.00	-29.87 ± 0.07	1.7 ± 0.2	1.3 ± 0.1	168 ± 17	1.5 ± 0.2	1.1 ± 0.2	168 ± 17	6.52 ± 0.78	1.3 ± 0.13	0.37 ± 0.22
10	CS(5–4)^t	40.19 ± 0.01	-30.48 ± 0.05	2.0 ± 0.2	1.4 ± 0.1	107 ± 7	1.9 ± 0.2	1.2 ± 0.1	107 ± 7	10.02 ± 0.91	1.6 ± 0.12	0.13 ± 0.18
11	CS(5–4)^t	40.25 ± 0.00	-29.66 ± 0.04	1.8 ± 0.1	1.3 ± 0.1	60 ± 8	1.7 ± 0.2	1.1 ± 0.1	60 ± 8	7.65 ± 0.65	1.4 ± 0.10	0.24 ± 0.15
12	CS(5–4)^n	39.98 ± 0.01	-30.57 ± 0.08	1.8 ± 0.2	1.1 ± 0.1	145 ± 8	1.7 ± 0.3	0.8 ± 0.2	148 ± 10	5.74 ± 0.78	1.4 ± 0.15	0.02 ± 0.03
13	CS(5–4)^t	39.49 ± 0.00	-28.46 ± 0.08	1.4 ± 0.2	0.9 ± 0.1	30 ± 8	1.3 ± 0.2	0.6 ± 0.2	30 ± 8	3.66 ± 0.58	1.3 ± 0.15	0.16 ± 0.02

Notes. For details on the procedure see Sect. 3.2.4. A finding chart is provided in Fig. A.10 $^{(t)}$ tapered beam size, i.e. 0.65" in band 6 and 7, 1.5" in band 3 ; $^{(n)}$ natural beam size at the given frequency

Table A.2: *Continued. Results of 2D Gauss fits to the molecular sources: Source positions are relative to $17^h40^m00.00^s$ and $-29°00'00.00''$ (J2000). (Credit: Moser et al. (2016b), reproduced with permission ©ESO.)*

region	line	peak position		convolved size			deconvolved size			flux		
		R.A. [s]	Dec [”]	$d_{\mathrm{maj,c}}$ [”]	$d_{\mathrm{min,c}}$ [”]	PA_c [°]	$d_{\mathrm{maj,d}}$ [”]	$d_{\mathrm{min,d}}$ [”]	PA_d [°]	S_{int} [Jy km s^{-1}]	S_{peak} [Jy bm^{-1} km s^{-1}]	S_{off} [Jy bm^{-1} km s^{-1}]
	SiO(6–5)^t	39.49 ± 0.00	-28.46 ± 0.05	0.4 ± 0.1	0.3 ± 0.1	25 ± 45	-	-	-	0.05 ± 0.04	0.2 ± 0.04	0.08 ± 0.01
	SO(7–6)^n	39.50 ± 0.01	-28.43 ± 0.14	0.8 ± 0.4	0.3 ± 0.0	27 ± 3	-	-	-	0.22 ± 0.13	0.4 ± 0.08	0.13 ± 0.01
	CH_3OH(7–6)^t	39.47 ± 0.00	-28.64 ± 0.01	0.3 ± 0.0	0.2 ± 0.0	83 ± 12	-	-	-	0.04 ± 0.03	0.3 ± 0.05	0.16 ± 0.01
14	CS(5–4)^t	40.47 ± 0.00	-30.60 ± 0.06	1.1 ± 0.2	0.9 ± 0.1	43 ± 29	0.8 ± 0.2	0.6 ± 0.2	43 ± 29	3.97 ± 0.72	1.8 ± 0.23	0.27 ± 0.03
	SiO(6–5)^n	40.47 ± 0.00	-30.58 ± 0.01	0.4 ± 0.0	0.3 ± 0.0	50 ± 4	-	-	-	0.25 ± 0.04	0.9 ± 0.05	0.09 ± 0.01
15	CS(5–4)^n	40.47 ± 0.00	-28.92 ± 0.03	0.9 ± 0.1	0.8 ± 0.1	152 ± 19	0.6 ± 0.1	0.2 ± 0.2	172 ± 22	1.61 ± 0.17	1.1 ± 0.08	0.01 ± 0.02
	C_2H(3–2)^t	40.46 ± 0.00	-28.90 ± 0.02	0.3 ± 0.0	0.3 ± 0.0	128 ± 26	-	-	-	0.11 ± 0.04	0.5 ± 0.05	0.14 ± 0.01
16	SiO(6–5)^n	40.47 ± 0.01	-29.06 ± 0.09	1.2 ± 0.4	0.4 ± 0.1	57 ± 4	-	-	-	0.65 ± 0.21	0.5 ± 0.09	0.09 ± 0.02
	SiO(8–7)^n	40.44 ± 0.00	-29.18 ± 0.03	0.3 ± 0.1	0.2 ± 0.0	135 ± 28	-	-	-	0.15 ± 0.09	0.4 ± 0.09	0.16 ± 0.01
17	SiO(6–5)^t	40.55 ± 0.00	-28.27 ± 0.06	1.2 ± 0.1	0.9 ± 0.1	20 ± 12	1.0 ± 0.2	0.6 ± 0.1	20 ± 12	2.66 ± 0.39	1.1 ± 0.12	0.06 ± 0.04
	SiO(8–7)^t	40.55 ± 0.00	-28.29 ± 0.02	1.1 ± 0.1	0.7 ± 0.1	98 ± 7	0.8 ± 0.1	0.2 ± 0.1	98 ± 7	2.91 ± 0.37	1.7 ± 0.15	0.02 ± 0.12
18	SiO(6–5)^n	40.62 ± 0.00	-23.98 ± 0.01	0.7 ± 0.0	0.6 ± 0.0	96 ± 11	-	-	-	1.21 ± 0.10	1.2 ± 0.06	-0.11 ± 0.02
	SiO(8–7)^n	40.62 ± 0.01	-23.99 ± 0.11	0.8 ± 0.3	0.6 ± 0.2	57 ± 49	0.7 ± 0.4	0.4 ± 0.3	51 ± 58	6.40 ± 3.50	2.7 ± 1.10	-1.50 ± 0.59
19	CS(5–4)^n	40.45 ± 0.01	-20.15 ± 0.07	0.9 ± 0.3	0.6 ± 0.1	115 ± 31	0.4 ± 0.4	0.1 ± 0.4	137 ± 61	0.91 ± 0.39	0.8 ± 0.19	0.27 ± 0.01
	C_2H(3–2)^t	40.41 ± 0.01	-20.43 ± 0.10	1.4 ± 0.4	0.7 ± 0.1	56 ± 9	1.2 ± 0.5	0.1 ± 0.4	56 ± 9	1.19 ± 0.39	0.6 ± 0.13	0.10 ± 0.04
20	CS(5–4)^t	40.09 ± 0.00	-21.53 ± 0.06	1.5 ± 0.2	1.1 ± 0.1	48 ± 12	1.3 ± 0.2	0.8 ± 0.1	48 ± 12	6.80 ± 0.89	1.8 ± 0.19	0.24 ± 0.03
	SO(7–6)^n	40.13 ± 0.00	-21.09 ± 0.01	0.4 ± 0.0	0.2 ± 0.0	102 ± 4	-	-	-	0.10 ± 0.03	0.5 ± 0.04	0.10 ± 0.00
	C_2H(3–2)^t	40.11 ± 0.00	-20.96 ± 0.03	0.7 ± 0.1	0.6 ± 0.1	49 ± 35	-	-	-	0.63 ± 0.15	0.7 ± 0.10	0.10 ± 0.03
	SiO(8–7)^t	40.07 ± 0.00	-20.96 ± 0.02	0.6 ± 0.1	0.4 ± 0.0	74 ± 6	-	-	-	1.01 ± 0.26	2.0 ± 0.21	0.31 ± 0.02
21	CS(5–4)^t	40.38 ± 0.00	-27.09 ± 0.06	1.3 ± 0.1	0.9 ± 0.1	13 ± 12	1.1 ± 0.2	0.7 ± 0.1	13 ± 12	2.18 ± 0.30	0.8 ± 0.08	0.25 ± 0.03
	C_2H(3–2)^t	40.38 ± 0.01	-27.07 ± 0.07	1.5 ± 0.3	0.7 ± 0.1	114 ± 7	1.4 ± 0.4	0.3 ± 0.2	114 ± 7	1.91 ± 0.42	0.7 ± 0.12	0.03 ± 0.06

Notes. For details on the procedure see Sect. 3.2.4. A finding chart is provided in Fig. A.10 $^{(t)}$ tapered beam size, i.e. 0.65” in band 6 and 7, 1.5” in band 3 ; $^{(n)}$ natural beam size at the given frequency

Table A.2: *Continued. Results of 2D Gauss fits to the molecular sources: Source positions are relative to $17^h40^m00.00^s$ and $-29°00'00.00''$(J2000). (Credit: Moser* et al. *(2016b), reproduced with permission ©ESO.)*

region	line	peak position		convolved size			deconvolved size			flux		
		R.A. [s]	Dec [”]	$d_{maj,c}$ [”]	$d_{min,c}$ [”]	PA_c [°]	$d_{maj,d}$ [”]	$d_{min,d}$ [”]	PA_d [°]	S_{int} [Jy km s^{-1}]	S_{peak} [Jy bm^{-1} km s^{-1}]	S_{off} [Jy bm^{-1} km s^{-1}]
22	CS(5–4)^n	39.81 ± 0.00	-18.58 ± 0.03	0.9 ± 0.1	0.7 ± 0.1	99 ± 13	0.6 ± 0.2	0.4 ± 0.2	102 ± 87	2.50 ± 0.35	1.6 ± 0.15	0.12 ± 0.02
	C_2H(3–2)^t	39.82 ± 0.00	-18.52 ± 0.01	0.5 ± 0.1	0.3 ± 0.0	80 ± 4	-	-	-	0.37 ± 0.08	1.0 ± 0.08	0.14 ± 0.01
	CH_3OH(7–6)^n	39.80 ± 0.01	-18.44 ± 0.05	0.4 ± 0.2	0.2 ± 0.0	120 ± 5	-	-	-	0.11 ± 0.10	0.3 ± 0.08	0.16 ± 0.01
23	SiO(6–5)^t	39.51 ± 0.00	-37.06 ± 0.04	1.2 ± 0.1	0.8 ± 0.1	57 ± 6	1.1 ± 0.2	0.4 ± 0.1	57 ± 6	3.85 ± 0.50	1.7 ± 0.16	0.14 ± 0.02
24	CS(5–4)^t	39.45 ± 0.00	-22.00 ± 0.11	1.1 ± 0.3	0.6 ± 0.1	169 ± 13	-	-	-	1.38 ± 0.43	0.9 ± 0.18	0.18 ± 0.02
25	CS(5–4)^t	40.24 ± 0.02	-33.06 ± 0.17	2.0 ± 0.8	0.7 ± 0.2	116 ± 7	1.9 ± 0.9	0.2 ± 0.4	116 ± 7	1.64 ± 0.67	0.5 ± 0.16	0.21 ± 0.02
26	CS(5–4)^n	40.32 ± 0.00	-35.01 ± 0.02	0.8 ± 0.1	0.5 ± 0.1	101 ± 9	-	-	-	0.53 ± 0.14	0.6 ± 0.08	0.10 ± 0.01
26	SiO(6–5)^n	40.27 ± 0.01	-34.24 ± 0.03	0.5 ± 0.3	0.3 ± 0.1	93 ± 16	-	-	-	0.04 ± 0.04	0.1 ± 0.05	0.09 ± 0.00
27	CS(5–4)^n	40.79 ± 0.01	-26.52 ± 0.05	1.2 ± 0.3	0.6 ± 0.1	112 ± 7	-	-	-	1.40 ± 0.42	1.0 ± 0.18	0.22 ± 0.01
	SiO(6–5)^n	40.80 ± 0.01	-26.60 ± 0.05	0.5 ± 0.2	0.3 ± 0.1	121 ± 13	-	-	-	0.11 ± 0.08	0.3 ± 0.07	0.11 ± 0.00
T1	CS(5–4)^n	39.27 ± 0.00	-18.36 ± 0.11	1.9 ± 0.3	0.9 ± 0.1	179 ± 5	1.8 ± 0.3	0.5 ± 0.2	180 ± 5	12.30 ± 1.80	3.3 ± 0.39	0.28 ± 0.04
	HC_3N(27–26)^t	39.24 ± 0.01	-18.79 ± 0.09	0.5 ± 0.3	0.2 ± 0.0	48 ± 8	-	-	-	0.06 ± 0.08	0.2 ± 0.08	0.17 ± 0.01
	SiO(6–5)^t	39.25 ± 0.01	-18.44 ± 0.19	1.0 ± 0.5	0.5 ± 0.2	154 ± 17	-	-	-	0.75 ± 0.46	0.6 ± 0.21	0.26 ± 0.01
	SO(7–6)^n	39.27 ± 0.00	-18.54 ± 0.11	0.7 ± 0.3	0.4 ± 0.1	158 ± 10	-	-	-	0.64 ± 0.36	0.9 ± 0.23	0.30 ± 0.01
	CH_3OH(7–6)^t	39.26 ± 0.01	-17.92 ± 0.22	1.1 ± 0.5	0.9 ± 0.4	178 ± 70	0.9 ± 0.6	0.6 ± 0.5	178 ± 70	4.00 ± 2.40	1.7 ± 0.75	0.72 ± 0.09
	SiO(8–7)^t	39.25 ± 0.01	-19.28 ± 0.04	0.6 ± 0.3	0.3 ± 0.0	103 ± 8	-	-	-	0.91 ± 0.82	2.1 ± 0.64	1.02 ± 0.11
T2	CS(5–4)^n	39.23 ± 0.01	-15.12 ± 0.08	1.5 ± 0.2	0.9 ± 0.1	133 ± 9	1.3 ± 0.3	0.6 ± 0.2	137 ± 16	8.50 ± 1.60	3.0 ± 0.43	0.36 ± 0.05
	$H^{13}CO^+$(3–2)^t	39.25 ± 0.00	-15.74 ± 0.01	0.6 ± 0.1	0.2 ± 0.0	82 ± 1	-	-	-	0.37 ± 0.16	1.5 ± 0.13	0.31 ± 0.05
	SO(7–6)^n	39.25 ± 0.00	-15.44 ± 0.03	0.3 ± 0.1	0.3 ± 0.1	19 ± 254	-	-	-	0.10 ± 0.08	0.5 ± 0.12	0.29 ± 0.03
T3	CS(5–4)^n	39.34 ± 0.00	-14.49 ± 0.03	0.8 ± 0.1	0.6 ± 0.1	116 ± 11	-	-	-	2.31 ± 0.54	2.2 ± 0.30	0.24 ± 0.04
	SO(7–6)^n	39.35 ± 0.00	-14.40 ± 0.01	0.5 ± 0.1	0.3 ± 0.0	91 ± 5	-	-	-	0.64 ± 0.22	2.1 ± 0.23	0.45 ± 0.03

Notes. For details on the procedure see Sect. 3.2.4. A finding chart is provided in Fig. A.10 $^{(t)}$ tapered beam size, i.e. 0.65” in band 6 and 7, 1.5” in band 3 ; $^{(n)}$ natural beam size at the given frequency

Table A.2: *Continued. Results of 2D Gauss fits to the molecular sources: Source positions are relative to $17^h40^m00.00^s$ and $-29°00'00.00''$ (J2000). (Credit: Moser et al. (2016b), reproduced with permission ©ESO.)*

region	line	peak position		convolved size			deconvolved size			flux		
		R.A. [s]	Dec [”]	$d_{\mathrm{maj,c}}$ [”]	$d_{\mathrm{min,c}}$ [”]	PA_c [°]	$d_{\mathrm{maj,d}}$ [”]	$d_{\mathrm{min,d}}$ [”]	PA_d [°]	S_{int} [Jy km s^{-1}]	S_{peak} [Jy bm^{-1} km s^{-1}]	S_{off} [Jy bm^{-1} km s^{-1}]
T4	CS(5–4)^n	39.14 ± 0.01	-13.25 ± 0.03	1.3 ± 0.2	0.7 ± 0.1	94 ± 7	1.0 ± 0.2	0.4 ± 0.2	92 ± 13	9.40 ± 1.50	4.5 ± 0.51	0.35 ± 0.09
T5	CS(5–4)^t	39.11 ± 0.01	-15.48 ± 0.12	2.5 ± 0.5	0.7 ± 0.1	56 ± 3	2.4 ± 0.5	0.4 ± 0.3	56 ± 3	6.90 ± 1.30	1.6 ± 0.24	0.37 ± 0.07
	SiO(6–5)^t	39.08 ± 0.00	-15.63 ± 0.01	0.3 ± 0.1	0.2 ± 0.0	79 ± 8	-	-	-	0.21 ± 0.09	1.2 ± 0.14	0.40 ± 0.02
	SO(7–6)^n	39.12 ± 0.00	-15.18 ± 0.03	0.4 ± 0.1	0.2 ± 0.0	126 ± 5	-	-	-	0.29 ± 0.16	1.1 ± 0.16	0.35 ± 0.02
T6	CS(5–4)^t	39.04 ± 0.01	-16.99 ± 0.05	1.6 ± 0.2	1.0 ± 0.1	71 ± 7	1.5 ± 0.2	0.7 ± 0.1	71 ± 7	11.20 ± 1.60	3.0 ± 0.35	0.25 ± 0.20
	N_2H^+(1–0)^n	39.02 ± 0.01	-17.43 ± 0.09	2.8 ± 0.4	1.3 ± 0.1	61 ± 4	-	-	-	0.64 ± 0.12	0.5 ± 0.05	0.41 ± 0.04
	CH_3OH(8–7)^t	39.08 ± 0.01	-16.90 ± 0.09	1.7 ± 0.4	0.8 ± 0.1	62 ± 4	-	-	-	0.13 ± 0.05	0.2 ± 0.03	0.11 ± 0.01
T7	CS(5–4)^t	39.07 ± 0.00	-18.51 ± 0.04	1.0 ± 0.1	0.8 ± 0.1	165 ± 14	0.8 ± 0.1	0.5 ± 0.1	165 ± 14	4.32 ± 0.57	2.2 ± 0.20	0.00 ± 0.20
	SiO(6–5)^t	39.08 ± 0.01	-18.46 ± 0.05	0.3 ± 0.3	0.2 ± 0.1	89 ± 58	-	-	-	0.02 ± 0.06	0.1 ± 0.09	0.25 ± 0.01
	C_2H(3–2)^t	39.10 ± 0.00	-18.55 ± 0.02	0.4 ± 0.1	0.3 ± 0.0	128 ± 10	-	-	-	0.24 ± 0.12	1.0 ± 0.15	0.33 ± 0.13
	^{13}CS(2–1)^n	39.07 ± 0.01	-18.39 ± 0.33	3.9 ± 0.8	1.9 ± 0.3	159 ± 7	-	-	-	0.36 ± 0.08	0.1 ± 0.03	-8.00 ± 0.01
T8	CS(5–4)^t	39.13 ± 0.01	-19.41 ± 0.10	0.9 ± 0.3	0.7 ± 0.2	122 ± 43	0.7 ± 0.4	0.3 ± 0.3	122 ± 43	2.13 ± 0.99	1.4 ± 0.42	0.37 ± 0.06
	SiO(6–5)^t	39.18 ± 0.01	-19.30 ± 0.05	0.5 ± 0.2	0.4 ± 0.1	113 ± 47	-	-	-	0.20 ± 0.15	0.4 ± 0.14	0.23 ± 0.02
	CH_3OH(7–6)^t	39.12 ± 0.00	-19.59 ± 0.04	0.6 ± 0.1	0.5 ± 0.1	37 ± 24	-	-	-	1.91 ± 0.60	2.6 ± 0.42	0.30 ± 0.39
	CH_3OH(8–7)^t	39.10 ± 0.00	-19.83 ± 0.05	0.8 ± 0.2	0.7 ± 0.1	65 ± 69	-	-	-	0.04 ± 0.03	0.2 ± 0.03	0.10 ± 0.01
T9	$H^{13}CO^+$(3–2)^t	38.93 ± 0.01	-19.19 ± 1.12	1.5 ± 2.6	0.2 ± 0.1	5 ± 4	-	-	-	0.29 ± 0.58	0.3 ± 0.23	0.45 ± 0.06
	SiO(6–5)^t	38.93 ± 0.00	-19.23 ± 0.02	0.4 ± 0.0	0.2 ± 0.0	145 ± 2	-	-	-	0.22 ± 0.07	1.4 ± 0.09	0.42 ± 0.02
T10	CS(5–4)^n	38.88 ± 0.00	-21.01 ± 0.06	2.6 ± 0.2	1.1 ± 0.1	47 ± 3	2.5 ± 0.2	0.9 ± 0.1	46 ± 3	30.70 ± 2.40	4.8 ± 0.33	-0.87 ± 0.24
	HC_3N(27–26)^t	38.87 ± 0.02	-21.00 ± 0.26	0.9 ± 0.8	0.5 ± 0.3	46 ± 36	-	-	-	0.33 ± 0.43	0.3 ± 0.24	0.30 ± 0.03
	$H^{13}CO^+$(3–2)^t	38.87 ± 0.01	-20.54 ± 0.23	1.1 ± 0.6	0.5 ± 0.1	9 ± 13	-	-	-	1.29 ± 0.79	0.9 ± 0.35	0.40 ± 0.07
	SiO(6–5)^t	38.89 ± 0.00	-20.62 ± 0.04	0.4 ± 0.1	0.3 ± 0.1	18 ± 31	-	-	-	0.31 ± 0.20	1.0 ± 0.23	0.43 ± 0.03

Notes. For details on the procedure see Sect. 3.2.4. A finding chart is provided in Fig. A.10 $^{(t)}$ tapered beam size, i.e. 0.65” in band 6 and 7, 1.5” in band 3 ; $^{(n)}$ natural beam size at the given frequency

Table A.2: *Continued. Results of 2D Gauss fits to the molecular sources: Source positions are relative to $17^h40^m00.00^s$ and $-29°00'00.00''$(J2000). (Credit: Moser et al. (2016b), reproduced with permission ©ESO.)*

region	line	peak position		convolved size			deconvolved size			flux		
		R.A. [s]	Dec ["]	$d_{\mathrm{maj,c}}$ ["]	$d_{\mathrm{min,c}}$ ["]	PA_c [°]	$d_{\mathrm{maj,d}}$ ["]	$d_{\mathrm{min,d}}$ ["]	PA_d [°]	S_{int} [Jy km s^{-1}]	S_{peak} [Jy bm^{-1} km s^{-1}]	S_{off} [Jy bm^{-1} km s^{-1}]
	SiO(6–5)^n	38.89 ± 0.01	-20.45 ± 0.27	0.7 ± 0.7	0.3 ± 0.1	150 ± 9	-	-	-	0.20 ± 0.30	0.4 ± 0.20	0.28 ± 0.02
	SO(7–6)^n	38.88 ± 0.00	-20.93 ± 0.04	0.6 ± 0.1	0.3 ± 0.0	164 ± 5	-	-	-	1.36 ± 0.36	2.9 ± 0.30	0.42 ± 0.03
	C_2H(3–2)^t	38.86 ± 0.01	-21.14 ± 0.18	1.8 ± 0.5	0.6 ± 0.1	34 ± 5	-	-	-	6.00 ± 1.70	2.3 ± 0.47	0.26 ± 0.23
	N_2H^+(1–0)^n	38.85 ± 0.01	-20.98 ± 0.20	3.5 ± 0.5	2.2 ± 0.3	33 ± 9	3.1 ± 0.7	1.1 ± 0.9	30 ± 11	1.90 ± 0.34	0.8 ± 0.10	-80.00 ± 0.10
	CH_3OH(8–7)^t	38.89 ± 0.01	-20.82 ± 0.11	2.1 ± 0.3	1.5 ± 0.1	26 ± 11	-	-	-	0.80 ± 0.14	0.6 ± 0.07	0.02 ± 0.04
T10-2	N_2H^+(1–0)^n	39.02 ± 0.01	-17.95 ± 0.19	6.4 ± 0.5	3.1 ± 0.2	25 ± 3	6.2 ± 0.5	2.4 ± 0.3	24 ± 3	5.88 ± 0.46	0.9 ± 0.06	-0.06 ± 0.07
T11	SiO(6–5)^t	38.79 ± 0.00	-19.92 ± 0.02	0.4 ± 0.0	0.3 ± 0.0	151 ± 11	-	-	-	0.62 ± 0.18	2.1 ± 0.21	0.41 ± 0.03
	SO(7–6)^n	38.83 ± 0.00	-20.06 ± 0.03	0.4 ± 0.1	0.2 ± 0.0	13 ± 7	-	-	-	0.33 ± 0.14	1.4 ± 0.17	0.36 ± 0.05
SEW1	SiO(6–5)^n	40.39 ± 0.01	-42.97 ± 0.09	0.9 ± 0.3	0.7 ± 0.2	120 ± 36	0.6 ± 0.4	0.3 ± 0.3	135 ± 64	1.21 ± 0.55	0.8 ± 0.23	0.30 ± 0.02
	SO(7–6)^n	40.41 ± 0.00	-42.81 ± 0.04	0.4 ± 0.1	0.4 ± 0.1	46 ± 69	-	-	-	0.40 ± 0.23	1.0 ± 0.24	0.54 ± 0.02
	C_2H(3–2)^t	40.41 ± 0.00	-42.69 ± 0.03	0.5 ± 0.2	0.3 ± 0.1	68 ± 14	-	-	-	0.45 ± 0.27	1.2 ± 0.26	0.53 ± 0.05
SEW1-2	$H^{13}CO^+$(3–2)^t	40.36 ± 0.00	-42.89 ± 0.02	0.4 ± 0.1	0.2 ± 0.0	111 ± 7	-	-	-	0.10 ± 0.08	0.5 ± 0.09	0.21 ± 0.04
SEW2	SiO(6–5)^n	40.34 ± 0.01	-43.00 ± 0.07	1.0 ± 0.3	0.6 ± 0.1	80 ± 20	0.7 ± 0.4	0.2 ± 0.3	72 ± 79	0.97 ± 0.42	0.6 ± 0.18	0.16 ± 0.02
	SO(7–6)^n	40.32 ± 0.00	-43.25 ± 0.05	1.3 ± 0.1	1.0 ± 0.1	34 ± 19	1.1 ± 0.2	0.8 ± 0.1	28 ± 20	7.36 ± 0.82	2.2 ± 0.19	-0.28 ± 0.13
	C_2H(3–2)^t	40.31 ± 0.01	-43.22 ± 0.05	1.9 ± 0.3	0.6 ± 0.0	66 ± 2	-	-	-	8.40 ± 1.30	3.2 ± 0.34	0.66 ± 0.08
	^{13}CS(2–1)^n	40.33 ± 0.00	-42.89 ± 0.23	1.5 ± 0.5	0.7 ± 0.1	6 ± 5	-	-	-	0.06 ± 0.04	0.2 ± 0.04	0.09 ± 0.01
SEW3	CS(5–4)^t	40.35 ± 0.00	-43.97 ± 0.04	1.3 ± 0.1	1.1 ± 0.1	103 ± 17	1.2 ± 0.2	0.9 ± 0.1	103 ± 17	16.40 ± 1.90	4.9 ± 0.45	3.35 ± 0.13
	SiO(6–5)^n	40.36 ± 0.01	-43.95 ± 0.07	0.8 ± 0.3	0.5 ± 0.1	59 ± 19	-	-	-	0.98 ± 0.53	1.0 ± 0.31	0.37 ± 0.03
	SO(7–6)^n	40.42 ± 0.03	-44.07 ± 0.26	2.3 ± 1.1	1.2 ± 0.5	114 ± 22	2.2 ± 1.2	1.0 ± 0.7	115 ± 27	5.10 ± 2.50	0.7 ± 0.31	0.33 ± 0.06
	^{13}CS(2–1)^n	40.35 ± 0.01	-44.05 ± 0.12	1.2 ± 0.3	0.8 ± 0.1	146 ± 15	-	-	-	0.07 ± 0.04	0.2 ± 0.04	0.08 ± 0.01
SEW4	CS(5–4)^t	40.21 ± 0.00	-43.85 ± 0.04	1.9 ± 0.1	1.5 ± 0.1	51 ± 10	1.8 ± 0.1	1.3 ± 0.1	51 ± 10	38.60 ± 2.70	6.0 ± 0.37	-1.24 ± 1.93

Notes. For details on the procedure see Sect. 3.2.4. A finding chart is provided in Fig. A.10 $^{(t)}$ tapered beam size, i.e. 0.65" in band 6 and 7, 1.5" in band 3 ; $^{(n)}$ natural beam size at the given frequency

Table A.2: *Continued. Results of 2D Gauss fits to the molecular sources: Source positions are relative to $17^h40^m00.00^s$ and $-29°00'00.00''$(J2000). (Credit: Moser* et al. *(2016b), reproduced with permission ©ESO.)*

		peak position		convolved size			deconvolved size			flux		
region	line	R.A. [s]	Dec [”]	$d_{\mathrm{maj,c}}$ [”]	$d_{\mathrm{min,c}}$ [”]	PA_c [°]	$d_{\mathrm{maj,d}}$ [”]	$d_{\mathrm{min,d}}$ [”]	PA_d [°]	S_{int} [Jy km s^{-1}]	S_{peak} [Jy bm^{-1} km s^{-1}]	S_{off}
	$C_2H(3–2)^t$	40.24 ± 0.01	-43.89 ± 0.05	0.5 ± 0.3	0.3 ± 0.1	69 ± 12	-	-	-	0.28 ± 0.32	1.0 ± 0.32	0.72 ± 0.09
SWE4-1	$C_2H(3–2)^t$	40.14 ± 0.00	-44.22 ± 0.01	0.7 ± 0.1	0.2 ± 0.0	86 ± 1	-	-	-	0.90 ± 0.25	2.3 ± 0.17	0.31 ± 0.18
SEW5	$CS(5–4)^n$	40.78 ± 0.01	-42.57 ± 0.04	1.6 ± 0.4	0.7 ± 0.1	84 ± 6	1.4 ± 0.5	0.3 ± 0.2	82 ± 10	4.20 ± 1.10	1.8 ± 0.34	0.35 ± 0.04
	$^{13}CS(2–1)^n$	40.85 ± 0.01	-42.53 ± 0.02	0.9 ± 0.2	0.4 ± 0.0	80 ± 3	-	-	-	0.02 ± 0.02	0.2 ± 0.02	0.10 ± 0.00
SEW6	$CS(5–4)^t$	40.88 ± 0.00	-38.92 ± 0.08	1.2 ± 0.2	0.8 ± 0.1	35 ± 17	1.0 ± 0.3	0.5 ± 0.2	35 ± 17	3.39 ± 0.72	1.4 ± 0.22	0.30 ± 0.07
	$C_2H(3–2)^t$	40.89 ± 0.01	-38.95 ± 0.05	0.6 ± 0.2	0.4 ± 0.1	55 ± 14	-	-	-	0.46 ± 0.23	0.8 ± 0.18	0.31 ± 0.01
SEW7	$CS(5–4)^n$	40.96 ± 0.01	-37.55 ± 0.09	1.0 ± 0.3	0.6 ± 0.1	142 ± 14	-	-	-	1.64 ± 0.54	1.2 ± 0.24	0.28 ± 0.02
	$C_2H(3–2)^t$	40.95 ± 0.00	-37.10 ± 0.03	0.6 ± 0.1	0.4 ± 0.0	145 ± 11	-	-	-	0.96 ± 0.28	1.9 ± 0.23	0.37 ± 0.03
SEW8	$CS(5–4)^n$	40.48 ± 0.01	-37.88 ± 0.03	1.4 ± 0.2	0.7 ± 0.1	82 ± 5	1.2 ± 0.3	0.3 ± 0.2	80 ± 8	2.25 ± 0.36	1.1 ± 0.12	0.14 ± 0.02
	$C_2H(3–2)^t$	40.48 ± 0.01	-38.31 ± 0.08	1.7 ± 0.4	0.4 ± 0.0	66 ± 2	-	-	-	1.95 ± 0.48	1.2 ± 0.17	0.40 ± 0.04
SEW9	$CS(5–4)^n$	41.11 ± 0.01	-38.04 ± 0.08	1.2 ± 0.2	1.0 ± 0.2	40 ± 65	1.0 ± 0.3	0.7 ± 0.3	25 ± 89	7.50 ± 1.80	2.8 ± 0.50	0.40 ± 0.14
	$SiO(6–5)^t$	41.12 ± 0.00	-38.08 ± 0.03	0.7 ± 0.2	0.3 ± 0.0	108 ± 6	-	-	-	0.47 ± 0.18	0.9 ± 0.14	0.16 ± 0.32
	$SO(7–6)^n$	41.09 ± 0.00	-38.18 ± 0.05	0.4 ± 0.1	0.3 ± 0.1	9 ± 47	-	-	-	0.14 ± 0.13	0.5 ± 0.16	0.35 ± 0.01
	$C_2H(3–2)^t$	41.12 ± 0.00	-37.61 ± 0.05	0.5 ± 0.2	0.2 ± 0.0	138 ± 2	-	-	-	0.23 ± 0.15	1.0 ± 0.14	0.34 ± 0.08
SEW10	$H^{13}CO^+(3–2)^t$	40.93 ± 0.00	-35.61 ± 0.00	0.4 ± 0.0	0.3 ± 0.0	101 ± 5	-	-	-	0.26 ± 0.03	1.0 ± 0.03	-0.07 ± 0.57
	$SiO(6–5)^n$	40.93 ± 0.00	-35.65 ± 0.00	0.5 ± 0.0	0.3 ± 0.0	76 ± 1	-	-	-	0.47 ± 0.04	1.4 ± 0.03	0.02 ± 0.05
SEW11	$CS(5–4)^n$	40.24 ± 0.01	-37.93 ± 0.08	1.4 ± 0.3	0.8 ± 0.1	52 ± 8	1.2 ± 0.3	0.3 ± 0.2	47 ± 13	1.35 ± 0.29	0.6 ± 0.09	0.13 ± 0.03
	$C_2H(3–2)^t$	40.25 ± 0.00	-37.89 ± 0.02	0.6 ± 0.1	0.4 ± 0.0	63 ± 6	-	-	-	0.52 ± 0.12	1.1 ± 0.10	0.33 ± 0.03
SEW12	$^{13}CS(2–1)^n$	40.51 ± 0.01	-42.47 ± 0.59	2.7 ± 1.4	1.3 ± 0.4	176 ± 13	-	-	-	0.25 ± 0.16	0.2 ± 0.08	0.10 ± 0.01
	$N_2H^+(1–0)^n$	40.96 ± 0.03	-40.28 ± 0.20	3.5 ± 0.8	2.4 ± 0.5	83 ± 21	2.9 ± 1.0	1.8 ± 0.9	80 ± 61	2.50 ± 0.69	0.9 ± 0.19	0.24 ± 0.01
CND-1	$CS(5–4)^t$	40.00 ± 0.01	-13.19 ± 0.35	2.5 ± 0.9	0.9 ± 0.2	17 ± 8	2.5 ± 0.9	0.6 ± 0.4	17 ± 8	5.00 ± 1.70	0.9 ± 0.27	0.36 ± 0.02

Notes. For details on the procedure see Sect. 3.2.4. A finding chart is provided in Fig. A.10 $^{(t)}$ tapered beam size, i.e. 0.65” in band 6 and 7, 1.5” in band 3 ; $^{(n)}$ natural beam size at the given frequency

Table A.2: *Continued. Results of 2D Gauss fits to the molecular sources: Source positions are relative to $17^h40^m00.00^s$ and $-29°00'00.00''$(J2000). (Credit: Moser* et al. *(2016b), reproduced with permission ©ESO.)*

region	line	peak position		convolved size			deconvolved size			flux		
		R.A. [s]	Dec [”]	$d_{\mathrm{maj,c}}$ [”]	$d_{\mathrm{min,c}}$ [”]	PA_c [°]	$d_{\mathrm{maj,d}}$ [”]	$d_{\mathrm{min,d}}$ [”]	PA_d [°]	S_{int} [Jy km s^{-1}]	S_{peak} [Jy bm^{-1} km s^{-1}]	S_{off} [Jy bm^{-1} km s^{-1}]
	SiO(6–5)^n	40.02 ± 0.01	-12.84 ± 0.08	0.8 ± 0.3	0.3 ± 0.0	127 ± 5	-	-	-	0.60 ± 0.33	0.9 ± 0.20	0.29 ± 0.01
	SO(7–6)^n	40.06 ± 0.01	-12.60 ± 0.02	0.9 ± 0.3	0.3 ± 0.0	91 ± 5	-	-	-	0.79 ± 0.39	1.1 ± 0.22	0.30 ± 0.01
	CH_3OH(7–6)^t	40.01 ± 0.00	-13.99 ± 0.05	0.4 ± 0.1	0.2 ± 0.0	3 ± 8	-	-	-	0.28 ± 0.21	1.4 ± 0.27	0.66 ± 0.04
	N_2H^+(1–0)^n	40.02 ± 0.07	-12.63 ± 0.55	4.2 ± 2.2	2.7 ± 1.1	111 ± 36	3.8 ± 2.4	2.1 ± 1.3	113 ± 40	6.10 ± 3.50	1.6 ± 0.76	-1.27 ± 3.01
	CH_3OH(8–7)^t	39.99 ± 0.03	-14.27 ± 0.90	1.0 ± 2.1	0.7 ± 1.0	174 ± 182	-	-	-	0.01 ± 0.04	0.03 ± 0.05	0.08 ± 0.01
CND-2	CS(5–4)^t	40.47 ± 0.00	-16.09 ± 0.08	1.5 ± 0.2	0.7 ± 0.1	14 ± 4	1.4 ± 0.2	0.3 ± 0.2	14 ± 4	4.56 ± 0.67	1.7 ± 0.19	0.22 ± 0.02
	C_2H(3–2)^t	40.43 ± 0.01	-16.86 ± 0.04	0.6 ± 0.2	0.3 ± 0.0	115 ± 9	-	-	-	0.33 ± 0.23	0.8 ± 0.19	0.32 ± 0.02
	CH_3OH(7–6)^t	40.43 ± 0.02	-17.27 ± 0.17	0.4 ± 0.6	0.3 ± 0.4	73 ± 263	-	-	-	0.04 ± 0.15	0.1 ± 0.19	0.36 ± 0.01
	SiO(8–7)^t	40.45 ± 0.00	-16.88 ± 0.09	0.5 ± 0.2	0.3 ± 0.1	3 ± 32	-	-	-	0.67 ± 0.58	1.7 ± 0.56	0.88 ± 0.09
CND-3	CS(5–4)^n	41.01 ± 0.02	-14.43 ± 0.13	1.8 ± 0.5	1.0 ± 0.2	63 ± 15	1.7 ± 0.6	0.8 ± 0.4	60 ± 45	11.70 ± 3.70	2.8 ± 0.73	0.80 ± 0.02
	C_2H(3–2)^t	40.94 ± 0.00	-14.52 ± 0.02	0.4 ± 0.1	0.1 ± 0.0	56 ± 1	-	-	-	0.35 ± 0.21	2.3 ± 0.20	0.65 ± 0.03
	N_2H^+(1–0)^n	41.12 ± 0.02	-13.87 ± 0.15	2.4 ± 0.8	1.1 ± 0.1	115 ± 6	-	-	-	0.39 ± 0.17	0.5 ± 0.10	0.12 ± 0.01
CND-4	CS(5–4)^n	41.18 ± 0.01	-18.36 ± 0.15	3.8 ± 0.4	2.4 ± 0.2	24 ± 8	3.7 ± 0.4	2.3 ± 0.2	23 ± 8	66.10 ± 6.60	3.4 ± 0.32	-0.34 ± 0.26
	C_2H(3–2)^t	41.15 ± 0.04	-17.51 ± 0.28	2.0 ± 1.3	0.6 ± 0.2	120 ± 11	-	-	-	4.60 ± 3.00	1.6 ± 0.75	0.82 ± 0.13
	^{13}CS(2–1)^n	41.26 ± 0.04	-17.78 ± 0.30	1.0 ± 1.4	0.7 ± 0.6	70 ± 92	-	-	-	0.01 ± 0.03	0.0 ± 0.04	0.10 ± 0.01
	N_2H^+(1–0)^n	41.29 ± 0.01	-19.04 ± 0.05	1.1 ± 0.2	0.7 ± 0.1	117 ± 10	-	-	-	0.14 ± 0.06	0.5 ± 0.07	0.16 ± 0.00
CND-5	CS(5–4)^n	41.16 ± 0.01	-20.35 ± 0.09	2.0 ± 0.2	1.8 ± 0.2	28 ± 31	1.9 ± 0.3	1.6 ± 0.2	24 ± 32	18.40 ± 2.20	2.4 ± 0.25	0.28 ± 0.03
	C_2H(3–2)^t	41.14 ± 0.00	-20.07 ± 0.08	0.5 ± 0.2	0.3 ± 0.1	8 ± 18	-	-	-	0.55 ± 0.43	1.5 ± 0.42	0.70 ± 0.06
	N_2H^+(1–0)^n	41.18 ± 0.01	-21.08 ± 0.06	1.3 ± 0.3	0.9 ± 0.1	93 ± 17	-	-	-	0.15 ± 0.07	0.4 ± 0.07	0.15 ± 0.01
CND-6	CS(5–4)^n	41.04 ± 0.00	-24.34 ± 0.13	1.8 ± 0.3	1.0 ± 0.1	2 ± 9	1.7 ± 0.3	0.7 ± 0.2	2 ± 9	7.90 ± 1.50	2.0 ± 0.31	0.42 ± 0.01
	SO(7–6)^n	41.03 ± 0.01	-24.07 ± 0.54	2.0 ± 1.3	0.4 ± 0.1	174 ± 4	-	-	-	1.04 ± 0.61	0.5 ± 0.17	0.25 ± 0.01

Notes. For details on the procedure see Sect. 3.2.4. A finding chart is provided in Fig. A.10 $^{(t)}$ tapered beam size, i.e. 0.65” in band 6 and 7, 1.5” in band 3 ; $^{(n)}$ natural beam size at the given frequency

Table A.2: *Continued. Results of 2D Gauss fits to the molecular sources: Source positions are relative to $17^h40^m00.00^s$ and $-29°00'00.00''$ (J2000). (Credit: Moser et al. (2016b), reproduced with permission ©ESO.)*

region	line	peak position		convolved size			deconvolved size			flux		
		R.A. [s]	Dec [”]	$d_{\mathrm{maj,c}}$ [”]	$d_{\mathrm{min,c}}$ [”]	PA_c [°]	$d_{\mathrm{maj,d}}$ [”]	$d_{\mathrm{min,d}}$ [”]	PA_d [°]	S_{int} [Jy km s^{-1}]	S_{peak} [Jy bm^{-1} km s^{-1}]	S_{off} [Jy bm^{-1} km s^{-1}]
	$N_2H^+(1–0)^n$	40.99 ± 0.01	-25.04 ± 0.16	2.6 ± 0.4	2.1 ± 0.3	133 ± 27	1.9 ± 0.9	1.1 ± 0.7	148 ± 40	1.19 ± 0.28	0.7 ± 0.11	0.11 ± 0.01
CND-7	$CS(5–4)^n$	41.01 ± 0.01	-26.83 ± 0.09	2.5 ± 0.3	1.4 ± 0.1	45 ± 6	2.4 ± 0.3	1.3 ± 0.2	44 ± 7	15.10 ± 1.60	1.9 ± 0.18	-0.11 ± 0.04
	$SiO(6–5)^n$	41.06 ± 0.05	-26.74 ± 0.59	2.1 ± 2.1	0.7 ± 0.4	49 ± 18	2.0 ± 2.1	0.3 ± 0.7	47 ± 19	0.62 ± 0.59	0.2 ± 0.12	0.13 ± 0.02
	$SO(7–6)^n$	41.02 ± 0.01	-27.11 ± 0.18	1.0 ± 0.5	0.4 ± 0.1	31 ± 7	-	-	-	0.45 ± 0.28	0.5 ± 0.14	0.17 ± 0.01
CND-8	$CS(5–4)^n$	40.79 ± 0.01	-26.52 ± 0.05	1.2 ± 0.3	0.6 ± 0.1	112 ± 6	-	-	-	1.43 ± 0.40	1.0 ± 0.17	0.21 ± 0.01
	$SiO(6–5)^n$	40.80 ± 0.01	-26.60 ± 0.05	0.6 ± 0.2	0.3 ± 0.1	120 ± 13	-	-	-	0.14 ± 0.08	0.3 ± 0.07	0.09 ± 0.00
	$SiO(8–7)^t$	40.82 ± 0.01	-25.76 ± 0.03	0.7 ± 0.2	0.3 ± 0.0	114 ± 5	-	-	-	0.87 ± 0.42	1.9 ± 0.32	0.51 ± 0.06
CND-9	$CS(5–4)^n$	41.13 ± 0.02	-30.56 ± 0.24	1.9 ± 0.8	1.1 ± 0.4	55 ± 22	1.8 ± 1.0	0.8 ± 0.5	52 ± 25	5.70 ± 2.70	1.3 ± 0.49	0.58 ± 0.01
	$SO(7–6)^n$	41.26 ± 0.00	-29.59 ± 0.03	0.6 ± 0.2	0.4 ± 0.1	71 ± 11	-	-	-	0.81 ± 0.36	1.5 ± 0.28	0.29 ± 0.02
	$^{13}CS(2–1)^n$	41.26 ± 0.04	-29.74 ± 0.45	1.0 ± 1.4	0.9 ± 0.9	123 ± 242	-	-	-	0.01 ± 0.04	0.0 ± 0.05	0.10 ± 0.00
	$N_2H^+(1–0)^n$	41.20 ± 0.02	-29.29 ± 0.20	4.0 ± 0.6	3.3 ± 0.5	88 ± 32	3.5 ± 0.7	2.9 ± 0.7	85 ± 46	3.24 ± 0.57	0.7 ± 0.11	0.04 ± 0.03
	$CH_3OH(8–7)^t$	41.19 ± 0.00	-30.86 ± 0.03	0.6 ± 0.1	0.5 ± 0.0	49 ± 16	-	-	-	0.03 ± 0.01	0.2 ± 0.02	0.07 ± 0.02
CND-10	$CS(5–4)^n$	41.09 ± 0.00	-31.66 ± 0.10	2.0 ± 0.2	1.0 ± 0.1	6 ± 5	1.9 ± 0.3	0.6 ± 0.2	6 ± 5	12.70 ± 1.60	2.9 ± 0.30	0.39 ± 0.02
	$SiO(6–5)^t$	41.05 ± 0.04	-32.57 ± 1.08	2.8 ± 2.8	0.2 ± 0.0	27 ± 1	-	-	-	0.32 ± 0.29	0.2 ± 0.08	0.16 ± 0.05
	$N_2H^+(1–0)^n$	41.10 ± 0.03	-32.11 ± 0.29	2.9 ± 1.1	1.7 ± 0.4	58 ± 19	-	-	-	0.52 ± 0.24	0.3 ± 0.10	0.09 ± 0.02
CND-W1	$CS(5–4)^t$	38.61 ± 0.01	-29.38 ± 0.13	2.9 ± 0.5	1.5 ± 0.2	61 ± 8	2.9 ± 0.5	1.3 ± 0.2	61 ± 8	19.50 ± 3.30	1.9 ± 0.29	0.40 ± 0.05
	$^{13}CS(2–1)^n$	38.55 ± 0.03	-29.28 ± 0.34	2.8 ± 1.1	1.3 ± 0.3	133 ± 9	-	-	-	0.31 ± 0.16	0.3 ± 0.08	0.10 ± 0.01
	$N_2H^+(1–0)^n$	38.52 ± 0.00	-29.13 ± 0.07	0.7 ± 0.2	0.4 ± 0.0	166 ± 7	-	-	-	0.02 ± 0.02	0.2 ± 0.03	0.15 ± 0.00
	$CH_3OH(8–7)^t$	38.58 ± 0.00	-29.60 ± 0.06	1.0 ± 0.1	0.9 ± 0.1	155 ± 51	-	-	-	0.12 ± 0.04	0.3 ± 0.04	0.05 ± 0.03
CND-W2	$CS(5–4)^n$	38.70 ± 0.01	-33.05 ± 0.23	2.4 ± 0.6	1.1 ± 0.2	156 ± 10	2.3 ± 0.6	0.9 ± 0.4	158 ± 12	15.00 ± 3.80	2.5 ± 0.55	0.45 ± 0.04
	$N_2H^+(1–0)^n$	38.67 ± 0.01	-33.05 ± 0.19	2.2 ± 0.5	1.5 ± 0.2	150 ± 14	-	-	-	0.63 ± 0.20	0.6 ± 0.11	0.12 ± 0.01

Notes. For details on the procedure see Sect. 3.2.4. A finding chart is provided in Fig. A.10 $^{(t)}$ tapered beam size, i.e. 0.65” in band 6 and 7, 1.5” in band 3 ; $^{(n)}$ natural beam size at the given frequency

Table A.2: *Continued. Results of 2D Gauss fits to the molecular sources: Source positions are relative to 17^{h}40^{m}00.00^s and −29°00′00.00″(J2000). (Credit:* Moser et al. (*2016b*), *reproduced with permission ©ESO.)*

region	line	peak position		convolved size			deconvolved size			flux		
		R.A. [s]	Dec [”]	$d_{maj,c}$ [”]	$d_{min,c}$ [”]	PA_c [°]	$d_{maj,d}$ [”]	$d_{min,d}$ [”]	PA_d [°]	S_{int} [Jy km s^{-1}]	S_{peak} [Jy bm^{-1} km s^{-1}]	S_{off} [Jy bm^{-1} km s^{-1}]
	CH_3OH(8–7)^t	38.70 ± 0.00	-32.96 ± 0.04	0.5 ± 0.1	0.5 ± 0.1	49 ± 100	-	-	-	0.02 ± 0.01	0.2 ± 0.03	0.10 ± 0.01
CND-W3	CS(5–4)^t	38.71 ± 0.01	-35.33 ± 0.23	2.8 ± 0.6	1.4 ± 0.3	26 ± 10	2.7 ± 0.6	1.2 ± 0.3	26 ± 10	31.60 ± 7.00	3.5 ± 0.70	1.16 ± 0.07
	CH_3OH(8–7)^t	38.72 ± 0.01	-35.05 ± 0.05	0.8 ± 0.2	0.6 ± 0.1	85 ± 26	-	-	-	0.05 ± 0.04	0.2 ± 0.05	0.10 ± 0.01
V1	N_2H^+(1–0)^n	43.78 ± 0.01	-15.18 ± 0.19	1.9 ± 0.5	1.8 ± 0.4	171 ± 121	-	-	-	3.00 ± 1.20	2.7 ± 0.63	0.61 ± 0.04
V2	N_2H^+(1–0)^n	43.83 ± 0.01	-16.96 ± 0.25	1.9 ± 0.7	1.2 ± 0.3	149 ± 18	-	-	-	1.70 ± 0.89	2.2 ± 0.57	0.67 ± 0.05
V2-1	CH_3OH(8–7)^t	43.78 ± 0.01	-16.02 ± 0.11	1.0 ± 0.3	0.9 ± 0.3	82 ± 128	-	-	-	0.54 ± 0.42	1.4 ± 0.44	0.80 ± 0.02
V3	CH_3OH(8–7)^t	43.93 ± 0.00	-19.96 ± 0.03	1.8 ± 0.1	1.6 ± 0.1	49 ± 11	1.1 ± 0.2	0.4 ± 0.2	49 ± 11	11.55 ± 0.88	9.1 ± 0.43	-0.86 ± 0.17
V4	N_2H^+(1–0)^n	43.74 ± 0.01	-24.63 ± 0.14	3.0 ± 0.5	2.1 ± 0.2	56 ± 12	2.5 ± 0.7	1.1 ± 1.0	48 ± 24	8.00 ± 1.50	3.9 ± 0.51	0.48 ± 0.03
V5	N_2H^+(1–0)^n	43.89 ± 0.02	-23.95 ± 0.10	2.2 ± 0.7	1.2 ± 0.2	99 ± 10	-	-	-	2.70 ± 1.30	3.3 ± 0.77	0.90 ± 0.04
V6	N_2H^+(1–0)^n	43.93 ± 0.02	-25.81 ± 0.28	2.0 ± 0.7	1.7 ± 0.5	173 ± 55	-	-	-	3.40 ± 1.70	3.1 ± 0.89	1.48 ± 0.17
V7	N_2H^+(1–0)^n	43.87 ± 0.01	-27.83 ± 0.24	2.4 ± 0.6	1.7 ± 0.3	18 ± 21	-	-	-	4.60 ± 1.60	3.5 ± 0.76	0.89 ± 0.11
V8	N_2H^+(1–0)^n	43.60 ± 0.01	-31.43 ± 0.11	3.4 ± 0.4	2.0 ± 0.2	64 ± 6	2.9 ± 0.6	1.0 ± 0.6	59 ± 10	9.50 ± 1.40	4.3 ± 0.46	0.63 ± 0.04
V9	CH_3OH(8–7)^t	43.88 ± 0.02	-25.46 ± 0.06	1.3 ± 0.5	0.5 ± 0.0	105 ± 4	-	-	-	0.43 ± 0.30	1.4 ± 0.26	0.60 ± 0.04
V10	CH_3OH(8–7)^t	43.82 ± 0.01	-29.89 ± 0.08	1.5 ± 0.3	1.1 ± 0.2	70 ± 21	-	-	-	1.16 ± 0.45	1.7 ± 0.32	0.34 ± 0.08
V11	N_2H^+(1–0)^n	43.31 ± 0.01	-32.35 ± 0.09	2.1 ± 0.4	1.6 ± 0.2	83 ± 19	-	-	-	2.14 ± 0.56	2.0 ± 0.30	0.45 ± 0.09
V12	N_2H^+(1–0)^n	42.83 ± 0.01	-27.65 ± 0.21	2.2 ± 0.5	1.4 ± 0.2	10 ± 12	-	-	-	0.88 ± 0.29	0.9 ± 0.16	2.07 ± 0.06
SEB1	N_2H^+(1–0)^n	41.57 ± 0.02	-52.49 ± 0.23	4.2 ± 0.8	2.7 ± 0.4	62 ± 15	3.7 ± 1.0	2.2 ± 0.7	59 ± 33	7.20 ± 1.60	1.9 ± 0.33	0.38 ± 0.02
SEB2	N_2H^+(1–0)^n	41.15 ± 0.01	-56.95 ± 0.13	4.4 ± 0.4	3.1 ± 0.3	117 ± 10	4.0 ± 0.5	2.6 ± 0.4	120 ± 15	11.90 ± 1.30	2.7 ± 0.24	0.43 ± 0.10
SEB3	N_2H^+(1–0)^n	41.30 ± 0.02	-1.01.22± 0.31	2.6 ± 0.8	2.0 ± 0.5	31 ± 33	2.1 ± 1.0	0.6 ± 1.2	24 ± 35	1.65 ± 0.66	1.0 ± 0.26	1.29 ± 0.04
SEB4	N_2H^+(1–0)^n	40.88 ± 0.02	-1.11.73± 0.16	3.7 ± 0.6	2.5 ± 0.3	70 ± 13	3.3 ± 0.8	1.9 ± 0.6	66 ± 28	10.40 ± 2.00	3.4 ± 0.50	0.29 ± 0.12
SEB5	N_2H^+(1–0)^n	40.37 ± 0.02	-1.00.45± 0.11	2.3 ± 0.6	1.3 ± 0.2	75 ± 10	-	-	-	0.94 ± 0.37	1.0 ± 0.21	0.38 ± 0.06

Notes. For details on the procedure see Sect. 3.2.4. A finding chart is provided in Fig. A.10 $^{(t)}$ tapered beam size, i.e. 0.65” in band 6 and 7, 1.5” in band 3 ; $^{(n)}$ natural beam size at the given frequency

A.3 Molecular source velocities

Table A.3: *Fluxes, velocities, and FWHM within a beam-sized aperture per region for CS(5–4), C_2H(3–2), SO(7–6), and $H^{13}CO^+$(3–2) (Credit: Moser et al. (2016b), reproduced with permission ©ESO.)*

	CS(5–4)				C_2H(3–2)				SO(7–6)				$H^{13}CO^+$(3–2)			
region	S_{int} [Jy km s^{-1}]	v [km s^{-1}]	FWHM [km s^{-1}]		S_{int} [Jy km s^{-1}]	v [km s^{-1}]	FWHM [km s^{-1}]		S_{int} [Jy km s^{-1}]	v [km s^{-1}]	FWHM [km s^{-1}]		S_{int} [Jy km s^{-1}]	v [km s^{-1}]	FWHM [km s^{-1}]	
1-all	1.62 ± 0.13	48 ± 1	43 ± 2		0.24 ± 0.04	44 ± 2	40 ± 5		0.10 ± 0.03	60 ± 7	53 ± 14	ND	0.14 ± 0.04	34 ± 20	71 ± 12	ND
1	1.79 ± 0.10	45 ± 1	39 ± 1		0.70 ± 0.10	45 ± 20	40 ± 20	hdp	0.20 ± 0.05	39 ± 2	34 ± 6		-	-	-	
2	1.44 ± 0.11	57 ± 1	39 ± 2		0.24 ± 0.03	53 ± 2	31 ± 3		0.14 ± 0.04	63 ± 3	37 ± 7		0.19 ± 0.03	45 ± 10	78 ± 9	
3	0.89 ± 0.18	55 ± 1	33 ± 3		0.16 ± 0.07	52 ± 3	25 ± 7		-	-	-		0.27 ± 0.03	47 ± 2	44 ± 4	
4	0.43 ± 0.10	59 ± 2	35 ± 4		-	-	-		-	-	-		0.14 ± 0.05	63 ± 10	53 ± 10	
	0.09 ± 0.05	-1 ± 5	33 ± 14	ND	-	-	-		-	-	-		-	-	- ± -	
5	1.03 ± 0.12	48 ± 2	39 ± 10		0.47 ± 0.10	45 ± 20	30 ± 20	hdp	0.22 ± 0.06	48 ± 3	33 ± 6		0.20 ± 0.05	54 ± 4	50 ± 9	
	0.46 ± 0.05	-57 ± 2	45 ± 4		-	-	-		-	-	-		-	-	-	
6	1.06 ± 0.14	44 ± 2	45 ± 3		0.09 ± 0.06	33 ± 4	28 ± 14	ND	0.14 ± 0.04	41 ± 3	29 ± 6		-	-	-	
	0.29 ± 0.09	-64 ± 3	37 ± 5		-	-	-		-	-	-		-	-	-	
7	0.91 ± 0.10	27 ± 1	32 ± 2		0.20 ± 0.06	6 ± 30	64 ± 13		0.13 ± 0.04	28 ± 3	35 ± 7		-	-	-	
8	0.81 ± 0.07	-38 ± 1	34 ± 2		-	-	-		-	-	-		-	-	-	
9	0.81 ± 0.06	-34 ± 1	51 ± 2		0.15 ± 0.06	-23 ± 20	53 ± 12		-	-	-		-	-	-	
10	0.82 ± 0.06	-30 ± 1	45 ± 2		-	-	-		-	-	-		-	-	-	
11	0.80 ± 0.12	-34 ± 2	52 ± 4		-	-	-		-	-	-		-	-	-	
12	0.76 ± 0.05	-25 ± 1	37 ± 2		0.17 ± 0.07	-30 ± 4	40 ± 10		-	-	-		-	-	-	
13	0.76 ± 0.11	49 ± 1	30 ± 3		-	-	-		0.16 ± 0.04	40 ± 3	34 ± 6		-	-	-	
14	0.96 ± 0.09	-63 ± 10	53 ± 3		0.34 ± 0.06	-91 ± 50	89 ± 12		-	-	-		-	-	-	
15	0.60 ± 0.10	-14 ± 2	30 ± 3		0.41 ± 0.09	-15 ± 9	50 ± 40		-	-	-		-	-	-	

Notes. The spectra are obtained from an aperture with the size of the beam centered onto the average position of all integrated emission line peaks in the corresponding region (see Fig. A.10). For details on the procedure see Sect. 3.2.4. $^{(ND)}$ line peak below $3\sigma_{\text{rms-ch}}$; $^{(h)}$ fit failed - instead estimates given; $^{(dp)}$ close double peak (either due to two velocity components, line multiplett, or overlapping transition lines).

Table A.3: *Continued. Fluxes, velocities, and FWHM within a beam-sized aperture per region for CS(5–4), C_2H(3–2), SO(7–6), and $H^{13}CO^+$(3–2) (Credit: Moser* et al. *(2016b), reproduced with permission ©ESO.)*

region	CS(5–4)				C_2H(3–2)				SO(7–6)				$H^{13}CO^+$(3–2)			
	S_{int} [Jy km s^{-1}]	v [km s^{-1}]	FWHM [km s^{-1}]		S_{int} [Jy km s^{-1}]	v [km s^{-1}]	FWHM [km s^{-1}]		S_{int} [Jy km s^{-1}]	v [km s^{-1}]	FWHM [km s^{-1}]		S_{int} [Jy km s^{-1}]	v [km s^{-1}]	FWHM [km s^{-1}]	
16	0.37 ± 0.15	-12 ± 4	27 ± 6		0.08 ± 0.06	-23 ± 7	27 ± 13	ND	-	-	-		-	-	-	
	0.12 ± 0.04	102 ± 4	57 ± 16	ND	-	-	-		-	-	-		-	-	-	
17	0.27 ± 0.05	115 ± 4	78 ± 30		-	-	-		-	-	-		-	-	-	
19	0.40 ± 0.13	65 ± 5	50 ± 10		0.13 ± 0.04	50 ± 4	44 ± 11	ND	-	-	-		-	-	-	
20	0.86 ± 0.27	33 ± 20	52 ± 20		0.49 ± 0.10	40 ± 20	40 ± 20	hdp	0.15 ± 0.04	46 ± 2	34 ± 5		0.04 ± 0.03	49 ± 5	24 ± 9	ND
21	0.54 ± 0.08	-10 ± 2	40 ± 3		0.25 ± 0.05	-15 ± 3	49 ± 6		-	-	-		-	-	-	
22	1.02 ± 0.09	71 ± 1	49 ± 2		0.30 ± 0.06	60 ± 20	30 ± 20	hdp	0.12 ± 0.06	51 ± 6	50 ± 14	ND	0.11 ± 0.06	63 ± 4	31 ± 12	ND
24	0.69 ± 0.08	149 ± 1	49 ± 3		-	-	-		0.23 ± 0.06	146 ± 5	56 ± 12	ND	-	-	-	
25	0.33 ± 0.07	163 ± 20	45 ± 20		-	-	-		0.07 ± 0.06	144 ± 9	36 ± 24	ND	-	-	-	
26	0.33 ± 0.09	114 ± 4	42 ± 7		-	-	-		-	-	-		-	-	-	
27	0.48 ± 0.11	137 ± 4	62 ± 9		-	-	-		-	-	-		-	-	-	
T1	1.65 ± 0.22	54 ± 10	41 ± 10		0.28 ± 0.09	1 ± 10	-44 ± 11		0.39 ± 0.14	65 ± 6	46 ± 12		-	-	-	
T2	1.72 ± 0.31	67 ± 3	46 ± 4		-	-	-		0.50 ± 0.15	78 ± 20	53 ± 12		1.50 ± 0.30	63 ± 30	88 ± 42	h
T3	1.57 ± 0.19	109 ± 3	62 ± 4		-	-	-		0.61 ± 0.22	109 ± 6	50 ± 13		-	-	-	
T4	3.24 ± 0.32	85 ± 1	44 ± 3		-	-	-		-	-	-		-	-	-	
T5	1.43 ± 0.22	54 ± 2	41 ± 4		0.69 ± 0.25	-3 ± 6	49 ± 13		-	-	-		-	-	-	
T6	2.13 ± 0.30	56 ± 20	46 ± 2		-	-	-		0.18 ± 0.21	66 ± 13	33 ± 29		0.60 ± 0.20	50 ± 20	30 ± 20	h
T7	1.53 ± 0.23	60 ± 20	73 ± 20		0.30 ± 0.13	22 ± 5	32 ± 11		-	-	-		0.47 ± 0.10	30 ± 20	40 ± 20	h
T8	1.23 ± 0.16	30 ± 20	51 ± 4		-	-	-		-	-	-		0.23 ± 0.08	35 ± 10	52 ± 12	
T9	0.51 ± 0.19	39 ± 6	38 ± 9		-	-	-		-	-	-		0.72 ± 0.12	63 ± 20	85 ± 10	

Notes. The spectra are obtained from an aperture with the size of the beam centered onto the average position of all integrated emission line peaks in the corresponding region (see Fig. A.10). For details on the procedure see Sect. 3.2.4. $^{(ND)}$ line peak below $3\sigma_{\text{rms-ch}}$; $^{(h)}$ fit failed - instead estimates given; $^{(dp)}$ close double peak (either due to two velocity components, line multiplett, or overlapping transition lines).

Table A.3: *Continued. Fluxes, velocities, and FWHM within a beam-sized aperture per region for CS(5–4), C_2H(3–2), SO(7–6), and $H^{13}CO^+$(3–2) (Credit: Moser* et al. *(2016b), reproduced with permission ©ESO.)*

region	CS(5–4)			C_2H(3–2)			SO(7–6)			$H^{13}CO^+$(3–2)		
	S_{int} [Jy km s^{-1}]	v [km s^{-1}]	FWHM [km s^{-1}]	S_{int} [Jy km s^{-1}]	v [km s^{-1}]	FWHM [km s^{-1}]	S_{int} [Jy km s^{-1}]	v [km s^{-1}]	FWHM [km s^{-1}]	S_{int} [Jy km s^{-1}]	v [km s^{-1}]	FWHM [km s^{-1}]
T10	2.63 ± 0.29	46 ± 1	43 ± 2	1.74 ± 0.28	4 ± 3	85 ± 10 hdp	0.95 ± 0.27	43 ± 7	73 ± 16	0.66 ± 0.17	42 ± 3	39 ± 7
T10-2	0.30 ± 0.10	40 ± 20	30 ± 20 h	-	-	-	-	-	-	-	-	-
	0.43 ± 0.06	100 ± 1	33 ± 3	-	-	-	-	-	-	-	-	-
T11	-	-	-	-	-	-	0.36 ± 0.25	49 ± 7	32 ± 15	-	-	-
SEW1	3.20 ± 0.45	-52 ± 2	41 ± 3	0.46 ± 0.11	-43 ± 5	48 ± 10	0.77 ± 0.13	-53 ± 3	48 ± 6	0.43 ± 0.05	-49 ± 2	54 ± 5
SEW1-2	3.94 ± 0.25	-52 ± 1	44 ± 1	1.95 ± 0.40	-50 ± 20	70 ± 20 hdp	0.56 ± 0.16	-53 ± 3	32 ± 7	0.48 ± 0.08	-56 ± 3	51 ± 7
SEW2	4.36 ± 0.22	-49 ± 1	42 ± 2	1.09 ± 0.14	-48 ± 3	68 ± 7	1.00 ± 0.11	-52 ± 2	43 ± 4	0.20 ± 0.13	-61 ± 9	37 ± 18
SEW3	4.68 ± 0.37	-44 ± 1	39 ± 2	0.80 ± 0.20	-53 ± 20	30 ± 20 h	0.66 ± 0.13	-46 ± 3	31 ± 5	-	-	-
SEW4	2.27 ± 0.27	-49 ± 1	35 ± 2	0.80 ± 0.20	-20 ± 20	40 ± 20 hdp	0.21 ± 0.12	-41 ± 6	36 ± 17	-	-	-
SEW4-1	1.10 ± 0.20	-50 ± 20	40 ± 20 h	0.90 ± 0.20	0 ± 20	30 ± 20 h	-	-	-	-	-	-
SEW5	1.20 ± 0.29	-5 ± 2	27 ± 5	0.50 ± 0.20	-18 ± 20	20 ± 10 h	-	-	-	-	-	-
SEW6	0.80 ± 0.11	-9 ± 1	30 ± 3	0.39 ± 0.11	-11 ± 3	28 ± 5	-	-	-	-	-	-
SEW7	0.78 ± 0.17	3 ± 2	29 ± 3	0.35 ± 0.10	-7 ± 4	29 ± 6	-	-	-	-	-	-
SEW8	1.26 ± 0.20	-30 ± 20	40 ± 20 h	0.61 ± 0.13	-30 ± 4	91 ± 9	-	-	-	-	-	-
	0.50 ± 0.10	50 ± 20	30 ± 20 h	-	-	-	-	-	-	-	-	-
SEW9	2.17 ± 0.23	8 ± 1	43 ± 3	-	-	-	0.55 ± 0.12	5 ± 2	36 ± 6	-	-	-
SEW10	0.40 ± 0.08	31 ± 5	65 ± 10	-	-	-	-	-	-	0.17 ± 0.11	27 ± 16	66 ± 30 dp
SEW11	0.36 ± 0.05	-47 ± 2	40 ± 4	0.37 ± 0.06	-45 ± 4	64 ± 9	-	-	-	-	-	-
	0.19 ± 0.05	33 ± 3	39 ± 6	-	-	-	-	-	-	-	-	-
SEW12	0.15 ± 0.21	-41 ± 8	40 ± 20 h	-	-	-	-	-	-	-	-	-

Notes. The spectra are obtained from an aperture with the size of the beam centered onto the average position of all integrated emission line peaks in the corresponding region (see Fig. A.10). For details on the procedure see Sect. 3.2.4. $^{(ND)}$ line peak below $3\sigma_{\text{rms-ch}}$; $^{(h)}$ fit failed - instead estimates given; $^{(dp)}$ close double peak (either due to two velocity components, line multiplett, or overlapping transition lines).

Table A.3: *Continued. Fluxes, velocities, and FWHM within a beam-sized aperture per region for CS(5–4), C_2H(3–2), SO(7–6), and $H^{13}CO^+$(3–2) (Credit: Moser* et al. *(2016b), reproduced with permission ©ESO.)*

region	CS(5–4)			C_2H(3–2)			SO(7–6)			$H^{13}CO^+$(3–2)		
	S_{int} [Jy km s^{-1}]	v [km s^{-1}]	FWHM [km s^{-1}]	S_{int} [Jy km s^{-1}]	v [km s^{-1}]	FWHM [km s^{-1}]	S_{int} [Jy km s^{-1}]	v [km s^{-1}]	FWHM [km s^{-1}]	S_{int} [Jy km s^{-1}]	v [km s^{-1}]	FWHM [km s^{-1}]
	0.30 ± 0.10	75 ± 20	30 ± 20 h	-	-	-	-	-	-	-	-	-
SEW13	0.68 ± 0.20	-19 ± 12	44 ± 22	-	-	-	-	-	-	-	-	-
CND-1	1.06 ± 0.16	68 ± 2	40 ± 3	-	-	-	-	-	-	0.19 ± 0.12	34 ± 10	44 ± 23
CND-2	0.72 ± 0.15	59 ± 3	44 ± 4	0.23 ± 0.06	56 ± 2	31 ± 6	-	-	-	-	-	-
CND-3	2.44 ± 0.13	30 ± 1	39 ± 2	-	-	-	0.40 ± 0.45	30 ± 11	28 ± 23	-	-	-
CND-4	1.83 ± 0.36	-14 ± 4	69 ± 7	0.50 ± 0.42	-20 ± 10	33 ± 18	-	-	-	-	-	-
CND-5	2.27 ± 0.16	-6 ± 2	106 ± 5 dp	-	-	-	-	-	-	-	-	-
CND-6	1.65 ± 0.12	12 ± 1	36 ± 1	-	-	-	0.51 ± 0.09	2 ± 2	38 ± 5	-	-	-
CND-7	1.21 ± 0.10	9 ± 1	37 ± 2	-	-	-	0.25 ± 0.13	1 ± 4	30 ± 12	-	-	-
CND-8	0.30 ± 0.07	-83 ± 10	38 ± 5	-	-	-	-	-	-	-	-	-
CND-9	0.68 ± 0.12	21 ± 2	35 ± 5	-	-	-	-	-	-	-	-	-
CND-10	1.89 ± 0.19	11 ± 10	49 ± 3	0.39 ± 0.13	4 ± 5	45 ± 10	-	-	-	-	-	-
CND-W1	0.50 ± 0.13	-46 ± 4	38 ± 8	-	-	-	-	-	-	-	-	-
	1.27 ± 0.25	83 ± 2	30 ± 3	-	-	-	-	-	-	-	-	-
CND-W2	2.40 ± 0.21	77 ± 1	39 ± 2	-	-	-	-	-	-	0.78 ± 0.41	-60 ± 20	45 ± 20 h
CND-W3	1.94 ± 0.27	-43 ± 2	43 ± 4	-	-	-	-	-	-	0.41 ± 0.44	50 ± 14	45 ± 32
	1.59 ± 0.27	84 ± 2	35 ± 4	-	-	-	-	-	-	-	-	-

Notes. The spectra are obtained from an aperture with the size of the beam centered onto the average position of all integrated emission line peaks in the corresponding region (see Fig. A.10). For details on the procedure see Sect. 3.2.4. $^{(ND)}$ line peak below $3\sigma_{\text{rms-ch}}$; $^{(h)}$ fit failed - instead estimates given; $^{(dp)}$ close double peak (either due to two velocity components, line multiplett, or overlapping transition lines).

Table A.4: *Fluxes, velocities, and FWHM within a beam-sized aperture per region for SiO(6–5), SiO(8–7), HC_3N(27–26), and CH_3OH(7–6) (Credit:* Moser et al. (*2016b*)*, reproduced with permission ©ESO.)*

region	SiO(6–5)				SiO(8–7)			HC_3N(27–26)				CH_3OH(7–6)			
	S_{int} [Jy km s^{-1}]	v [km s^{-1}]	FWHM [km s^{-1}]		S_{int} [Jy km s^{-1}]	v [km s^{-1}]	FWHM [km s^{-1}]	S_{int} [Jy km s^{-1}]	v [km s^{-1}]	FWHM [km s^{-1}]		S_{int} [Jy km s^{-1}]	v [km s^{-1}]	FWHM [km s^{-1}]	
1	0.13 ± 0.03	39 ± 2	35 ± 6	ND	-	-	-	-	-	-		-	-	-	
4	-	-	-		-	-	-	0.14 ± 0.06	50 ± 20	59 ± 20	ND	0.23 ± 0.05	61 ± 3	51 ± 8	
	-	-	-		-	-	-	0.08 ± 0.02	68 ± 3	35 ± 6	ND	0.70 ± 0.20	80 ± 20	50 ± 20	hdp
5	0.10 ± 0.02	44 ± 2	32 ± 4		-	-	-	-	-	-		0.21 ± 0.05	15 ± 2	30 ± 4	hdp
6	0.17 ± 0.04	34 ± 3	47 ± 7		-	-	-	-	-	-		-	-	-	
7	0.06 ± 0.04	19 ± 6	34 ± 18	ND	-	-	-	-	-	-		-	-	-	
13	0.14 ± 0.03	46 ± 3	38 ± 6		-	-	-	-	-	-		-	-	-	
14	0.07 ± 0.02	-65 ± 4	41 ± 9	ND	-	-	-	-	-	-		-	-	-	
16	0.31 ± 0.05	140 ± 3	54 ± 6		-	-	-	-	-	-		-	-	-	
17	0.66 ± 0.06	139 ± 20	66 ± 3		0.32 ± 0.05	152 ± 2	37 ± 4	-	-	-		-	-	-	
18	0.54 ± 0.09	-31 ± 2	36 ± 3		0.74 ± 0.13	-26 ± 2	36 ± 4	-	-	-		-	-	-	
23	1.14 ± 0.13	118 ± 10	83 ± 6		-	-	-	-	-	-		0.80 ± 0.20	90 ± 20	40 ± 20	hdp
25	0.11 ± 0.05	167 ± 7	68 ± 16	ND	-	-	-	-	-	-		-	-	-	
27	0.25 ± 0.06	124 ± 20	86 ± 20		-	-	-	-	-	-		-	-	-	
T1	0.40 ± 0.07	64 ± 3	39 ± 5		-	-	-	-	-	-		-	-	-	
T2	-	-	-		-	-	-	0.30 ± 0.07	62 ± 2	42 ± 7		0.79 ± 0.18	70 ± 20	30 ± 20	hdp
T5	0.66 ± 0.26	47 ± 11	93 ± 30		-	-	-	0.33 ± 0.31	66 ± 8	29 ± 22		-	-	-	
T7	0.07 ± 0.12	51 ± 16	18 ± 23		-	-	-	-	-	-		-	-	-	
	0.08 ± 0.13	129 ± 5	26 ± 37		-	-	-	-	-	-		-	-	-	

Notes. The spectra are obtained from an aperture with the size of the beam centered onto the average position of all integrated emission line peaks in the corresponding region. $^{(ND)}$ line peak below $3\sigma_{\text{rms-ch}}$; $^{(h)}$ fit failed - instead estimates given; $^{(dp)}$ close double peak (either due to two velocity components, line multiplett, or overlapping transition lines).

__Table A.4:__ Continued. Fluxes, velocities, and FWHM within a beamsized aperture per region for SiO(6–5), SiO(8–7), HC_3N(27–26), and CH_3OH(7–6) (Credit: Moser et al. *(2016b), reproduced with permission ©ESO.)*

region	SiO(6–5)			SiO(8–7)			HC_3N(27–26)			CH_3OH(7–6)		
	S_{int} [Jy km s^{-1}]	v [km s^{-1}]	FWHM [km s^{-1}]	S_{int} [Jy km s^{-1}]	v [km s^{-1}]	FWHM [km s^{-1}]	S_{int} [Jy km s^{-1}]	v [km s^{-1}]	FWHM [km s^{-1}]	S_{int} [Jy km s^{-1}]	v [km s^{-1}]	FWHM [km s^{-1}]
T8	0.14 ± 0.07	39 ± 10	41 ± 15	-	-	-	-	-	-	-	-	-
T9	0.24 ± 0.13	45 ± 6	29 ± 13	-	-	-	-	-	-	2.00 ± 0.40	70 ± 20	30 ± 20 hdp
T10	0.41 ± 0.15	47 ± 4	36 ± 9	-	-	-	-	-	-	-	-	-
T10-2	-	-	-	-	-	-	0.62 ± 0.06	54 ± 1	50 ± 3	-	-	-
T11	1.71 ± 0.34	50 ± 20	50 ± 20 h	-	-	-	-	-	-	-	-	-
SEW1	0.46 ± 0.13	-56 ± 3	31 ± 6	-	-	-	-	-	-	-	-	-
SEW1-2	0.56 ± 0.11	-55 ± 2	36 ± 6	-	-	-	-	-	-	-	-	-
SEW2	0.54 ± 0.11	-50 ± 2	37 ± 5	-	-	-	-	-	-	-	-	-
SEW3	0.80 ± 0.11	-48 ± 2	46 ± 4	-	-	-	-	-	-	-	-	-
SEW9	0.62 ± 0.17	5 ± 5	55 ± 10	-	-	-	-	-	-	-	-	-
CND-1	0.23 ± 0.09	73 ± 3	31 ± 10	-	-	-	-	-	-	-	-	-
CND-6	0.33 ± 0.05	-5 ± 3	47 ± 6	-	-	-	-	-	-	-	-	-
CND-7	0.21 ± 0.06	2 ± 3	31 ± 6	-	-	-	-	-	-	-	-	-
CND-9	0.31 ± 0.12	13 ± 19	127 ± 39 dp	-	-	-	-	-	-	-	-	-

Notes. The spectra are obtained from an aperture with the size of the beam centered onto the average position of all integrated emission line peaks in the corresponding region. $^{(ND)}$ line peak below $3\sigma_{\text{rms-ch}}$; $^{(h)}$ fit failed - instead estimates given; $^{(dp)}$ close double peak (either due to two velocity components, line multiplett, or overlapping transition lines).

Table A.5: *Fluxes, velocities, and FWHM within a beamsized aperture per region for N_2H^+(1–0), CH_3OH(8–7), and ^{13}CS(2–1) (Credit: Moser* et al. *(2016b), reproduced with permission ©ESO.)*

region	N_2H^+(1–0)				CH_3OH(8–7)				^{13}CS(2–1)			
	S_{int} [Jy km s^{-1}]	v [km s^{-1}]	FWHM [km s^{-1}]		S_{int} [Jy km s^{-1}]	v [km s^{-1}]	FWHM [km s^{-1}]		S_{int} [Jy km s^{-1}]	v [km s^{-1}]	FWHM [km s^{-1}]	
T1	0.31 ± 0.05	13 ± 20	121 ± 14		0.11 ± 0.03	56 ± 7	78 ± 14	ND	-	-	-	
T2	0.11 ± 0.08	31 ± 31	94 ± 50	ND	0.07 ± 0.04	62 ± 14	78 ± 29	ND	-	-	-	
T4	0.12 ± 0.10	38 ± 21	70 ± 34		-	-	-		-	-	-	
T5	0.21 ± 0.09	35 ± 12	91 ± 23		-	-	-		-	-	-	
T6	0.67 ± 0.07	19 ± 4	109 ± 8		0.27 ± 0.03	47 ± 3	103 ± 9		0.18 ± 0.03	43 ± 20	130 ± 21	ND
T7	0.52 ± 0.08	20 ± 4	99 ± 8		0.20 ± 0.04	54 ± 6	102 ± 16	ND	0.59 ± 0.14	80 ± 20	80 ± 40	h-ND
T8	0.29 ± 0.08	12 ± 9	98 ± 17		0.16 ± 0.05	54 ± 10	96 ± 19	ND	0.06 ± 0.04	36 ± 23	86 ± 39	ND
T9	0.59 ± 0.08	16 ± 5	114 ± 10		0.14 ± 0.04	52 ± 11	107 ± 27	ND	-	-	-	
T10	0.48 ± 0.10	34 ± 10	84 ± 7		0.35 ± 0.06	41 ± 4	89 ± 10		-	-	-	
T10-2	0.65 ± 0.07	15 ± 4	104 ± 8		0.26 ± 0.05	50 ± 4	115 ± 14		0.24 ± 0.07	80 ± 20	80 ± 40	h-ND
T11	0.24 ± 0.12	24 ± 11	78 ± 24		-	-	-		-	-	-	
SEW1	-	-	-		-	-	-		0.32 ± 0.05	-68 ± 20	217 ± 31	ND
SEW1-2	-	-	-		-	-	-		0.27 ± 0.04	-72 ± 6	167 ± 22	
SEW2	-	-	-		-	-	-		0.29 ± 0.06	-69 ± 12	188 ± 40	
SEW5	0.42 ± 0.08	-19 ± 20	158 ± 19		-	-	-		-	-	-	
SEW6	0.43 ± 0.15	-27 ± 10	117 ± 17.3		-	-	-		-	-	-	
SEW7	0.36 ± 0.04	-23 ± 4	108 ± 9		-	-	-		-	-	-	
SEW9	0.22 ± 0.19	-25 ± 12	67 ± 43		-	-	-		-	-	-	
SEW10	0.19 ± 0.06	-41 ± 20	92 ± 17		-	-	-		-	-	-	

Notes. The spectra are obtained from an aperture with the size of the beam centered onto the average position of all integrated emission line peaks in the corresponding region. $^{(ND)}$ line peak below $3\sigma_{\text{rms-ch}}$; $^{(h)}$ fit failed - instead estimates given; $^{(dp)}$ close double peak (either due to two velocity components, line multiplett, or overlapping transition lines).

Table A.5: *Continued. Fluxes, velocities, and FWHM within a beamsized aperture per region for N_2H^+, $CH_3OH(8–7)$, and $^{13}CS(2–1)$ (Credit: Moser et al. (2016b), reproduced with permission ©ESO.)*

region	$N_2H^+(1–0)$				$CH_3OH(8–7)$				$^{13}CS(2–1)$			
	S_{int} [Jy km s^{-1}]	v [km s^{-1}]	FWHM [km s^{-1}]		S_{int} [Jy km s^{-1}]	v [km s^{-1}]	FWHM [km s^{-1}]		S_{int} [Jy km s^{-1}]	v [km s^{-1}]	FWHM [km s^{-1}]	
SEW12	-	-	-		-	-	-		0.47 ± 0.08	-80 ± 20	300 ± 50	
SEW13	0.79 ± 0.07	-14 ± 3	103 ± 7		-	-	-		-	-	-	
CND-1	-	-	-		0.10 ± 0.05	76 ± 17	119 ± 43	ND	-	-	-	
CND-3	0.13 ± 0.08	0 ± 20	128 ± 51	h	-	-	-		-	-	-	
CND-4	0.78 ± 0.20	0 ± 20	130 ± 50	h	-	-	-		-	-	-	
CND-6	0.38 ± 0.08	-17 ± 20	123 ± 13		-	-	-		-	-	-	
CND-7	0.32 ± 0.03	-14 ± 10	101 ± 6.8		-	-	-		-	-	-	
CND-9	0.48 ± 0.08	-11 ± 4	101 ± 11		0.16 ± 0.06	16 ± 14	131 ± 33	ND	0.27 ± 0.08	-50 ± 20	261 ± 57	ND
CND-10	0.26 ± 0.04	-20 ± 5	90 ± 9		-	-	-		0.12 ± 0.09	9 ± 40	141 ± 75	ND
CND-W1	0.16 ± 0.06	55 ± 11	85 ± 21		0.14 ± 0.06	78 ± 11	83 ± 24	ND	0.17 ± 0.06	49 ± 10	85 ± 22	
CND-W2	0.62 ± 0.10	20 ± 20	80 ± 20	h	0.11 ± 0.05	73 ± 4	67 ± 24	ND	0.33 ± 0.06	60 ± 6	121 ± 15	
CND-W3	-	-	-		0.20 ± 0.05	79 ± 9	118 ± 20	ND	0.16 ± 0.04	64 ± 8	87 ± 17	
V1	2.37 ± 0.30	16 ± 4	108 ± 9		1.48 ± 0.38	43 ± 7	109 ± 18		-	-	-	
V2	1.92 ± 0.34	13 ± 5	97 ± 11		1.35 ± 0.21	52 ± 5	90 ± 11		-	-	-	
V2-1	1.96 ± 0.36	10 ± 5	97 ± 11		1.89 ± 0.23	37 ± 4	118 ± 10		-	-	-	
V3	-	-	-		4.65 ± 0.76	46 ± 3	87 ± 8		-	-	-	
V4	2.86 ± 0.25	39 ± 4	107 ± 8		1.20 ± 0.20	50 ± 20	100 ± 40	h	-	-	-	
V5	2.42 ± 0.37	41 ± 6	103 ± 12		-	-	-		-	-	-	
V6	3.06 ± 0.33	33 ± 4	110 ± 9		1.98 ± 0.43	7 ± 10	210 ± 32		-	-	-	

Notes. The spectra are obtained from an aperture with the size of the beam centered onto the average position of all integrated emission line peaks in the corresponding region. $^{(ND)}$ line peak below $3\sigma_{\text{rms-ch}}$; $^{(h)}$ fit failed - instead estimates given; $^{(dp)}$ close double peak (either due to two velocity components, line multiplett, or overlapping transition lines).

Table A.5: *Continued. Fluxes, velocities, and FWHM within a beamsized aperture per region for N_2H^+, CH_3OH(8–7), and ^{13}CS(2–1) (Credit: Moser* et al. *(2016b), reproduced with permission ©ESO.)*

region	N_2H^+(1–0)			CH_3OH(8–7)			^{13}CS(2–1)		
	S_{int} [Jy km s^{-1}]	v [km s^{-1}]	FWHM [km s^{-1}]	S_{int} [Jy km s^{-1}]	v [km s^{-1}]	FWHM [km s^{-1}]	S_{int} [Jy km s^{-1}]	v [km s^{-1}]	FWHM [km s^{-1}]
V7	3.05 ± 0.40	37 ± 5	119 ± 11	-	-	-	-	-	-
V8	3.23 ± 0.37	21 ± 3	107 ± 6	-	-	-	-	-	-
V9	2.85 ± 0.33	34 ± 4	103 ± 9	1.22 ± 0.30	47 ± 7	106 ± 18	-	-	-
V10	1.35 ± 0.31	49 ± 7	87 ± 15	1.39 ± 0.25	43 ± 4	95 ± 11	-	-	-
V11	1.65 ± 0.17	22 ± 3	110 ± 7	-	-	-	-	-	-
V12	1.99 ± 0.20	15 ± 3	118 ± 5.9	-	-	-	-	-	-
SEB1	1.55 ± 0.10	2 ± 2	99 ± 5	-	-	-	-	-	-
SEB2	2.23 ± 0.13	-2 ± 2	125 ± 5	-	-	-	-	-	-
SEB3	1.51 ± 0.14	-2 ± 3	107 ± 7	-	-	-	-	-	-
SEB4	2.52 ± 0.28	1 ± 3	118 ± 9	-	-	-	-	-	-
SEB5	1.09 ± 0.14	-35 ± 30	172 ± 17	-	-	-	-	-	-
SEB6	1.37 ± 0.10	-2 ± 3	120 ± 7	0.28 ± 0.08	16 ± 9	118 ± 22	0.16 ± 0.10	-27 ± 20	92 ± 41

Notes. The spectra are obtained from an aperture with the size of the beam centered onto the average position of all integrated emission line peaks in the corresponding region. $^{(ND)}$ line peak below $3\sigma_{\text{rms-ch}}$; $^{(h)}$ fit failed - instead estimates given; $^{(dp)}$ close double peak (either due to two velocity components, line multiplett, or overlapping transition lines).

A.4 Velocities of the gas towards IRS stars and minispiral filaments

Table A.6: *Fluxes, velocities, and FWHM within a beamsized aperture per star or filament for H39α, H36β, and CS(5–4) (Credit:* Moser et al. *(2016b), reproduced with permission ©ESO.)*

region	H39α			H36β			CS(5–4)		
	S_{int} [Jy km s^{-1}]	v [km s^{-1}]	FWHM [km s^{-1}]	S_{int} [Jy km s^{-1}]	v [km s^{-1}]	FWHM [km s^{-1}]	S_{int} [Jy km s^{-1}]	v [km s^{-1}]	FWHM [km s^{-1}]
IRS 1W[P06]	2.35 ± 0.28	32 ± 4	99 ± 7	0.42 ± 0.06	5 ± 3	65 ± 6	-	-	-
IRS 1E[P06]	0.96 ± 0.31	34 ± 5	103 ± 10	-	-	-	-	-	-
IRS 2L[V06]	2.99 ± 0.45	-251 ± 4	110 ± 7	0.44 ± 0.08	-284 ± 2	46 ± 4	-	-	-
IRS 2S[V06]	1.18 ± 0.31	-237 ± 7	122 ± 12	0.21 ± 0.05	-289 ± 4	65 ± 13	-	-	-
	0.33 ± 0.29	22 ± 5	52 ± 32	-	-	-	-	-	-
IRS 3[V06]	-	-	-	-	-	-	0.34 ± 0.10	61 ± 3	31 ± 6
IRS 3E[P06]	-	-	-	-	-	-	0.34 ± 0.11	63 ± 3	29 ± 5
IRS 4[V06]	0.91 ± 0.16	175 ± 6	106 ± 9	-	-	-	0.14 ± 0.05	-20 ± 3	32 ± 8
IRS 5[V06]	0.92 ± 0.19	125 ± 5	93 ± 10	-	-	-	-0.15 ± -0.12	66 ± 13	-58 ± 27
IRS 5E[V06]	0.47 ± 0.07	124 ± 6	130 ± 13	-	-	-	-	-	-
IRS 5S[V06]	0.67 ± 0.10	118 ± 4	101 ± 9	-	-	-	-	-	-
IRS 5SE1[V06]	0.60 ± 0.10	170 ± 10	218 ± 26	0.17 ± 0.08	184 ± 5	36 ± 11	-	-	-
IRS 5SE2[V06]	0.47 ± 0.09	167 ± 14	197 ± 30	-	-	-	-	-	-
IRS 6E[V06]	1.71 ± 0.37	-134 ± 7	166 ± 15	0.18 ± 0.07	-67 ± 24	195 ± 56	-0.06 ± -0.06	28 ± 12	-23 ± 14
IRS 6W[V06]	2.08 ± 0.36	-128 ± 6	123 ± 8	0.25 ± 0.06	-147 ± 7	73 ± 13	0.10 ± 0.03	99 ± 3	29 ± 7
	-	-	-	0.05 ± 0.02	21 ± 4	33 ± 11	-	-	-
IRS 7[V06]	0.17 ± 0.06	-110 ± 5	66 ± 18	0.07 ± 0.03	-118 ± 5	43 ± 13	0.39 ± 0.03	-53 ± 1	41 ± 3
IRS 7SW[P06]	-	-	-	-	-	-	0.12 ± 0.11	61 ± 7	31 ± 14
IRS 7E2(ESE)[P06]	0.78 ± 0.23	102 ± 9	145 ± 17	-	-	-	-	-	-

Notes. The spectra are obtained from an aperture with the size of the beam centered onto the average position of all integrated emission line peaks in the corresponding region (see Fig. 3.1 and A.11). For details on the procedure see Sect. 3.2.4, for dicussion of the velocities see Sect. 3.4.3. References for the source positions are [(P06)] Paumard *et al.* (2006), [(V06)] Viehmann *et al.* (2006), and [(M07)] Mužić *et al.* (2007) .

Table A.6: *Continued. Fluxes, velocities, and FWHM within a beamsized aperture per star or filament for H39α, H36β, and CS(5–4) (Credit: Moser* et al. *(2016b), reproduced with permission ©ESO.)*

region	H39α			H36β			CS(5–4)		
	S_{int} [Jy km s^{-1}]	v [km s^{-1}]	FWHM [km s^{-1}]	S_{int} [Jy km s^{-1}]	v [km s^{-1}]	FWHM [km s^{-1}]	S_{int} [Jy km s^{-1}]	v [km s^{-1}]	FWHM [km s^{-1}]
IRS 9^{V06}	1.56 ± 0.18	173 ± 5	104 ± 8	-	-	-	-	-	-
IRS 9N^{V06}	1.44 ± 0.21	170 ± 7	105 ± 9	0.18 ± 0.04	160 ± 10	101 ± 20	-	-	-
IRS 9W^{P06}	0.32 ± 0.16	-70 ± 13	91 ± 25	-	-	-	-	-	-
	1.10 ± 0.22	273 ± 9	188 ± 20	-	-	-	-	-	-
IRS 9SE^{P06}	1.09 ± 0.14	198 ± 4	118 ± 8	-	-	-	0.11 ± 0.05	-31 ± 6	28 ± 9
IRS 9SW^{P06}	1.14 ± 0.19	202 ± 7	128 ± 12	-	-	-	-	-	-
IRS 10W^{V06}	1.47 ± 0.18	91 ± 4	100 ± 6	0.38 ± 0.05	65 ± 2	48 ± 4	-	-	-
IRS 10EE^{V06}	0.58 ± 0.12	102 ± 7	96 ± 10	-	-	-	-	-	-
IRS 12N^{V06}	0.49 ± 0.17	-207 ± 11	114 ± 19	-	-	-	-	-	-
IRS 13N^{V06}	1.74 ± 0.31	-43 ± 10	162 ± 19	0.14 ± 0.04	-33 ± 5	72 ± 14	-	-	-
IRS 13NE^{V06}	1.89 ± 0.29	-41 ± 8	160 ± 16	0.18 ± 0.03	-34 ± 3	65 ± 8	-	-	-
IRS 13E^{V06}	1.85 ± 0.19	-40 ± 5	154 ± 12	-	-	-	-	-	-
IRS 13E1^{P06}	2.12 ± 0.30	-49 ± 8	182 ± 18	0.13 ± 0.03	-45 ± 5	66 ± 10	-	-	-
IRS 13E2^{P06}	2.37 ± 0.32	-61 ± 8	209 ± 21	0.10 ± 0.02	-55 ± 4	52 ± 9	-	-	-
IRS 13E3c^{P06}	1.95 ± 0.21	-44 ± 5	166 ± 12	-	-	-	-	-	-
IRS 13E4^{P06}	1.84 ± 0.19	-39 ± 5	152 ± 11	-	-	-	-	-	-
IRS 13W^{V06}	2.20 ± 0.37	-123 ± 13	265 ± 23	-	-	-	-	-	-
IRS 14NE^{V06}	0.14 ± 0.07	-100 ± 12	97 ± 27	-	-	-	-	-	-

Notes. The spectra are obtained from an aperture with the size of the beam centered onto the average position of all integrated emission line peaks in the corresponding region (see Fig. 3.1 and A.11). For details on the procedure see Sect. 3.2.4, for dicussion of the velocities see Sect. 3.4.3. References for the source positions are [(P06)] Paumard *et al.* (2006), [(V06)] Viehmann *et al.* (2006), and [(M07)] Mužić *et al.* (2007) .

Table A.6: *Continued. Fluxes, velocities, and FWHM within a beamsized aperture per star or filament for H39α, H36β, and CS(5–4) (Credit: Moser* et al. *(2016b), reproduced with permission ©ESO.)*

	H39α			H36β			CS(5–4)		
region	S_{int} [Jy km s^{-1}]	v [km s^{-1}]	FWHM [km s^{-1}]	S_{int} [Jy km s^{-1}]	v [km s^{-1}]	FWHM [km s^{-1}]	S_{int} [Jy km s^{-1}]	v [km s^{-1}]	FWHM [km s^{-1}]
IRS 16C[P06]	-	-	-	0.07 ± 0.02	37 ± 6	50 ± 14	0.81 ± 0.07	-41 ± 1	34 ± 2
	-	-	-	-	-	-	0.11 ± 0.04	45 ± 4	32 ± 8
IRS 16CC[P06]	0.58 ± 0.17	-52 ± 16	315 ± 59	-	-	-	0.25 ± 0.15	-41 ± 3	23 ± 8
IRS 16NE[P06]	0.98 ± 0.24	-19 ± 15	408 ± 85	-	-	-	-	-	-
IRS 16NW[P06]	-	-	-	-	-	-	0.16 ± 0.07	46 ± 4	28 ± 7
IRS 16S[P06]	2.64 ± 0.36	-128 ± 7	248 ± 16	0.57 ± 0.10	-155 ± 11	243 ± 31	0.79 ± 0.07	-34 ± 1	49 ± 2
IRS 16SE1[P06]	1.68 ± 0.39	-93 ± 11	207 ± 24	-0.02 ± -0.04	-30 ± 13	-25 ± 37	-	-	-
IRS 16SE2[P06]	1.98 ± 0.27	-40 ± 7	153 ± 10	0.17 ± 0.04	-72 ± 5	68 ± 13	0.65 ± 0.09	-38 ± 3	75 ± 5
IRS 16SE3[P06]	2.16 ± 0.21	-30 ± 5	145 ± 8	0.20 ± 0.03	-54 ± 3	63 ± 7	-	-	-
IRS 16SSE1[P06]	1.96 ± 0.37	-117 ± 8	236 ± 18	0.11 ± 0.05	-133 ± 6	46 ± 14	0.66 ± 0.09	-33 ± 2	71 ± 5
IRS 16SSE2[P06]	2.04 ± 0.36	-122 ± 8	238 ± 17	0.13 ± 0.05	-137 ± 6	55 ± 15	0.73 ± 0.07	-34 ± 1	57 ± 3
IRS 16SW[P06]	1.49 ± 0.33	-130 ± 11	283 ± 30	0.12 ± 0.04	-155 ± 10	79 ± 22	0.51 ± 0.06	-36 ± 2	42 ± 3
IRS 16SSW[P06]	2.25 ± 0.42	-157 ± 11	273 ± 24	0.22 ± 0.07	-222 ± 10	93 ± 21	0.51 ± 0.11	-36 ± 2	47 ± 4
IRS 17[V06]	-	-	-	-	-	-	0.39 ± 0.14	16 ± 6	51 ± 9
IRS 20[V06]	1.08 ± 0.23	-199 ± 7	134 ± 11	-	-	-	-	-	-
IRS 21[V06]	2.23 ± 0.26	-84 ± 8	165 ± 12	0.31 ± 0.05	-96 ± 3	61 ± 6	0.54 ± 0.06	-9 ± 4	70 ± 6
IRS 29[V06]	-	-	-	-	-	-	1.34 ± 0.18	46 ± 1	38 ± 2
IRS 29N[P06]	-	-	-	-	-	-	1.36 ± 0.24	46 ± 2	38 ± 3
IRS 29NE1[P06]	-	-	-	-	-	-	1.17 ± 0.25	46 ± 2	39 ± 3
IRS 33N[P06]	3.13 ± 0.34	-190 ± 11	353 ± 24	0.47 ± 0.09	-295 ± 10	141 ± 20	0.34 ± 0.12	-29 ± 4	38 ± 7

Notes. The spectra are obtained from an aperture with the size of the beam centered onto the average position of all integrated emission line peaks in the corresponding region (see Fig. 3.1 and A.11). For details on the procedure see Sect. 3.2.4, for dicussion of the velocities see Sect. 3.4.3. References for the source positions are [(P06)] Paumard *et al.* (2006), [(V06)] Viehmann *et al.* (2006), and [(M07)] Mužić *et al.* (2007) .

Table A.6: Continued. Fluxes, velocities, and FWHM within a beamsized aperture per star or filament for H39α, H36β, and CS(5–4) (Credit: Moser et al. (2016b), reproduced with permission ©ESO.)

	H39α			H36β			CS(5–4)		
region	S_{int} [Jy km s^{-1}]	v [km s^{-1}]	FWHM [km s^{-1}]	S_{int} [Jy km s^{-1}]	v [km s^{-1}]	FWHM [km s^{-1}]	S_{int} [Jy km s^{-1}]	v [km s^{-1}]	FWHM [km s^{-1}]
	2.77 ± 0.29	-133 ± 6	265 ± 14	-	-	-	-	-	-
	0.62 ± 0.10	19 ± 7	116 ± 14	-	-	-	-	-	-
IRS 33NW[V06]	2.30 ± 0.69	-331 ± 79	583 ± 161	0.11 ± 0.03	-312 ± 6	60 ± 14	0.54 ± 0.06	-30 ± 1	33 ± 3
	0.50 ± 0.12	18 ± 7	103 ± 15	-	-	-	-	-	-
IRS 33E[P06]	2.77 ± 0.29	-133 ± 6	265 ± 14	0.47 ± 0.08	-167 ± 10	163 ± 21	-	-	-
IRS 33SW[V06]	2.57 ± 0.28	-142 ± 12	349 ± 27	-	-	-	0.43 ± 0.08	-27 ± 2	39 ± 4
	0.66 ± 0.08	29 ± 3	98 ± 9	-	-	-	0.16 ± 0.03	138 ± 2	43 ± 4
IRS 34NW[P06]	0.24 ± 0.04	-248 ± 9	131 ± 18	-0.05 ± -0.09	-200 ± 9	-22 ± 27	1.08 ± 0.13	55 ± 1	35 ± 2
IRS 34E[P06]	0.65 ± 0.16	-139 ± 17	362 ± 57	-	-	-	0.19 ± 0.07	63 ± 7	64 ± 10
IRS 34W[P06]	0.88 ± 0.21	-124 ± 13	312 ± 42	-	-	-	0.12 ± 0.12	40 ± 8	26 ± 16
AFNW[P06]	-	-	-	0.07 ± 0.04	74 ± 3	34 ± 17	-	-	-
AFNWNW[P06]	-	-	-	0.01 ± 0.01	84 ± 0	5 ± 0	-	-	-
W7b[P06]	0.21 ± 0.14	31 ± 22	85 ± 39	-	-	-	0.15 ± 0.07	79 ± 11	51 ± 17
W10b[P06]	0.18 ± 0.17	27 ± 24	74 ± 50	-	-	-	0.35 ± 0.08	-30 ± 2	32 ± 5
W11b[P06]	0.73 ± 0.26	-295 ± 23	258 ± 66	-	-	-	0.63 ± 0.08	-34 ± 1	32 ± 2
	0.18 ± 0.16	22 ± 16	68 ± 43	-	-	-	-	-	-
W13b[P06]	0.85 ± 0.34	-301 ± 36	300 ± 96	-	-	-	0.56 ± 0.09	-33 ± 1	30 ± 3
	0.27 ± 0.16	20 ± 15	82 ± 31	-	-	-	-	-	-
W14b[P06]	0.43 ± 0.21	11 ± 20	104 ± 33	-	-	-	0.25 ± 0.09	-26 ± 3	29 ± 8

Notes. The spectra are obtained from an aperture with the size of the beam centered onto the average position of all integrated emission line peaks in the corresponding region (see Fig. 3.1 and A.11). For details on the procedure see Sect. 3.2.4, for dicussion of the velocities see Sect. 3.4.3. References for the source positions are [(P06)] Paumard *et al.* (2006), [(V06)] Viehmann *et al.* (2006), and [(M07)] Mužić *et al.* (2007) .

Table A.6: *Continued. Fluxes, velocities, and FWHM within a beamsized aperture per star or filament for H39α, H36β, and CS(5–4) (Credit: Moser* et al. *(2016b), reproduced with permission ©ESO.)*

region	H39α			H36β			CS(5–4)		
	S_{int} [Jy km s^{-1}]	v [km s^{-1}]	FWHM [km s^{-1}]	S_{int} [Jy km s^{-1}]	v [km s^{-1}]	FWHM [km s^{-1}]	S_{int} [Jy km s^{-1}]	v [km s^{-1}]	FWHM [km s^{-1}]
B1b^{P06}	-	-	-	-	-	-	-0.01 ± -0.01	9 ± -	-6 ± 0
B9b^{P06}	0.32 ± 0.11	145 ± 17	204 ± 34	-0.05 ± -0.04	130 ± 13	-48 ± 25	0.73 ± 0.08	3 ± 2	53 ± 4
NE1^{M07}	1.45 ± 0.25	83 ± 4	144 ± 11	0.20 ± 0.06	49 ± 3	39 ± 5	-	-	-
NE2^{M07}	1.29 ± 0.33	1 ± 7	165 ± 16	0.20 ± 0.05	-27 ± 7	80 ± 15	0.11 ± 0.07	1 ± 6	30 ± 13
NE3^{M07}	1.10 ± 0.24	-28 ± 6	199 ± 18	-	-	-	0.35 ± 0.05	-28 ± 4	88 ± 9
NE4^{M07}	1.97 ± 0.43	-178 ± 15	318 ± 38	0.06 ± 0.03	58 ± 8	47 ± 18	0.39 ± 0.05	-39 ± 1	41 ± 3
	0.45 ± 0.16	-7 ± 18	132 ± 38	-	-	-	-	-	-
SW1^{M07}	1.51 ± 0.34	-122 ± 7	130 ± 11	0.16 ± 0.06	-122 ± 6	47 ± 12	-	-	-
SW2^{M07}	2.13 ± 0.35	-127 ± 6	122 ± 8	0.30 ± 0.06	-153 ± 7	88 ± 13	-	-	-
SW3^{M07}	1.71 ± 0.20	-83 ± 5	142 ± 8	-	-	-	-	-	-
SW4^{M07}	1.14 ± -0.28	-166 ± 10	172 ± 19	-	-	-	-	-	-
SW5^{M07}	2.04 ± 0.41	-164 ± 12	263 ± 24	0.24 ± 0.06	-251 ± 7	101 ± 15	-	-	-
	0.99 ± 0.28	-37 ± 11	123 ± 20	-	-	-	-	-	-
SW6^{M07}	2.44 ± 0.29	-225 ± 5	125 ± 7	0.18 ± 0.05	-235 ± 7	70 ± 16	-	-	-
	0.16 ± 0.09	36 ± 11	58 ± 19	-	-	-	-	-	-
SW7^{M07}	2.29 ± 0.41	-238 ± 5	115 ± 8	0.28 ± 0.05	-275 ± 6	84 ± 12	-	-	-
	-	-	-	0.07 ± 0.03	-20 ± 7	40 ± 14	-	-	-
SW8^{M07}	0.53 ± 0.16	-217 ± 9	97 ± 17	0.15 ± 0.05	-257 ± 4	38 ± 8	0.13 ± 0.06	-5 ± 5	31 ± 11
X1^{M07}	0.43 ± 0.12	133 ± 13	172 ± 23	-	-	-	0.60 ± 0.12	6 ± 3	57 ± 6
X2^{M07}	1.38 ± 0.25	260 ± 12	145 ± 17	-	-	-	-	-	-

Notes. The spectra are obtained from an aperture with the size of the beam centered onto the average position of all integrated emission line peaks in the corresponding region (see Fig. 3.1 and A.11). For details on the procedure see Sect. 3.2.4, for dicussion of the velocities see Sect. 3.4.3. References for the source positions are [(P06)] Paumard *et al.* (2006), [(V06)] Viehmann *et al.* (2006), and [(M07)] Mužić *et al.* (2007) .

Table A.6: *Continued. Fluxes, velocities, and FWHM within a beamsized aperture per star or filament for H39α, H36β, and CS(5–4) (Credit: Moser* et al. *(2016b), reproduced with permission ©ESO.)*

region	H39α			H36β			CS(5–4)		
	S_{int} [Jy km s^{-1}]	v [km s^{-1}]	FWHM [km s^{-1}]	S_{int} [Jy km s^{-1}]	v [km s^{-1}]	FWHM [km s^{-1}]	S_{int} [Jy km s^{-1}]	v [km s^{-1}]	FWHM [km s^{-1}]
X3^{M07}	3.61 ± 0.44	-131 ± 6	321 ± 18	-	-	-	-	-	-
	1.04 ± 0.21	-1 ± 8	98 ± 13	-	-	-	-	-	-
X5^{M07}	1.23 ± 0.22	166 ± 7	105 ± 10	-	-	-	-	-	-
X6^{M07}	2.05 ± 0.33	-120 ± 6	166 ± 11	0.22 ± 0.04	-150 ± 2	50 ± 6	-	-	-
X7^{M07}	-	-	-	-	-	-	0.46 ± 0.33	-38 ± 3	24 ± 13

Notes. The spectra are obtained from an aperture with the size of the beam centered onto the average position of all integrated emission line peaks in the corresponding region (see Fig. 3.1 and A.11). For details on the procedure see Sect. 3.2.4, for dicussion of the velocities see Sect. 3.4.3. References for the source positions are $^{(P06)}$ Paumard *et al.* (2006), $^{(V06)}$ Viehmann *et al.* (2006), and $^{(M07)}$ Mužić *et al.* (2007) .

A.5 Source line ratios

Table A.7: Molecular line ratios per region (Credit: Moser et al. (2016b), reproduced with permission ©ESO.)

region	v_{ch}^{20b}	$\frac{CS}{C_2H}$	$\frac{CS}{SO}$	$\frac{CS}{H^{13}CO^+}$	$\frac{CS}{SiO}$	$\frac{CS}{HC_3N}$	$\frac{CS}{CH_3OH(76)}$	$\frac{C_2H}{SO}$	$\frac{C_2H}{H^{13}CO^+}$	$\frac{C_2H}{SiO}$	$\frac{SO}{SiO}$	$\frac{SO}{H^{13}CO^+}$	$\frac{SiO}{H^{13}CO^+}$	v_{ch}^{50b}	$\frac{CS}{N_2H^+}$	$\frac{CS}{CH_3OH(87)}$	$\frac{CS}{^{13}CS}$	$\frac{N_2H^+}{H^{13}CO^+}$	$\frac{N_2H^+}{CH_3OH(87)}$	$\frac{N_2H^+}{^{13}CS}$	$\frac{^{13}CS}{CH_3OH(87)}$
1-all	60	7.3	14.6	15.6	-	8.2^{80}	-	2.0	2.2	-	-	1.1	-	-	-	-	-	-	-	-	-
1	60	7.0	10.7	11.7^{40}	16.5	-	-	1.5	3.0^{40}	2.5	1.7	1.9^{40}	1.1^{40}	-	-	-	-	-	-	-	-
2	60	5.0	10.4	10.0	11.7	-	-	2.1	2.0	2.2	1.1	1.0	0.8	-	-	-	-	-	-	-	-
3	60	4.7	8.1	5.2	-	8.7	7.9	1.8	1.2	-	-	0.7	-	-	-	-	-	-	-	-	-
4	60	-	3.5	4.7	-	5.6	3.9	-	-	-	-	-	-	-	-	-	-	-	-	-	-
5	60	3.6	4.7	7.3	10.2	-	-	1.3	2.1	2.6	2.4	1.6	0.6	-	-	-	-	-	-	-	-
6	60	-	6.3	10.3	9.0	-	10.8^{40}	-	-	-	1.5	1.6	1.7^{40}	-	-	-	-	-	-	-	-
7	60	5.4	8.3	-	4.9^{20}	-	-	1.4^{20}	-	-	-	-	-	-	-	-	-	-	-	-	-
8	-20	6.7	-	-	-	-	-	-	-	-	-	-	-	-	-	-	-	-	-	-	-
9	-20	5.8	-	-	-	-	-	-	-	-	-	-	-	-	-	-	-	-	-	-	-
10	-20	6.8	-	-	-	-	-	-	-	-	-	-	-	-	-	-	-	-	-	-	-
12	-20	4.1	-	-	-	-	-	-	-	-	-	-	-	-	-	-	-	-	-	-	-
13	60	-	6.8	-	7.0	-	7.7	-	-	-	1.0	-	-	-	-	-	-	-	-	-	-
14	-60	4.6	-	8.1	7.1	-	-	-	1.8	1.5	-	-	-	-	-	-	-	-	-	-	-
15	0	5.4	-	-	-	-	-	-	-	-	-	-	-	-	-	-	-	-	-	-	-
16	0	5.8	-	-	-	-	-	-	-	-	-	-	-	-	-	-	-	-	-	-	-
17	140	-	-	-	0.5	-	-	-	-	-	-	-	-	-	-	-	-	-	-	-	-
19	60	1.9	-	-	-	-	-	-	-	-	-	-	-	-	-	-	-	-	-	-	-
20	60	4.2	7.9	11.5	-	-	-	1.4	-	-	-	-	-	-	-	-	-	-	-	-	-
21	0	3.6	-	-	-	-	-	-	-	-	-	-	-	-	-	-	-	-	-	-	-
22	60	1.6	1.7	5.2^{80}	-	2.9^{80}	4.3	1.2	-	-	-	-	-	-	-	-	-	-	-	-	-

Notes. Ratios are obtained from a beamsized aperture of 0.65″ centered onto the average position of all integrated emission line peaks in the corresponding region (finding chart: Fig. A.10). For ratios with N_2H^+, CH_3OH(8–7), and ^{13}CS a beamsized aperture of 1.5″ is used. For details on the procedure see Sect. 3.2.4. SiO denotes the J = 6–5 transition; $^{(20b,50b)}$ velocity channel (typically covering line centroid in the given region) at which the ratio has been taken from data cubes binned at 20 km s^{-1} and 50 km s^{-1} (band 3 lines); $^{(numbers)}$ alternative velocity channel. The SiO(6â€“-5)/SiO(8â€“7) ratio is 0.4 for clump 5 (v_{ch} = −120 km s^{-1}; IRS 7), 1.2 for clump 17 (v_{ch} = 140 km s^{-1}; YZ1-2), and 1.4 for clump 18 (v_{ch} = −20 km s^{-1}; IRS 10EE).

Table A.7: *Continued. Molecular line ratios per region*

region	v_{ch}^20b^	$\frac{CS}{C_2H}$	$\frac{CS}{SO}$	$\frac{CS}{H^{13}CO^+}$	$\frac{CS}{SiO}$	$\frac{CS}{HC_3N}$	$\frac{CS}{CH_3OH(76)}$	$\frac{C_2H}{SO}$	$\frac{C_2H}{H^{13}CO^+}$	$\frac{C_2H}{SiO}$	$\frac{SO}{SiO}$	$\frac{SO}{H^{13}CO^+}$	$\frac{SiO}{H^{13}CO^+}$	v_{ch}^50b^	$\frac{CS}{N_2H^+}$	$\frac{CS}{CH_3OH(87)}$	$\frac{CS}{^{13}CS}$	$\frac{N_2H^+}{H^{13}CO^+}$	$\frac{N_2H^+}{CH_3OH(87)}$	$\frac{N_2H^+}{^{13}CS}$	$\frac{^{13}CS}{CH_3OH(87)}$
24	160	-	3.4	-	-	-	-	-	-	-	-	-	-	-	-	-	-	-	-	-	-
25	160	-	1.7	-	1.7^{180}	-	-	-	-	-	-	-	-	-	-	-	-	-	-	-	-
27	140	-	-	-	1.9	-	-	-	-	-	-	-	-	-	-	-	-	-	-	-	-
T1	60	-	6.2^{80}	-	4.7	6.0	-	-	-	-	1.0	-	-	50	4.0	6.3	-	-	1.6	-	-
T2	60	-	2.3	2.4	-	-	-	-	-	-	-	-	-	50	-	3.9	-	0.8	-	-	-
T3	100	-	2.2	-	-	-	-	-	-	-	-	-	-	-	-	-	-	-	-	-	-
T4	80	-	-	-	-	2.9	-	-	-	-	-	-	-	-	-	-	-	-	-	-	-
T5	60	-	-	-	2.6	-	-	-	-	-	-	-	-	50	4.2	7.5	-	-	2.1	-	-
T6	60	-	-	3.5	-	-	-	-	-	-	-	-	-	50	2.4	4.6	6.0^{100}	1.2	1.9	-	-
T7	40	1.1	-	1.6	2.9^{60}	-	-	-	1.6	-	-	-	-	50	2.2	5.5	6.7	1.3	2.5	2.5	0.8
T8	40	-	-	3.1	3.1^{60}	-	-	-	-	-	-	-	-	50	3.0	4.3	6.4	1.3	1.5	2.3	0.8
T9	60	-	-	1.5^{40}	1.4	-	-	-	-	-	-	-	1.2	50	2.4	6.4	-	0.9	2.5	-	-
T10	60	1.9	3.8	4.3	4.2	6.5	-	1.5^{40}	1.4^{40}	-	1.2	1.2	1.1	50	4.4	5.9	-	1	1.3	-	-
T10-2	-	-	-	-	-	-	-	-	-	-	-	-	-	50	2.2	5.2	4.9^{100}	1.1	2.4	-	-
T11	40	-	-	-	-	-	-	-	-	-	-	-	1.2	50	2.9	4.6	-	0.6	1.5	-	-

Notes. Ratios are obtained from a beamsized aperture of 0.65″ centered onto the average position of all integrated emission line peaks in the corresponding region (finding chart: Fig. A.10). For ratios with N_2H^+, CH_3OH(8–7), and ^{13}CS a beamsized aperture of 1.5″ is used. For details on the procedure see Sect. 3.2.4. SiO denotes the J = 6–5 transition; ^(20b,50b)^ velocity channel (typically covering line centroid in the given region) at which the ratio has been taken from data cubes binned at 20 km s^{-1} and 50 km s^{-1} (band 3 lines); ^(numbers)^ alternative velocity channel. The SiO(6â€“-5)/SiO(8â€“7) ratio is 0.4 for clump 5 ($v_{ch} = -120$ km s^{-1}; IRS 7), 1.2 for clump 17 ($v_{ch} = 140$ km s^{-1}; YZ1-2), and 1.4 for clump 18 ($v_{ch} = -20$ km s^{-1}; IRS 10EE).

Table A.7: *Continued. Molecular line ratios per region*

region	v_{ch}^{20b}	$\frac{CS}{C_2H}$	$\frac{CS}{SO}$	$\frac{CS}{H^{13}CO^+}$	$\frac{CS}{SiO}$	$\frac{CS}{HC_3N}$	$\frac{CS}{CH_3OH(76)}$	$\frac{C_2H}{SO}$	$\frac{C_2H}{H^{13}CO^+}$	$\frac{C_2H}{SiO}$	$\frac{SO}{SiO}$	$\frac{SO}{H^{13}CO^+}$	$\frac{SiO}{H^{13}CO^+}$	v_{ch}^{50b}	$\frac{CS}{N_2H^+}$	$\frac{CS}{CH_3OH(87)}$	$\frac{CS}{^{13}CS}$	$\frac{N_2H^+}{H^{13}CO^+}$	$\frac{N_2H^+}{CH_3OH(87)}$	$\frac{N_2H^+}{^{13}CS}$	$\frac{^{13}CS}{CH_3OH(87)}$
SEW1	-40	5.0	5.6	11.0	7.2	-	-	1.1	2.1	1.4	1.3	1.7	1.6	-50	-	-	28.2	-	-	-	-
SEW1-2	-40	5.5	7.2	13.5	8.9	-	-	1.3	2.6	1.6	1.3	1.8	1.5	-50	-	-	28.1	-	-	-	-
SEW2	-40	4.4	4.9	8.1^{-60}	8.5	-	-	1.1	2.2^{-60}	1.9	1.7	2.3^{-60}	1.6^{-60}	-50	-	-	28.7	-	-	-	-
SEW3	-40	6.7	6.1	-	7.2	-	-	1.0	-	1.1	1.2	-	-	-50	-	-	33	-	-	-	-
SEW4	-40	4.9	8.1	-	-	-	-	1.6	-	-	-	-	-	-	-	-	-	-	-	-	-
SEW5	-	-	-	-	-	-	-	-	-	-	-	-	-	0	7.4	-	-	-	-	-	-
SEW6	0	1.6	-	-	-	-	-	-	-	-	-	-	-	0	3.4	-	-	-	-	-	-
SEW7	20	2.0	-	-	-	-	-	-	-	-	-	-	-	0	3.1	-	-	-	-	-	-
SEW8	-20	1.5	-	-	-	-	-	-	-	-	-	-	-	0	-	-	-	-	-	-	-
SEW9	20	-	3.7	-	3.8	-	-	-	-	-	-	-	-	0	4.6	-	-	-	-	-	-
SEW11	-40	1.1	-	-	-	-	-	-	-	-	-	-	-	-	-	-	-	-	-	-	-
SEW12	-	-	-	-	-	-	-	-	-	-	-	-	-	-50	-	-	8.2	-	-	-	-
SEW13	-	-	-	-	-	-	-	-	-	-	-	-	-	0	1.1	-	-	-	-	-	-
CND-1	80	-	-	-	2.4	-	-	-	-	-	-	-	-	50	2.4	-	-	1.1	-	-	-
CND-2	60	2.9	-	-	-	-	-	-	-	-	-	-	-	-	-	-	-	-	-	-	-
CND-3	40	-	1.8	-	-	-	-	-	-	-	-	-	-	-	-	-	-	-	-	-	-
CND-4	20	0.8^{0}	-	-	-	-	-	-	-	-	-	-	-	0	5.5	-	-	-	-	-	-
CND-5	20	-	-	-	-	-	-	-	-	-	-	-	-	0	4.7	-	-	-	-	-	-
CND-6	0	-	4.0	-	2.2	-	-	-	-	-	1.3	-	-	0	2.8	-	-	-	-	-	-
CND-7	20	-	3.7	-	5.2	-	-	-	-	-	1.4	-	-	0	2.3	-	-	-	-	-	-
CND-8	-	-	-	-	-	-	-	-	-	-	-	-	-	-50	0.9	-	-	2	-	-	-

Notes. Ratios are obtained from a beamsized aperture of 0.65″ centered onto the average position of all integrated emission line peaks in the corresponding region (finding chart: Fig. A.10). For ratios with N_2H^+, CH_3OH(8–7), and ^{13}CS a beamsized aperture of 1.5″ is used. For details on the procedure see Sect. 3.2.4. SiO denotes the J = 6–5 transition; $^{(20b,50b)}$ velocity channel (typically covering line centroid in the given region) at which the ratio has been taken from data cubes binned at 20 km s^{-1} and 50 km s^{-1} (band 3 lines); $^{(numbers)}$ alternative velocity channel. The SiO(6â€“-5)/SiO(8â€“7) ratio is 0.4 for clump 5 (v_{ch} = −120 km s^{-1}; IRS 7), 1.2 for clump 17 (v_{ch} = 140 km s^{-1}; YZ1-2), and 1.4 for clump 18 (v_{ch} = −20 km s^{-1}; IRS 10EE).

Table A.7: *Continued. Molecular line ratios per region*

region	v_{ch}[20b]	$\frac{CS}{C_2H}$	$\frac{CS}{SO}$	$\frac{CS}{H^{13}CO^+}$	$\frac{CS}{SiO}$	$\frac{CS}{HC_3N}$	$\frac{CS}{CH_3OH(76)}$	$\frac{C_2H}{SO}$	$\frac{C_2H}{H^{13}CO^+}$	$\frac{C_2H}{SiO}$	$\frac{SO}{SiO}$	$\frac{SO}{H^{13}CO^+}$	$\frac{SiO}{H^{13}CO^+}$	v_{ch}[50b]	$\frac{CS}{N_2H^+}$	$\frac{CS}{CH_3OH(87)}$	$\frac{CS}{^{13}CS}$	$\frac{N_2H^+}{H^{13}CO^+}$	$\frac{N_2H^+}{CH_3OH(87)}$	$\frac{N_2H^+}{^{13}CS}$	$\frac{^{13}CS}{CH_3OH(87)}$
CND-9	-	-	-	-	-	-	-	-	-	-	-	-	-	-50	1.3	7.5[50]	-	-	2.3[50]	3.2	-
CND-10	20	4.1	-	-	-	-	-	-	-	-	-	-	-	0	2.1	-	4.2	-	-	1.9	-
CND-W1	-	-	-	-	-	-	-	-	-	-	-	-	-	100	-	14.6	12.6	-	1.3[50]	1.1	1.2
CND-W2	-	-	-	-	-	-	-	-	-	-	-	-	-	50	1.6[0]	13.6[100]	7.9[100]	0.8	2.1	1.6	1.7[100]
CND-W3	-	-	-	-	-	-	-	-	-	-	-	-	-	100	8.3	9.8	8.9	-	-	1.0	1.1
V1	-	-	-	-	-	-	-	-	-	-	-	-	-	50	-	-	-	-	1.7	-	-
V2	-	-	-	-	-	-	-	-	-	-	-	-	-	50	-	-	-	-	1.3	-	-
V2-1	-	-	-	-	-	-	-	-	-	-	-	-	-	50	-	-	-	-	1.2	-	-
V4	-	-	-	-	-	-	-	-	-	-	-	-	-	50	-	-	-	-	1.9	-	-
V6	-	-	-	-	-	-	-	-	-	-	-	-	-	50	-	-	-	-	1.7	-	-
V9	-	-	-	-	-	-	-	-	-	-	-	-	-	50	-	-	-	-	1.5	-	-
V10	-	-	-	-	-	-	-	-	-	-	-	-	-	50	-	-	-	-	1.0	-	-
SEB6	-	-	-	-	-	-	-	-	-	-	-	-	-	0	-	-	-	-	4.0	3.9	-

Notes. Ratios are obtained from a beamsized aperture of 0.65″ centered onto the average position of all integrated emission line peaks in the corresponding region (finding chart: Fig. A.10). For ratios with N_2H^+, CH_3OH(8–7), and ^{13}CS a beamsized aperture of 1.5″ is used. For details on the procedure see Sect. 3.2.4. SiO denotes the J = 6–5 transition; [(20b,50b)] velocity channel (typically covering line centroid in the given region) at which the ratio has been taken from data cubes binned at 20 km s^{-1} and 50 km s^{-1} (band 3 lines); [(numbers)] alternative velocity channel. The SiO(6â€“-5)/SiO(8â€“7) ratio is 0.4 for clump 5 ($v_{ch} = -120$ km s^{-1}; IRS 7), 1.2 for clump 17 (v_{ch} = 140 km s^{-1}; YZ1-2), and 1.4 for clump 18 ($v_{ch} = -20$ km s^{-1}; IRS 10EE).

Back matter

Bibliography

Aalto, S. (2007). Molecular gas properties in interacting and merging galaxies. *NewAR*, **51**, 52–57. ADS-Link.

Aalto, S., Johansson, L. E. B., Booth, R. S., and Black, J. H. (1991). Large CO-12/CO-13 intensity ratios in luminous mergers. *A&A*, **249**, 323–326. ADS-Link.

Aalto, S., Booth, R. S., Black, J. H., and Johansson, L. E. B. (1995). Molecular gas in starburst galaxies: line intensities and physical conditions. *A&A*, **300**, 369. ADS-Link.

Aalto, S., Beswick, R., and Jütte, E. (2010). ^{13}CO 1-0 imaging of the Medusa merger, NGC 4194. Large scale variations in molecular cloud properties. *A&A*, **522**, A59. ADS-Link.

Amo-Baladrón, M. A., Martín-Pintado, J., and Martín, S. (2011). Mapping photodissociation and shocks in the vicinity of Sagittarius A*. *A&A*, **526**, A54. ADS-Link.

Andernach, H. (1999). Internet Resources for Radio Astronomy. In M. R. Kidger, I. Perez-Fournon, and F. Sanchez, editors, *Internet Resources for Professional Astronomy*, pages 67–130. ADS-Link.

Antonucci, R. (1993). Unified models for active galactic nuclei and quasars. *ARA&A*, **31**, 473–521. ADS-Link.

Athanassoula, E. and Misiriotis, A. (2002). Morphology, photometry and kinematics of N -body bars - I. Three models with different halo central concentrations. *MNRAS*, **330**, 35–52. ADS-Link.

Baganoff, F. (2004). Simultaneous Gamma-Ray to Sub-Millimeter Monitoring of Sagittarius A*. In *Chandra Proposal*, pages 1826–+. ADS-Link.

Baganoff, F. K. (2003). Multiwavelength Monitoring of Sgr A* During Chandra Observations of Multiple X-ray Flares. In *AAS/High Energy Astrophysics Division #7*, volume 35 of *Bulletin of the American Astronomical Society*, pages 606–+. ADS-Link.

Baganoff, F. K., Bautz, M. W., Brandt, W. N., Chartas, G., Feigelson, E. D., Garmire, G. P., Maeda, Y., Morris, M., Ricker, G. R., Townsley, L. K., and Walter, F. (2001). Rapid X-ray flaring from the direction of the supermassive black hole at the Galactic Centre. *Nature*, **413**, 45–48. ADS-Link.

Baganoff, F. K., Maeda, Y., Morris, M., Bautz, M. W., Brandt, W. N., Cui, W., Doty, J. P., Feigelson, E. D., Garmire, G. P., Pravdo, S. H., Ricker, G. R., and Townsley, L. K. (2003). Chandra X-Ray Spectroscopic Imaging of Sagittarius A* and the Central Parsec of the Galaxy. *ApJ*, **591**, 891–915. ADS-Link.

Bartko, H., Martins, F., Fritz, T. K., Genzel, R., Levin, Y., Perets, H. B., Paumard, T., Nayakshin, S., Gerhard, O., Alexander, T., Dodds-Eden, K., Eisenhauer, F., Gillessen, S., Mascetti, L., Ott, T., Perrin, G., Pfuhl, O., Reid, M. J., Rouan, D., Sternberg, A., and Trippe, S. (2009). Evidence for Warped Disks of Young Stars in the Galactic Center. *ApJ*, **697**, 1741–1763. ADS-Link.

Bartko, H., Martins, F., Trippe, S., Fritz, T. K., Genzel, R., Ott, T., Eisenhauer, F., Gillessen, S., Paumard, T., Alexander, T., Dodds-Eden, K., Gerhard, O., Levin, Y., Mascetti, L., Nayakshin, S., Perets, H. B., Perrin, G., Pfuhl, O., Reid, M. J., Rouan, D., Zilka, M., and Sternberg, A. (2010). An Extremely Top-Heavy Initial Mass Function in the Galactic Center Stellar Disks. *ApJ*, **708**, 834–840. ADS-Link.

Becklin, E. E. and Neugebauer, G. (1968). Infrared Observations of the Galactic Center. *ApJ*, **151**, 145–+. ADS-Link.

Becklin, E. E., Neugebauer, G., Willner, S. P., and Matthews, K. (1978). Infrared observations of the galactic center. IV - The interstellar extinction. *ApJ*, **220**, 831–835. ADS-Link.

Beckmann, V. and Shrader, C. (2012). The AGN phenomenon: open issues. In *Proceedings of ”An INTEGRAL view of the high-energy sky (the first 10 years)” - 9th INTEGRAL Workshop and celebration of the 10th anniversary of the launch (INTEGRAL 2012). 15-19 October 2012. Bibliotheque Nationale de France, Paris, France. Published online at <A href=”http://pos.sissa.it/cgi-bin/reader/conf.cgi?confid=176”>http://pos.sissa.it/cgi-bin/reader/conf.cgi?confid=176</A>, id.69*, page 69. ADS-Link.

Benz, A. O., Stäuber, P., Bourke, T. L., van der Tak, F. F. S., van Dishoeck, E. F., and Jørgensen, J. K. (2007). Energetic radiation and the sulfur chemistry of protostellar envelopes: submillimeter interferometry of AFGL 2591. *A&A*, **475**, 549–558. ADS-Link.

Bergin, E. A., Ciardi, D. R., Lada, C. J., Alves, J., and Lada, E. A. (2001). Molecular Excitation and Differential Gas-Phase Depletions in the IC 5146 Dark Cloud. *ApJ*, **557**, 209–225. ADS-Link.

Bertram, T., Eckart, A., Fischer, S., Zuther, J., Straubmeier, C., Wisotzki, L., and Krips, M. (2007). Molecular gas in nearby low-luminosity QSO host galaxies. *A&A*, **470**, 571–583. ADS-Link.

Bigiel, F., Leroy, A., Walter, F., Brinks, E., de Blok, W. J. G., Madore, B., and Thornley, M. D. (2008). The Star Formation Law in Nearby Galaxies on Sub-Kpc Scales. *AJ*, **136**, 2846–2871. ADS-Link.

Blandford, R. D. and Begelman, M. C. (1999). On the fate of gas accreting at a low rate on to a black hole. *MNRAS*, **303**, L1–L5. ADS-Link.

Böker, T., Falcón-Barroso, J., Schinnerer, E., Knapen, J. H., and Ryder, S. (2008). A SINFONI View of Galaxy Centers: Morphology and Kinematics of Five Nuclear Star Formation-Rings. *AJ*, **135**, 479–495. ADS-Link.

Bolatto, A. D., Wolfire, M., and Leroy, A. K. (2013). The CO-to-H_2 Conversion Factor. *ARA&A*, **51**, 207–268. ADS-Link.

Bower, G. C., Markoff, S., Dexter, J., Gurwell, M. A., Moran, J. M., Brunthaler, A., Falcke, H., Fragile, P. C., Maitra, D., Marrone, D., Peck, A., Rushton, A., and Wright, M. C. H. (2015). Radio and Millimeter Monitoring of Sgr A*: Spectrum, Variability, and Constraints on the G2 Encounter. *ApJ*, **802**, 69. ADS-Link.

Busch, G., Zuther, J., Valencia-S., M., Moser, L., Fischer, S., Eckart, A., Scharwächter, J., Gadotti, D. A., and Wisotzki, L. (2014). A low-luminosity type-1 QSO sample. I. Overluminous host spheroidals or undermassive black holes. *A&A*, **561**, A140. ADS-Link.

Busch, G., Smajić, S., Scharwächter, J., Eckart, A., Valencia-S., M., Moser, L., Husemann, B., Krips, M., and Zuther, J. (2015). A low-luminosity type-1 QSO sample. II. Tracing circumnuclear star formation in HE 1029-1831 with SINFONI. *A&A*, **575**, A128. ADS-Link.

Caldú-Primo, A., Schruba, A., Walter, F., Leroy, A., Sandstrom, K., de Blok, W. J. G., Ianjamasimanana, R., and Mogotsi, K. M. (2013). A High-dispersion Molecular Gas Component in Nearby Galaxies. *AJ*, **146**, 150. ADS-Link.

Caldú-Primo, A., Schruba, A., Walter, F., Leroy, A., Bolatto, A. D., and Vogel, S. (2015). Spatially Extended and High-Velocity Dispersion Molecular Component in Spiral Galaxies: Single-Dish Versus Interferometric Observations. *AJ*, **149**, 76. ADS-Link.

Carroll, T. J. and Goldsmith, P. F. (1981). Infrared pumping and rotational excitation of molecules in interstellar clouds. *ApJ*, **245**, 891–897. ADS-Link.

Casasola, V., Combes, F., García-Burillo, S., Hunt, L. K., Léon, S., and Baker, A. J. (2008). Molecular gas in NUclei of GAlaxies (NUGA). X. The Seyfert 2 galaxy NGC 3147. *A&A*, **490**, 61–76. ADS-Link.

Casasola, V., Hunt, L. K., Combes, F., García-Burillo, S., Boone, F., Eckart, A., Neri, R., and Schinnerer, E. (2010). Molecular gas in NUclei of GAlaxies (NUGA) XIII. The interacting Seyfert 2/LINER galaxy NGC 5953. *A&A*, **510**, A52. ADS-Link.

Casasola, V., Hunt, L. K., Combes, F., García-Burillo, S., and Neri, R. (2011a). Molecular Gas in NUclei of GAlaxies (NUGA). XIV. The barred LINER/Seyfert 2 galaxy NGC 3627. *A&A*, **527**, A92. ADS-Link.

Casasola, V., García-Burillo, S., Combes, F., Hunt, L. K., Krips, M., Schinnerer, E., Baker, A. J., Boone, F., Eckart, A., Léon, S., Neri, R., and Tacconi, L. J. (2011b). New views on bar pattern speeds from the NUGA survey. *Memorie della Societa Astronomica Italiana Supplementi*, **18**, 43. ADS-Link.

Casasola, V., Hunt, L., Combes, F., and García-Burillo, S. (2015). The resolved star-formation relation in nearby active galactic nuclei. *A&A*, **577**, A135. ADS-Link.

Casey, C. M. (2012). Far-infrared spectral energy distribution fitting for galaxies near and far. *MNRAS*, **425**, 3094–3103. ADS-Link.

Casey, C. M., Narayanan, D., and Cooray, A. (2014). Dusty star-forming galaxies at high redshift. *Phys. Rep.*, **541**, 45–161. ADS-Link.

Casoli, F., Dupraz, C., and Combes, F. (1992). The case of missing (C-13)O in mergers. *A&A*, **264**, 55–67. ADS-Link.

Charnley, S. B. (1997). Sulfuretted Molecules in Hot Cores. *ApJ*, **481**, 396–405. ADS-Link.

Christopher, M. H., Scoville, N. Z., Stolovy, S. R., and Yun, M. S. (2005). HCN and HCO^+ Observations of the Galactic Circumnuclear Disk. *ApJ*, **622**, 346–365. ADS-Link.

Churchwell, E. (2006). Recent Results from GLIMPSE. In L. Armus & W. T. Reach, editor, *Astronomical Society of the Pacific Conference Series*, volume 357 of *Astronomical Society of the Pacific Conference Series*, pages 116–+. ADS-Link.

Ciurlo, A., Paumard, T., Rouan, D., and Clénet, Y. (2016). Hot molecular hydrogen in the central parsec of the Galaxy through near-infrared 3D fitting. *A&A*, **594**, A113. ADS-Link.

Clénet, Y., Rouan, D., Gendron, E., Montri, J., Rigaut, F., Léna, P., and Lacombe, F. (2001). Adaptive optics L-band observations of the Galactic Center region. *A&A*, **376**, 124–135. ADS-Link.

Coil, A. L. and Ho, P. T. P. (1999). Infalling Gas toward the Galactic Center. *ApJ*, **513**, 752–766. ADS-Link.

Coil, A. L. and Ho, P. T. P. (2000). The Dynamics of Molecular Material within 15 PARSECS of the Galactic Center. *ApJ*, **533**, 245–259. ADS-Link.

Combes, F. (2001). Fueling the AGN. In I. Aretxaga, D. Kunth, and R. Mújica, editors, *Advanced Lectures on the Starburst-AGN*, page 223. ADS-Link.

Combes, F., García-Burillo, S., Boone, F., Hunt, L. K., Baker, A. J., Eckart, A., Englmaier, P., Leon, S., Neri, R., Schinnerer, E., and Tacconi, L. J. (2004). Molecular gas in NUclei of GAlaxies (NUGA). II. The ringed LINER NGC 7217. *A&A*, **414**, 857–872. ADS-Link.

Combes, F., García-Burillo, S., Braine, J., Schinnerer, E., Walter, F., and Colina, L. (2011). Galaxy evolution and star formation efficiency at $0.2 < z < 0.6$. *A&A*, **528**, A124. ADS-Link.

Combes, F., García-Burillo, S., Casasola, V., Hunt, L., Krips, M., Baker, A. J., Boone, F., Eckart, A., Marquez, I., Neri, R., Schinnerer, E., and Tacconi, L. J. (2013). ALMA observations of feeding and feedback in nearby Seyfert galaxies: an AGN-driven outflow in NGC 1433. *A&A*, **558**, A124. ADS-Link.

Combes, F., García-Burillo, S., Casasola, V., Hunt, L. K., Krips, M., Baker, A. J., Boone, F., Eckart, A., Marquez, I., Neri, R., Schinnerer, E., and Tacconi, L. J. (2014). ALMA reveals the feeding of the Seyfert 1 nucleus in NGC 1566. *A&A*, **565**, A97. ADS-Link.

Contini, M. and Contini, T. (2003). Dust-to-gas ratios in the starburst regions of luminous infrared galaxies. *MNRAS*, **342**, 299–313. ADS-Link.

Costagliola, F., Aalto, S., Rodriguez, M. I., Muller, S., Spoon, H. W. W., Martín, S., Peréz-Torres, M. A., Alberdi, A., Lindberg, J. E., Batejat, F., Jütte, E., van der Werf, P., and Lahuis, F. (2011). Molecules as tracers of galaxy evolution: an EMIR survey. I. Presentation of the data and first results. *A&A*, **528**, A30. ADS-Link.

Cotera, A., Morris, M., Ghez, A. M., Becklin, E. E., Tanner, A. M., Werner, M. W., and Stolovy, S. R. (1999). Mid-Infrared Imaging of the Central Parsec with Keck. In H. Falcke, A. Cotera, W. J. Duschl, F. Melia, and M. J. Rieke, editors, *The Central Parsecs of the Galaxy*, volume 186 of *Astronomical Society of the Pacific Conference Series*, page 240. ADS-Link.

Crenshaw, D. M., Kraemer, S. B., and Gabel, J. R. (2003). The Host Galaxies of Narrow-Line Seyfert 1 Galaxies: Evidence for Bar-Driven Fueling. *AJ*, **126**, 1690–1698. ADS-Link.

Dame, T. M. and Thaddeus, P. (1994). Detection of a thick molecular disk in the galaxy. *ApJ*, **436**, L173–L176. ADS-Link.

Davis, T. A. (2014). Systematic variation of the 12CO/13CO ratio as a function of star-formation rate surface density. *ArXiv e-prints*. ADS-Link.

Deo, R. P., Crenshaw, D. M., and Kraemer, S. B. (2006). The Host Galaxies of Narrow-Line Seyfert 1 Galaxies: Nuclear Dust Morphology and Starburst Rings. *AJ*, **132**, 321–346. ADS-Link.

Devereux, N., Taniguchi, Y., Sanders, D. B., Nakai, N., and Young, J. S. (1994). (12)CO (3-2) & (1-0) emission line observations of nearby starburst galaxy nuclei. *AJ*, **107**, 2006–2016. ADS-Link.

Dexter, J., Agol, E., Fragile, P. C., and McKinney, J. C. (2010). The Submillimeter Bump in Sgr A* from Relativistic MHD Simulations. *ApJ*, **717**, 1092–1104. ADS-Link.

Di Francesco, J., Hogerheijde, M. R., Welch, W. J., and Bergin, E. A. (2002). Abundances of Molecular Species in Barnard 68. *AJ*, **124**, 2749–2755. ADS-Link.

Di Matteo, T., Springel, V., and Hernquist, L. (2005). Black Holes in Galaxy Mergers. In A. Merloni, S. Nayakshin, & R. A. Sunyaev, editor, *Growing Black Holes: Accretion in a Cosmological Context*, pages 340–345. ADS-Link.

Dodds-Eden, K., Sharma, P., Quataert, E., Genzel, R., Gillessen, S., Eisenhauer, F., and Porquet, D. (2010). Time-Dependent Models of Flares from Sagittarius A*. *ApJ*, **725**, 450–465. ADS-Link.

Doeleman, S. S., Weintroub, J., Rogers, A. E. E., Plambeck, R., Freund, R., Tilanus, R. P. J., Friberg, P., Ziurys, L. M., Moran, J. M., Corey, B., Young, K. H., Smythe, D. L., Titus, M., Marrone, D. P., Cappallo, R. J., Bock, D. C.-J., Bower, G. C., Chamberlin, R., Davis, G. R., Krichbaum, T. P., Lamb, J., Maness, H., Niell, A. E., Roy, A., Strittmatter, P., Werthimer, D., Whitney, A. R., and Woody, D. (2008). Event-horizon-scale structure in the supermassive black hole candidate at the Galactic Centre. *Nature*, **455**, 78–80. ADS-Link.

Donovan, J. L., Herrnstein, R. M., and Ho, P. T. P. (2006). Exploring High-Velocity NH_3(6,6) Emission at the Center of Our Galaxy. *ApJ*, **647**, 1159–1169. ADS-Link.

Downes, D. and Solomon, P. M. (1998). Rotating Nuclear Rings and Extreme Starbursts in Ultraluminous Galaxies. *ApJ*, **507**, 615–654. ADS-Link.

Dumas, G., Mundell, C. G., Emsellem, E., and Nagar, N. M. (2007). Central kiloparsec of Seyfert and inactive host galaxies: a comparison of two-dimensional stellar and gaseous kinematics. *MNRAS*, **379**, 1249–1278. ADS-Link.

Dumke, M., Nieten, C., Thuma, G., Wielebinski, R., and Walsh, W. (2001). Warm gas in central regions of nearby galaxies. Extended mapping of CO(3-2) emission. *A&A*, **373**, 853–880. ADS-Link.

Eckart, A. and Genzel, R. (1996). Observations of stellar proper motions near the Galactic Centre. *Nature*, **383**, 415–417. ADS-Link.

Eckart, A. and Genzel, R. (1997). Stellar proper motions in the central 0.1 PC of the Galaxy. *MNRAS*, **284**, 576–598. ADS-Link.

Eckart, A., Genzel, R., Hofmann, R., Sams, B. J., and Tacconi-Garman, L. E. (1995). High angular resolution spectroscopic and polarimetric imaging of the galactic center in the near-infrared. *ApJ*, **445**, L23–L26. ADS-Link.

Eckart, A., Ott, T., and Genzel, R. (1999). The Sgr A* stellar cluster: New NIR imaging and spectroscopy. *A&A*, **352**, L22–L25. ADS-Link.

Eckart, A., Genzel, R., Ott, T., and Schödel, R. (2002). Stellar orbits near Sagittarius A*. *MNRAS*, **331**, 917–934. ADS-Link.

Eckart, A., Baganoff, F. K., Morris, M., Bautz, M. W., Brandt, W. N., Garmire, G. P., Genzel, R., Ott, T., Ricker, G. R., Straubmeier, C., Viehmann, T., Schödel, R., Bower, G. C., and Goldston, J. E. (2004a). First simultaneous NIR/X-ray detection of a flare from Sgr A*. *A&A*, **427**, 1–11. ADS-Link.

Eckart, A., Moultaka, J., Viehmann, T., Straubmeier, C., and Mouawad, N. (2004b). Young Stars at the Center of the Milky Way? *ApJ*, **602**, 760–769. ADS-Link.

Eckart, A., Schödel, R., and Straubmeier, C. (2005a). *The black hole at the center of the Milky Way*. ADS-Link.

Eckart, A., Schödel, R., Moultaka, J., Straubmeier, C., Viehmann, T., Pfalzner, S., and Pott, J.-U. (2005b). The Galactic Center: The Stellar Cluster and the Massive Black Hole. In S. Hüttmeister, E. Manthey, D. Bomans, & K. Weis, editor, *The Evolution of Starbursts*, volume 783 of *American Institute of Physics Conference Series*, pages 17–25. ADS-Link.

Eckart, A., Baganoff, F. K., Schödel, R., Morris, M., Genzel, R., Bower, G. C., Marrone, D., Moran, J. M., Viehmann, T., Bautz, M. W., Brandt, W. N., Garmire, G. P., Ott, T., Trippe, S., Ricker, G. R., Straubmeier, C., Roberts, D. A., Yusef-Zadeh, F., Zhao, J. H., and Rao, R. (2006). The flare activity of Sagittarius A*. New coordinated mm to X-ray observations. *A&A*, **450**, 535–555. ADS-Link.

Eckart, A., García-Marín, M., Vogel, S. N., Teuben, P., Morris, M. R., Baganoff, F., Dexter, J., Schödel, R., Witzel, G., Valencia-S., M., Karas, V., Kunneriath, D., Straubmeier, C., Moser, L., Sabha, N., Buchholz, R., Zamaninasab, M., Mužić, K., Moultaka, J., and Zensus, J. A. (2012). Millimeter to X-ray flares from Sagittarius A*. *A&A*, **537**, A52. ADS-Link.

Eckart, A., Mužić, K., Yazici, S., Sabha, N., Shahzamanian, B., Witzel, G., Moser, L., Garcia-Marin, M., Valencia-S., M., Jalali, B., Bremer, M., Straubmeier, C., Rauch, C., Buchholz, R., Kunneriath, D., and Moultaka, J. (2013). Near-infrared proper motions and spectroscopy of infrared excess sources at the Galactic center. *A&A*, **551**, A18. ADS-Link.

Eisenhauer, F., Schödel, R., Genzel, R., Ott, T., Tecza, M., Abuter, R., Eckart, A., and Alexander, T. (2003). A Geometric Determination of the Distance to the Galactic Center. *ApJ*, **597**, L121–L124. ADS-Link.

Eisenhauer, F., Genzel, R., Alexander, T., Abuter, R., Paumard, T., Ott, T., Gilbert, A., Gillessen, S., Horrobin, M., Trippe, S., Bonnet, H., Dumas, C., Hubin, N., Kaufer, A., Kissler-Patig, M., Monnet, G., Ströbele, S., Szeifert, T., Eckart, A., Schödel, R., and Zucker, S. (2005). SINFONI in the Galactic Center: Young Stars and Infrared Flares in the Central Light-Month. *ApJ*, **628**, 246–259. ADS-Link.

Ekers, R. D., van Gorkom, J. H., Schwarz, U. J., and Goss, W. M. (1983). The radio structure of SGR A. *A&A*, **122**, 143–150. ADS-Link.

Evans, A. S., Frayer, D. T., Surace, J. A., and Sanders, D. B. (2001). Molecular Gas in Infrared-Excess, Optically Selected and the Quasars Connection with Infrared-Luminous Galaxies. *AJ*, **121**, 1893–1902. ADS-Link.

Evans, A. S., Solomon, P. M., Tacconi, L. J., Vavilkin, T., and Downes, D. (2006). Dense Molecular Gas and the Role of Star Formation in the Host Galaxies of Quasi-stellar Objects. *AJ*, **132**, 2398–2408. ADS-Link.

Fabian, A. C. (1979). Theories of the nuclei of active galaxies. *Proceedings of the Royal Society of London Series A*, **366**, 449–459. ADS-Link.

Falcke, H. and Markoff, S. (2000). The jet model for Sgr A*: Radio and X-ray spectrum. *A&A*, **362**, 113–118. ADS-Link.

Falcke, H., Goss, W. M., Matsuo, H., Teuben, P., Zhao, J.-H., and Zylka, R. (1998). The Simultaneous Spectrum of Sagittarius A* from 20 Centimeters to 1 Millimeter and the Nature of the Millimeter Excess. *ApJ*, **499**, 731–734. ADS-Link.

Falcón-Barroso, J., Bacon, R., Bureau, M., Cappellari, M., Davies, R. L., de Zeeuw, P. T., Emsellem, E., Fathi, K., Krajnović, D., Kuntschner, H., McDermid, R. M., Peletier, R. F., and Sarzi, M. (2006). The SAURON project - VII. Integral-field absorption and emission-line kinematics of 24 spiral galaxy bulges. *MNRAS*, **369**, 529–566. ADS-Link.

Farrah, D., Rowan-Robinson, M., Oliver, S., Serjeant, S., Borne, K., Lawrence, A., Lucas, R. A., Bushouse, H., and Colina, L. (2001). HST/WFPC2 imaging of the QDOT ultraluminous infrared galaxy sample. *MNRAS*, **326**, 1333–1352. ADS-Link.

Feldmeier-Krause, A., Neumayer, N., Schödel, R., Seth, A., Hilker, M., de Zeeuw, P. T., Kuntschner, H., Walcher, C. J., Lützgendorf, N., and Kissler-Patig, M. (2015). KMOS view of the Galactic centre. I. Young stars are centrally concentrated. *A&A*, **584**, A2. ADS-Link.

Ferland, G. J., Peterson, B. M., Horne, K., Welsh, W. F., and Nahar, S. N. (1992). Anisotropic line emission and the geometry of the broad-line region in active galactic nuclei. *ApJ*, **387**, 95–108. ADS-Link.

Ferrarese, L. and Ford, H. (2005). Supermassive Black Holes in Galactic Nuclei: Past, Present and Future Research. *Space Sci. Rev.*, **116**, 523–624. ADS-Link.

Fischer, S., Iserlohe, C., Zuther, J., Bertram, T., Straubmeier, C., Schödel, R., and Eckart, A. (2006). Nearby AGN and their hosts in the near infrared. *A&A*, **452**, 827–837. ADS-Link.

Fontani, F., Cesaroni, R., and Furuya, R. S. (2010). Class I and Class II methanol masers in high-mass star-forming regions. *A&A*, **517**, A56. ADS-Link.

Ford, G. P., Gear, W. K., Smith, M. W. L., Eales, S. A., Baes, M., Bendo, G. J., Boquien, M., Boselli, A., Cooray, A. R., De Looze, I., Fritz, J., Gentile, G., Gomez, H. L., Gordon, K. D., Kirk, J., Lebouteiller, V., O'Halloran, B., Spinoglio, L., Verstappen, J., and Wilson, C. D. (2013). Herschel Exploitation of Local Galaxy Andromeda (HELGA). III. The Star Formation Law in M31. *ApJ*, **769**, 55. ADS-Link.

Frank, J., King, A., and Raine, D. J. (2002). *Accretion Power in Astrophysics: Third Edition*. ADS-Link.

Gaffney, N. I., Lester, D. F., and Doppmann, G. (1995). Measuring stellar kinematics in galaxies with the near-infrared (2-0) (12) CO absorption bandhead. *PASP*, **107**, 68–76. ADS-Link.

Gao, Y. and Solomon, P. M. (2004a). HCN Survey of Normal Spiral, Infrared-luminous, and Ultraluminous Galaxies. *ApJS*, **152**, 63–80. ADS-Link.

Gao, Y. and Solomon, P. M. (2004b). The Star Formation Rate and Dense Molecular Gas in Galaxies. *ApJ*, **606**, 271–290. ADS-Link.

García-Burillo, S. and Combes, F. (2012). The feeding of activity in galaxies: a molecular line perspective. *Journal of Physics Conference Series*, **372**(1), 012050. ADS-Link.

García-Burillo, S., Combes, F., Eckart, A., Tacconi, L. J., Hunt, L. K., Leon, S., Baker, A. J., Englmaier, P. P., Boone, F., Schinnerer, E., and Neri, R. (2003). NUGA: The IRAM Survey of AGN Spiral Hosts. In S. Collin, F. Combes, and I. Shlosman, editors, *Active Galactic Nuclei: From Central Engine to Host Galaxy*, volume 290 of *Astronomical Society of the Pacific Conference Series*, page 423. ADS-Link.

García-Burillo, S., Combes, F., Usero, A., Aalto, S., Krips, M., Viti, S., Alonso-Herrero, A., Hunt, L. K., Schinnerer, E., Baker, A. J., Boone, F., Casasola, V., Colina, L., Costagliola, F., Eckart, A., Fuente, A., Henkel, C., Labiano, A., Martín, S., Márquez, I., Muller, S., Planesas, P., Ramos Almeida, C., Spaans, M., Tacconi, L. J., and van der Werf, P. P. (2014). Molecular line emission in NGC 1068 imaged with ALMA. I. An AGN-driven outflow in the dense molecular gas. *A&A*, **567**, A125. ADS-Link.

García-Marín, M., Eckart, A., Weiss, A., Witzel, G., Bremer, M., Zamaninasab, M., Schödel, R., Kunneriath, D., Sabha, N., Baganoff, F., Dovvciak, M., Duschl, W. J., Moultaka, J., Karas, V., Najarro, F., Mužić, K., Straubmeier, C., Vogel, S. N., Krips, M., and Wiesemeyer, H. (2011). Sub-Millimeter View of the Galactic Center. In M. R. Morris, Q. D. Wang, & F. Yuan, editor, *Astronomical Society of the Pacific Conference Series*, volume 439 of *Astronomical Society of the Pacific Conference Series*, pages 315–+. ADS-Link.

Geballe, T. R., Baas, F., and Wade, R. (1989). Carbon monoxide along the line of sight to galactic center infrared sources. *A&A*, **208**, 255–260. ADS-Link.

Gebhardt, K., Bender, R., Bower, G., Dressler, A., Faber, S. M., Filippenko, A. V., Green, R., Grillmair, C., Ho, L. C., Kormendy, J., Lauer, T. R., Magorrian, J., Pinkney, J., Richstone, D., and Tremaine, S. (2000). A Relationship between Nuclear Black Hole Mass and Galaxy Velocity Dispersion. *ApJ*, **539**, L13–L16. ADS-Link.

Genzel, R., Pichon, C., Eckart, A., Gerhard, O. E., and Ott, T. (2000). Stellar dynamics in the Galactic Centre: proper motions and anisotropy. *MNRAS*, **317**, 348–374. ADS-Link.

Genzel, R., Schödel, R., Ott, T., Eckart, A., Alexander, T., Lacombe, F., Rouan, D., and Aschenbach, B. (2003a). Near-infrared flares from accreting gas around the supermassive black hole at the Galactic Centre. *Nature*, **425**, 934–937. ADS-Link.

Genzel, R., Schödel, R., Ott, T., Eisenhauer, F., Hofmann, R., Lehnert, M., Eckart, A., Alexander, T., Sternberg, A., Lenzen, R., Clénet, Y., Lacombe, F., Rouan, D., Renzini, A., and Tacconi-Garman, L. E. (2003b). The Stellar Cusp around the Supermassive Black Hole in the Galactic Center. *ApJ*, **594**, 812–832. ADS-Link.

Genzel, R., Tacconi, L. J., Gracia-Carpio, J., Sternberg, A., Cooper, M. C., Shapiro, K., Bolatto, A., Bouché, N., Bournaud, F., Burkert, A., Combes, F., Comerford, J., Cox, P., Davis, M., Schreiber, N. M. F., Garcia-Burillo, S., Lutz, D., Naab, T., Neri, R., Omont, A., Shapley, A., and Weiner, B. (2010a). A study of the gas-star formation relation over cosmic time. *MNRAS*, **407**, 2091–2108. ADS-Link.

Genzel, R., Eisenhauer, F., and Gillessen, S. (2010b). The Galactic Center massive black hole and nuclear star cluster. *Reviews of Modern Physics*, **82**, 3121–3195. ADS-Link.

Gezari, D. Y., Shu, P., Lamb, G., Tresch-Fienberg, R., Fazio, G. G., Hoffmann, W. F., Gatley, I., and McCreight, C. (1985). 8.3 and 12.4 micron imaging of the Galactic Center source complex with the Goddard infrared array camera. *ApJ*, **299**, 1007–1016. ADS-Link.

Ghez, A. M. (2004). The Supermassive Black Hole at the Center of the Milky Way. *Coevolution of Black Holes and Galaxies*, pages 53–+. ADS-Link.

Ghez, A. M., Morris, M., Becklin, E. E., Tanner, A., and Kremenek, T. (2000). The accelerations of stars orbiting the Milky Way's central black hole. *Nature*, **407**, 349–351. ADS-Link.

Ghez, A. M., Becklin, E., Duchjne, G., Hornstein, S., Morris, M., Salim, S., and Tanner, A. (2003). Full Three Dimensional Orbits For Multiple Stars on Close Approaches to the Central Supermassive Black Hole. *Astronomische Nachrichten Supplement*, **324**, 527–533. ADS-Link.

Ghez, A. M., Salim, S., Hornstein, S. D., Tanner, A., Lu, J. R., Morris, M., Becklin, E. E., and Duchêne, G. (2005). Stellar Orbits around the Galactic Center Black Hole. *ApJ*, **620**, 744–757. ADS-Link.

Ghez, A. M., Salim, S., Weinberg, N. N., Lu, J. R., Do, T., Dunn, J. K., Matthews, K., Morris, M. R., Yelda, S., Becklin, E. E., Kremenek, T., Milosavljevic, M., and Naiman, J. (2008). Measuring Distance and Properties of the Milky Way's Central Supermassive Black Hole with Stellar Orbits. *ApJ*, **689**, 1044–1062. ADS-Link.

Gillessen, S., Eisenhauer, F., Trippe, S., Alexander, T., Genzel, R., Martins, F., and Ott, T. (2009a). Monitoring Stellar Orbits Around the Massive Black Hole in the Galactic Center. *ApJ*, **692**, 1075–1109. ADS-Link.

Gillessen, S., Eisenhauer, F., Trippe, S., Alexander, T., Genzel, R., Martins, F., and Ott, T. (2009b). Monitoring Stellar Orbits Around the Massive Black Hole in the Galactic Center. *ApJ*, **692**, 1075–1109. ADS-Link.

Gillessen, S., Eisenhauer, F., Fritz, T. K., Bartko, H., Dodds-Eden, K., Pfuhl, O., Ott, T., and Genzel, R. (2009c). The Orbit of the Star S2 Around SGR A* from Very Large Telescope and Keck Data. *ApJ*, **707**, L114–L117. ADS-Link.

Goicoechea, J. R., Pety, J., Gerin, M., Teyssier, D., Roueff, E., Hily-Blant, P., and Baek, S. (2006). Low sulfur depletion in the Horsehead PDR. *A&A*, **456**, 565–580. ADS-Link.

Goicoechea, J. R., Etxaluze, M., Cernicharo, J., Gerin, M., Neufeld, D. A., Contursi, A., Bell, T. A., De Luca, M., Encrenaz, P., Indriolo, N., Lis, D. C., Polehampton, E. T., and Sonnentrucker, P. (2013). Herschel* Far-infrared Spectroscopy of the Galactic Center. Hot Molecular Gas: Shocks versus Radiation near Sgr A. *ApJ*, **769**, L13. ADS-Link.

Gordon, M. A. and Walmsley, C. M. (1990). An observational study of millimeter-wave recombination lines. *ApJ*, **365**, 606–614. ADS-Link.

Goto, M., Usuda, T., Takato, N., Hayashi, M., Sakamoto, S., Gaessler, W., Hayano, Y., Iye, M., Kamata, Y., Kanzawa, T., Kobayashi, N., Minowa, Y., Nedachi, K., Oya, S., Pyo, T.-S., Saint-Jacques, D., Suto, H., Takami, H., Terada, H., and Mitchell, G. F. (2003). Carbon Isotope Ratio in ^{12}CO/^{13}CO toward Local Molecular Clouds with Near-Infrared High-Resolution Spectroscopy of Vibrational Transition Bands. *ApJ*, **598**, 1038–1047. ADS-Link.

Goto, M., Geballe, T. R., Indriolo, N., Yusef-Zadeh, F., Usuda, T., Henning, T., and Oka, T. (2014). Infrared H_3^+ and CO Studies of the Galactic Core: GCIRS 3 and GCIRS 1W. *ApJ*, **786**, 96. ADS-Link.

Greve, T. R., Bertoldi, F., Smail, I., Neri, R., Chapman, S. C., Blain, A. W., Ivison, R. J., Genzel, R., Omont, A., Cox, P., Tacconi, L., and Kneib, J.-P. (2005). An interferometric CO survey of luminous submillimetre galaxies. *MNRAS*, **359**, 1165–1183. ADS-Link.

Guesten, R., Genzel, R., Wright, M. C. H., Jaffe, D. T., Stutzki, J., and Harris, A. I. (1987). Aperture synthesis observations of the circumnuclear ring in the Galactic center. *ApJ*, **318**, 124–138. ADS-Link.

Haan, S., Schinnerer, E., Emsellem, E., García-Burillo, S., Combes, F., Mundell, C. G., and Rix, H.-W. (2009). Dynamical Evolution of AGN Host Galaxies – Gas In/Out-Flow Rates in Seven NUGA Galaxies. *ApJ*, **692**, 1623–1661. ADS-Link.

Haller, J. W., Rieke, M. J., Rieke, G. H., Tamblyn, P., Close, L., and Melia, F. (1996). Stellar Kinematics and the Black Hole in the Galactic Center. *ApJ*, **456**, 194–+. ADS-Link.

Harris, G. L. H., Rejkuba, M., and Harris, W. E. (2010). The Distance to NGC 5128 (Centaurus A). *PASA*, **27**, 457–462. ADS-Link.

Heckman, T. M. (1980). An optical and radio survey of the nuclei of bright galaxies - Activity in normal galactic nuclei. *A&A*, **87**, 152–164. ADS-Link.

Heckman, T. M. and Best, P. N. (2014). The Coevolution of Galaxies and Supermassive Black Holes: Insights from Surveys of the Contemporary Universe. *ARA&A*, **52**, 589–660. ADS-Link.

Helfer, T. T., Thornley, M. D., Regan, M. W., Wong, T., Sheth, K., Vogel, S. N., Blitz, L., and Bock, D. C.-J. (2003). The BIMA Survey of Nearby Galaxies (BIMA SONG). II. The CO Data. *ApJS*, **145**, 259–327. ADS-Link.

Hicks, E. K. S., Davies, R. I., Maciejewski, W., Emsellem, E., Malkan, M. A., Dumas, G., Müller-Sánchez, F., and Rivers, A. (2013). Fueling Active Galactic Nuclei. I. How the Global Characteristics of the Central Kiloparsec of Seyferts Differ from Quiescent Galaxies. *ApJ*, **768**, 107. ADS-Link.

Hinz, J. L. and Rieke, G. H. (2006). Dynamical Masses in Luminous Infrared Galaxies. *ApJ*, **646**, 872–880. ADS-Link.

Ho, L. C., Filippenko, A. V., and Sargent, W. L. W. (1993). A Reevaluation of the Excitation Mechanism of LINERs. *ApJ*, **417**, 63. ADS-Link.

Ho, P. T. P., Moran, J. M., and Lo, K. Y. (2004). The Submillimeter Array. *ApJ*, **616**, L1–L6. ADS-Link.

Holland, S. (1998). *The Globular Clusters and Halo of M31*. Ph.D. thesis, THE UNIVERSITY OF BRITISH COLUMBIA (CANADA. ADS-Link.

Hopkins, P. F. and Quataert, E. (2010). How do massive black holes get their gas? *MNRAS*, **407**, 1529–1564. ADS-Link.

Hopkins, P. F., Hernquist, L., Cox, T. J., and Kereš, D. (2008). A Cosmological Framework for the Co-Evolution of Quasars, Supermassive Black Holes, and Elliptical Galaxies. I. Galaxy Mergers and Quasar Activity. *ApJS*, **175**, 356–389. ADS-Link.

Horrobin, M., Eisenhauer, F., Tecza, M., Thatte, N., Genzel, R., Abuter, R., Iserlohe, C., Schreiber, J., Schegerer, A., Lutz, D., Ott, T., and Schödel, R. (2004). First results from SPIFFI. I: The Galactic Center. *Astronomische Nachrichten*, **325**, 88–91. ADS-Link.

Hubble, E. P. (1926). Extragalactic nebulae. *ApJ*, **64**, 321–369. ADS-Link.

Hughes, A., Meidt, S. E., Schinnerer, E., Colombo, D., Pety, J., Leroy, A. K., Dobbs, C. L., García-Burillo, S., Thompson, T. A., Dumas, G., Schuster, K. F., and Kramer, C. (2013). Probability Distribution Functions of ^{12}CO(J = 1 –> 0) Brightness and Integrated Intensity in M51: The PAWS View. *ApJ*, **779**, 44. ADS-Link.

Hunt, L. K., Malkan, M. A., Rush, B., Bicay, M. D., Nelson, B. O., Stanga, R. M., and Webb, W. (1999). Morphology of the 12 Micron Seyfert Galaxies. II. Optical and Near-Infrared Image Atlas. *ApJS*, **125**, 349–362. ADS-Link.

Hunt, L. K., Combes, F., García-Burillo, S., Schinnerer, E., Krips, M., Baker, A. J., Boone, F., Eckart, A., Léon, S., Neri, R., and Tacconi, L. J. (2008). Molecular Gas in NUclei of GAlaxies (NUGA). IX. The decoupled bars and gas inflow in NGC 2782. *A&A*, **482**, 133–150. ADS-Link.

Hutchings, J. B. and Neff, S. G. (1992). Optical imaging of QSOs with 0.5 arcsec resolution. *AJ*, **104**, 1–14. ADS-Link.

Hüttemeister, S., Aalto, S., Das, M., and Wall, W. F. (2000). Changing molecular gas properties in the bar and center of NGC 7479. *A&A*, **363**, 93–107. ADS-Link.

Iono, D., Yun, M. S., and Ho, P. T. P. (2005). Atomic and Molecular Gas in Colliding Galaxy Systems. I. The Data. *ApJS*, **158**, 1–37. ADS-Link.

Iono, D., Wilson, C. D., Yun, M. S., Baker, A. J., Petitpas, G. R., Peck, A. B., Krips, M., Cox, T. J., Matsushita, S., Mihos, J. C., and Pihlstrom, Y. (2009). Luminous Infrared Galaxies with the Submillimeter Array. II. Comparing the CO (3-2) Sizes and Luminosities of Local and High-Redshift Luminous Infrared Galaxies. *ApJ*, **695**, 1537–1549. ADS-Link.

Irons, W. T., Lacy, J. H., and Richter, M. J. (2012). Ionized Gas in the Galactic Center: New Observations and Interpretation. *ApJ*, **755**, 90. ADS-Link.

Israel, F. P. (2005). Molecular gas in compact galaxies. *A&A*, **438**, 855–866. ADS-Link.

Israel, F. P. (2009). CI and CO in nearby galaxy centers. The bright galaxies NGC 1068 (M 77), NGC 2146, NGC 3079, NGC 4826 (M 64), and NGC 7469. *A&A*, **493**, 525–538. ADS-Link.

Ivison, R. J., Papadopoulos, P., Seaquist, E. R., and Eales, S. A. (1996). A search for molecular gas in a high-redshift radio galaxy. *MNRAS*, **278**, 669–672. ADS-Link.

Jackson, J. M., Geis, N., Genzel, R., Harris, A. I., Madden, S., Poglitsch, A., Stacey, G. J., and Townes, C. H. (1993). Neutral gas in the central 2 parsecs of the Galaxy. *ApJ*, **402**, 173–184. ADS-Link.

Kaldare, R., Colless, M., Raychaudhury, S., and Peterson, B. A. (2003). FLASH redshift survey - I. Observations and catalogue. *MNRAS*, **339**, 652–662. ADS-Link.

Kamenetzky, J., Rangwala, N., Glenn, J., Maloney, P. R., and Conley, A. (2014). A Survey of the Molecular ISM Properties of Nearby Galaxies Using the Herschel FTS. *ApJ*, **795**, 174. ADS-Link.

Kang, H., Kim, K.-T., Byun, D.-Y., Lee, S., and Park, Y.-S. (2015). Simultaneous Observation of Water and Class I Methanol Masers toward Class II Methanol Maser Sources. *ApJS*, **221**, 6. ADS-Link.

Karlsson, R., Sjouwerman, L. O., Sandqvist, A., and Whiteoak, J. B. (2003). 18-cm VLA observations of OH towards the Galactic Centre. Absorption and emission in the four ground-state OH lines. *A&A*, **403**, 1011–1021. ADS-Link.

Karlsson, R., Sandqvist, A., Fathi, K., and Martín, S. (2015). The OH-streamer in Sagittarius A revisited: analysis of hydroxyl absorption within 10 pc from the Galactic centre. *A&A*, **582**, A118. ADS-Link.

Kawaguchi, T., Nakanishi, K., Kohno, K., Ohta, K., and Aoki, K. (2008). Molecular Gas in Narrow-line Seyfert 1 Galaxies: A Search for Coevolving Massive Black Holes and Galaxies. In T. Kodama, T. Yamada, & K. Aoki, editor, *Panoramic Views of Galaxy Formation and Evolution*, volume 399 of *Astronomical Society of the Pacific Conference Series*, pages 427–+. ADS-Link.

Keel, W. C. (1996). Rotation Curves and Velocity Measures for Spiral Galaxies in Pairs. *ApJS*, **106**, 27. ADS-Link.

Kenney, J. D. P., Wilson, C. D., Scoville, N. Z., Devereux, N. A., and Young, J. S. (1992). Twin peaks of CO emission in the central regions of barred galaxies. *ApJ*, **395**, L79–L82. ADS-Link.

Kennicutt, R. C. and Evans, N. J. (2012). Star Formation in the Milky Way and Nearby Galaxies. *ARA&A*, **50**, 531–608. ADS-Link.

Kennicutt, Jr., R. C. (1998a). Star Formation in Galaxies Along the Hubble Sequence. *ARA&A*, **36**, 189–232. ADS-Link.

Kennicutt, Jr., R. C. (1998b). The Global Schmidt Law in Star-forming Galaxies. *ApJ*, **498**, 541–552. ADS-Link.

Kewley, L. J., Heisler, C. A., Dopita, M. A., and Lumsden, S. (2001). Optical Classification of Southern Warm Infrared Galaxies. *ApJS*, **132**, 37–71. ADS-Link.

King, A. (2008). Disc accretion in active galactic nuclei. *NewAR*, **52**, 253–256. ADS-Link.

Klein, U. and Emerson, D. T. (1981). A Survey of the Distributions of 2.8-CM Radio Continuum in Nearby Galaxies - Part One - Observations of 16 Spiral. *A&A*, **94**, 29. ADS-Link.

Kocevski, D. D., Faber, S. M., Mozena, M., Koekemoer, A. M., Nandra, K., Rangel, C., Laird, E. S., Brusa, M., Wuyts, S., Trump, J. R., Koo, D. C., Somerville, R. S., Bell, E. F., Lotz, J. M., Alexander, D. M., Bournaud, F., Conselice, C. J., Dahlen, T., Dekel, A., Donley, J. L., Dunlop, J. S., Finoguenov, A., Georgakakis, A., Giavalisco, M., Guo, Y., Grogin, N. A., Hathi, N. P., Juneau, S., Kartaltepe, J. S., Lucas, R. A., McGrath, E. J., McIntosh, D. H., Mobasher, B., Robaina, A. R., Rosario, D., Straughn, A. N., van der Wel, A., and Villforth, C. (2012). CANDELS: Constraining the AGN-Merger Connection with Host Morphologies at z ˜ 2. *ApJ*, **744**, 148. ADS-Link.

Koehler, T., Groote, D., Reimers, D., and Wisotzki, L. (1997). The local luminosity function of QSOs and Seyfert 1 nuclei. *A&A*, **325**, 502–510. ADS-Link.

Kohno, K., Kawabe, R., and Vila-Vilaró, B. (1999). Dense Molecular Gas Associated with the Circumnuclear Star-forming Ring in the Barred Spiral Galaxy NGC 6951. *ApJ*, **511**, 157–177. ADS-Link.

Kollatschny, W. and Fricke, K. J. (1983). ESO 438-G 9 - A Seyfert galaxy with unusual properties. *A&A*, **125**, 276–279. ADS-Link.

König, S., Eckart, A., García-Marín, M., and Huchtmeier, W. K. (2009). H I in nearby low-luminosity QSO host galaxies. *A&A*, **507**, 757–768. ADS-Link.

Kormendy, J. (2001). Supermassive Black Holes in Galactic Nuclei. In J. Cantó & L. F. Rodríguez, editor, *Revista Mexicana de Astronomia y Astrofisica Conference Series*, volume 10 of *Revista Mexicana de Astronomia y Astrofisica, vol. 27*, pages 69–78. ADS-Link.

Kormendy, J. and Ho, L. C. (2013). Coevolution (Or Not) of Supermassive Black Holes and Host Galaxies. *ARA&A*, **51**, 511–653. ADS-Link.

Kormendy, J. and Kennicutt, Jr., R. C. (2004). Secular Evolution and the Formation of Pseudobulges in Disk Galaxies. *ARA&A*, **42**, 603–683. ADS-Link.

Krabbe, A., Genzel, R., Drapatz, S., and Rotaciuc, V. (1991). A cluster of He I emission-line stars in the Galactic center. *ApJ*, **382**, L19–L22. ADS-Link.

Krabbe, A., Genzel, R., Eckart, A., Najarro, F., Lutz, D., Cameron, M., Kroker, H., Tacconi-Garman, L. E., Thatte, N., Weitzel, L., Drapatz, S., Geballe, T., Sternberg, A., and Kudritzki, R. (1995). The Nuclear Cluster of the Milky Way: Star Formation and Velocity Dispersion in the Central 0.5 Parsec. *ApJ*, **447**, L95+. ADS-Link.

Krips, M., Eckart, A., Neri, R., Bertram, T., Straubmeier, C., Fischer, S., Staguhn, J. G., and Vogel, S. N. (2007a). Barred CO emission in HE 1029-1831. *A&A*, **464**, 187–191. ADS-Link.

Krips, M., Neri, R., García-Burillo, S., Combes, F., Schinnerer, E., Baker, A. J., Eckart, A., Boone, F., Hunt, L., Leon, S., and Tacconi, L. J. (2007b). Molecular gas in NUclei of

GAlaxies (NUGA): VI. Detection of a molecular gas disk/torus via HCN in the Seyfert 2 galaxy NGC 6951? *A&A*, **468**, L63–L66. ADS-Link.

Krips, M., Neri, R., and Cox, P. (2012). CO Emission in Optically Obscured (Type-2) Quasars at Redshifts z ~ 0.1-0.4. *ApJ*, **753**, 135. ADS-Link.

Krist, J. E., Hook, R. N., and Stoehr, F. (2011). 20 years of Hubble Space Telescope optical modeling using Tiny Tim. In *Society of Photo-Optical Instrumentation Engineers (SPIE) Conference Series*, volume 8127 of *Society of Photo-Optical Instrumentation Engineers (SPIE) Conference Series*. ADS-Link.

Krolik, J. H. and Kallman, T. R. (1987). Fe K features as probes of the nuclear reflection region in Seyfert galaxies. *ApJ*, **320**, L5–L8. ADS-Link.

Kunneriath, D., Eckart, A., Zamaninasab, M., Witzel, G., Schödel, R., García-Marín, M., König, S., Krichbaum, T. P., Lu, R., Moultaka, J., Mužić, K., Sabha, N., Sjouwerman, L. O., Straubmeier, C., Vogel, S. N., Teuben, P., and Zensus, J. A. (2011). The Galactic Centre in the Millimeter Regime: Observations with CARMA. In M. R. Morris, Q. D. Wang, & F. Yuan, editor, *Astronomical Society of the Pacific Conference Series*, volume 439 of *Astronomical Society of the Pacific Conference Series*, pages 327–+. ADS-Link.

Kunneriath, D., Eckart, A., Vogel, S. N., Teuben, P., Mužić, K., Schödel, R., García-Marín, M., Moultaka, J., Staguhn, J., Straubmeier, C., Zensus, J. A., Valencia-S., M., and Karas, V. (2012a). The Galactic centre mini-spiral in the mm-regime. *A&A*, **538**, A127. ADS-Link.

Kunneriath, D., Eckart, A., Vogel, S. N., Teuben, P., Mužić, K., Schödel, R., García-Marín, M., Moultaka, J., Staguhn, J., Straubmeier, C., Zensus, J. A., Valencia-S, M., and Karas, V. (2012b). The Galactic centre mini-spiral with CARMA. *Journal of Physics Conference Series*, **372**(1), 012063. ADS-Link.

Lacy, J. H., Townes, C. H., and Hollenbach, D. J. (1982). The nature of the central parsec of the Galaxy. *ApJ*, **262**, 120–134. ADS-Link.

Lau, R. M., Herter, T. L., Morris, M. R., Becklin, E. E., and Adams, J. D. (2013). SOFIA/FORCAST Imaging of the Circumnuclear Ring at the Galactic Center. *ApJ*, **775**, 37. ADS-Link.

Lepp, S., Dalgarno, A., van Dishoeck, E. F., and Black, J. H. (1988). Large molecules in diffuse interstellar clouds. *ApJ*, **329**, 418–424. ADS-Link.

Lequeux, J. (1983). Rotation curves and masses of galaxies. *A&A*, **125**, 394. ADS-Link.

Leroy, A. K., Walter, F., Brinks, E., Bigiel, F., de Blok, W. J. G., Madore, B., and Thornley, M. D. (2008). The Star Formation Efficiency in Nearby Galaxies: Measuring Where Gas Forms Stars Effectively. *AJ*, **136**, 2782–2845. ADS-Link.

Li, J., An, T., Shen, Z.-Q., and Miyazaki, A. (2010). ATCA Observations of SiO Masers in the Galactic Center. *ApJ*, **720**, L56–L61. ADS-Link.

Liu, H. B., Hsieh, P.-Y., Ho, P. T. P., Su, Y.-N., Wright, M., Sun, A.-L., and Minh, Y. C. (2012). Milky Way Supermassive Black Hole: Dynamical Feeding from the Circumnuclear Environment. *ApJ*, **756**, 195. ADS-Link.

Lo, K. Y. and Claussen, M. J. (1983). High-resolution observations of ionized gas in central 3 parsecs of the Galaxy - Possible evidence for infall. *Nature*, **306**, 647–651. ADS-Link.

Low, F. J., Kleinmann, D. E., Forbes, F. F., and Aumann, H. H. (1969). The Infrared Spectrum, Diameter, and Polarization of the Galactic Nucleus. *ApJ*, **157**, L97+. ADS-Link.

Lu, J. R., Ghez, A. M., Hornstein, S. D., Morris, M. R., Becklin, E. E., and Matthews, K. (2009). A Disk of Young Stars at the Galactic Center as Determined by Individual Stellar Orbits. *ApJ*, **690**, 1463–1487. ADS-Link.

Lucas, R. and Liszt, H. S. (2002). Comparative chemistry of diffuse clouds. III. Sulfur-bearing molecules. *A&A*, **384**, 1054–1061. ADS-Link.

Maeda, Y., Baganoff, F. K., Feigelson, E. D., Morris, M., Bautz, M. W., Brandt, W. N., Burrows, D. N., Doty, J. P., Garmire, G. P., Pravdo, S. H., Ricker, G. R., and Townsley, L. K. (2002). A Chandra Study of Sagittarius A East: A Supernova Remnant Regulating the Activity of Our Galactic Center? *ApJ*, **570**, 671–687. ADS-Link.

Malkan, M. A., Gorjian, V., and Tam, R. (1998). A Hubble Space Telescope Imaging Survey of Nearby Active Galactic Nuclei. *ApJS*, **117**, 25. ADS-Link.

Maness, H., Martins, F., Trippe, S., Genzel, R., Graham, J. R., Sheehy, C., Salaris, M., Gillessen, S., Alexander, T., Paumard, T., Ott, T., Abuter, R., and Eisenhauer, F. (2007). Evidence for a Long-standing Top-heavy Initial Mass Function in the Central Parsec of the Galaxy. *ApJ*, **669**, 1024–1041. ADS-Link.

Mao, R. Q., Henkel, C., Schulz, A., Zielinsky, M., Mauersberger, R., Störzer, H., Wilson, T. L., and Gensheimer, P. (2000). Dense gas in nearby galaxies. XIII. CO submillimeter line emission from the starburst galaxy M 82. *A&A*, **358**, 433–450. ADS-Link.

Mao, R.-Q., Schulz, A., Henkel, C., Mauersberger, R., Muders, D., and Dinh-V-Trung (2010). An Extragalactic ^{12}CO J = 3-2 Survey with the Heinrich Hertz Telescope. *ApJ*, **724**, 1336–1356. ADS-Link.

Markoff, S., Bower, G. C., and Falcke, H. (2007). How to hide large-scale outflows: size constraints on the jets of Sgr A*. *MNRAS*, **379**, 1519–1532. ADS-Link.

Marr, J. M., Wright, M. C. H., and Backer, D. C. (1993). HCO(+), H(C-13)N, and H(C-12)N aperture synthesis observations of the circumnuclear ring in the Galactic center. *ApJ*, **411**, 667–673. ADS-Link.

Marrone, D. P. (2006). *Submillimeter properties of Sagittarius A*: The polarization and spectrum from 230 to 690 GHz and the submillimeter array polarimeter*. Ph.D. thesis, Harvard University. ADS-Link.

Marrone, D. P., Moran, J. M., Zhao, J.-H., and Rao, R. (2006a). Interferometric Measurements of Variable 340 GHz Linear Polarization in Sagittarius A*. *ApJ*, **640**, 308–318. ADS-Link.

Marrone, D. P., Moran, J. M., Zhao, J.-H., and Rao, R. (2006b). The Submillimeter Polarization of Sgr A*. *Journal of Physics Conference Series*, **54**, 354–362. ADS-Link.

Martín, S., Martín-Pintado, J., Montero-Castaño, M., Ho, P. T. P., and Blundell, R. (2012). Surviving the hole. I. Spatially resolved chemistry around Sagittarius A*. *A&A*, **539**, A29. ADS-Link.

Mathur, S. (2011). Host galaxies of NLS1s. In *Proceedings of the conference "Narrow-Line Seyfert 1 Galaxies and their place in the Universe". April 4-6, 2011. Milano, Italy. Editorial Board: Luigi Foschini (chair), Monica Colpi, Luigi Gallo, Dirk Grupe, Stefanie Komossa, Karen Leighly, Smita Mathur. Published online at <A href="http://pos.sissa.it/cgi-bin/reader/conf.cgi?confid=126">http://pos.sissa.it/cgi-bin/reader/conf.cgi?confid=126</A>, id.35*. ADS-Link.

Matsushita, S., Sakamoto, K., Kuo, C.-Y., Hsieh, P.-Y., Dinh-V-Trung, Mao, R.-Q., Iono, D., Peck, A. B., Wiedner, M. C., Liu, S.-Y., Ohashi, N., and Lim, J. (2004). Submillimeter Array ^{12}CO (J=3-2) Interferometric Observations of the Central Region of M51. *ApJ*, **616**, L55–L58. ADS-Link.

Mauersberger, R., Henkel, C., Walsh, W., and Schulz, A. (1999). Dense gas in nearby galaxies . XII. A survey for CO J=3-2 emission. *A&A*, **341**, 256–263. ADS-Link.

McEwen, B. C., Pihlström, Y. M., and Sjouwerman, L. O. (2014). Class I Methanol (CH_3OH) Maser Conditions near Supernova Remnants. *ApJ*, **793**, 133. ADS-Link.

McMullin, J. P., Waters, B., Schiebel, D., Young, W., and Golap, K. (2007). CASA Architecture and Applications. In R. A. Shaw, F. Hill, and D. J. Bell, editors, *Astronomical Data Analysis Software and Systems XVI*, volume 376 of *Astronomical Society of the Pacific Conference Series*, page 127. ADS-Link.

Meier, D. S. and Turner, J. L. (2005). Spatially Resolved Chemistry in Nearby Galaxies. I. The Center of IC 342. *ApJ*, **618**, 259–280. ADS-Link.

Meier, D. S. and Turner, J. L. (2012). Spatially Resolved Chemistry in nearby Galaxies. II. The Nuclear Bar in Maffei 2. *ApJ*, **755**, 104. ADS-Link.

Meier, D. S., Turner, J. L., and Hurt, R. L. (2000). Molecular Gas Properties of the Starburst Nucleus of IC 342: High-Resolution ^{13}CO (2-1) Imaging. *ApJ*, **531**, 200–209. ADS-Link.

Melia, F. and Falcke, H. (2001). The Supermassive Black Hole at the Galactic Center. *ARA&A*, **39**, 309–352. ADS-Link.

Merritt, D. and Ferrarese, L. (2001). The $M_{¢}$-σ Relation for Supermassive Black Holes. *ApJ*, **547**, 140–145. ADS-Link.

Mezger, P. G. and Henderson, A. P. (1967). Galactic H II Regions. I. Observations of Their Continuum Radiation at the Frequency 5 GHz. *ApJ*, **147**, 471. ADS-Link.

Mills, E. A. C., Güsten, R., Requena-Torres, M. A., and Morris, M. R. (2013). The Excitation of HCN and HCO^+ in the Galactic Center Circumnuclear Disk. *ApJ*, **779**, 47. ADS-Link.

Monje, R. R., Blain, A. W., and Phillips, T. G. (2011). Comparison of Millimeter-wave and X-Ray Emission in Seyfert Galaxies. *ApJS*, **195**, 23. ADS-Link.

Montero-Castaño, M., Herrnstein, R. M., and Ho, P. T. P. (2009). Gas Infall Toward Sgr A* from the Clumpy Circumnuclear Disk. *ApJ*, **695**, 1477–1494. ADS-Link.

Mori, K., Hailey, C. J., Krivonos, R., Hong, J., Ponti, G., Bauer, F., Perez, K., Nynka, M., Zhang, S., Tomsick, J. A., Alexander, D. M., Baganoff, F. K., Barret, D., Barrière, N., Boggs, S. E., Canipe, A. M., Christensen, F. E., Craig, W. W., Forster, K., Giommi, P., Grefenstette, B. W., Grindlay, J. E., Harrison, F. A., Hornstrup, A., Kitaguchi, T., Koglin, J. E., Luu, V., Madsen, K. K., Mao, P. H., Miyasaka, H., Perri, M., Pivovaroff, M. J., Puccetti, S., Rana, V., Stern, D., Westergaard, N. J., Zhang, W. W., and Zoglauer, A. (2015). NuSTAR Hard X-Ray Survey of the Galactic Center Region I: Hard X-Ray Morphology and Spectroscopy of the Diffuse Emission. *ApJ*, **814**, 94. ADS-Link.

Moser, L., Eckart, A., Borkar, A., García-Marin, M., Kunneriath, D., Jalali, B., Sabha, N., Shahzamanian, B., Valencia-S., M., Zamaninasab, M., Bronfman, L., and Finger, R. (2014). Sgr A West in the light of molecules: cold and dense gas east of the circumnuclear disk. In L. O. Sjouwerman, C. C. Lang, and J. Ott, editors, *IAU Symposium*, volume 303 of *IAU Symposium*, pages 86–88. ADS-Link.

Moser, L., Krips, M., Busch, G., Scharwächter, J., König, S., Eckart, A., Smajić, S., García-Marin, M., Valencia-S., M., Fischer, S., and Dierkes, J. (2016a). A low-luminosity type-1 QSO sample . IV. Molecular gas contents and conditions of star formation in three nearby Seyfert galaxies. *A&A*, **587**, A137. ADS-Link.

Moser, L., Sánchez-Monge, Á., Eckart, A., Requena-Torres, M. A., García-Marin, M., Kunneriath, D., Zensus, A., Britzen, S., Sabha, N., Shahzamanian, B., Borkar, A., and Fischer, S. (2016b). Approaching hell's kitchen: molecular daredevil clouds in the vicinity of Sgr A*. *ArXiv e-prints*. ADS-Link.

Moser, L., Sánchez-Monge, Á., Eckart, A., Borkar, A., García-Marin, M., Kunneriath, D., Sabha, N., and Shahzamanian, B. (2017). TBD. *in prep.*

Moultaka, J., Eckart, A., Viehmann, T., Mouawad, N., Straubmeier, C., Ott, T., and Schödel, R. (2004a). Dust embedded sources at the Galactic Center. 2 to 4 μm imaging and spectroscopy in the central parsec. *A&A*, **425**, 529–542. ADS-Link.

Moultaka, J., Eckart, A., Viehmann, T., Schödel, R., Mouawad, N., and Straubmeier, C. (2004b). IR excess stars and shock filaments at the Galactic center. In T. Storchi-Bergmann, L. C. Ho, & H. R. Schmitt, editor, *The Interplay Among Black Holes, Stars and ISM in Galactic Nuclei*, volume 222 of *IAU Symposium*, pages 141–144. ADS-Link.

Moultaka, J., Eckart, A., Schödel, R., Viehmann, T., and Najarro, F. (2005). VLT L-band mapping of the Galactic center IRS 3-IRS 13 region. Evidence for new Wolf-Rayet type stars. *A&A*, **443**, 163–173. ADS-Link.

Moultaka, J., Eckart, A., and Mužić, K. (2015a). "Ice Cubes" in the Center of the Milky Way: Water-ice and Hydrocarbons in the Central Parsec. *ApJ*, **806**, 202. ADS-Link.

Moultaka, J., Eckart, A., and Mužić, K. (2015b). "Ice Cubes" in the Center of the Milky Way: Water-ice and Hydrocarbons in the Central Parsec. *ApJ*, **806**, 202. ADS-Link.

Mullaney, J. R. and Ward, M. J. (2008). Optical emission-line properties of narrow-line Seyfert 1 galaxies and comparison active galactic nuclei. *MNRAS*, **385**, 53–74. ADS-Link.

Muraoka, K., Kohno, K., Tosaki, T., Kuno, N., Nakanishi, K., Sorai, K., Okuda, T., Sakamoto, S., Endo, A., Hatsukade, B., Kamegai, K., Tanaka, K., Cortes, J., Ezawa, H., Yamaguchi, N., Sakai, T., and Kawabe, R. (2007). ASTE CO (3-2) Observations of the Barred Spiral Galaxy M 83: I. Correlation between CO (3-2)/ CO (1-0) Ratios and Star Formation Efficiencies. *PASJ*, **59**, 43–54. ADS-Link.

Murphy, E. J., Condon, J. J., Schinnerer, E., Kennicutt, R. C., Calzetti, D., Armus, L., Helou, G., Turner, J. L., Aniano, G., Beirão, P., Bolatto, A. D., Brandl, B. R., Croxall, K. V., Dale, D. A., Donovan Meyer, J. L., Draine, B. T., Engelbracht, C., Hunt, L. K., Hao, C.-N., Koda, J., Roussel, H., Skibba, R., and Smith, J.-D. T. (2011). Calibrating Extinction-free Star Formation Rate Diagnostics with 33 GHz Free-free Emission in NGC 6946. *ApJ*, **737**, 67. ADS-Link.

Mužić, K., Eckart, A., Schödel, R., Meyer, L., and Zensus, A. (2007). First proper motions of thin dust filaments at the Galactic center. *A&A*, **469**, 993–1002. ADS-Link.

Mužić, K., Schödel, R., Eckart, A., Meyer, L., and Zensus, A. (2008). The nature of IRS 13N: YSOs in the central parsec of the galaxy? *Journal of Physics Conference Series*, **131**(1), 012016–+. ADS-Link.

Nagao, T., Murayama, T., and Taniguchi, Y. (2001). The Narrow-Line Region of Seyfert Galaxies: Narrow-Line Seyfert 1 Galaxies versus Broad-Line Seyfert 1 Galaxies. *ApJ*, **546**, 744–758. ADS-Link.

Najarro, F., Krabbe, A., Genzel, R., Lutz, D., Kudritzki, R. P., and Hillier, D. J. (1997). Quantitative spectroscopy of the HeI cluster in the Galactic center. *A&A*, **325**, 700–708. ADS-Link.

Narayan, R. and Yi, I. (1995). Advection-dominated Accretion: Underfed Black Holes and Neutron Stars. *ApJ*, **452**, 710–+. ADS-Link.

Narayan, R., Mahadevan, R., Grindlay, J. E., Popham, R. G., and Gammie, C. (1998). Advection-dominated accretion model of Sagittarius A*: evidence for a black hole at the Galactic center. *ApJ*, **492**, 554–568. ADS-Link.

Nardini, E., Risaliti, G., Salvati, M., Sani, E., Imanishi, M., Marconi, A., and Maiolino, R. (2008). Spectral decomposition of starbursts and active galactic nuclei in 5-8 μm Spitzer-IRS spectra of local ultraluminous infrared galaxies. *MNRAS*, **385**, L130–L134. ADS-Link.

Nayakshin, S., Cuadra, J., and Springel, V. (2007). Simulations of star formation in a gaseous disc around Sgr A* - a failed active galactic nucleus. *MNRAS*, **379**, 21–33. ADS-Link.

Netzer, H. (2009). Radiation Pressure Force and Black Hole Mass Determination in Low-Redshift Type-I and Type-II Active Galactic Nuclei. *ApJ*, **695**, 793–797. ADS-Link.

Netzer, H. (2015). Revisiting the Unified Model of Active Galactic Nuclei. *ARA&A*, **53**, 365–408. ADS-Link.

Oka, T., Hasegawa, T., Sato, F., Tsuboi, M., and Miyazaki, A. (1998). A Large-Scale CO Survey of the Galactic Center. *ApJS*, **118**, 455–515. ADS-Link.

Orban de Xivry, G., Davies, R., Schartmann, M., Komossa, S., Marconi, A., Hicks, E., Engel, H., and Tacconi, L. (2011a). The Role of Secular Evolution in the Black Hole Growth of Narrow-Line Seyfert 1 Galaxies. *ArXiv e-prints*. ADS-Link.

Orban de Xivry, G., Davies, R., Schartmann, M., Komossa, S., Marconi, A., Hicks, E., Engel, H., and Tacconi, L. (2011b). The role of secular evolution in the black hole growth of narrow-line Seyfert 1 galaxies. *MNRAS*, **417**, 2721–2736. ADS-Link.

Ott, T., Eckart, A., and Genzel, R. (1999). Variable and Embedded Stars in the Galactic Center. *ApJ*, **523**, 248–264. ADS-Link.

Paglione, T. A. D., Wall, W. F., Young, J. S., Heyer, M. H., Richard, M., Goldstein, M., Kaufman, Z., Nantais, J., and Perry, G. (2001). A Mapping Survey of the ^{13}CO and ^{12}CO Emission in Galaxies. *ApJS*, **135**, 183–200. ADS-Link.

Panuzzo, P., Bressan, A., Granato, G. L., Silva, L., and Danese, L. (2003). Dust and nebular emission. I. Models for normal galaxies. *A&A*, **409**, 99–114. ADS-Link.

Papadopoulos, P. P., Kovacs, A., Evans, A. S., and Barthel, P. (2008). High-excitation molecular gas in local luminous AGN hosts. *A&A*, **491**, 483–487. ADS-Link.

Papadopoulos, P. P., van der Werf, P. P., Xilouris, E. M., Isaak, K. G., Gao, Y., and Mühle, S. (2012a). The molecular gas in luminous infrared galaxies - I. CO lines, extreme physical conditions and their drivers. *MNRAS*, **426**, 2601–2629. ADS-Link.

Papadopoulos, P. P., van der Werf, P., Xilouris, E., Isaak, K. G., and Gao, Y. (2012b). The Molecular Gas in Luminous Infrared Galaxies. II. Extreme Physical Conditions and Their Effects on the X $_{co}$ Factor. *ApJ*, **751**, 10. ADS-Link.

Paumard, T., Maillard, J. P., Morris, M., and Rigaut, F. (2001). New results on the helium stars in the galactic center using BEAR spectro-imagery. *A&A*, **366**, 466–480. ADS-Link.

Paumard, T., Maillard, J.-P., and Morris, M. (2004). Kinematic and structural analysis of the <ASTROBJ>Minispiral</ASTROBJ> in the Galactic Center from BEAR spectro-imagery. *A&A*, **426**, 81–96. ADS-Link.

Paumard, T., Genzel, R., Martins, F., Nayakshin, S., Beloborodov, A. M., Levin, Y., Trippe, S., Eisenhauer, F., Ott, T., Gillessen, S., Abuter, R., Cuadra, J., Alexander, T., and Sternberg, A. (2006). The Two Young Star Disks in the Central Parsec of the Galaxy: Properties, Dynamics, and Formation. *ApJ*, **643**, 1011–1035. ADS-Link.

Perez, K., Hailey, C. J., Bauer, F. E., Krivonos, R. A., Mori, K., Baganoff, F. K., Barrière, N. M., Boggs, S. E., Christensen, F. E., Craig, W. W., Grefenstette, B. W., Grindlay, J. E., Harrison, F. A., Hong, J., Madsen, K. K., Nynka, M., Stern, D., Tomsick, J. A., Wik, D. R., Zhang, S., Zhang, W. W., and Zoglauer, A. (2015). Extended hard-X-ray emission in the inner few parsecs of the Galaxy. *Nature*, **520**, 646–649. ADS-Link.

Perger, M., Moultaka, J., Eckart, A., Viehmann, T., Schödel, R., and Muzic, K. (2008). Compact mid-IR sources east of Galactic Center source IRS5. *A&A*, **478**, 127–135. ADS-Link.

Peterson, B. M. (1997). *An Introduction to Active Galactic Nuclei*. ADS-Link.

Pety, J., Schinnerer, E., Leroy, A. K., Hughes, A., Meidt, S. E., Colombo, D., Dumas, G., García-Burillo, S., Schuster, K. F., Kramer, C., Dobbs, C. L., and Thompson, T. A. (2013). The Plateau de Bure + 30 m Arcsecond Whirlpool Survey Reveals a Thick Disk of Diffuse Molecular Gas in the M51 Galaxy. *ApJ*, **779**, 43. ADS-Link.

Pfuhl, O., Alexander, T., Gillessen, S., Martins, F., Genzel, R., Eisenhauer, F., Fritz, T. K., and Ott, T. (2014). Massive Binaries in the Vicinity of Sgr A*. *ApJ*, **782**, 101. ADS-Link.

Pihlström, Y. M., Sjouwerman, L. O., and Fish, V. L. (2011). Expanded Very Large Array Detection of 44.1 GHz Class I Methanol Masers in Sagittarius A. *ApJ*, **739**, L21. ADS-Link.

Polk, K. S., Knapp, G. R., Stark, A. A., and Wilson, R. W. (1988). Molecules in galaxies. VI - Diffuse and dense cloud contributions to the large-scale CO emission of the Galaxy. *ApJ*, **332**, 432–438. ADS-Link.

Pott, J.-U., Eckart, A., Glindemann, A., Kraus, S., Schödel, R., Ghez, A. M., Woillez, J., and Weigelt, G. (2008a). First VLTI infrared spectro-interferometry on GCIRS 7. Characterizing the prime reference source for Galactic center observations at highest angular resolution. *A&A*, **487**, 413–418. ADS-Link.

Pott, J.-U., Eckart, A., Glindemann, A., Schödel, R., Viehmann, T., and Robberto, M. (2008b). The enigma of GCIRS 3. Constraining the properties of the mid-infrared reference star of the central parsec of the Milky Way with optical long-baseline interferometry. *A&A*, **480**, 115–131. ADS-Link.

Pratap, P., Shute, P. A., Keane, T. C., Battersby, C., and Sterling, S. (2008). Class i Methanol Masers: Signposts of Star Formation? *AJ*, **135**, 1718–1730. ADS-Link.

Rao, A. R., Singh, K. P., and Vahia, M. N. (1992). X-ray variability in the Seyfert galaxy Markarian 618. *MNRAS*, **255**, 197–202. ADS-Link.

Rees, M. J. (1984). Black Hole Models for Active Galactic Nuclei. *ARA&A*, **22**, 471–506. ADS-Link.

Regan, M. W. and Teuben, P. (2003). The Formation of Nuclear Rings in Barred Spiral Galaxies. *ApJ*, **582**, 723–742. ADS-Link.

Reid, M. J., Menten, K. M., Trippe, S., Ott, T., and Genzel, R. (2007). The Position of Sagittarius A*. III. Motion of the Stellar Cusp. *ApJ*, **659**, 378–388. ADS-Link.

Requena-Torres, M. A., Güsten, R., Weiß, A., Harris, A. I., Martín-Pintado, J., Stutzki, J., Klein, B., Heyminck, S., and Risacher, C. (2012). GREAT confirms transient nature of the circum-nuclear disk. *A&A*, **542**, L21. ADS-Link.

Rieke, G. H. and Low, F. J. (1972). Infrared Photometry of Extragalactic Sources. *ApJ*, **176**, L95+. ADS-Link.

Roberts, D. A. and Goss, W. M. (1993). Multiconfiguration VLA H92-alpha observations of Sagittarius A West at 1 arcsecond resolution. *ApJS*, **86**, 133–152. ADS-Link.

Roberts, D. A., Goss, W. M., van Gorkom, J. H., and Leahy, J. P. (1991). VLA radio recombination line observations of Sagittarius A West. *ApJ*, **366**, L15–L18. ADS-Link.

Roberts, D. A., Yusef-Zadeh, F., and Goss, W. M. (1996). Kinematics of the Ionized Gas in Sagittarius A West: Mass Estimates of the Inner 0.13 Parsecs of the Galaxy. *ApJ*, **459**, 627. ADS-Link.

Rodríguez, M. I., Villar-Martín, M., Emonts, B., Humphrey, A., Drouart, G., García Burillo, S., and Pérez Torres, M. (2014). The molecular gas content of ULIRG type 2 quasars at z < 1. *A&A*, **565**, A19. ADS-Link.

Rodríguez-Ardila, A., Binette, L., Pastoriza, M. G., and Donzelli, C. J. (2000). The Narrow-Line Region of Narrow-Line Seyfert 1 Galaxies. *ApJ*, **538**, 581–593. ADS-Link.

Rosolowsky, E., Keto, E., Matsushita, S., and Willner, S. P. (2007). High-Resolution Molecular Gas Maps of M33. *ApJ*, **661**, 830–844. ADS-Link.

Ryan, C. J., De Robertis, M. M., Virani, S., Laor, A., and Dawson, P. C. (2007). The Central Engines of Narrow-Line Seyfert 1 Galaxies. *ApJ*, **654**, 799–813. ADS-Link.

Sabha, N., Witzel, G., Eckart, A., Buchholz, R. M., Bremer, M., Gießübel, R., García-Marín, M., Kunneriath, D., Muzic, K., Schödel, R., Straubmeier, C., Zamaninasab, M., and Zernickel, A. (2010). The extreme luminosity states of Sagittarius A*. *A&A*, **512**, A2+. ADS-Link.

Sabha, N., Eckart, A., Mužić, K., Moser, L., and Jalali, B. (2016). A New MIR Bow shock Source at the Galactic Centre? *MNRAS*, **0**, submitted.

Saintonge, A., Kauffmann, G., Wang, J., Kramer, C., Tacconi, L. J., Buchbender, C., Catinella, B., Graciá-Carpio, J., Cortese, L., Fabello, S., Fu, J., Genzel, R., Giovanelli, R., Guo, Q., Haynes, M. P., Heckman, T. M., Krumholz, M. R., Lemonias, J., Li, C., Moran, S., Rodriguez-Fernandez, N., Schiminovich, D., Schuster, K., and Sievers, A. (2011). COLD GASS, an IRAM legacy survey of molecular gas in massive galaxies - II. The non-universality of the molecular gas depletion time-scale. *MNRAS*, **415**, 61–76. ADS-Link.

Sakamoto, K., Ho, P. T. P., Iono, D., Keto, E. R., Mao, R.-Q., Matsushita, S., Peck, A. B., Wiedner, M. C., Wilner, D. J., and Zhao, J.-H. (2006). Molecular Superbubbles in the Starburst Galaxy NGC 253. *ApJ*, **636**, 685–697. ADS-Link.

Sakamoto, K., Ho, P. T. P., Mao, R.-Q., Matsushita, S., and Peck, A. B. (2007). Detection of CO Hot Spots Associated with Young Clusters in the Southern Starburst Galaxy NGC 1365. *ApJ*, **654**, 782–798. ADS-Link.

Sanchez-Bermudez, J., Schödel, R., Alberdi, A., Muzić, K., Hummel, C. A., and Pott, J.-U. (2014). Properties of bow-shock sources at the Galactic center. *A&A*, **567**, A21. ADS-Link.

Sanders, D. (1999). The Nuclei of 'Warm' Ultraluminous Infrared Galaxies – Superstarbursts or AGN. In *HST Proposal*, pages 8190–+. ADS-Link.

Sanders, D. B. and Mirabel, I. F. (1996). Luminous Infrared Galaxies. *ARA&A*, **34**, 749. ADS-Link.

Sanders, D. B., Scoville, N. Z., Soifer, B. T., Young, J. S., and Danielson, G. E. (1987). Detection of CO(1-0) emission and optical imaging of the Seyfert galaxy/QSO Markarian 231. *ApJ*, **312**, L5–L9. ADS-Link.

Sanders, D. B., Soifer, B. T., Elias, J. H., Madore, B. F., Matthews, K., Neugebauer, G., and Scoville, N. Z. (1988). Ultraluminous infrared galaxies and the origin of quasars. *ApJ*, **325**, 74–91. ADS-Link.

Sanders, D. B., Scoville, N. Z., and Soifer, B. T. (1991). Molecular gas in luminous infrared galaxies. *ApJ*, **370**, 158–171. ADS-Link.

Sandstrom, K. M., Leroy, A. K., Walter, F., Bolatto, A. D., Croxall, K. V., Draine, B. T., Wilson, C. D., Wolfire, M., Calzetti, D., Kennicutt, R. C., Aniano, G., Donovan Meyer, J., Usero, A., Bigiel, F., Brinks, E., de Blok, W. J. G., Crocker, A., Dale, D., Engelbracht, C. W., Galametz, M., Groves, B., Hunt, L. K., Koda, J., Kreckel, K., Linz, H., Meidt, S., Pellegrini, E., Rix, H.-W., Roussel, H., Schinnerer, E., Schruba, A., Schuster, K.-F., Skibba, R., van der Laan, T., Appleton, P., Armus, L., Brandl, B., Gordon, K., Hinz, J., Krause, O., Montiel, E., Sauvage, M., Schmiedeke, A., Smith, J. D. T., and Vigroux, L. (2013). The CO-to-H_2 Conversion Factor and Dust-to-gas Ratio on Kiloparsec Scales in Nearby Galaxies. *ApJ*, **777**, 5. ADS-Link.

Sani, E., Marconi, A., Hunt, L. K., and Risaliti, G. (2011). The Spitzer/IRAC view of black hole-bulge scaling relations. *MNRAS*, **413**, 1479–1494. ADS-Link.

Sato, M. T. and Tsuboi, M. (2008). Infalling gas onto the Galactic center circumnuclear ring. *Journal of Physics Conference Series*, **131**(1), 012033. ADS-Link.

Sawada, T., Hasegawa, T., Handa, T., Morino, J.-I., Oka, T., Booth, R., Bronfman, L., Hayashi, M., Luna Castellanos, A., Nyman, L.-Å., Sakamoto, S., Seta, M., Shaver, P., Sorai, K., and Usuda, K. S. (2001). The Tokyo-Onsala-ESO-Calán Galactic CO J=2-1 Survey. I. The Galactic Center Region. *ApJS*, **136**, 189–219. ADS-Link.

Scharwächter, J., Dopita, M. A., Zuther, J., Fischer, S., Komossa, S., and Eckart, A. (2011). Extended Narrow-line Emission in the Bright Seyfert 1.5 Galaxy HE 2211-3903. *AJ*, **142**, 43. ADS-Link.

Schawinski, K., Treister, E., Urry, C. M., Cardamone, C. N., Simmons, B., and Yi, S. K. (2011). HST WFC3/IR Observations of Active Galactic Nucleus Host Galaxies at z ˜ 2: Supermassive Black Holes Grow in Disk Galaxies. *ApJ*, **727**, L31. ADS-Link.

Schinnerer, E., Meidt, S. E., Pety, J., Hughes, A., Colombo, D., García-Burillo, S., Schuster, K. F., Dumas, G., Dobbs, C. L., Leroy, A. K., Kramer, C., Thompson, T. A., and Regan, M. W. (2013). The PdBI Arcsecond Whirlpool Survey (PAWS). I. A Cloud-scale/Multi-wavelength View of the Interstellar Medium in a Grand-design Spiral Galaxy. *ApJ*, **779**, 42. ADS-Link.

Schödel, R., Ott, T., Genzel, R., Hofmann, R., Lehnert, M., Eckart, A., Mouawad, N., Alexander, T., Reid, M. J., Lenzen, R., Hartung, M., Lacombe, F., Rouan, D., Gendron, E., Rousset, G., Lagrange, A.-M., Brandner, W., Ageorges, N., Lidman, C., Moorwood, A. F. M., Spyromilio, J., Hubin, N., and Menten, K. M. (2002a). A star in a 15.2-year orbit around the supermassive black hole at the centre of the Milky Way. *Nature*, **419**, 694–696. ADS-Link.

Schödel, R., Ott, T., Genzel, R., Hofmann, R., Lehnert, M., Eckart, A., Mouawad, N., Alexander, T., Reid, M. J., Lenzen, R., Hartung, M., Lacombe, F., Rouan, D., Gendron, E., Rousset, G., Lagrange, A.-M., Brandner, W., Ageorges, N., Lidman, C., Moorwood, A. F. M., Spyromilio, J., Hubin, N., and Menten, K. M. (2002b). A star in a 15.2-year orbit around the supermassive black hole at the centre of the Milky Way. *Nature*, **419**, 694–696. ADS-Link.

Schödel, R., Ott, T., Genzel, R., Eckart, A., Mouawad, N., and Alexander, T. (2003). Stellar Dynamics in the Central Arcsecond of Our Galaxy. *ApJ*, **596**, 1015–1034. ADS-Link.

Schödel, R., Eckart, A., Alexander, T., Merritt, D., Genzel, R., Sternberg, A., Meyer, L., Kul, F., Moultaka, J., Ott, T., and Straubmeier, C. (2007). The structure of the nuclear stellar cluster of the Milky Way. *A&A*, **469**, 125–146. ADS-Link.

Schödel, R., Merritt, D., and Eckart, A. (2009). The nuclear star cluster of the Milky Way: proper motions and mass. *A&A*, **502**, 91–111. ADS-Link.

Schöier, F. L., van der Tak, F. F. S., van Dishoeck, E. F., and Black, J. H. (2005). An atomic and molecular database for analysis of submillimetre line observations. *A&A*, **432**, 369–379. ADS-Link.

Schwarz, U. J., Bregman, J. D., and van Gorkom, J. H. (1989). The distribution and kinematics of the ionized gas in the Galactic centre region. *A&A*, **215**, 33–47. ADS-Link.

Scoville, N. Z., Frayer, D. T., Schinnerer, E., and Christopher, M. (2003). The Host Galaxies of Optically Bright Quasi-stellar Objects: Molecular Gas in z<=0.1 Palomar-Green Quasi-stellar Objects. *ApJ*, **585**, L105–L108. ADS-Link.

Seaquist, E., Yao, L., Dunne, L., and Cameron, H. (2004). Revised masses of dust and gas of SCUBA Local Universe Survey far-infrared bright galaxies based on a recent CO survey. *MNRAS*, **349**, 1428–1434. ADS-Link.

Sellgren, K., McGinn, M. T., Becklin, E. E., and Hall, D. N. (1990). Velocity dispersion and the stellar population in the central 1.2 parsecs of the Galaxy. *ApJ*, **359**, 112–120. ADS-Link.

Serabyn, E. and Lacy, J. H. (1985). Forbidden NE II observations of the galactic center - Evidence for a massive block hole. *ApJ*, **293**, 445–458. ADS-Link.

Serabyn, E., Lacy, J. H., and Achtermann, J. M. (1991). A gaseous tail ablated from the supergiant IRS 7 near the Galactic center. *ApJ*, **378**, 557–564. ADS-Link.

Serjeant, S., Gruppioni, C., and Oliver, S. (2002). The local star formation rate and radio luminosity density. *MNRAS*, **330**, 621–624. ADS-Link.

Shakura, N. I. and Sunyaev, R. A. (1973). Black holes in binary systems. Observational appearance. *A&A*, **24**, 337–355. ADS-Link.

Shetty, R., Clark, P. C., and Klessen, R. S. (2014). Interpreting the sub-linear Kennicutt-Schmidt relationship: the case for diffuse molecular gas. *MNRAS*, **442**, 2208–2215. ADS-Link.

Shirley, Y. L. (2015). The Critical Density and the Effective Excitation Density of Commonly Observed Molecular Dense Gas Tracers. *PASP*, **127**, 299–310. ADS-Link.

Shlosman, I. (1990). Induced starburst and nuclear activity: Faith, facts, and theory. In J. W. Sulentic, W. C. Keel, & C. M. Telesco, editor, *NASA Conference Publication*, volume 3098 of *NASA Conference Publication*, pages 689–704. ADS-Link.

Silk, J. and Rees, M. J. (1998). Quasars and galaxy formation. *A&A*, **331**, L1–L4. ADS-Link.

Sjouwerman, L. O., Pihlström, Y. M., and Fish, V. L. (2010). Expanded Very Large Array Detection of 36.2 GHz Class I Methanol Masers in Sagittarius A. *ApJ*, **710**, L111–L114. ADS-Link.

Smajić, S., Moser, L., Eckart, A., Valencia-S., M., Combes, F., Horrobin, M., García-Burillo, S., García-Marín, M., Fischer, S., and Zuther, J. (2014). ALMA-backed NIR high resolution integral field spectroscopy of the NUGA galaxy NGC 1433. *A&A*, **567**, A119. ADS-Link.

Smajić, S., Moser, L., Eckart, A., Busch, G., Combes, F., García-Burillo, S., Valencia-S., M., and Horrobin, M. (2015). The nuclear gas disk of NGC 1566 dissected by SINFONI and ALMA. *A&A*, **583**, A104. ADS-Link.

Soifer, B. T., Sanders, D. B., Neugebauer, G., Danielson, G. E., Lonsdale, C. J., Madore, B. F., and Persson, S. E. (1986). The luminosity function and space density of the most luminous galaxies in the IRAS survey. *ApJ*, **303**, L41–L44. ADS-Link.

Solomon, P. M. and Barrett, J. W. (1991). The CO - H_2 Mass Conversion Factor. In F. Combes and F. Casoli, editors, *Dynamics of Galaxies and Their Molecular Cloud Distributions*, volume 146 of *IAU Symposium*, page 235. ADS-Link.

Solomon, P. M. and Rivolo, A. R. (1989). A face-on view of the first galactic quadrant in molecular clouds. *ApJ*, **339**, 919–925. ADS-Link.

Solomon, P. M., Sanders, D. B., and Scoville, N. Z. (1979). Giant molecular clouds in the Galaxy - The distribution of CO-13 emission in the galactic plane. *ApJ*, **232**, L89–L93. ADS-Link.

Solomon, P. M., Downes, D., and Radford, S. J. E. (1992). Dense molecular gas and starbursts in ultraluminous galaxies. *ApJ*, **387**, L55–L59. ADS-Link.

Staguhn, J. G., Schinnerer, E., Eckart, A., and Scharwächter, J. (2004). Resolving the Host Galaxy of the Nearby QSO I Zw 1 with Subarcsecond Multitransition Molecular Line Observations. *ApJ*, **609**, 85–93. ADS-Link.

Steiner, J. E., Menezes, R. B., and Amorim, D. (2013). Identification of a high-velocity compact nebular filament 2.2 arcsec south of the Galactic Centre. *MNRAS*, **431**, 2789–2795. ADS-Link.

Storchi-Bergmann, T. (2014). The co-evolution of galaxies and supermassive black holes in the near Universe. *ArXiv e-prints*. ADS-Link.

Tacconi, L. J., Neri, R., Chapman, S. C., Genzel, R., Smail, I., Ivison, R. J., Bertoldi, F., Blain, A., Cox, P., Greve, T., and Omont, A. (2006). High-Resolution Millimeter Imaging of Submillimeter Galaxies. *ApJ*, **640**, 228–240. ADS-Link.

Tan, Q.-H., Gao, Y., Zhang, Z.-Y., and Xia, X.-Y. (2011). ^{12}CO, ^{13}CO and C^{18}O observations along the major axes of nearby bright infrared galaxies. *Research in Astronomy and Astrophysics*, **11**, 787–810. ADS-Link.

Tanner, A., Ghez, A. M., Morris, M., Becklin, E. E., Cotera, A., Ressler, M., Werner, M., and Wizinowich, P. (2002). Spatially Resolved Observations of the Galactic Center Source IRS 21. *ApJ*, **575**, 860–870. ADS-Link.

Tanner, A., Ghez, A. M., Morris, M. R., and Christou, J. C. (2005). Stellar Bow Shocks in the Northern Arm of the Galactic Center: More Members and Kinematics of the Massive Star Population. *ApJ*, **624**, 742–750. ADS-Link.

Theureau, G., Coudreau, N., Hallet, N., Hanski, M., Alsac, L., Bottinelli, L., Gouguenheim, L., Martin, J.-M., and Paturel, G. (2005). Kinematics of the local universe . XII. 21-cm line measurements of 586 galaxies with the new Nançay receiver. *A&A*, **430**, 373–383. ADS-Link.

Thornley, M. D., Lutz, D., Spoon, H. W. W., Kunze, D., Bertoldi, F., and Sternberg, A. (1997). Constraints on Star-Forming Regions and Starburst Galaxies from SWS Spectroscopy. In A. M. Heras, K. Leech, N. R. Trams, & M. Perry, editor, *The first ISO workshop on Analytical Spectroscopy*, volume 419 of *ESA Special Publication*, pages 155–+. ADS-Link.

Tremaine, S., Gebhardt, K., Bender, R., Bower, G., Dressler, A., Faber, S. M., Filippenko, A. V., Green, R., Grillmair, C., Ho, L. C., Kormendy, J., Lauer, T. R., Magorrian, J., Pinkney, J., and Richstone, D. (2002). The Slope of the Black Hole Mass versus Velocity Dispersion Correlation. *ApJ*, **574**, 740–753. ADS-Link.

Tremou, E., Garcia-Marin, M., Zuther, J., Eckart, A., Valencia-Schneider, M., Vitale, M., and Shan, C. (2015). A low-luminosity type-1 QSO sample. III. Optical spectroscopic properties and activity classification. *A&A*, **580**, A113. ADS-Link.

Urry, C. M. and Padovani, P. (1995). Unified Schemes for Radio-Loud Active Galactic Nuclei. *PASP*, **107**, 803. ADS-Link.

Urry, M. (2003). The AGN Paradigm for Radio-Loud Objects. In S. Collin, F. Combes, and I. Shlosman, editors, *Active Galactic Nuclei: From Central Engine to Host Galaxy*, volume 290 of *Astronomical Society of the Pacific Conference Series*, page 3. ADS-Link.

van den Bergh, S. (1988). Inclinations and axial ratios of spiral and irregular galaxies. *PASP*, **100**, 344. ADS-Link.

van der Tak, F. F. S., Boonman, A. M. S., Braakman, R., and van Dishoeck, E. F. (2003). Sulphur chemistry in the envelopes of massive young stars. *A&A*, **412**, 133–145. ADS-Link.

Vasyunina, T., Vasyunin, A. I., Herbst, E., and Linz, H. (2012). Chemical Modeling of Infrared Dark Clouds: The Role of Surface Chemistry. *ApJ*, **751**, 105. ADS-Link.

Veilleux, S., Rupke, D. S. N., Kim, D.-C., Genzel, R., Sturm, E., Lutz, D., Contursi, A., Schweitzer, M., Tacconi, L. J., Netzer, H., Sternberg, A., Mihos, J. C., Baker, A. J., Mazzarella, J. M., Lord, S., Sanders, D. B., Stockton, A., Joseph, R. D., and Barnes, J. E. (2009). Spitzer Quasar and Ulirg Evolution Study (QUEST). IV. Comparison of 1 Jy Ultraluminous Infrared Galaxies with Palomar-Green Quasars. *ApJS*, **182**, 628–666. ADS-Link.

Viehmann, T., Eckart, A., Schödel, R., Pott, J.-U., and Moultaka, J. (2006). Dusty Sources at the Galactic Center the N- and Q-Band Views with VISIR. *ApJ*, **642**, 861–867. ADS-Link.

Villar-Martín, M., Rodríguez, M., Drouart, G., Emonts, B., Colina, L., Humphrey, A., García Burillo, S., Graciá Carpio, J., Planesas, P., Pérez Torres, M., and Arribas, S. (2013). Molecular gas in type 2 quasars at z ~ 0.2-0.3. *MNRAS*, **434**, 978–991. ADS-Link.

Vollmer, B. and Duschl, W. J. (2000). The Minispiral in the Galactic Center revisited. *New Ast.*, **4**, 581–590. ADS-Link.

Voronkov, M. A., Caswell, J. L., Ellingsen, S. P., Breen, S. L., Britton, T. R., Green, J. A., Sobolev, A. M., and Walsh, A. J. (2012). New class I methanol masers. In R. S. Booth, W. H. T. Vlemmings, and E. M. L. Humphreys, editors, *IAU Symposium*, volume 287 of *IAU Symposium*, pages 433–440. ADS-Link.

Wang, J.-M. and Zhang, E.-P. (2007). The Unified Model of Active Galactic Nuclei. II. Evolutionary Connection. *ApJ*, **660**, 1072–1092. ADS-Link.

Weingartner, J. C. and Draine, B. T. (2001). Dust Grain-Size Distributions and Extinction in the Milky Way, Large Magellanic Cloud, and Small Magellanic Cloud. *ApJ*, **548**, 296–309. ADS-Link.

Wild, V., Heckman, T., and Charlot, S. (2010). Timing the starburst-AGN connection. *MNRAS*, **405**, 933–947. ADS-Link.

Wilkes, B. (2004). Spectral Energy Distributions of Quasars and AGN. In G. T. Richards and P. B. Hall, editors, *AGN Physics with the Sloan Digital Sky Survey*, volume 311 of *Astronomical Society of the Pacific Conference Series*, page 37. ADS-Link.

Wilkes, B. J., Schmidt, G. D., Smith, P. S., Mathur, S., and McLeod, K. K. (1995). Optical Detection of the Hidden Nuclear Engine in NGC 4258. *ApJ*, **455**, L13. ADS-Link.

Wilson, C. D. and Walker, C. E. (1994). Diffuse molecular clouds and the molecular interstellar medium from (13)CO observations of M33. *ApJ*, **432**, 148–157. ADS-Link.

Wilson, C. D., Howe, J. E., and Balogh, M. L. (1999). The Large-Scale J = 3 –> 2 and J = 2 –> 1 CO Emission from M17 and Its Implications for Extragalactic CO Observations. *ApJ*, **517**, 174–187. ADS-Link.

Wilson, C. D., Petitpas, G. R., Iono, D., Baker, A. J., Peck, A. B., Krips, M., Warren, B., Golding, J., Atkinson, A., Armus, L., Cox, T. J., Ho, P., Juvela, M., Matsushita, S., Mihos, J. C., Pihlstrom, Y., and Yun, M. S. (2008). Luminous Infrared Galaxies with the Submillimeter Array. I. Survey Overview and the Central Gas to Dust Ratio. *ApJS*, **178**, 189–224. ADS-Link.

Wilson, C. D., Warren, B. E., Israel, F. P., Serjeant, S., Attewell, D., Bendo, G. J., Butner, H. M., Chanial, P., Clements, D. L., Golding, J., Heesen, V., Irwin, J., Leech, J., Matthews, H. E., Mühle, S., Mortier, A. M. J., Petitpas, G., Sánchez-Gallego, J. R., Sinukoff, E., Shorten, K., Tan, B. K., Tilanus, R. P. J., Usero, A., Vaccari, M., Wiegert, T., Zhu, M., Alexander, D. M., Alexander, P., Azimlu, M., Barmby, P., Brar, R., Bridge, C., Brinks, E., Brooks, S., Coppin, K., Côté, S., Côté, P., Courteau, S., Davies, J., Eales, S., Fich, M., Hudson, M., Hughes, D. H., Ivison, R. J., Knapen, J. H., Page, M., Parkin, T. J., Rigopoulou, D., Rosolowsky, E., Seaquist, E. R., Spekkens, K., Tanvir, N., van der Hulst, J. M., van der Werf, P., Vlahakis, C., Webb, T. M., Weferling, B., and White, G. J. (2012). The JCMT Nearby Galaxies Legacy Survey - VIII. CO data and the $L_{CO(3-2)}$-L_{FIR} correlation in the SINGS sample. *MNRAS*, **424**, 3050–3080. ADS-Link.

Wisotzki, L., Christlieb, N., Bade, N., Beckmann, V., Köhler, T., Vanelle, C., and Reimers, D. (2000). The Hamburg/ESO survey for bright QSOs. III. A large flux-limited sample of QSOs. *A&A*, **358**, 77–87. ADS-Link.

Wright, E. L. (2006). A Cosmology Calculator for the World Wide Web. *PASP*, **118**, 1711–1715. ADS-Link.

Wright, M. C. H., Coil, A. L., McGary, R. S., Ho, P. T. P., and Harris, A. I. (2001). Molecular Tracers of the Central 12 Parsecs of the Galactic Center. *ApJ*, **551**, 254–268. ADS-Link.

Xu, C. K., Cao, C., Lu, N., Gao, Y., Diaz-Santos, T., Herrero-Illana, R., Meijerink, R., Privon, G., Zhao, Y.-H., Evans, A. S., König, S., Mazzarella, J. M., Aalto, S., Appleton, P., Armus, L., Charmandaris, V., Chu, J., Haan, S., Inami, H., Murphy, E. J., Sanders, D. B., Schulz, B., and van der Werf, P. (2015). ALMA Observations of Warm Dense Gas in NGC 1614 – Breaking of the Star Formation Law in the Central Kiloparsec. *ApJ*, **799**, 11. ADS-Link.

Young, J. S. and Sanders, D. B. (1986). Distributions of (C-13)O emission in the disks of late-type spiral galaxies. *ApJ*, **302**, 680–692. ADS-Link.

Young, J. S. and Scoville, N. Z. (1991). Molecular gas in galaxies. *ARA&A*, **29**, 581–625. ADS-Link.

Yuan, F., Markoff, S., and Falcke, H. (2002). A Jet-ADAF model for Sgr A*. *A&A*, **383**, 854–863. ADS-Link.

Yuan, F., Quataert, E., and Narayan, R. (2003). Nonthermal Electrons in Radiatively Inefficient Accretion Flow Models of Sagittarius A*. *ApJ*, **598**, 301–312. ADS-Link.

Yuan, T.-T., Kewley, L. J., and Sanders, D. B. (2010). The Role of Starburst-Active Galactic Nucleus Composites in Luminous Infrared Galaxy Mergers: Insights from the New Optical Classification Scheme. *ApJ*, **709**, 884–911. ADS-Link.

Yusef-Zadeh, F. and Morris, M. (1991). A windswept cometary tail on the Galactic center supergiant IRS 7. *ApJ*, **371**, L59–L62. ADS-Link.

Yusef-Zadeh, F., Stolovy, S. R., Burton, M., Wardle, M., and Ashley, M. C. B. (2001). High Spectral and Spatial Resolution Observations of Shocked Molecular Hydrogen at the Galactic Center. *ApJ*, **560**, 749–762. ADS-Link.

Yusef-Zadeh, F., Roberts, D., Wardle, M., Heinke, C. O., and Bower, G. C. (2006). Flaring Activity of Sagittarius A* at 43 and 22 GHz: Evidence for Expanding Hot Plasma. *ApJ*, **650**, 189–194. ADS-Link.

Yusef-Zadeh, F., Wardle, M., and Roy, S. (2007). Cosmic-Ray Heating of Molecular Gas in the Nuclear Disk: Low Star Formation Efficiency. *ApJ*, **665**, L123–L126. ADS-Link.

Yusef-Zadeh, F., Royster, M., Wardle, M., Arendt, R., Bushouse, H., Lis, D. C., Pound, M. W., Roberts, D. A., Whitney, B., and Wootten, A. (2013). ALMA Observations of the Galactic Center: SiO Outflows and High-mass Star Formation near Sgr A*. *ApJ*, **767**, L32. ADS-Link.

Zhao, J.-H. (2013). Miriad for SMA Data Reduction. In D. N. Friedel, editor, *Astronomical Data Analysis Software and Systems XXII*, volume 475 of *Astronomical Society of the Pacific Conference Series*, page 181. ADS-Link.

Zhao, J.-H., Goss, W. M., and Ho, P. T. P. (1995). VLA OH Observations of High Negative Velocity Gas toward Sagittarius A West: A High-Velocity Cloud Interacting with the Galactic Center. *ApJ*, **450**, 122. ADS-Link.

Zhao, J.-H., Morris, M. R., Goss, W. M., and An, T. (2009). Dynamics of Ionized Gas at the Galactic Center: Very Large Array Observations of the Three-dimensional Velocity Field and Location of the Ionized Streams in Sagittarius A West. *ApJ*, **699**, 186–214. ADS-Link.

Zhao, J.-H., Blundell, R., Moran, J. M., Downes, D., Schuster, K. F., and Marrone, D. P. (2010). The High-density Ionized Gas in the Central Parsec of the Galaxy. *ApJ*, **723**, 1097–1109. ADS-Link.

List of Figures

List of Tables

List of Acronyms

A&A	Astronomy & Astrophysics (journal)
ADAF	Advection Dominated Accretion Flow
ADIOS	Advection Dominated Inflow-Outflow Solution
AGN	active galactic nucleus
AKARI	AKARI/ASTRO-F satellite
ALMA	Atacama Large Millimeter/submillimeter Array
BH	black hole
BIMA	Berkeley-Illinois-Maryland Association
BLR	broad line region
CA	central association (of molecular gas clumps around Sgr A*)
CARMA	Combined Array for Research in Millimeter-wave Astronomy
CASA	Common Astronomy Software Application
CDM	Cold Dark Matter
CNA	CND-Northern Arm
CND	circumnuclear disk
CR	cosmic ray
CSO	Caltech Submillimeter Observatory
DR	dynamic range
EA	Eastern Arm (minispiral)
EB	Eastern Bridge (minispiral)
ESO	European Southern Observatory
FIR	far-infared
FOV	field of view
FOV10	field given by the 10% power full width of the primary beam
FWHM	full width at half maximum
FWZI	full width at zero intensity
GC	Galactic Center
GMC	giant molecular cloud
HST	Hubble Space Telescope
IMBH	intermediate mass black hole
IR	infared
IRAM	Institut de Radio Astronomie Millimétrique

IRAS	Infrared Astronomical Satellite
IRDC	infrared dark cloud
ISM	interstellar matter
ISO	Infrared Space Observatory
kpc	kiloparsec
ΛCDM	Λ Cold Dark Matter
LINER	low ionisation nuclear emission region galaxy
LIRG	Luminous Infrared Galaxy
LLAGN	low-luminosity active galactic nucleus
LLQSO	low-luminosity quasi stellar object
LOS	line of sight
LTE	local thermal equilibrium
MIR	mid-infared
NA	Northern Arm (minispiral)
NE	Northeastern (lobe; CND)
NEA	Northeastern Arm (CND)
NEE	Northeastern Extension (CND)
NLS1	Narrow-line Seyfert 1 galaxy
NIR	near-infared
NLR	narrow line region
NSC	nuclear stellar/star cluster
PA	position angle
pc	parsec
PdBI	Plateau de Bure Interferometer
PDR	photon dominated region
PSF	point spread function
PV	position-velocity (diagram, cut)
QSO	quasi stellar object
quasar	quasi stellar radio source
RIAF	Radiatively Inefficient Accretion Flow
rms	root mean square
RRL	radio recombination line
SED	spectral energy distribution
SE	Southern Extension (CND)
SEE	Southern Extension East (CND)
SEW	Southern Extension West (CND)
SFG	star-forming galaxy
SFR	starformation rate
Sgr A*	Sagittarius A*
SLED	spectral line energy distribution
SMA	Submillimeter Array
SMBH	supermassive black hole

SMG	sub-millimeter galaxy
SN	supernova
SNR	supernova remnant
S/N	signal to noise ratio
SSC	Synchrotron Self-Compton (emission)
sub-mm	sub-millimeter
SW	Southwestern (lobe; CND)
ULIRG	Ultraluminous Infrared Galaxy
UV	ultraviolet
VLBI	Very long baseline interferometry
WA	Western Arc (minispiral)
WR	Wolf-Rayet (star)
XDR	X-ray dominated region
YSO	young stellar object

Acknowledgements

I thank every one who supported me during my life with a PhD thesis.

In the first place, I want express my gratitude to Prof. Dr. Andreas Eckart for supervising my PhD thesis, for his guidance, his support and advice, and the many fruitful and often funny discussions. I also want to thank Prof. Dr. Anton Zensus und Silke Britzen for their support towards the end of my thesis. I thank Alvaro for giving me the orientation necessary for not getting lost in my data. The four of you - my belated thesis committee - gave me the advice, courage, and kick needed to finalize the GC paper and with it my thesis.

Alvaro, Miguel, Melanie, and Julia - thank you so much for your support and advice on my work! Your expert knowledge was vital for my courage for publication! To all my co-authors - thank you so much for your time and advice that put the papers into the shape they are now!

This work was supported in part by the German Deutsche Forschungsgemeinschaft, DFG, via grant SFB 956 and the International Max Planck Research School (IMPRS) for Astronomy and Astrophysics at the MPIfR and the Universities of Bonn and Cologne.

Above all, I appreciate it very much that I was allowed to visit and observe with some of the world's best telescopes - I thank the staff at the VLT and APEX (and ALMA), and the staff and MPIfR VLBI group people at the Effelsberg 100 m telescope for the great experience!

Nadeen and Banafsheh, my therapists! The many chats with you were comforting and often enough superfunny - and accompanied with a lot of ice cream! Banafsheh, I will never forget our time as a room mates in Santa Fe! It made me feel like being back at school times - so cool!

I thank my former office mates Imke, Steffen, Jens, Matthew, Marzieh, Nastaran, Celine, and Dhanya for the relaxed and cheerful atmosphere and chats! And I miss the traditional salad sessions with Imke and Rebekka as well as the coffee breaks and chats with them and our secretaries Stefanie and Tanja who gave me all kinds of non-science help and advice. Semir, Senol, Gerold - thanks for the many - often funny silly - talks on science and life! Macarena, your humour, motherly support, and calmth are magic! We are missing you here! Greetings to my old Ph1 colleagues and new ALMA comrades Devaky and Abhijeet!

I am grateful to have met so many people from all over the world and for learning about aspects of their culture, politics, social life, souls, and food.

I will miss the people and the life at Ph1! Thanks to everyone, also the ones I forgot to mention here, for the good time!

Toni, Mary, Mama & Papa - hanging out several afternoons and evening with my BFFs and family was always the right medicine - laughing about all kinds of things - at least as long as you didn't mention the thesis. Thank you for you emotional support and being there when I needed you.

Mama: Do you know how much your words meant to me, when you said: 'No matter how you decide, we will support you!'

My Sebastian - you went with me through my diploma thesis, so you knew what was ahead and didn't run for your life. You watched me hitting dead points, dead motivation and my self-pity and you always tried to change my view and encouraged me to keep on, while you were covering my back. Thank you so much for your sacrifices, your patience and your love!

Astronomy and Astrophysics
Editor in Chief: T. Forveille

T. Forveille
Astronomy & Astrophysics
Observatoire de Paris
61, avenue de l'Observatoire
75014 Paris, France

Tel.: 33 0(1) 43 29 05 41
Fax: 33 0(1) 43 29 05 57
e-mail: aanda.paris@obspm.fr
Web: http://www.aanda.org

merging
Annales d'Astrophysique
Arkiv for Astronomi
Bulletin of the Astronomical Institutes of the Netherlands
Bulletin Astronomique
Journal des Observateurs
Zeitschrift fur Astrophysik
Bulletin of the Astronomical Institutes of Czechoslovakia

Paris, March 21, 2016

Reprint Permission

Material:
Figs. 1-11 and Tables 1-9 from Moser et al. 2016, A&A, 587, A137

To be used in:
PhD thesis, University of Cologne

Permission granted to:
Lydia Moser
University of Cologne
moser@ph1.uni-koeln.de

I hold copyright on the material referred to above, and hereby grant permission for its use as requested herewith. The credit should be given as follows:
Credit: Author, A&A, vol, page, year, reproduced with permission © ESO.

Thierry Forveille
A&A Editor-in-Chief

Sponsored by Argentina, Austria, Belgium, Brazil, Chile, Czech Republic, Denmark, Estonia, Finland, France, Germany, Greece, Hungary, Italy, Netherlands, Poland, Portugal, Slovak Republic, Spain, Sweden, and Switzerland.
Produced and distributed by EDP Sciences for ESO.

Astronomy and Astrophysics
Editor in Chief: T. Forveille

T. Forveille
Astronomy & Astrophysics
Observatoire de Paris
61, avenue de l'Observatoire
75014 Paris, France

Tel.: 33 0(1) 43 29 05 41
Fax: 33 0(1) 43 29 05 57
e-mail: aanda.paris@obspm.fr
Web: http://www.aanda.org

merging
Annales d'Astrophysique
Arkiv for Astronomi
Bulletin of the Astronomical Institutes
of the Netherlands
Bulletin Astronomique
Journal des Observateurs
Zeitschrift fur Astrophysik
Bulletin of the Astronomical Institutes
of Czechoslovakia

Paris, May 16, 2017

Reprint Permission

Material:
All tables and figures in Moser et al. 2017, A&A, in press, DOI 10.1051/0004-6361/201628385

To be used in:
PhD thesis, University of Cologne

Permission granted to:
Lydia Moser
1. Physikalisches Institut
University of Cologne
Zuelpicher Str. 77
50937 Cologne
Germany
moser@ph1.uni-koeln.de

I hold copyright on the material referred to above, and hereby grant permission for its use as requested herewith. Credit should be given as follows:
Credit: Author, A&A, vol, page, year, reproduced with permission © ESO.

Thierry Forveille
A&A Editor-in-Chief

Sponsored by Argentina, Austria, Belgium, Brazil, Chile, Czech Republic, Denmark, Estonia, Finland, France, Germany, Greece, Hungary, Italy, Netherlands, Poland, Portugal, Slovak Republic, Spain, Sweden, and Switzerland.
Produced and distributed by EDP Sciences for ESO.

Erklärung

Ich versichere, daß ich die von mir vorgelegte Dissertation selbständig angefertigt, die benutzten Quellen und Hilfsmittel vollständig angegeben und die Stellen der Arbeit – einschließlich Tabellen, Karten und Abbildungen –, die anderen Werken im Wortlaut oder dem Sinn nach entnommen sind, in jedem Einzelfall als Entlehnung kenntlich gemacht habe; daß diese Dissertation noch keiner anderen Fakultät oder Universität zur Prüfung vorgelegen hat; daß sie – abgesehen von unten angegebenen Teilpublikationen – noch nicht veröffentlicht worden ist, sowie, daß ich eine solche Veröffentlichung vor Abschluß des Promotionsverfahrens nicht vornehmen werde. Die Bestimmungen dieser Promotionsordnung sind mir bekannt.

Die von mir vorgelegte Dissertation ist von Prof. Dr. Andreas Eckart betreut worden.

Köln, 30.05.2017

Teilpublikationen

- **Moser, L.**; Sánchez-Monge, Á.; Eckart, A.; Requena-Torres, M. A., García-Marín, M.; Kunneriath, D.; Zensus, A.; Britzen, S.; Sabha, N.; Shahzamanian, B.; Borkar, A.; Fischer, S.; *"Approaching hell's kitchen: molecular daredevil clouds in the vicinity of Sgr A*"*, Astronomy & Astrophysics, accepted 12-2016, in press

- **Moser, L.**; Krips, M.; Busch, G.; Scharwächter, J.; König, S.; Eckart, A.; Smajić, S.; García-Marín, M.; Valencia-S., M.; Fischer, S.; Dierkes, J.; *"A low-luminosity type-1 QSO sample: IV. Molecular gas contents and conditions of star formation in three nearby Seyfert galaxies"*, Astronomy & Astrophysics, Volume 587, id.A137

- **Moser, L.**; Eckart, A.; Borkar, A.; García-Marín, M.; Kunneriath, D.; Jalali, B.; Sabha, N.; Shahzamanian, B.; Valencia-S., M.; Zamaninasab, M.; Bronfman, L.; Finger, R.;*"Sgr A West in the light of molecules: cold and dense gas east of the circumnuclear disk"*, Proceedings of the International Astronomical Union, Volume 303, pp. 86-88

- **Moser, L.**; Zuther, J.; Busch, G.; Valencia-S., M.; Eckart, A.; *"A low-redshift low luminosity QSO sample: Comparison with NUGA galaxies and PG QSOs and first*

interferometric images of three sample members", Proceedings of Nuclei of Seyfert galaxies and QSOs - Central engine & conditions of star formation (Seyfert 2012). 6-8 November, 2012. Max-Planck-Insitut für Radioastronomie (MPIfR), Bonn, Germany. Online at http://pos.sissa.it/cgi-bin/reader/conf.cgi?confid=169, id.69

- **Moser, L.**; Zuther, J.; Fischer, S.; Eckart, A.; *"The Radio nucluei of z~2 X-ray bright AGN"*, Proceedings of the 10th European VLBI Network Symposium and EVN Users Meeting: VLBI and the new generation of radio arrays. September 20-24, 2010. Manchester, UK. Published online at http://pos.sissa.it/cgi-bin/reader/conf.cgi?confid=125, id.102

- **Moser, L.**; Eckart, A.; Horrobin, M.; Lindhorst, B.; Rost, S.; Straubmeier, C.; Tremou, E.; Wank, I.; Zuther, J.; Bertram, T.; *"The LINC-NIRVANA fringe and flexure tracker: first measurements of the testbed interferometer"*, Proceedings of the SPIE, Volume 7734, id. 77342X (2010)

Weitere Publikationen

Refereed

- Busch, G.; Fazeli, N.; Eckart, A.; Valencia-S., M.; Smajić, S.; **Moser, L.**; Scharwächter, J.; M.; Dierkes, J.; Fischer, S.; *"A low-luminosity type-1 QSO sample. V. Overluminous host spheroids and their excitation mechanisms"*, Astronomy & Astrophysics, Volume 587, id.A138

- Smajić, S.; **Moser, L.**; Eckart, A.; Busch, G.; Combes, F.; García-Burillo, S.; Valencia-S., M.; Horrobin, M.; *"The nuclear gas disk of NGC 1566 dissected by SINFONI and ALMA"*, Astronomy & Astrophysics, Volume 583, id.A104

- Busch, G.; Smajić, S.; Scharwächter, J.; Eckart, A.; Valencia-S., M.; **Moser, L.**; Husemann, B.; Krips, M.; Zuther, J.; *"A low-luminosity type-1 QSO sample. II. Tracing circumnuclear star formation in HE 1029-1831 with SINFONI"*, Astronomy & Astrophysics, Volume 575, id.A128

- Valencia-S., M.; Eckart, A.; Zajacek, M.; Peissker, F.; Parsa, M.; Grosso, N.; Mossoux, E.; Porquet, D.; Jalali, B.; Karas, V.; Yazici, S.; Shahzamanian, B.; Sabha, N.; Saalfeld, R.; Smajić, S.; Grellmann, R.; **Moser, L.**; Horrobin, M.; Borkar, A.; García-Marín, M.; Dovciak, M.; Kunneriath, D.; Karssen, G. D.; Bursa, M.; Straubmeier, C.; Bushouse, H.; *"Monitoring the Dusty S-cluster Object (DSO/G2) on its Orbit toward the Galactic Center Black Hole"*, The Astrophysical Journal, Volume 800, Issue 2, article id. 125

- Jalali, B.; Pelupessy, F. I.; Eckart, A.; Portegies Zwart, S.; Sabha, N.; Borkar, A.; Moultaka, J.; Muzic, K.; **Moser, L.**; *"Star formation in the vicinity of nuclear black holes: young stellar objects close to Sgr A*"*, Monthly Notices of the Royal Astronomical Society, Volume 444, Issue 2

- Smajić, S.; **Moser, L.**; Eckart, A.; Valencia-S., M.; Combes, F.; Horrobin, M.; García-Burillo, S.; García-Marín, M.; Fischer, S.; Zuther, J.; *"ALMA-backed NIR high resolution integral field spectroscopy of the NUGA galaxy NGC 1433"*, Astronomy & Astrophysics, Volume 567, id.A119

- Busch, G.; Zuther, J.; Valencia-S., M.; **Moser, L.**; Fischer, S.; Eckart, A.; Scharwächter, J.; Gadotti, D. A.; Wisotzki, L.; *"A low-luminosity type-1 QSO sample. I. Overluminous host spheroidals or undermassive black holes"*, Astronomy & Astrophysics, Volume 561, id.A140

- Eckart, A.; Muzic, K.; Yazici, S.; Sabha, N.; Shahzamanian, B.; Witzel, G.; **Moser, L.**; García-Marín, M.; Valencia-S., M.; Jalali, B.; Bremer, M.; Straubmeier, C.; Rauch, C.; Buchholz, R.; Kunneriath, D. and Moultaka, J.; *"Near-infrared proper motions and spectroscopy of infrared excess sources at the Galactic center"*, Astronomy & Astrophysics, Volume 551, id.A18

- Eckart, A.; García-Marín, M.; Vogel, S. N.; Teuben, P.; Morris, M. R.; Baganoff, F.; Dexter, J.; Schödel, R.; Witzel, G.; Valencia-S., M.; Karas, V.; Kunneriath, D.; Straubmeier, C.; **Moser, L.**; Sabha, N.; Buchholz, R.; Zamaninasab, M.; Muzic, K.; Moultaka, J. and Zensus, J. A.; *"Millimeter to X-ray flares from Sagittarius A*"*, Astronomy & Astrophysics, Volume 537, id.A52

Conference Proceedings

- Gima, K.; Mills, E. A.; Rosero, V. A.; Liu, H. B.; Harada, N.; Requena Torres, M. A.; Morris, M.; Riquelme, D.; Zhao, J.-H.; **Moser, L.**; Martin, S.; Ho, P. T. P.; Ginsburg, A.; Wardle, M.; Guesten, R.; *"Estimating Circumnuclear Disk temperatures using ALMA data"*, American Astronomical Society, AAS Meeting #227, id.341.09

- Busch, G.; Fazeli, N.; Smajić, S.; Eckart, A.; **Moser, L.**; Valencia-S., M.; *"Conditions for Star Formation in nearby AGN and QSO hosts observed with near-infrared integral-field spectroscopy"*, Demographics and Environment of AGN from Multi-Wavelength Surveys, Proceedings of a conference held 21-24 September, 2015 on Crete Island, Chania, id.13

- Busch, G.; Smajić, S.; **Moser, L.**; Valencia-S., M.; Zuther, J.; Scharwächter, Julia; Eckart, A.; *"A low-luminosity type-1 QSO sample: Insight from integral-field spectroscopy"*, Galaxies in 3D across the Universe, Proceedings of the International Astronomical Union, IAU Symposium, Volume 309

- Sabha, N.; Zamaninasab, M.; Eckart, A.; **Moser, L.**;*"A new MIR bow shock source in the Galactic center"*, Proceedings of the International Astronomical Union, Volume 303, pp. 150-152

- Eckart, A.; Horrobin, M.; Britzen, S.; Zamaninasab, M.; Muzic, K.; Sabha, N.; Shahzamanian, B.; Yazici, S.; **Moser, L.**; García-Marín, M.; Valencia-S., M.; Borkar, A.; Bursa, M.; Karssen, G.; Karas, V.; Zajacek, M.; Bronfman, L.; Finger, R.; Jalali, B.; Vitale, M.; Rauch, C.; Kunneriath, D.; Moultaka, J.; Straubmeier, C.; Rashed, Y. E.; Markakis, K.; Zensus, A.;*"The infrared K-band identification of the DSO/G2 source from VLT and Keck data"*, Proceedings of the International Astronomical Union, Volume 303, pp. 269-273

- Jalali, B.; Pelupessy, F. I.; Eckart, A.; Portegies Zwart, S.; Sabha, N.; Borkar, A.; Moultaka, J.; Muzic, K.; **Moser, L.**; *"Young stellar objects close to Sgr A*"*, Proceedings of the International Astronomical Union, Volume 303, pp. 144-146

- Eckart, A.; Muzic, K.; Yazici, S.; Sabha, N.; Shahzamanian, B.; Witzel, G.; **Moser, L.**; Garcia-Marin, M.; Valencia-S., M.; Jalali, B.; Bremer, M.; Straubmeier, C.; Rauch, C.; Buchholz, R.; Kunneriath, D.; Moultaka, J.;*"The broad band spectral properties of SgrA* . The fate of the dusty object approaching the center"*, Memorie della Societa Astronomica Italiana, v.84, p.618

- Eckart, A.; Sabha, N.; Witzel, G.; Straubmeier, C.; Shahzamanian, B.; Valencia-S., M.; García-Marín, M.; Horrobin, M.; **Moser, L.**; Zuther, J.; Fischer, S.; Rauch, C.; Rost, S.; Iserlohe, C.; Yazici, S.; Smajić, S.; Wiest, M.; Araujo-Hauck, C.; Wank, I.;*"Beating the confusion limit: the necessity of high angular resolution for probing the physics of Sagittarius A* and its environment: opportunities for LINC-NIRVANA (LBT), GRAVITY (VLTI) and and METIS (E-ELT)"*, Optical and Infrared Interferometry III. Proceedings of the SPIE, Volume 8445, article id. 84451F

- Valencia-S, M.; Eckart, A.; Zuther, J.; Fischer, S.; Smajić, S.; Iserlohe, C.; GarcÃa-MarÃn, M.; **Moser, L.**; Bremer, M.; Vitale, M.; *"Discovery of an Intermediate Mass Black Hole at the center of the starburst/Seyfert composite galaxy IRAS 01072+4954"*, Journal of Physics: Conference Series, Volume 372, Issue 1, id. 012048

- Eckart, A.; García-Marín, M.; Vogel, S. N.; Teuben, P.; Morris, M. R.; Baganoff, F.; Dexter, J.; Schödel, R.; Witzel, G.; Valencia-S, M.; Karas, V.; Kunneriath, D.; Bremer, M.; Straubmeier, C.; **Moser, L.**; Sabha, N.; Buchholz, R.; Zamaninasab, M.; MuÅ¾iÄ‡, K.; Moultaka, J.; Zensus, J. A.;*"Flare emission from Sagittarius A*"*, Journal of Physics: Conference Series, Volume 372, Issue 1, id. 012022

- Eckart, A.; Britzen, S.; Horrobin, M.; Zamaninasab, M.; Muzic, K.; Sabha, N.; Shahzamanian, B.; Yazici, S.; **Moser, L.**; Zuther, J.; Garcia-Marin, M.; Valencia-S., M.; Bursa, M.; Karssen, G.; Karas, V.; Jalali, B.; Vitale, M.; Bremer, M.; Fischer, S.; Smajić, S.; Rauch, C.; Kunneriath, D.; Moultaka, J.; Straubmeier, C.; Rashed, Y. E.; Iserlohe, C.; Busch, G.; Markakis, K.; Borkar, A.; Zensus, A. J.;*"The Galactic Center as a paradigm for low-luminosity nuclei? What can be learned from SgrA* for the central engine and conditions of star formation in nuclei of Seyfert galaxies and low* *luminosity nearby QSOs; The K-band identification of the DSO/G2 source from VLT and Keck data"*, Proceedings of Nuclei of Seyfert galaxies and QSOs - Central engine & conditions of star formation (Seyfert 2012). 6-8 November, 2012. Max-Planck-Insitut für Radioastronomie (MPIfR), Bonn, Germany. Online at http://pos.sissa.it/cgi-bin/reader/conf.cgi?confid=169, id.4

- Busch, G.; Zuther, J.; Valencia-S., M.; **Moser, L.**; Eckart, A.; *"A low-luminosity type-1 QSO sample: Near-infrared study of nearby AGN host galaxies"*, Proceedings of Nuclei of Seyfert galaxies and QSOs - Central engine & conditions of star formation (Seyfert 2012). 6-8 November, 2012. Max-Planck-Insitut für Radioastronomie (MPIfR), Bonn, Germany. Online at http://pos.sissa.it/cgi-bin/reader/conf.cgi?confid=169, id.60

- Valencia-S., M.; Zuther, J.; Eckart, A.; Smajić, S.; Iserlohe, C.; Garcia-Marin, M.; Busch, G.; Vitale, M.; Bremer, M.; Horrobin, M.; **Moser, L.**; Rashed, Y. E.; *"Are Narrow Line Seyfert 1 galaxies a special class of Active Galactic Nuclei?"*, Proceedings of Nuclei of Seyfert galaxies and QSOs - Central engine & conditions of star formation (Seyfert 2012). 6-8 November, 2012. Max-Planck-Insitut für Radioastronomie (MPIfR), Bonn, Germany. Online at http://pos.sissa.it/cgi-bin/reader/conf.cgi?confid=169, id.17

- Zuther, J.; Eckart, A.; Bertram, T.; Horrobin, M.; Lindhorst, B.; Lindhorst, U.; **Moser, L.**; Rost, S.; Straubmeier, C.; Tremou, E.; Wank, I.; *"The LINC-NIRVANA fringe and flexure tracker: an update of the opto-mechanical system"*, Proceedings of the SPIE, Volume 7734, id. 773448 (2010)

- Tremou, E.; Eckart, A.; Horrobin, M.; Lindhorst, B.; **Moser, L.**; Rost, S.; Smajić, S.; Straubmeier, C.; Wank, I.; Zuther, J.; Bertram, T.; *"The LINC-NIRVANA fringe and flexure tracker: laboratory tests"*, Proceedings of the SPIE, Volume 7734, id. 773441 (2010)

- Horrobin, M.; Eckart, A.; Lindhorst, B.; Lindhorst, U.; **Moser, L.**; Rost, S.; Smajić, S.; Straubmeier, C.; Tremou, E.; Wank, I.; Zuther, J.; Bertram, T.; Arcidiacono, C.; *"Fringe detection and piston variability in LINC-NIRVANA"*, Proceedings of the SPIE, Volume 7734, id. 77341X (2010)

- Rost, S.; Eckart, A.; Horrobin, M.; Lindhorst, B.; Lindhorst, U.; **Moser, L.**; Smajić, S.; Straubmeier, C.; Tremou, E.; Wank, I.; Zuther, J.; Bertram, T.; *"The LINC-NIRVANA fringe and flexure tracker: control design overview"*, Proceedings of the SPIE, Volume 7734, id. 77341V (2010)